Engineering Smart Skis

Peter Watson

A thesis submitted to the University of Edinburgh
for the Degree of Doctor of Philosophy

Centre for Materials Science & Engineering
September 2004

EX LIBRIS UNIV. EDINBURGH

Acknowledgements

Financial support from an EPSRC CASE sponsored award is appreciated, as is input provided by ARUP's Advanced Technology Group (EPSRC CASE sponsors). The financial support provided by ReacTec Ltd. is similarly appreciated, with a significant portion of the hardware costs having been met by the Company - initially established with the aim of realising the commercial potential of this research.

The continued support from Dr. Jane Blackford (postgraduate supervisor) throughout the course of this project is greatly appreciated. Without Jane's enthusiasm and interest in sports engineering research this work would not have started and subsequently ReacTec would never have existed.

Thanks are owed to colleagues at ReacTec, who have contributed to a unique experience. In particular, thanks to Mark-Paul Buckingham and Tim Kent for seeing the potential in the technology and investing themselves in the commercial effort. Thanks also to Michael 'Jimmy' van Zwanenberg for helping field-test the instrumented skis and for his analytical and practical input, particularly with regard to work on MR fluid devices. The contribution made by Angus Wardlaw on the design and build of the ski simulator is similarly recognised.

The assistance provided by Grant Wheeler (Scottish Enterprise) with the 2001 Edinburgh Technology Fund Student Business Plan Competition and the confidence shown by Keith Winton (Edinburgh Technology Fund) have had a significant impact on the direction of this research and the ReacTec experience. Patent advice and assistance from Arlene Campbell (Kennedys Group) has been instrumental in raising the value of ReacTec, helping to establish and develop IPR (i.e., Intellectual Property Rights) from this research.

The support provided by my partner, Lucia Cardone, is appreciated above all. Lucia's contribution in the lab and her analytical input has been invaluable to the completion of this work.

Abstract

A concept has been evaluated for adaptive vibration control of shaped alpine skis using magnetorheological (MR) fluid. This work presents the motivation behind the concept and the work to verify its viability, technically and commercially. The technical literature is reviewed, relevant to understanding ski dynamics. Literature on smart materials is similarly researched and presented to establish understanding of the use of the technology for dynamic control.

The influence of geometry, materials and construction on ski dynamics is presented and conventional vibration control techniques and their influence on the dynamic control of modern alpine skis are explained. A review of the boundary conditions used in modelling ski dynamics is presented and the influence of skier position and environmental conditions are examined. Existing applications of smart technology in skis are discussed, with reference to a shape memory alloy concept and commercially available piezo-systems.

Procedures for quantifying the physical characteristics of a ski are examined and a custom-built laboratory rig is used to test skis under controlled, repeatable conditions. Results from static and dynamic laboratory tests on skis are used to perform system analysis, with reference to the technical literature. Analysis of the vibration dynamics of the moving ski during skiing (i.e., signal analysis) is carried out on results from field-tests of instrumented skis.

An introduction to the physics, chemistry and application of controllable rheological fluids is presented with emphasis on MR fluid. Considerations are discussed for MR fluid device design - including control concepts. Applications of MR fluid are discussed as examples of what can be achieved, with damping being of particular interest to this work. Preliminary test results from a prototype MR fluid damper are presented.

The technical objectives and perceived benefits of adaptive vibration control of skis with MR fluid are examined and technical and commercial system constraints are identified. Results are presented from laboratory tests investigating ski fore-body vibration control on a concept demonstrator, comprising a MR fluid damper integrated into a simplified ski-like structure. Subsequent analysis is carried out to review the technical and commercial viability of the concept.

CONTENTS

Appendices

Table of Figures

Tables

1 Introduction

This work establishes a concept for controlling ski vibrations by changing viscoelastic characteristics, based on the monitored vibratory response of the ski. Original research is presented following advanced study of technical literature on ski dynamics, with verification of the concept supporting commercial efforts to launch a collaborative development with a ski manufacturer.

A novel system is proposed for adaptive vibration control of skis, using a combination of smart materials (see §1.2). The system aims to improve dynamic stability of skis over an increased operating range, by changing the viscoelastic properties of a damper filled with a controllable fluid (i.e., magnetorheological fluid), based on monitored vibrations from an integrated piezo-polymer sensor array. It is intended that the system be parasitically powered by piezo-ceramic elements that harvest power (proportional to rate of change of strain) – not from the vibrating ski, but from the movement of the skier in the bindings.

The movement of the skier (i.e., the positioning of the skier's legs and centre of gravity) to "edge" the ski (i.e., to put the ski onto a metal edge) provides direction and speed control. Enhanced control over variable snow conditions is the perceived benefit of the adaptive ski, improving the ability to "hold" an edge by semi-actively reducing "chatter" (i.e., when the ski and particularly the edge vibrates) and damping vibration prior to the initiation and execution of a turn. The premise of the concept presented here is that stiffness and damping characteristics of the ski can be adapted to better suit the surface conditions and either enhance control or reduce skier fatigue.

Skiing has been transformed with the introduction of shaped, carving skis. Ski width, geometry and length has evolved faster in the last 10-15 years than any time before. The theoretical top speed is being reduced with shorter ski length, while performance is increasing as a result of enhanced handling characteristics. It is not only race skiers that benefit from the shaped ski revolution. Recreational skiers are now required to do less work, enabling them to ski over a wider range of snow conditions and reducing fatigue to make it possible to ski longer - assuming the attraction of piste cafés can be resisted. The reduction in fatigue provides a real commercial advantage for ski manufacturers – not only increasing the "feel good" factor, but also encouraging ageing customers to maintain an active interest in the sport.

In this work, an understanding of ski dynamics is established with reference to technical literature and engineering texts (see §2). The influence of the composite construction and constituent materials on the physical properties of the ski is discussed. Viscoelasticity is introduced with regard to conventional passive vibration control of skis. Research on alpine skis is reviewed with focus on

work that either models or measures dynamic behaviour. Dynamic stability as a function of stiffness and damping is recognised, with reference to their influence on a harmonically excited system. Modelling considerations are presented for a ski as a distributed or discrete system. Skier position and environmental conditions (also recognised to be difficult to quantify) are acknowledged to be significant to the ski response, with increased modelling complexity if included. Previous attempts to engineer smart skis are discussed.

Ski dynamic measurements are made on custom-built laboratory hardware with the aim of identifying system characteristics (see §3). This includes quantification of ski stiffness and investigation of dynamic response. Techniques are established to analyse the dynamic response of skis from laboratory based tests. Field-tests of instrumented skis are carried out to investigate the feasibility of feedback control for the adaptive system, based on an integrated array of piezo-polymer sensors.

The physical behaviour of magnetorheological fluid is reviewed (see §4) and compared to other controllable fluids. The chemical composition of MR fluid is considered, to understand factors that influence the design and behaviour of a MR fluid device suitable for application on a ski. MR fluid damping is investigated experimentally, with a prototype diaphragm sealed damper being designed, built and tested and its viscoelastic behaviour qualitatively and quantitatively appraised.

The direction of this research has been influenced by efforts (on behalf of ReacTec Ltd. – see §1.1) to commercialise the technology – particularly, the necessity to physically demonstrate the use of MR fluid in controlling a ski-like structure and thereby verify the concept to interested parties in the European ski industry.

The adaptive ski system comprises a mix of materials: specifically piezoelectric polymer sensors, magnetorheological (MR) fluid actuators and a piezo-ceramic power generator. The adaptive ski concept is explained (see §5), with specifications being established, technical risk recognised and commercialisation efforts reported. The practicalities of vibration control with MR fluid are examined and include results from laboratory demonstration on a ski-like structure. The design of the concept demonstrator is appraised with reference to observations from field-tests of a custom-built shim and a finite element model.

More testing is required to provide quantitative information on ski dynamic characteristics; therefore, the concept demonstrator must not be considered a fully specified system. Opportunities are presented for further work (see §6): to provide data on ski behaviour for improved modelling; to develop a prototype MR fluid device; and, confront the primary technical concerns associated with the adaptive ski system (i.e., power supply).

1.1 ReacTec

ReacTec (Ltd.) was established in 2001, following a runner-up place in the Edinburgh Technology Fund (ETF) student business plan competition. A patent application [Watson, 2001] relating to the adaptive ski concept was filed in December 2001 to protect the intellectual property rights (IPR) assigned to the Company (i.e., ReacTec owns the patent).

Initial focus was on the development of the adaptive ski concept and, coincided with field-testing of instrumented skis. Contact was made with a number of European ski manufacturers to gauge interest. First round investment funding was secured in 2002 and supported with a Scottish Innovation Support (SCIS) award from Scottish Enterprise. The funding was used to develop custom-built laboratory hardware to test skis and snowboards. The funding also enabled the practicalities of vibration control with MR fluid to be examined. A concept demonstrator was constructed on a ski-like structure and shown to a number of European ski companies, with a view to securing funding for further development.

Commercial efforts have influenced the direction of this work and following press interest in the adaptive ski, an opportunity was presented to develop the adaptive system for a diverse application (i.e., hand-held power tools). A second patent application [Watson, 2004] was drafted in 2003 to protect the intellectual property associated with a short stroke, diaphragm sealed MR fluid damper.

The Company was also runner-up in the 2002 Scottish Enterprise, student business plan competition and in 2003 a Department of Trade and Industry (DTI) SMART award was used to fund development of a generic microprocessor controller (not covered in this work). The Company has since (in 2004) secured a substantial second round of investment funding and is seeking to develop commercial opportunities.

Fundamentally, this work would not have been possible (and ReacTec not established) without the gratefully acknowledged financial support from an EPSRC grant, CASE sponsored by ARUP Advanced Technology Group (ATG).

1.2 Smart technology in sport

In a similar way that nerves interact with muscles in the human body, sensors integrated in a smart structure monitor environmental parameters, such as vibrations, providing feedback to a control interface that determines an appropriate response from an active material. Transducers that provide some measurable change with the environmental conditions that are to be controlled can be considered for use as sensors (e.g., piezo-ceramics and piezo-polymers). The required force-control should dictate the selection of the active (smart) material (e.g., piezo-ceramics, controllable fluids, shape memory alloys) able to provide the desired enhanced structural functionality. Control of the actuator output is provided by an interface that is capable of processing the sensor input.

There is a significant body of work on the application of smart technology, some of which has been commercialised for use in sports equipment.

Smart sports bras have been researched (at the University of Wollongong, Australia), with polymer sensors monitoring breast loading. The information from the sensors is used by an integrated microchip as the basis for control of a polymer fabric (i.e., based on a polyacrylamide) that expands and contracts to tighten and loosen straps or cups depending on breast movement. The system is being commercially developed with initial support from Marks and Spencer.

Smart technology has been proposed for use on mountain-bike suspension, with Specialized aiming to introduce automatically adjustable rear shock absorbers. Smart shock absorbers are commercially available on K2 bikes [www.K2bike.com], with a piezo-controlled valve being used to adjust the suspension performance. The K2 system was produced in collaboration with Active Control eXperts (ACX), who have also developed piezoelectric damping systems for skis and snowboards (see §2.5). A piezo-polymer fibre vibration control system is presently available on Head skis [www.head.com/ski/] and has been extended for use in their tennis rackets [www.head.com/tennis/] with the aim of alleviating tennis elbow by reducing shock induced vibration.

Adaptive cushioning on the Adidas "1" sports shoe is achieved with microprocessor control of an electromagnetic actuator, based on readings from electronic sensors. There is additional manual control, with the wearer able to alter cushioning by operating buttons on the side of the shoe. The system has taken Adidas three years to develop and is battery powered and weighs 40g (i.e., 10% of the weight of the 400g shoes).

A variety of vibration control applications for MR fluid have been reported (see §4.3.6) – including automotive suspension and engine mounts (commercially available on some cars from Cadillac).

The adaptive ski proposed here requires (due to International Ski Federation rules and manufacturer requirements) a significant feature additional to the sensor-control-actuator smart system. The ski must ultimately be able to harvest enough electrical-energy to power the smart system. Although this work focuses on the MR fluid actuator, considerations are given to power supply constraints. Proposals for vibration monitoring are investigated and, while control is not studied in this work, dynamic signal processing techniques are discussed and may form the basis for development of control algorithms. Therefore, this research is the foundation for work to engineer adaptive smart skis with MR fluid actuators.

2 Ski Dynamics

Factors that influence the dynamic performance of skis are presented with reference to literature on skis and research that is primarily focused on alpine skis. This is supported with explanation of the relevant engineering principles. Subsequent work builds on the fundamental understanding that is established here.

Ski dynamics are introduced with a review of the materials and construction methods used, particularly in the manufacture of modern alpine skis. The mechanical and dynamic properties are considered and methods of vibration control in skis are presented. Dynamic performance is discussed in terms of deflection, velocity and acceleration. The mechanics of alpine skiing are considered, with a view to establishing dynamic models that can be investigated experimentally (see §3) and used in subsequent work. The motivation for considering integration of smart technology is discussed (see §2.5) and the state-of-the-art is evaluated with respect to commercially available smart skis (i.e., from Head, and previously from K2) and those under investigation (i.e., from Stöckli).

2.1 Ski properties

It is necessary to understand how a ski responds to skier movement and how it interacts with its environment in order to understand the potential advantage of applying smart technology to enhance dynamic performance.

The interaction of the composite structure of the ski with its environment is a complex dynamic problem - with random excitation and other varying boundary conditions. The behaviour of a ski, and therefore its suitability for a particular application or skier, depends on the physical properties of the ski. The materials and construction technique (see §2.1.2) used to produce the composite structure influence how the ski will respond to static and, more importantly, dynamic loading. Geometry (see §2.1.1) is also an important performance related factor that has evolved to meet the particular requirements of different disciplines of the sport (e.g., the shape of an alpine carving-ski is significantly different from the shape of a cross-country ski) – see Figure 2-1.

Work by Lind and Sanders [1996], Howe [1983] and Glenne [1981] provide a good fundamental understanding of ski geometry, materials and construction. This is supported by a variety of sources of information on pre-carving skis (e.g., [Piziali and Motte, 1972] and [Gamma, 1981]) and is furthered by more recent work on carving skis (e.g., [Nordt et al, 2000], [Glenne et al, 1997]). Engineering texts ([Shackelford, 2000], [Strong, 2000], [Hull and Clyne, 1996]) are used to provide additional clarification.

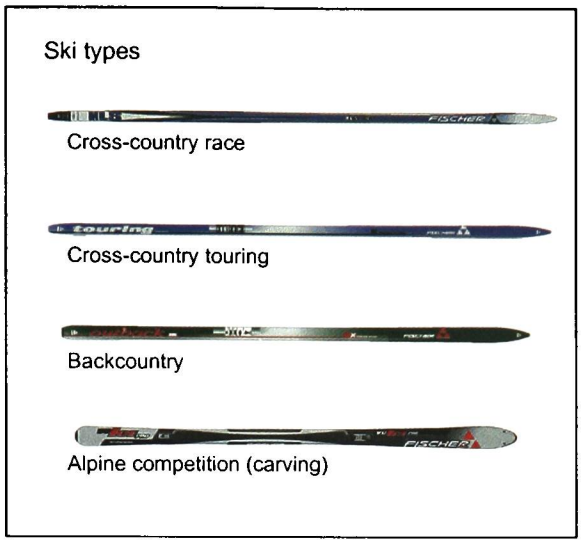

Figure 2-1: Ski types [www.fischer.com]

2.1.1 Ski geometry

For competition skiing, the International Ski Federation (or Federation Internationale de Ski: FIS) specify geometric restrictions for alpine (i.e., downhill, slalom, giant slalom and super G) and nordic (i.e., cross-country and ski-jumping) skis. Geometric terminology for alpine skis (see Figure 2-2) is defined in a standard [ASTM: F 472-92 (1998)] from the American Society for Testing and Materials (ASTM).

The fore-body is considered [Glenne, 1981] the half of the ski from the centre to the tip and the aft-body is the other half, from the centre to the tail. The mid-running surface (MRS) is the portion of the ski under the binding. The forward control point (FCP) and aft control point (ACP) are [Nordt et al, 1999], respectively, where the fore-body and aft-body of the unloaded ski make contact with the surface. In this work, the ski is divided into three distinct segments (for modelling purposes – see §2.4): the fore-body, MRS and aft-body (illustrated in Figure 2-2). The fore-body is taken to measure from in front of the binding toe-piece to the tip, with the MRS between the binding toe and heel-piece and the aft-body measuring from behind the binding heel-piece to the tail. The central-axis is taken to be the axis that separates the left and right sides, down the length of the ski, in plan view.

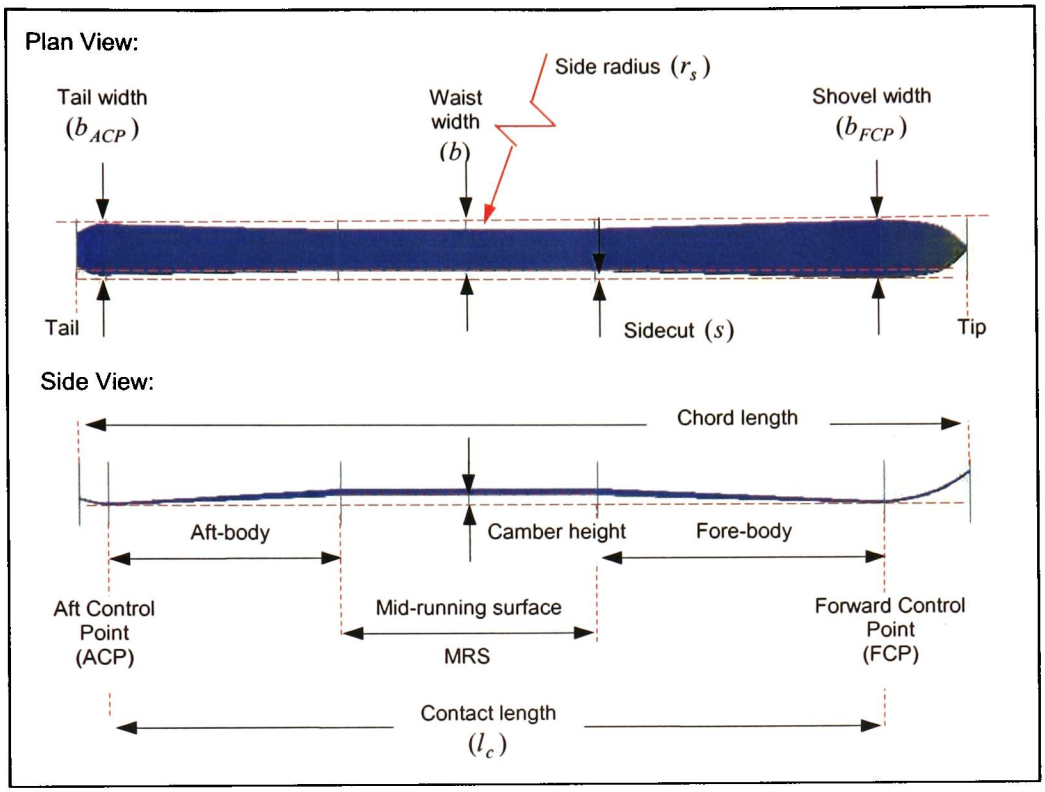

Figure 2-2: Ski nomenclature

The neutral-axis is the longitudinal axis (passing through the centroid of the structure) within the ski, which is not strained when the ski is bent.

Stiffness is a function of the second moment of area (about an axis – e.g., the neutral axis) and the tensile modulus (discussed in §2.1.3). The second moment of area (I_X) depends on the shape of the beam section and the position of the axis (XX) – see Figure 2-3.

$$I_X = \int y^2 b dy \qquad [2\text{-}1]$$

If the axis (XX) corresponds to the neutral axis (NA), then

$$I_{NA} = \int_{-d/2}^{d/2} y^2 b dy \qquad [2\text{-}2]$$

$$I_{NA} = \frac{bd^3}{12} \qquad [2\text{-}3]$$

where, I_{NA} is the second moment of area about the neutral-axis, b is the beam width (or breadth) and d is the beam thickness (or depth).

The second moment of area changes down the length of the beam, as does the tensile modulus, resulting in a beam with non-constant stiffness.

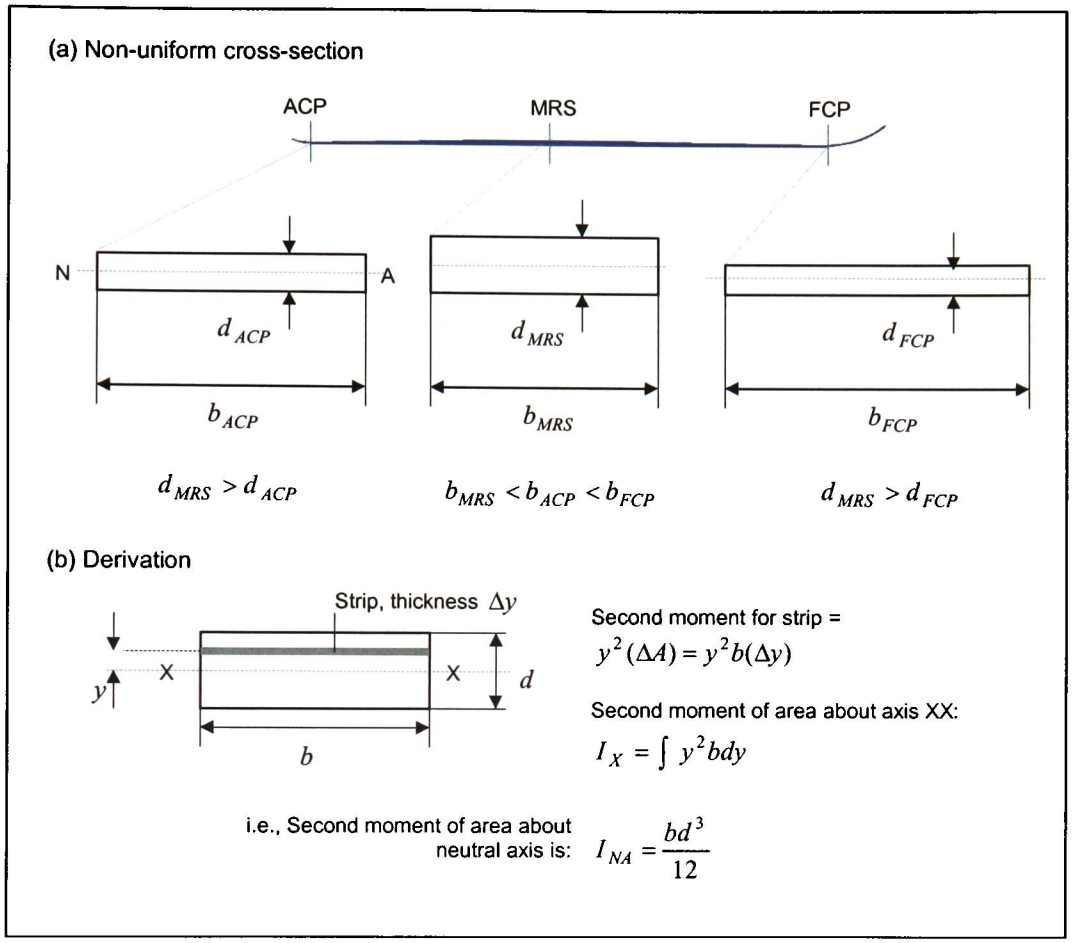

Figure 2-3: Variation of second moment of area in a ski

The geometry of a ski (see Figure 2-2) may be further described [Lind and Sanders, 1996] - in terms of length, width, camber and thickness.

- Length: from tip to tail is referred to as the chord length, while the contact length (or running surface length) is the distance between the FCP (forward control point) and the ACP (aft control point). The contact length determines the carving radius of a ski (i.e., the turn radius).
- Width: with the exception of cross-country skis, the width of modern skis is not uniform down the length of the ski. In general, shovel (or shoulder) width > tail (or heel) width > waist width. Sidecut is a measure of the depth of the curved edge at the waist of the ski. The sidecut and contact length gives the sidecut radius (see equation [2-4]), used as a measure of the radius of a turn.
- Camber: viewed in profile, as the curvature of the running surface under no load. Softer flex (note that flex is the inverse of stiffness) skis allow the camber to be reversed more easily - for

edge control when turning. When pressed together at the mid-point (i.e., base against base), the skis should close simultaneously in the middle. Manufacturers use this "camber closing rule" [Glenne et al, 1997] to promote smooth and consistent load distribution between skis and it is used as a quality control check in the factory.

- Thickness: generally determined by the structure necessary to incorporate materials that provide the required damping and stiffness along the length of the ski. The cross-sectional area is not uniform down the length of the ski – it is greatest over the MRS (mid-running surface) and decreases toward the FCP and ACP.

The length, width and thickness contribute to how a ski supports the weight of the skier and to the stability (fore, aft and laterally) when skiing (e.g., short skis are considered less stable, but easier to manoeuvre). Length, thickness and width may be measured and used to quantify sidecut radius and taper [Lind and Sanders, 1996]:

$$\text{Sidecut radius } (r_S) = \frac{l_C^{\,2}}{8s} \qquad [2\text{-}4]$$

where (with reference to Figure 2-2), l_C is the contact length and s is the sidecut:

$$(s) = \tfrac{1}{4}(b_{FCP} - 2b + b_{ACP}) \qquad [2\text{-}5]$$

where, b_{FCP} is shovel width (at the FCP), b is waist width and b_{ACP} is tail width (at the ACP) and

$$\text{taper} = \tfrac{1}{2}(b_{FCP} - b_{ACP}) \cdot \qquad [2\text{-}6]$$

Carving skis with pronounced sidecut facilitate carving rather than skidding turns [Sahashi and Ichino, 2001] – providing increased handling with reduced skier effort [Yoneyama et al, 2000]. Sidecut is often used as a measure of the potential of a ski to carve a turn, however, it is too simplistic to only consider geometry and not include flex (longitudinal bending and torsional).

One of the turning characteristics of a ski is the ease with which a turn may be initiated [Glenne, 1981] and may be quantified in terms of the swing weight [Lind and Sanders, 1996]. The swing weight is proportional to the moment of inertia (a function of mass and geometry) about a vertical axis drawn through the boot, and the torque (see Figure 2-4) required to put the ski onto an edge (a measure of the energy required to edge the ski.

i.e., $\qquad$ Swing Weight $\propto$ Moment of Inertia $\propto$ Torque

A high swing weight may be achieved by placing mass at the tip and tail, resulting in a high rotational inertia – making the ski more stable (i.e., advantageous for skiing at high speeds). A low-mass ski (with a lower swing weight) is relatively less stable, but easier to manoeuvre (in terms of angulation).

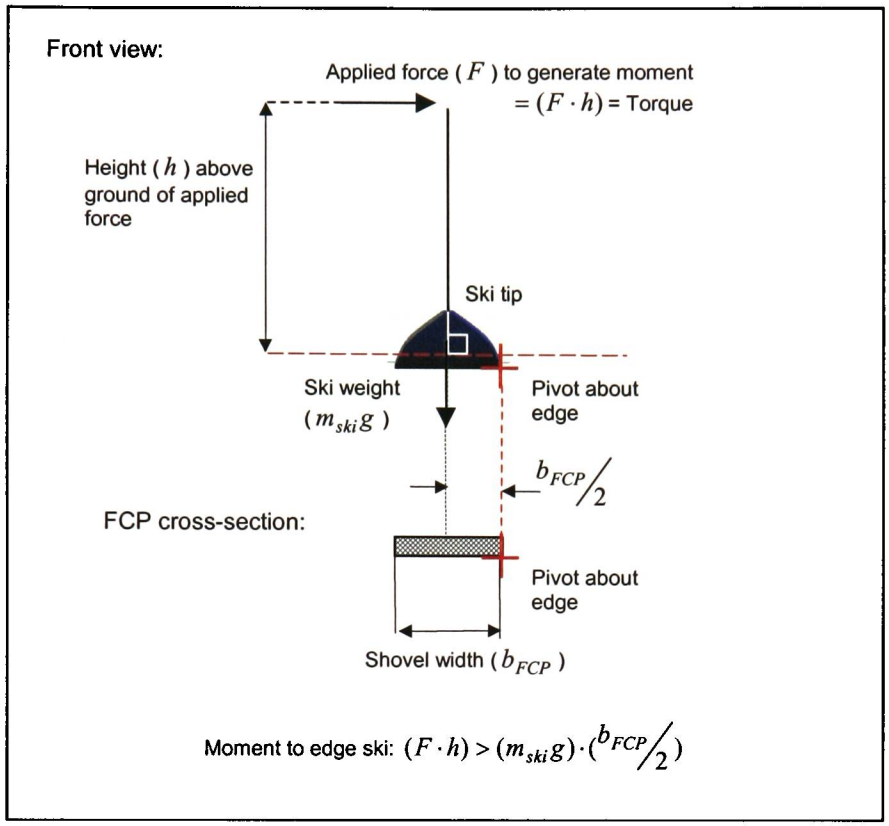

Figure 2-4: Moment required to edge ski
(front view of tip; cross-section at FCP)

The moment that is required to initiate a turn is a function of mass and ski geometry. The geometric characteristics that contribute to the ability to edge, combined with bending and torsional flex characteristics, determine the load distribution along the ski that influences how well a ski is able to carve.

The camber height is reduced when the ski is loaded at the mid-point, with the load being distributed between the ACP and FCP of the ski (see Figure 2-5 a). The centre spring constant (as defined by [ASTM F 498-77 (1998)]) is proportional to the load, at the centre, required to deflect the centre of the simply supported structure.

Moving the application of the load forward of the mid-point produces a relative increase in reaction force on the FCP and, similarly, the ACP reaction force is increased if the load is applied aft of the mid-point. Practically this translates to fore-body control, if the centre of gravity of the skier is made to act through the ball of the foot, and aft-body control - if the resultant force is made to act through the heel (see §2.4.1). As the load increases, the contact area increases and the reaction force peaks at the FCP and ACP move towards the centre.

(a) Profile:

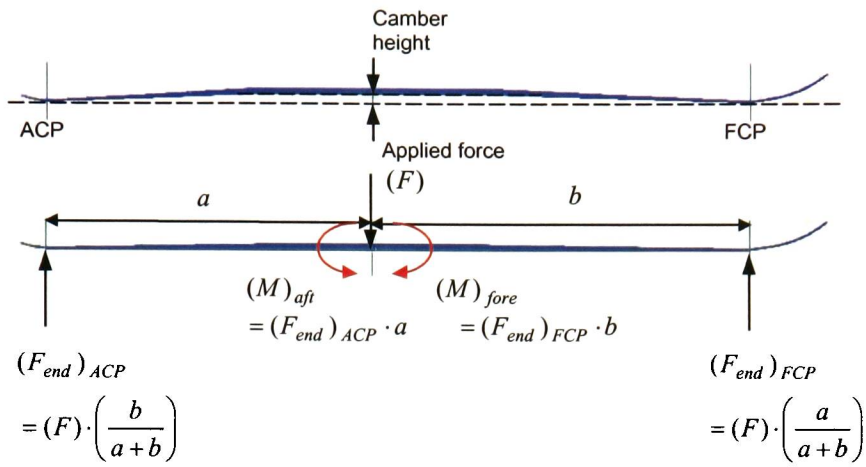

End forces at the FCP and ACP proportional to applied force that overcomes fore-body and aft-body bending stiffness to reduce camber.

(b) Shear force diagram:

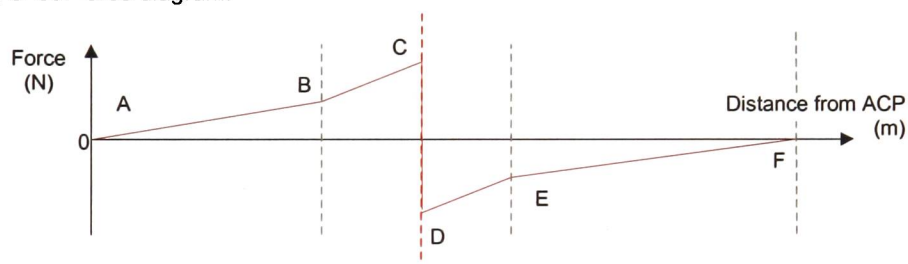

(c) Flex pattern:

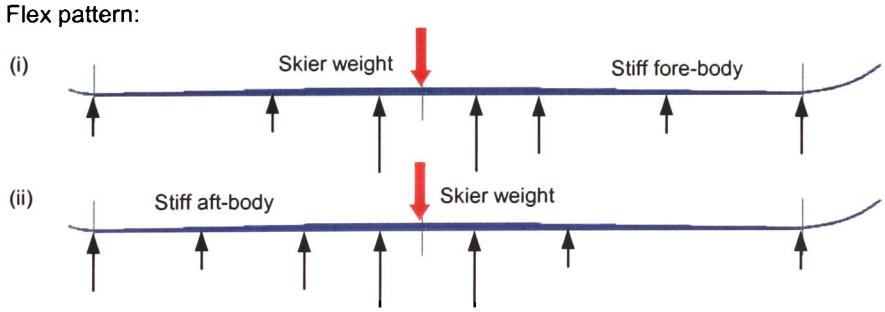

(d) Bending moment diagram:

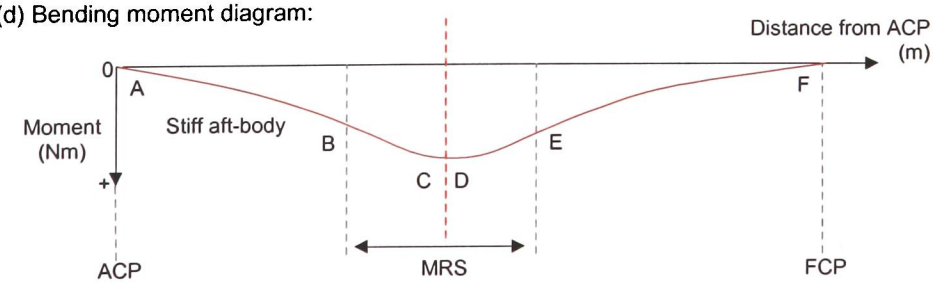

Figure 2-5: Relationship between load distribution and ski stiffness

The load distribution is also influenced by the flex pattern of the ski (see Figure 2-5 b) and the relationship may be illustrated by shear force and bending moment diagrams (see Figure 2-5 c and d, respectively). The shear force diagram illustrates the load distribution, with the magnitude of the gradient in the bending moment diagram corresponding to stiffness (the inverse of flex). For example, a stiffer aft-body (than fore-body) produces a bending moment diagram with a greater gradient magnitude A→B compared with the gradient magnitude E→F (see Figure 2-5 d). Load distribution is discussed further (see §2.4), to quantify the end forces that contribute to steering.

2.1.2 Construction

Ski construction (see Figure 2-6) may be classified by the internal structure [Gamma, 1981]:

- Sandwich – a traditional technique, where the structure is built as successive layers, with two, load-bearing layers being laminated over a lightweight core. This construction technique permits high manufacturing tolerances to be achieved, but is prone to delamination. This construction technique is used to manufacture competition race skis that operate over a relatively narrower range than recreational skis, but are expected to perform to a considerably higher standard.
- Foam-core – load bearing top and bottom layers are built around a lightweight foam core (e.g., polyurethane) injected into a mould containing pre-assembled top and bottom components. Extra reinforcement may be added in, or around the core. In its simplest form this is a relatively cheap construction technique.
- Torsion box – may be added to foam, honeycomb, or wood core skis, using wet-wrap construction techniques, where a synthetic fibre cloth is pressed or wrapped around the core and infiltrated with epoxy resin in a mould. Better torsional rigidity is a benefit of this "tubular" [Lind and Sanders, 1996], or "box" configuration [Glenne, 1981].
- Cap (or monocoque) – a variation of the torsion-box technique, where the core is surrounded by a braided fibreglass sock. Additional layers and cross-weaves provide extra strength and stiffness (particularly in torsion), with a one-piece shell (cap) of acrylic plastic encasing the entire structure. This technique enables the manufacturer to control ski camber, torsional stiffness and sideflex. The core may be reinforced with carbon-fibre rods or Kevlar wraps.

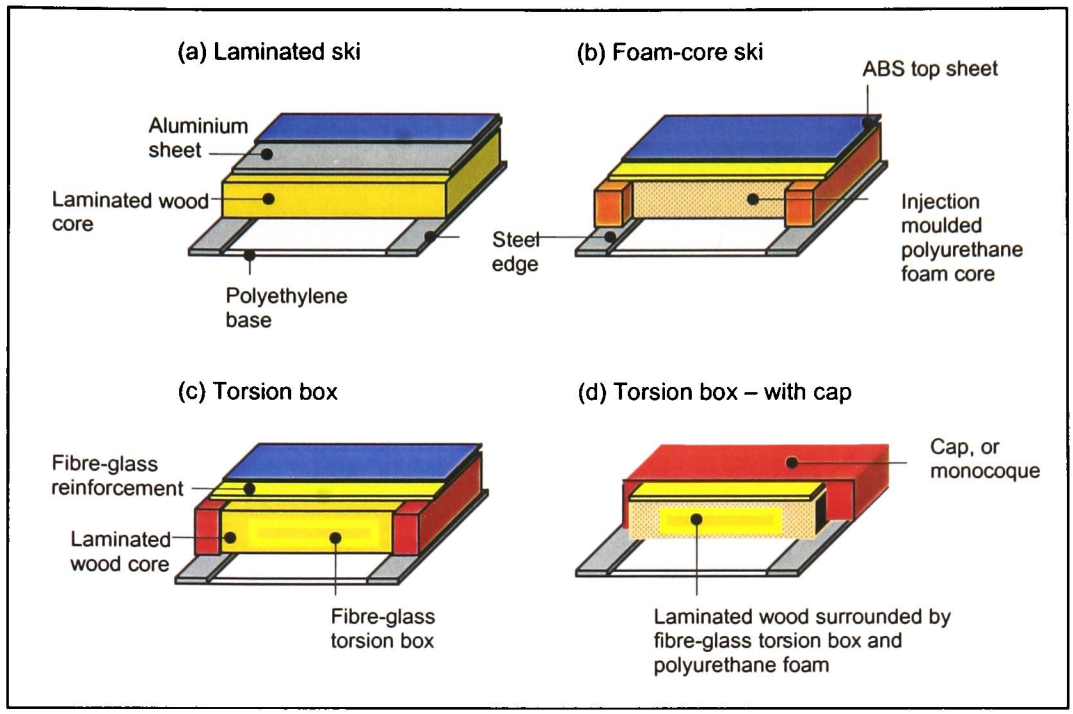

Figure 2-6: Cross-section of possible ski structures (produced with reference to Gamma [1981])

The ability to control vibration around the ACP and FCP (in particular) results in improved handling due to increased and more consistent edge contact – particularly important when turning. It is necessary to engineer the correct amount of stiffness and damping into the ski, with advances in composite materials and modern construction methods helping to achieve better results. However, traditional sandwich construction techniques are used to achieve better tolerances – explaining why competition race skis, with relatively narrow operating bandwidth, are fabricated in this way. Mixed-construction skis (circa 2003/2004), manufactured by Dynastar, have a sandwich structure from the ACP to MRS and a cap-constructed fore-body (probably to achieve higher torsional rigidity in the part of the ski used to initiate and control turns).

Manufacture of modern skis conventionally involves the components of the composite being pressed together, with pressure and temperature specified with respect to time. Temperature is used to optimise adhesive bonding within the composite and is used to process the top-sheet (e.g., to form a cap construction). The press is designed to give the ski camber and contributes to tip and tail geometry. A ski press is expensive to set-up and a vacuum or pressure bag manufacturing method may be used as an alternative (e.g., for prototyping purposes).

The manufacturing process puts constraints on any new materials or technologies that are to be integrated into the composite. An additional temperature constraint of 90°C applies to the finished

ski and therefore also applies to components retro-fitted to the composite. From anecdotal comments from contacts within the ski industry, skis must be designed to survive transport in (car) roof top boxes, where the temperature may reach 90°C.

Modern alpine skis are often fitted with a shim. Located between the binding and ski, a shim provides increased stiffness (and damping) over the mid-running surface. Also, by raising the binding, the shim decreases the moment required to edge the ski - at the cost of increased force on the knees of the skier. The raised binding (and therefore boot) is advantageous in powder snow conditions – reducing drag when the ski is edged. For competition, the International Ski Federation (i.e., Federation Internationale de Ski, or FIS) specify regulations for acceptable shim dimensions.

2.1.3 Materials

A modern alpine ski comprises a core packed between the base and top-sheet, with steel edges for control during turning (see Figure 2-7). The physical properties relating to dynamic performance are of importance to this work. The frictional effects (between the base, or edge, and surface of the slope) will not be discussed. Mass, vibration damping and stiffness (longitudinal and torsional) depend on the constituent materials that make-up the ski composite. Fibre reinforcement (see §2.1.3.1) is used in modern skis to increase stiffness and viscoelastic materials are added to enhance damping characteristics (see §2.1.3.2).

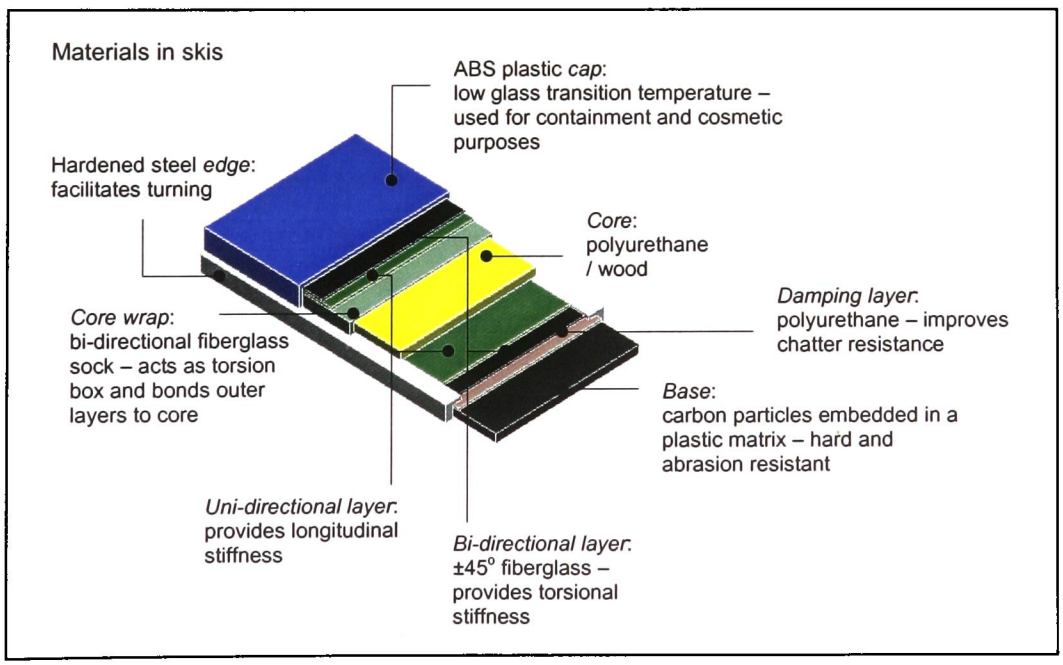

Figure 2-7: Materials in skis

The mechanical properties of the ski structure depend on the properties of the constituent materials (see Figure 2-7) and the geometric design of the various structural elements. Property averaging (a rule of mixtures approach [Shackelford, 2000]) can be used to provide a simplified representation of the composite in terms of the constituent elements. For example, consider the strain of a model composite ski made up of a core bonded with two reinforcing layers – a base and a wet-wrap (comprising long-fibres, running parallel to the induced force):

$$\varepsilon_{ski} = \frac{\sigma_{ski}}{E_{ski}} = \varepsilon_{core} = \frac{\sigma_{core}}{E_{core}} = \varepsilon_{base} = \frac{\sigma_{base}}{E_{base}} = \varepsilon_{wet-wrap} = \frac{\sigma_{wet-wrap}}{E_{wet-wrap}} \qquad [2\text{-}7]$$

i.e., the strain experienced by the ski (ε_{ski}) is equal to the strain in the core (ε_{core}) and the reinforcing layers (i.e., base (ε_{base}) and wet-wrap ($\varepsilon_{wet-wrap}$)).

Tensile modulus (also known as the modulus of elasticity, or Young's modulus) is characteristic of a material and is the constant of proportionality between the applied stress (σ) and the resulting strain (ε):

i.e., $$\text{Tensile modulus } (E) = \frac{\sigma}{\varepsilon} = \frac{F}{A} \cdot \frac{l}{\delta} \qquad [2\text{-}8]$$

where, F is the applied force; A is the cross-sectional area; l is the original length and δ is the elongation under the applied load.

Poisson's ratio (generally: $0 < \upsilon < 0.5$) is also characteristic of a material and quantifies the contraction perpendicular to the extension caused by a tensile stress (often around 0.3 for elastic materials) – i.e., the ratio of the transverse strain (ε_z) to the longitudinal strain (ε_x):

$$\upsilon = -\frac{\varepsilon_z}{\varepsilon_x} \cdot \qquad [2\text{-}9]$$

$$G = \frac{\tau}{\gamma} \qquad [2\text{-}10]$$

The shear modulus, or modulus of rigidity (G) is defined as the ratio of shear stress (τ) to shear strain (γ) and is related to the tensile modulus (E), for small strains, by Poisson's ratio:

$$E = 2G(1 + \upsilon) \cdot \qquad [2\text{-}11]$$

The load (F) carried by the composite is the sum of the load carried by each component:

i.e., $$\sum F = F_{ski} = F_{core} + F_{base} + F_{wet-wrap} \quad [2\text{-}12]$$

and since force is equal to the product of stress and area:

$$\sigma_{ski} A_{ski} = \sigma_{core} A_{core} + \sigma_{base} A_{base} + \sigma_{wet-wrap} A_{wet-wrap} \quad [2\text{-}13]$$

Combining this with equation [2-7] gives,

$$E_{ski} \varepsilon_{ski} A_{ski} = E_{core} \varepsilon_{core} A_{core} + E_{base} \varepsilon_{base} A_{base} + E_{wet-wrap} \varepsilon_{wet-wrap} A_{wet-wrap} \quad [2\text{-}14]$$

Since $\varepsilon_{ski} = \varepsilon_{core} = \varepsilon_{base} = \varepsilon_{wet-wrap}$, equation [2-14] can be divided by A_{ski} and rewritten in terms of volume fractions, where $V_{core} + V_{base} + V_{wet-wrap} = 1$, to give,

$$E_{ski} = V_{core} E_{core} + V_{base} E_{base} + V_{wet-wrap} E_{wet-wrap} \quad [2\text{-}15]$$

Equation [2-15] shows that properties of a composite are a function of those of the constituent materials. The ability to vary the properties of one component will have a proportional affect on the composite as a whole. This concept explains part of the initial motivation for investigating the integration of smart materials technology in skis.

2.1.3.1 Fibre reinforcement

Wood has traditionally been used in the manufacture of skis and its fibrous structure gives good longitudinal stiffness. The arrangement and distribution of man-made long fibres contributes significantly to the properties of the composite matrix [Hull and Clyne, 1996] in modern skis. Fibre reinforcement aims to provide enhanced stiffness and strength – particularly torsional strength, in the case of modern alpine skis. The torsional strength of modern alpine skis is achieved with cross-ply (i.e., bi-directional) and woven fibre (i.e., uni-directional) laminate reinforcement (see Figure 2-7).

The 'rule of mixtures' approach is valid when the induced force is parallel to the reinforcing fibres, provided the fibres are long enough for the equal strain assumption (often described as a 'Voigt model') to apply. Prediction of transverse stiffness of a composite from elastic properties of the constituent materials is more difficult than the axial value. An estimate of stiffness may be obtained using the 'rule of mixtures' approach and including the contribution of fibres subject to predominantly axial rather than transverse strains. Therefore, longitudinal stiffness should be calculated with consideration of fibres parallel to the central axis (i.e., 0°) and ±45° off the central-

axis, while torsional stiffness should be calculated with consideration of fibres between ±45° and 90° to the central axis (see Figure 2-8).

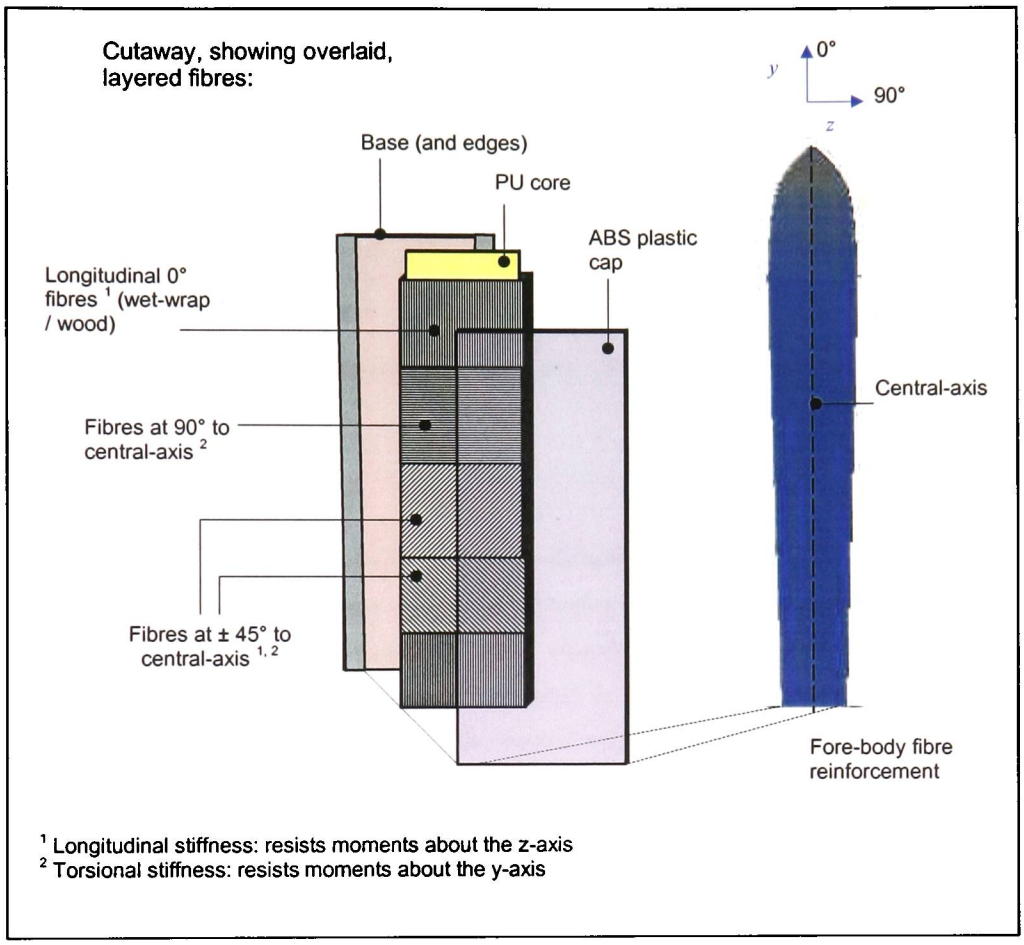

Figure 2-8: Longitudinal and torsional fibre reinforcement of ski core

Lind and Sanders [1996] report a comparison of properties of high-modulus and high-strength fibres with metallic materials used in skis (see Table 2-1).

Fibre		Density (g/cm^3)	Tensile modulus (GNm^{-2})	Tensile strength (GNm^{-2})
Organic				
Carbon	(Graphite)	1.66	228 - 379	2.21 - 3.10
Aramid	(Kevlar)	1.44	68.9 - 172	2.76
Polyethylene	(Spectra)	0.97	117 - 172	2.62 - 2.96
Ceramic				
Fiberglass	(S. Glass)	2.50	89.6	3.45 - 4.55
Aluminium - borate - silicon	(Nextel)	2.85	152 - 228	1.72 - 2.07
Metallic				
Hardened steel		7.85	207.0	2.00
Aluminium alloy	(7075-T6)	2.75	71.70	0.52
Aluminium - magnesium - titanium	(Titanal)	2.75	71.70	0.58

Table 2-1: Physical material properties (compiled with reference to Lind and Sanders [1996])

2.1.3.2 Viscoelastic damping

The materials used in the core contribute to vibration damping and, therefore, the dynamic stability (see §2.3) of the ski. In this section the use of viscoelastic layers to conventionally control ski vibration is discussed. Also, the representation of viscoelastic properties as simple mechanical devices (i.e., with stiffness and damping components) is introduced, with consideration of an alternative rheological model to better explain the thermal response of viscous materials.

Laminated wood (e.g., ash, birch, maple, hickory, fir, spruce, or poplar) is commonly used [Lind and Sanders, 1996] to provide good stiffness and structural stability. Viscoelastic damping layers (e.g., neoprene and urethane sheets – see Table 2-2) are added (between the core and base – see Figure 2-7) to prevent structural resonance. Edges may also be segmented to prevent shock excitation at the edge propagating into the structure (i.e., chatter – see §2.3).

Viscoelastic dampener	Density g/cm^3	Tensile modulus MNm^{-2}	Uses
Thermoplastics			
Acrynotitrile-butadiene-styrene (ABS)	1.04	2140	Tops and sidewalls
Nylon 12	1.02	1240	Tops and alloyed with ABS
UHMW polyethylene	0.93	827	-base material
Elastomers			
(poly) Urethane	1.18	5.52	Inlays, top and heel protection
Surflyn	0.96	248	Sidewalls and inlays
Polyamide	1.01	3.86	Inlays, heel protector
Thermosets			
Epoxy resin	1.16	2760	Fiberglass and carbon matrix

Table 2-2: Viscoelastic material properties (compiled with reference to Lind and Sanders [1996])

Elastic components in the composite store potential energy as displacements increase and release potential energy as displacements decrease [Meirovitch, 2001]. Elastic components may be represented as (massless) springs (see Figure 2-9 a) that undergo a change in length ($\Delta x = x_2 - x_1$) when subjected to a force.

The change in length is proportional to the applied force when the spring is operating in the linear range (see Figure 2-9 b), with spring constant (or spring stiffness) k (quantified in N/m). The elastic restoring force of the spring acts in the opposite direction of the applied force and is equal in magnitude - assuming the spring is massless:

i.e., $$F_{applied} = -F_{elastic} = k(\Delta x) \qquad [2\text{-}16]$$

Substituting equation [2-16] in equation [2-8], the tensile modulus may be redefined in terms of spring constant, length (l) and area (A):

i.e., $$E = \frac{k \cdot l}{A} \qquad [2\text{-}17]$$

Similarly (referring back to equation [2-16]), for a torsional spring:

$$M_s = k_T(\theta_2 - \theta_1) \qquad [2\text{-}18]$$

where M_s is the torque acting on the spring, k_T is the torsional spring constant, with θ_2 and θ_1 being the angular displacements of the end points.

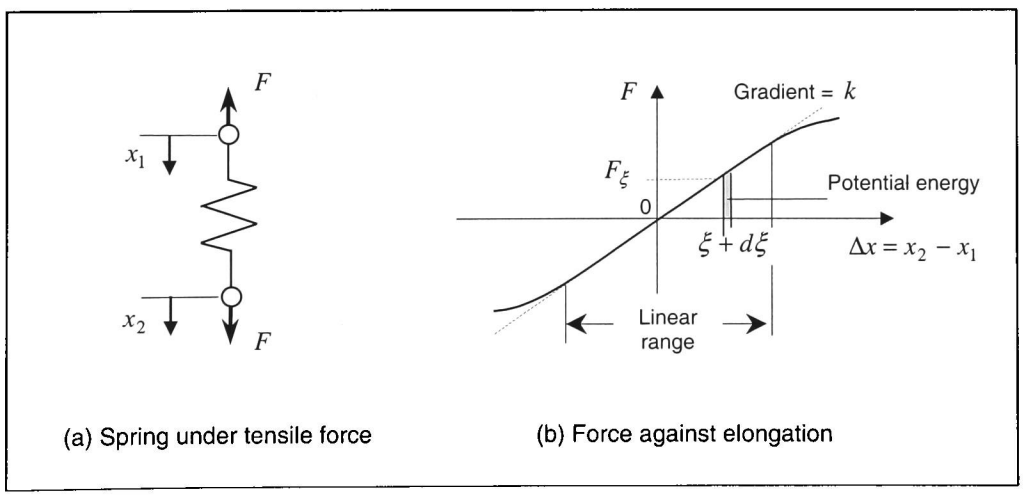

Figure 2-9: Spring restoring forces (produced with reference to Meirovitch [2001])

In the linear range (the non-linear range is not considered here), the elastic restoring force is $-k\xi$ where ξ is an incremental change in length (see Figure 2-9 b).

So, the potential energy is: $U_{PE} = \int_{\delta}^{0}(-k\xi)d\xi = \frac{1}{2}k(\Delta x)^2$ [2-19]

Alternatively, the potential energy (U_{PE}) may be determined geometrically as the area under the force-extension ($F-(\Delta x)$) graph (see Figure 2-9 b).

Components of the composite that dissipate energy may be represented by a (massless) viscous damper, or dashpot (see Figure 2-10 a). It is assumed that the forces cause smooth shear in the viscous fluid, so that there is a linear relationship between force and the velocity of separation of the end points ($(\Delta\dot{x}) = \dot{x}_2 - \dot{x}_1$), where the coefficient of viscous damping (c , in Ns/m) is the proportionality constant.

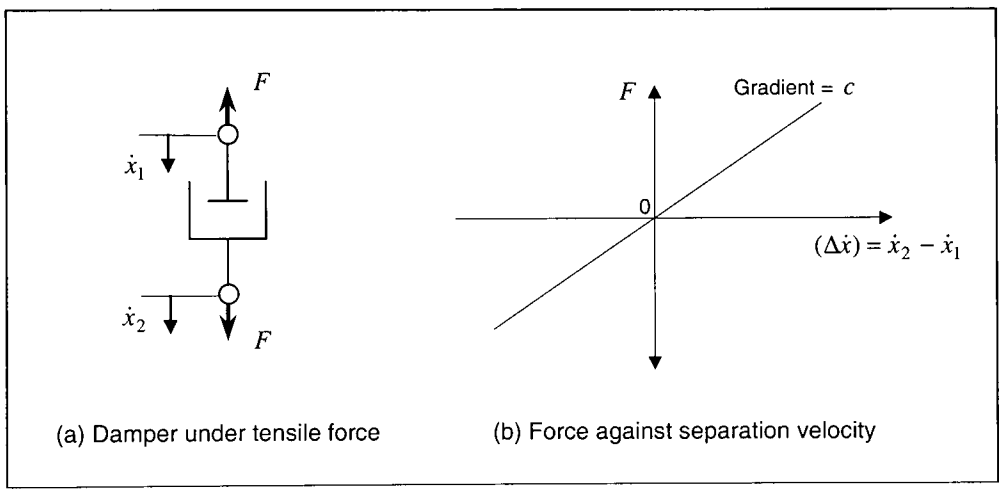

Figure 2-10: Damper forces (produced with reference to Meirovitch [2001])

The damper force acts in the opposite direction of the externally applied force and is equal in magnitude - assuming the damper is massless:

i.e., $F_{applied} = -F_{damper} = c(\Delta\dot{x})$ [2-20]

Similarly, for a torsional damper:

$$M_d = c_T(\dot{\theta}_2 - \dot{\theta}_1)$$ [2-21]

where M_d is the torque acting on the damper, c_T is the torsional coefficient of viscous damping, with $\dot{\theta}_2$ and $\dot{\theta}_1$ being the angular velocities of the end points.

The energy dissipated by the damper is proportional to the velocity:

i.e., $$\dot{U} = (-c(\Delta\dot{x}))(\Delta\dot{x}) = -c(\Delta\dot{x})^2 \qquad [2\text{-}22]$$

Elasticity and damping are represented, respectively, by massless springs and dampers throughout this work and may be used to represent viscoelastic materials (see Figure 2-11).

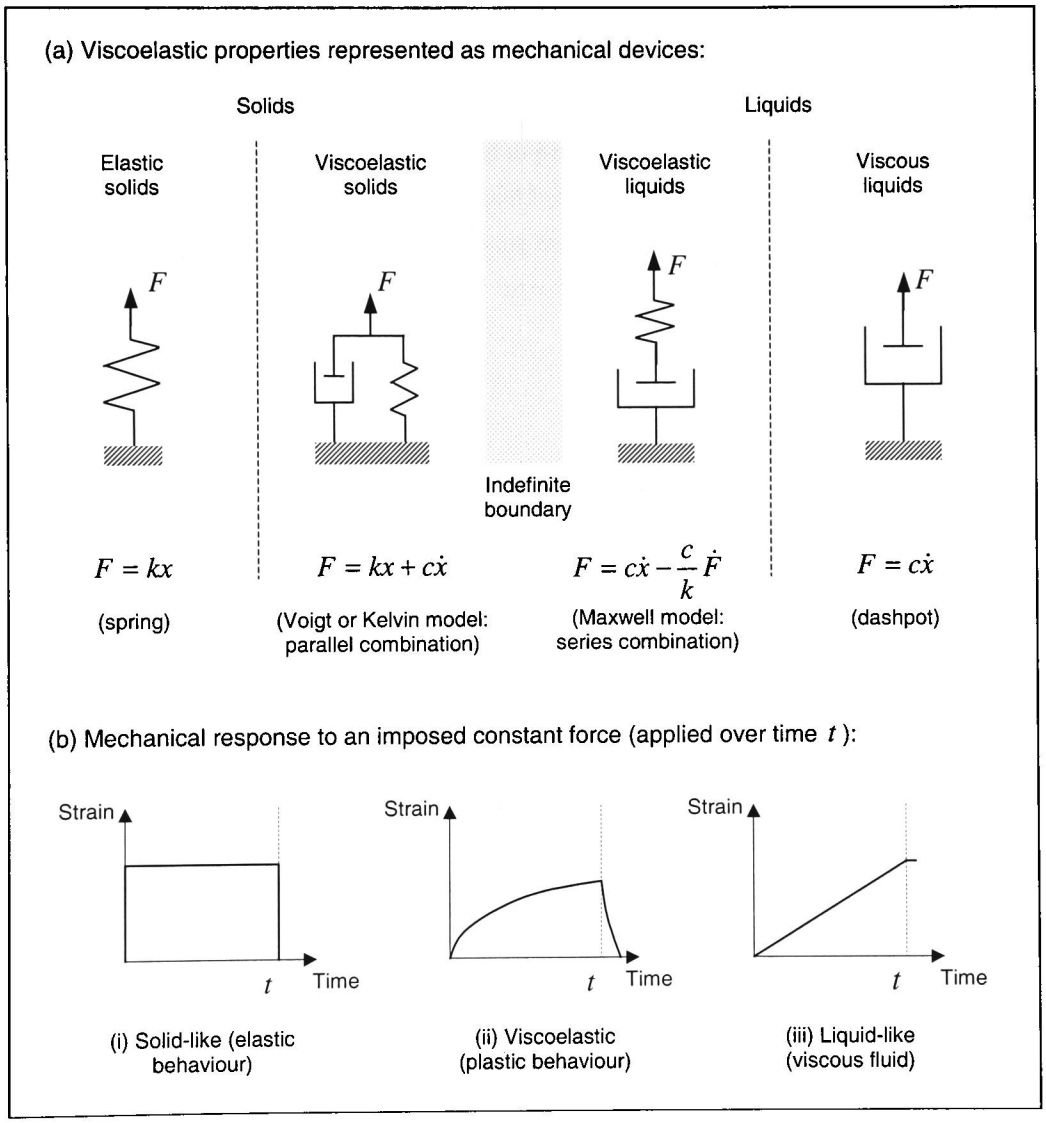

Figure 2-11: Viscoelastic properties represented as simple mechanical devices (produced with reference to Strong [2000])

Stress induced strain in polymers (e.g., see Table 2-2) produces time dependent viscous-creep referred to as viscoelastic deformation (stress induced strain, leading to visco-plastic deformation is not considered here). Such solids may be modelled as viscoelastic materials having viscous and elastic components (i.e., modelled as a spring and damper in parallel – see Figure 2-11). A rheological model can be used for the viscous component:

i.e., $$(\eta = \frac{\sigma}{\dot{\varepsilon}}) \equiv (\eta_\tau = \frac{\tau}{\dot{\gamma}}) \qquad [2\text{-}23]$$

where, η is the tensile viscosity, σ is the tensile stress and $\dot{\varepsilon}$ is the tensile strain rate – respectively equivalent to viscosity (η_τ), shear stress (τ) and strain rate ($\dot{\gamma}$), used to quantify fluid flow (i.e., rheology).

Temperature affects the viscoelastic behaviour, with a decrease in temperature resulting in a decrease in viscous-creep and an increase in tensile modulus. This is significant in skis, as the viscoelastic materials added to control vibration are required to perform below 0°C (certainly to –20°C). Should a temperature drop reduce the viscous mechanical behaviour, the material will behave more spring-like, with reduced damping – therefore, dissipating less energy. Temperature is acknowledged to be an important factor in ski response, but is not investigated in detail in this work (or in any of the research into ski dynamics referenced here).

2.2 Alpine skis

There has been considerable development of alpine skis in the last 10-15 years. Modern alpine skis have a more pronounced geometry (in terms of sidecut) and are relatively shorter, with a softer flex (i.e., less stiff), but increased vibration control (i.e., in terms of damping). The change in geometry (including a reduction in camber) has introduced carving skis that are wider in the fore-body and aft-body, than at the waist (i.e., fore-body width > aft-body width > width at the mid-running surface). Carving ski geometry makes it easier to initiate and hold a turn, requiring less effort from the skier (see §2.4.1) with improved control (i.e., small movements by the skier to position, weight and edge the skis are rewarded with greater control, when comparing skiing on carving and pre-carving skis). This is verified by quantitative experimental analysis of skier biomechanics [Yoneyama et al, 2000], with comparison of joint angle motion and leg reaction forces measured during field tests of carving and non-carving skis.

Work by Sahashi and Ichino [2001], investigating carving-turn descents experimentally, concluded that a carving turn comprises an accumulation of slight skidding and that more skidding is evident on parallel turns of non-carving skis. Renshaw and Mote [1991] established a computational model for skidding and carving turns. The model assumes that carving occurs when a section of the ski follows

the track in the snow cut by a preceding section (i.e., the ski slides along its own track without shearing new snow – unlike a skidding turn that would involve shearing a new snow surface). The influence of skier position on ski geometry (in terms of rotations) was considered and results were presented for force distribution along the ski during skidding and carving turns. The model was developed to include variation in longitudinal bending stiffness and snow hardness, which was modelled as a spring (a common simplification of the snow surface that does not consider energy dissipation – see §2.4.2).

The development of the modern alpine ski is presented by Glenne et al [1997]. Glenne et al [1997] established a model for steering force (see §2.3) - based on load distribution, and with respect to ski properties (i.e., physical characteristics and geometry). Work by Sakata and Ito [1997] provides a quantitative comparison of ski development, compiled from measurements taken over a 22-year period. This work concluded that for skis post-1980, relative to their predecessors, the torsional rigidity of the fore-body had increased over time, while that of the aft-body had decreased. Also, there was a decrease in flexural stiffness and, although there was a decrease in mass, the moment of inertia remained relatively constant over time. However, no information was provided (by Sakata and Ito [1997]) on damping properties and there is little emphasis on changing geometry.

Work on development of a mass damper for skis is presented by Hosokawa et al [2002], with references to previous studies (in Japanese) on the damping properties of commercially available skis. Despite this work, Hosokawa et al [2002] reported that there was no clear theoretical or experimental evidence concerning the effect of damping on skis. Computational work by Devaux and Trompette [1980] does compare measured values of damping (see Table 2-4), with those calculated assuming a free-free boundary condition in the model of the ski. The free-free boundary condition is considered (here) to not be representative of skiing mechanics (and boundary conditions are discussed in more detail later – see §2.4, on modelling ski dynamics). The work by Devaux and Trompette [1980] pre-dates carving skis.

2.3 Dynamic stability

Intermittent loss of edge contact due to induced vibrations is described as chatter and results in reduced control, with the ski skidding rather than carving. The problem is compounded at speed, as the frequency of the pulse induced vibrations increases – reducing control when it is most needed (i.e., at speed and when turning). In a pre-carving ski, edge chatter manifests itself as a result of longitudinal vibrations and insufficient damping. However, despite improved vibration control being engineered into the composite structure of modern alpine skis (as a result of advances in use of materials and construction - see §2.1.3 and §2.1.2), edge chatter remains a problem that has evolved with the technology. The wider fore-body on carving skis, while facilitating turns, causes it (i.e., the

fore-body) to be more susceptible to torsional forces (investigated later – see §3.2.1.3 and §3.3.2.1). The decreasing cross-section down the length of the fore-body, from the MRS to the tip contributes to a reduction in torsional rigidity. As the ski moves over the surface, the wide-band (i.e., in terms of magnitude and frequency) forces that act on the edge, produce moments that twist the fore-body against the angulation of the ski with respect to the slope (see Figure 2-12).

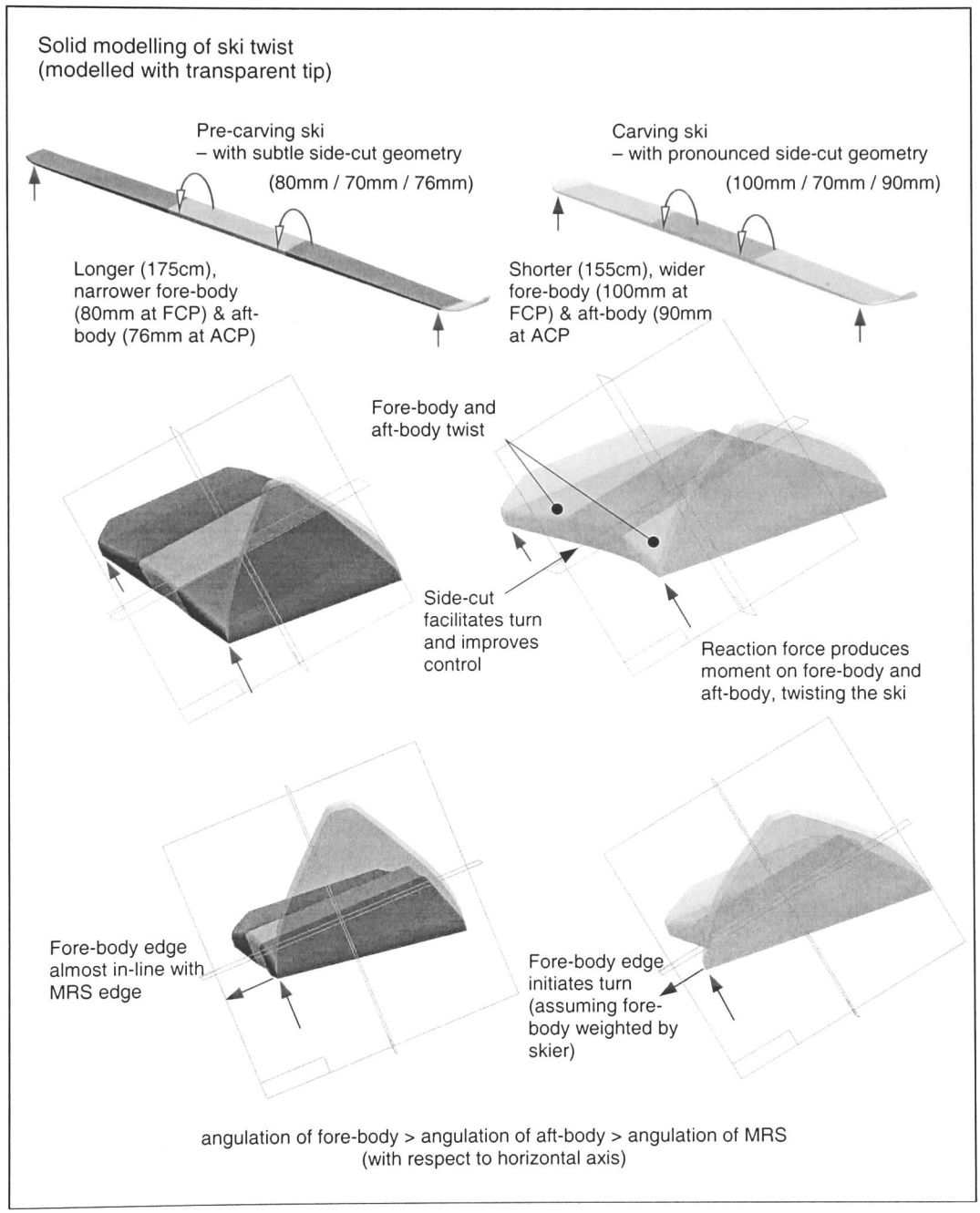

Figure 2-12: Fore-body twist (modelled using Solid Edge, based on side-cut dimensions of the Atomic "Telemark OT" ski and the Line "Maverick" carving ski)

Vibration ($F(t)$) can cause loss of edge contact due to edge chatter and reduce control. Subject to a forced vibration, the dynamic response is influenced by the physical characteristics of the ski (see appendix A-1). The physical characteristics (i.e., mass, stiffness and damping - see equation [2-24]) that influence the dynamic response have implications for the qualitative "feel" of the ski (most often reported based on expert skier feedback). The feel of a ski depends on the size (weight) and ability of the skier and the snow conditions. For example a smaller, lighter-weight skier may feel that a stiffer ski is less responsive, while it may be too difficult to manoeuvre if it is too heavy. Damping should dissipate unwanted vibrations and it is the opinion here that the skier would benefit from as much damping as possible (see also §2.4.1), specified to suit the ski stiffness.

$$F(t) = m\ddot{x} + c\dot{x} + kx \qquad [2\text{-}24]$$

From the equation of motion (see equation [2-24]) for a single-degree-of-freedom system, the values of mass (m), damping constant (c) and elastic spring constant (k) determine the deflection (primarily in the vertical (x) axis) under loading and the amount of vibration (i.e., acceleration ($\ddot{x}$), velocity ($\dot{x}$) and displacement (x), respectively).

Similarly, for torsional motion (primarily about the longitudinal y-axis):

$$M(t) = m\ddot{\theta}_y + c_T\dot{\theta}_y + k_T\theta_y \qquad [2\text{-}25]$$

where, $M(t)$ is time dependent torque, c_T is the torsional damping coefficient, k_T is the torsional elastic spring constant and $\ddot{\theta}_y$ is angular acceleration, $\dot{\theta}_y$ is angular velocity and θ_y is angular displacement.

The torsional deflection of the fore-body and aft-body is related to the angulation of the ski and the resultant force exerted by the skier (see §2.4.1). When there is a fast rate of transfer between the left and right edges (i.e., shorter, faster turns), torsional and vertical damping of longitudinal vibration is required to stabilise the ski before it initiates a turn. Torsional and vertical damping is also required to stabilise the ski during a turn, where there is greater amount of time spent on a particular edge and angulation may be increasing with time.

The frequency bandwidth of pulses subjected to the ski on loose-packed snow differ in magnitude and frequency compared with those experienced over hard-packed, rutted or icy surfaces (see §2.4.2). A ski that operates well in a particular snow condition does therefore not necessarily perform as well in another. The stiffness (see appendix A-1.1) and damping (see appendix A-1.2) characteristics that control the vibratory response of a ski over a particular operating range should also be compatible with the weight (and ability) of the skier. The possibility to vary physical components of the

composite and alter its properties (see equation [2-14]) is a motivating factor for this work to investigate methods to adapt values of stiffness and damping as a means of vibration control, without imposing a weight penalty that would reduce manoeuvrability.

It is acknowledged that an alternative to damping with materials that absorb, or dissipate, vibrations is tuned-mass damping. Quantitative laboratory results and qualitative field-testing of a steel ball damper (total mass: 22.3g, or 37.8g, or 68.8g) on skis are presented by Hosokawa et al [2002], with the damper-located approximately 800mm from the binding toe-piece. The aim of the proposed mass damper was to control free vibrations by damping modes, with laboratory results showing improved damping and qualitative feedback from field-tests being used to suggest increased stability. However, accepting claims that the mass damper controlled free vibrations, it remains unclear how successful the system actually was in reducing chatter (i.e., at other non-resonant, forced frequencies).

2.4 Modelling ski dynamics

Skis are expected to perform when subjected to a variety of possible force conditions, with the response of the ski depending on its physical characteristics. Alpine skis are expected to remain dynamically stable and operate under variable load conditions. The response to the variable load conditions depends on the mass (not discussed in detail), stiffness and damping characteristics of the ski (see appendix A-1.1 and appendix A-1.2). Leg movement and resultant weight of the skier (see §2.4.1) influence how the ski is controlled (e.g., fore-body or aft-body; left or right edge), with environmental conditions (see §2.4.2) affecting the reaction force of the slope on the ski.

A model represents an approximation of the actual physical system and should retain essential dynamic characteristics of the system, with the implication that the behaviour predicted by the model correlates with observed behaviour. Mechanical properties of alpine skis have been computationally modelled by Nordt et al [1999], with characteristics of interest including:

1. Bending stiffness and flex
2. Torsional stiffness and twist
3. Natural frequency
4. Pressure distribution along the base.

The modelling process [Nordt et al, 1999] begins with the ski being divided into segments and continues with the ski being represented by rods connected at the nodes by springs. In this work the ski is divided into three segments: the fore-body, the mid-running surface and the aft-body (see Figure 2-13). Analysis is focussed on the fore-body, which is further subdivided (see Figure 2-14) and subsequently investigated experimentally (see §3).

The boundary conditions and control forces (i.e., as a result of skier movement and ground reaction forces – see Figure 2-13 a) are modelled as distributed parameters (see Figure 2-13 b), acting on the MRS, aft-body and fore-body. Aft-body and fore-body reaction forces are distributed to the ACP and FCP respectively. Time dependent, normal reaction forces produce longitudinal and torsional vibration leading to edge chatter and reduced control. Skier movement rolls and pitches the ski (see §2.4.1) to produce (edge) control forces over the MRS and at the fore-body and (or) aft-body. The weight of the skier is largely supported over the MRS, with control forces distributed (see §2.1.1, Figure 2-5) to the fore-body and (or) aft-body edge (depending on skier position, slope and ski flex). Therefore, in this work, the MRS is modelled as being tied to an unfixed surface (i.e., the MRS translates with the surface). Acted upon by the skier and possibly reinforced with a shim, it is assumed that the MRS is a rigid structure clamped between the skier and surface. The aft-body and fore-body structures are modelled as cantilevers (see Figure 2-13 c) with a skier-induced moment (at the built-in support) and a time dependent force acting at the ACP and FCP respectively.

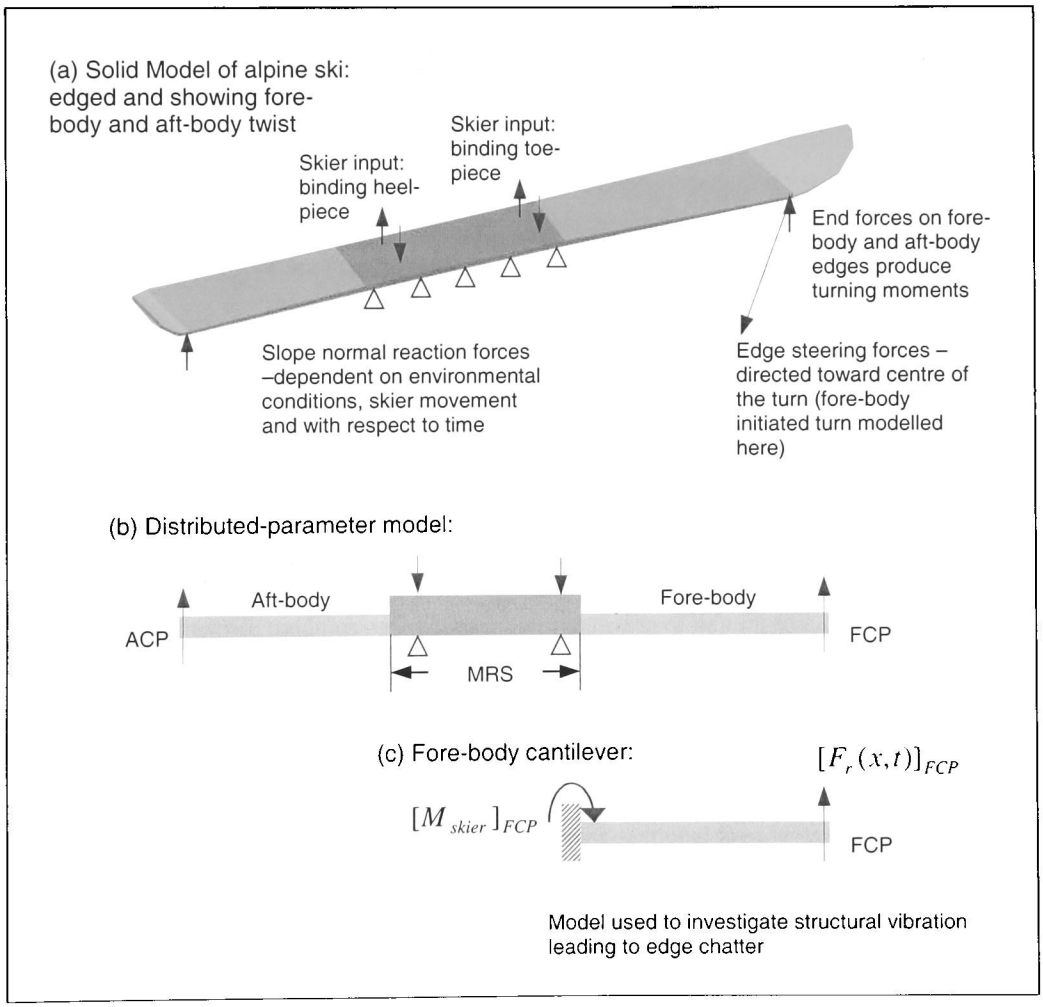

Figure 2-13: Distributed-parameter model
(illustrating boundary conditions advocated in this work)

Steering forces (see Figure 2-13) have been quantified [Glenne et al, 1997] in terms of end force (F_{end}) at the shovel or heel, with the ski edged:

$$F_{end} = \frac{x_c + 0.5 \cdot s \cdot \tan A}{1/k + w^2/(4 \cdot k_t)} \qquad [2\text{-}26]$$

where, k is the fore-body, or aft-body spring constant (see §3.1.2 for measurement procedures); w is the maximum width of the shovel, or heel; k_t is the fore-body, or aft-body torsional spring constant; s is the width offset from the centre-line to the edge; A is the angulation at the MRS, and x_c is the deflection required to overcome the camber (i.e., flatten the ski).

Skier weight is not considered in the equation, [2-26], which quantifies end forces produced when camber height is zeroed under loading. Referring back to the cantilever model of the fore-body (see Figure 2-13), with distributed reaction force (F_r). The addition of a skier-induced moment at the built-in support increases the reaction force distributed to the control point. The skier-induced moment (M_{skier}) can be replaced by a virtual force (F_{skier}) and added to the end force at the FCP and the elastic restoring force in the fore-body:

i.e., $$F_{skier} = \frac{M_{skier}}{l_{fore}} \qquad [2\text{-}27]$$

where l_{fore} is the length of the fore-body;

so, $$F_{end} + F_{skier} + k_{fore} x(t) = -F_r(t) \qquad [2\text{-}28]$$

where $x(t)$ is time dependant vertical displacement of the FCP and k_{fore} is the fore-body spring constant (see §3.1.2), which can be determined by testing with reference to ASTM F 498-77 [1998]. The reaction force can therefore be quantified using equation [2-28].

Modelling the fore-body as a cantilever with uniform cross-section (i.e., constant second moment of area) and constant tensile modulus enables an initial prediction of natural frequencies to be made (see Figure 2-14).

$$\text{Natural frequency } f_n = \frac{K}{2\pi}\sqrt{\frac{EI}{\rho A l^4}} \qquad [2\text{-}29]$$

where ρ is the mass density of the beam, A is the cross-sectional area, l is the length of the beam and K is a mode dependent coefficient (see Figure 2-14 a). Assuming uniform cross-section and constant stiffness (EI) - i.e., constant modulus of elasticity (E).

The cantilever model assigns a clamped – free boundary condition to the fore-body structure (see Figure 2-14 b i), constraining three degrees of freedom. Horizontal and vertical reaction forces constrain translation and a bending moment constrains one axis of rotation. A hinged – free boundary condition (see Figure 2-14 b ii) would not include a bending moment and is therefore not considered a suitable model of the fore-body (or aft-body) structure.

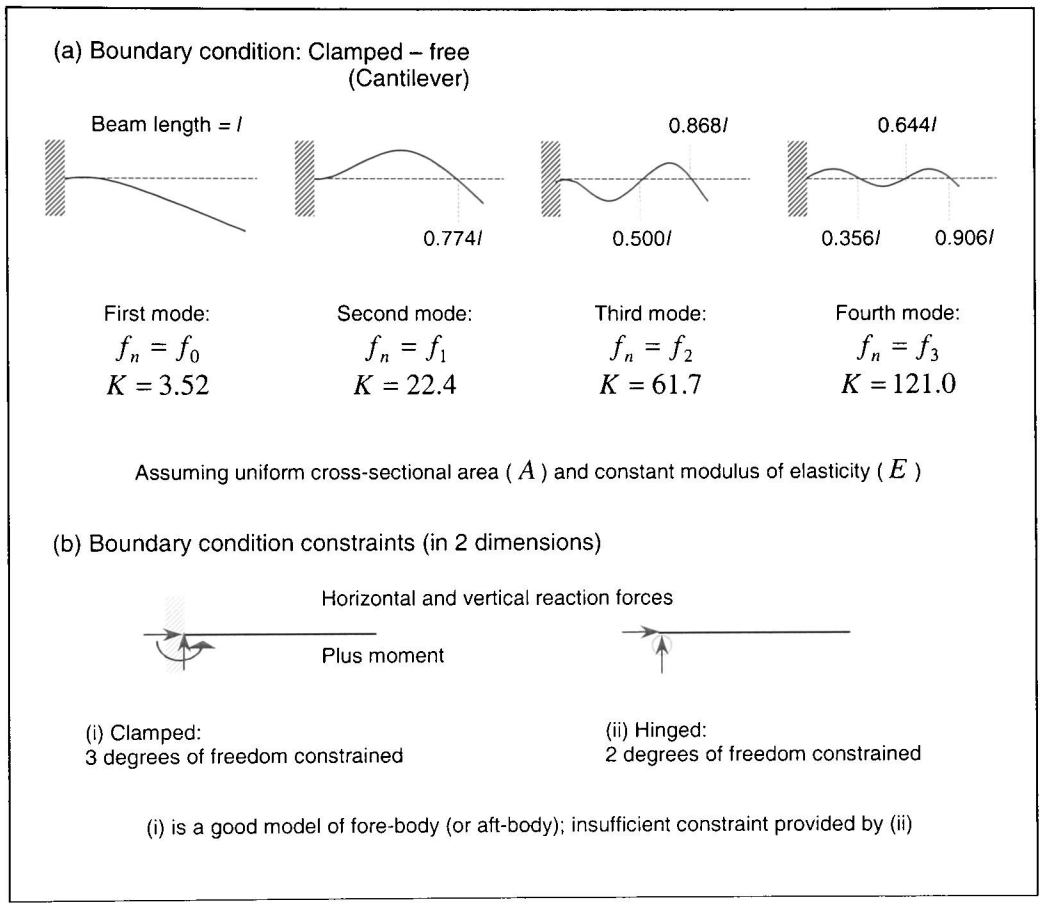

Figure 2-14: Cantilever mode shapes (produced with reference to [Broch, 1984]) and support conditions

Modelling the ski as discrete lumped masses (connected by rods – see Figure 2-15) and investigating the response of these masses enables a more detailed investigation of the structural vibration – with a focus on the fore-body, in this work. The relative amplitude and phase of the movement (as an acceleration, velocity, or displacement) of the lumped masses can be used to analyse the vibratory response of the structure. The rods connecting the lumped masses represent springs, with stiffness between the masses depending on the material properties that make up the composite and the geometry (i.e., stiffness is proportional to the modulus of elasticity and the second moment of area).

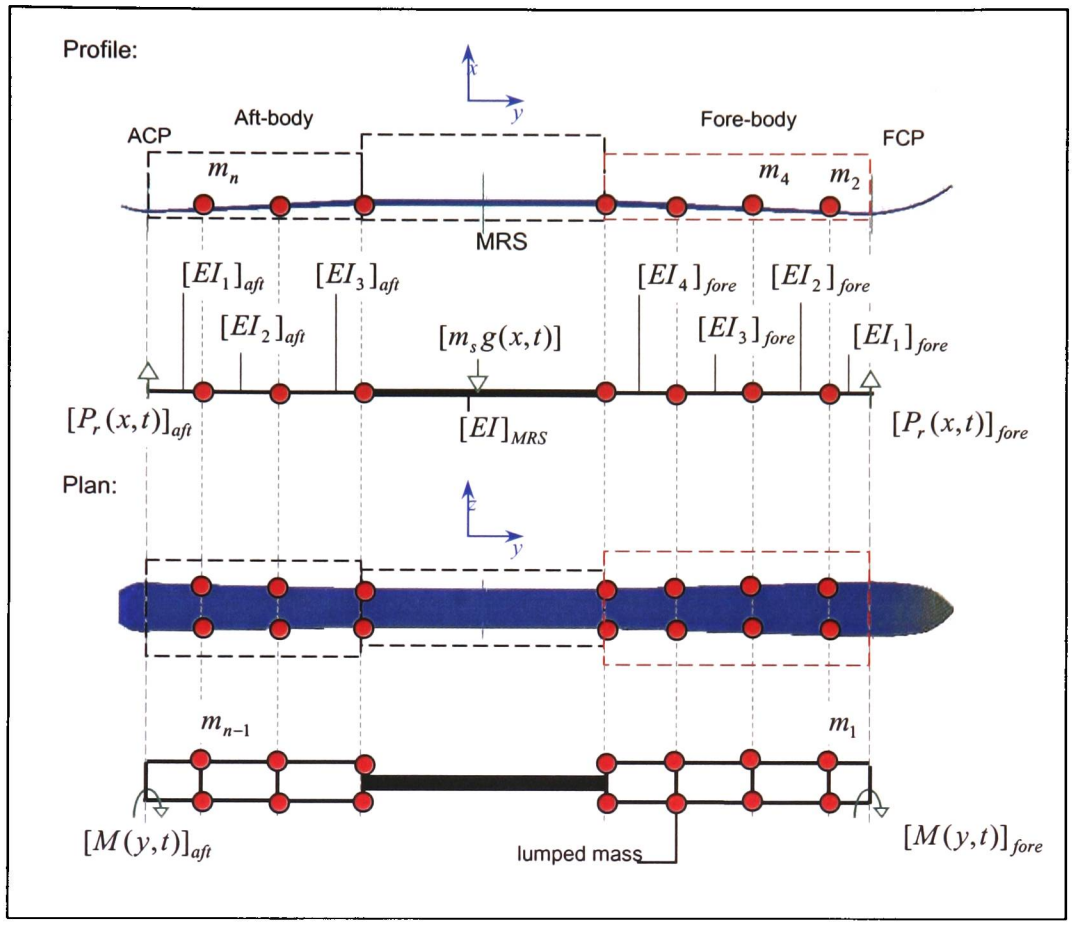

Figure 2-15: Discrete-parameter model
(and sensor layout of piezo-polymer instrumented ski – see §3.4)

Dividing the structure into elements is the basis for finite element analysis. Clerc et al [1989] and Pärsinnen and Lehtovaara [1991] presented finite element techniques for predicting pressure distribution between a ski (modelled with free-free boundary conditions at the ACP and FCP) and the snow surface (modelled by both, as elastic with constant stiffness in compression and zero stiffness in tension). In addition to presenting a comparison of computational and measured results for pressure distribution (in terms of force per unit length), Clerc et al [1989] presented a comparison of measured and calculated frequencies for an alpine ski - showing good agreement between the measured and calculated results (see Table 2-3).

Mode	Frequency (Hz)	
	Measured	Calculated
F1	18	17.2
F2	41	38.1
C1	71	68.0
F3	72	67.0
F4	111	104.0
C2	117	110.0

F=plane flex; C=coupled flex and torsion

Table 2-3: Measured and calculated frequencies of an alpine ski with free-free boundary conditions [Clerc et al, 1989]

Devaux and Trompette [1980] used finite element techniques for modal analysis of a ski (i.e., quantifying the first four modal frequencies and the damping factor). The snow surface is not included in the model, with homogeneous cantilevers and free-free beams used to model the ski and obtain the first resonance frequencies. The computational results for frequency and damping (factor) are compared (see Table 2-4) with measured results from a ski with free-free boundary conditions.

Mode	Frequency (Hz)		Damping values (%)	
	Measured	Calculated	Measured	Calculated
First	19.0	17.9	0.60	0.82
Second	38.4	36.3	0.58	0.82
Third	67.3	64.9	0.67	0.82
Fourth	105.5	103.8	0.62	0.82

Table 2-4: Ski modal analysis (with free-free boundary conditions): comparing measured and calculated modes [Devaux and Trompette, 1980]

The measured and calculated frequencies presented by Clerc et al [1989] (see Table 2-3) and Devaux and Trompette [1980] (see Table 2-4) pre-dates carving skis and does not include the skier in the model (i.e., a force, or moment acting over the MRS). The omission of a load on top of the ski over the MRS is significant, since it coincides approximately with the position of the nodal displacement of the first mode (with the ski modelled as a free-free beam). Including the skier will suppress the first mode in a model with free-free boundary conditions, since the weight of the skier is applied at the point of maximum displacement.

Mode	Frequency (Hz)
First	9.75
Second	39.05
Third	95.85
Fourth	178.60

Table 2-5: Measured fore-body natural frequencies with clamped-free supports [Hosokawa et al, 2002]

The cantilever model of the fore-body was adopted by Hosokawa et al [2002], in laboratory tests investigating the performance of a mass damper located on the fore-body of a ski. Natural

frequencies (see Table 2-5) are presented [Hosokawa et al, 2002] following impact tests on the cantilever supported fore-body of a ski (unspecified in terms of length, sidecut and make). There are clearly differences between the results presented by Hosokawa et al [2002], adopting clamped-free boundary conditions, and those presented by Devaux and Trompette [1980] and Clerc et al [1989] - assuming free-free boundary conditions. The significance of the boundary conditions on results is clear if mode shapes are compared (see Figure 2-14 and Figure 2-16) for the various support configurations that are used for ski analysis.

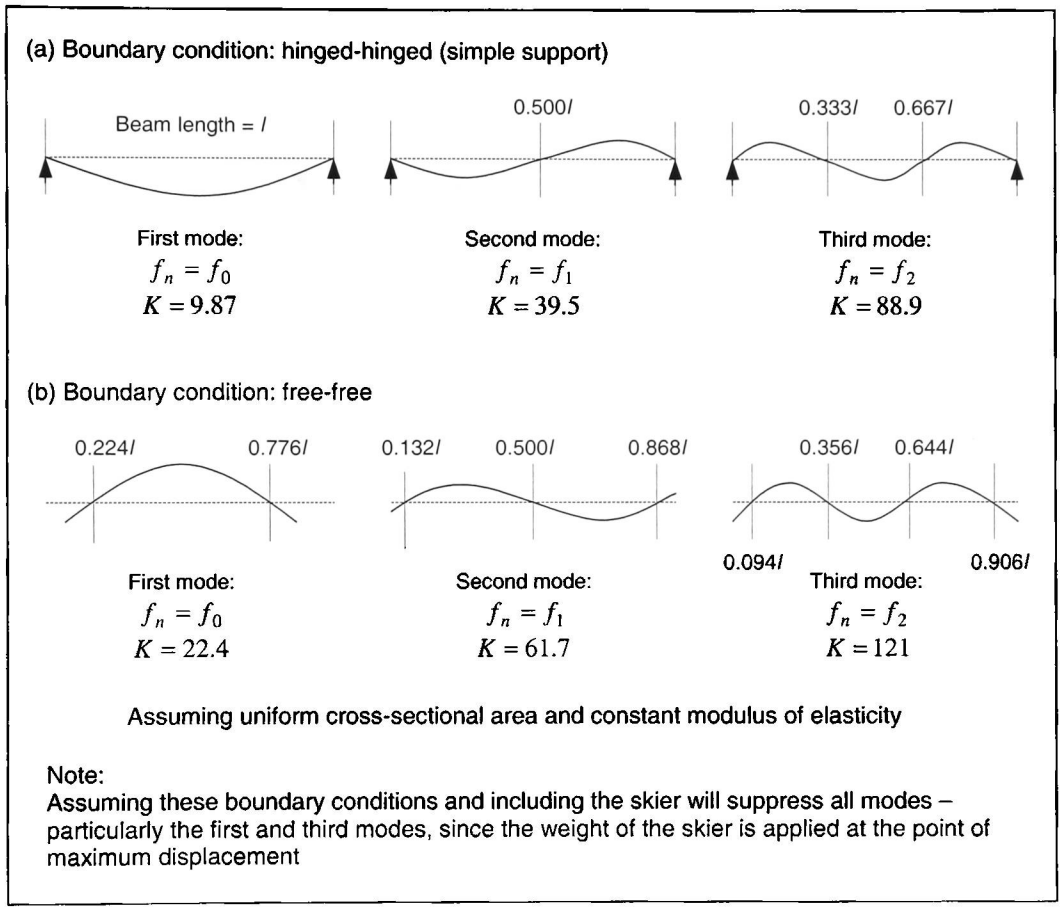

Figure 2-16: Comparing hinged-hinged and free-free boundary conditions
(produced with reference to [Broch, 1984])

Reducing the ski to fore-body and aft-body cantilevers (rather than simple support free-free boundary conditions) with skier-induced moments at the support is considered here a simple, but more representative model of the boundary conditions experienced by the system. However, there are limitations with this model, which assumes the MRS is continuously loaded and in effect isolated. The model does not hold if the MRS is not loaded and is therefore not suitable to analyse vibrations that may propagate down the structure as the skier unweights the ski.

2.4.1 Skier

While it is not the intention to analyse the biomechanics of the ski-skier system, it is necessary to understand skier movement and the bearing on ski control forces. The position of the centre of mass of the skier relative to the ski is considered (see Figure 2-17), to establish the resultant weight on the ski and how this relates to the skier-induced moment in the model presented earlier (see §2.4, Figure 2-13 c). Technique is not discussed: the motivation here is to understand the influence of skier position on ski dynamics.

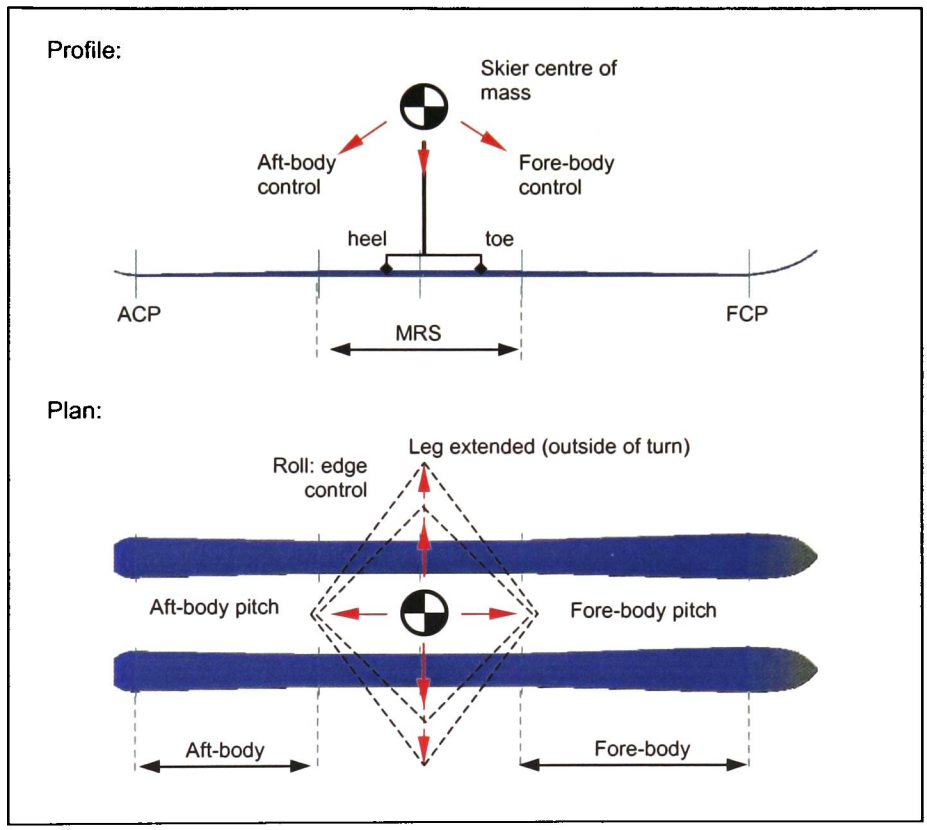

Figure 2-17: Influence of skier position on ski control

The turn is initiated on the fore-body with the weight of the skier forward (i.e., the skier turns on the ball of the foot) and on the inside of the turn (i.e., left turn: skier weight is left of the central-axis of the ski). Similarly, the aft-body is used to turn with the weight of the skier back (i.e., the skier turning on the heels) and on the inside of the turn. Holding the turn, the weight stays on the inside of the turn, but moves into a more central position (relative to the bindings). The displacement of the centre of mass from the central-axis controls the angulation of the ski and influences the reaction force of the slope that holds the ski in a turn (see Figure 2-18).

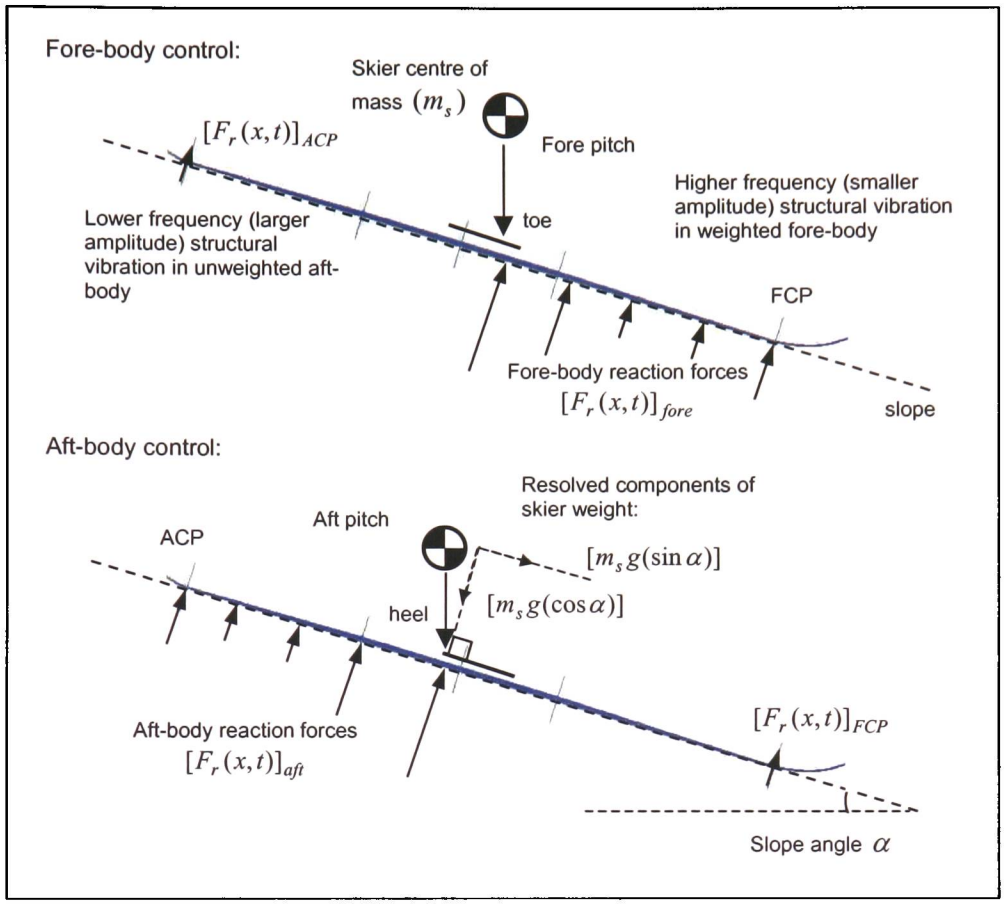

Figure 2-18: Relationship between reaction force and skier position

Comparison of skier joint motions (i.e., at the hip and knee) and reaction forces (measured through a force plate between the boot and binding) on carving and non-carving skis were investigated experimentally by Yoneyama et al [2000]. Data was used to graphically model skier biomechanics, from the waist down, during skidding and carving turns.

A ski is described as "feeling dead" if it provides the skier with insufficient feedback. Skis are damped to prevent resonance induced by forced vibration and it is claimed [Lind and Sanders, 1996] that over-damping makes the skis feel dead. However, it is considered here that the flex determines the useful feedback provided to the skier. Damping serves to control the ski from undesirable structural vibrations (refer again to §2.3 on dynamic stability), which cause loss of control due to edge chatter and skier fatigue (i.e., as a result of the increased muscle activity required to control the vibrating ski). Therefore, it is the opinion here that the skier would benefit from as much damping as possible (i.e., the damping factor $\zeta \to 1$ – see appendix A-1.2). However, this does not mean that a set value of viscous damping can be specified, because skis are not and should not be manufactured with a standard flex pattern. Different ski stiffness (i.e., the inverse of flex) suits different skiers,

depending on their size, weight, ability and snow condition (see §2.4.2). Finding the correct ski is not always easy.

Recreational skis are expected to perform over a broad range of conditions, with their dynamic response being influenced by the skier. Therefore, a lightweight skier may find relatively stiffer skis to be unresponsive (e.g., a female skier on male biased downhill skis) and a heavier skier may feel that softer flex skis are too pliable and possibly too lively, if insufficiently damped. Skier ability should also influence the choice of ski, with softer flex being more suitable for novice skiers – since less effort is required to make the ski respond.

Increased edge control is one motivation for vibration control; another is reduced skier fatigue. The effects of vibration on the human body range from annoyance and fatigue, to reduced comfort and safety. The intensity with which the body reacts to different frequencies and amplitudes is widely influenced by muscle development, nevertheless an approximation of the mechanical system is presented by Babiel et al [1997] – see Figure 2-19.

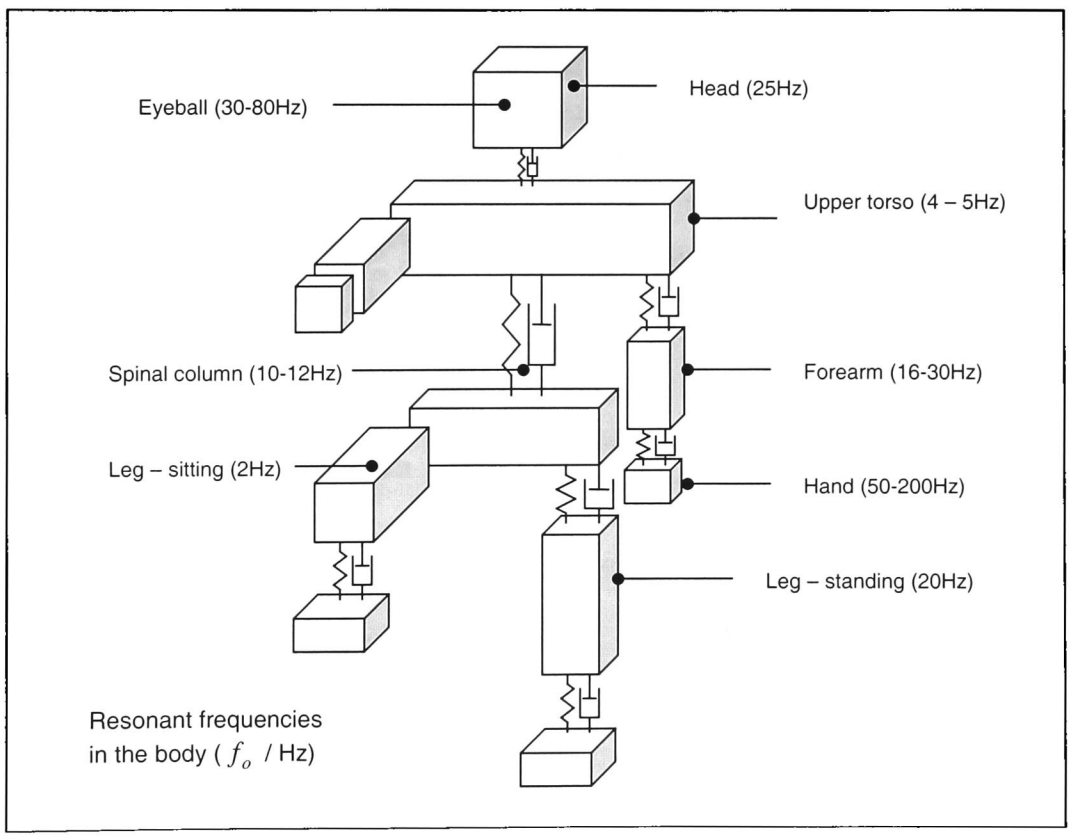

Figure 2-19: Human mechanical system (produced with reference to Babiel et al [1997])

This work focuses primarily on investigating edge control, particularly in the fore-body, with a view to enhancing performance - using a smart damper to improve carving characteristics. The tests carried out on skis and the location and distribution of sensors are for performance evaluation. Investigation of skier fatigue would require the tests to be adapted and sensors should be located closer to the boot (i.e., distributed around the binding).

2.4.2 Environmental conditions

The environmental influence on ski dynamic stability is of interest, with a focus on structural vibration and disregard for ski-surface friction. The movement of the ski over the snow surface not only induces vibration, but also absorbs vibration (see Figure 2-20). Therefore, it is accurate to use a viscoelastic model (see Figure 2-11) of the snow. For simplicity, Clerc et al [1989] and Pärsinnen and Lehtovaara [1991] modelled the ski-snow interaction as compression-only linear springs (i.e., not including the energy dissipating damper). Clerc et al [1989] acknowledged the limitation of this representation and Pärsinnen and Lehtovaara [1991] referred to work by Aichner [1978] that includes plasticity in the snow model.

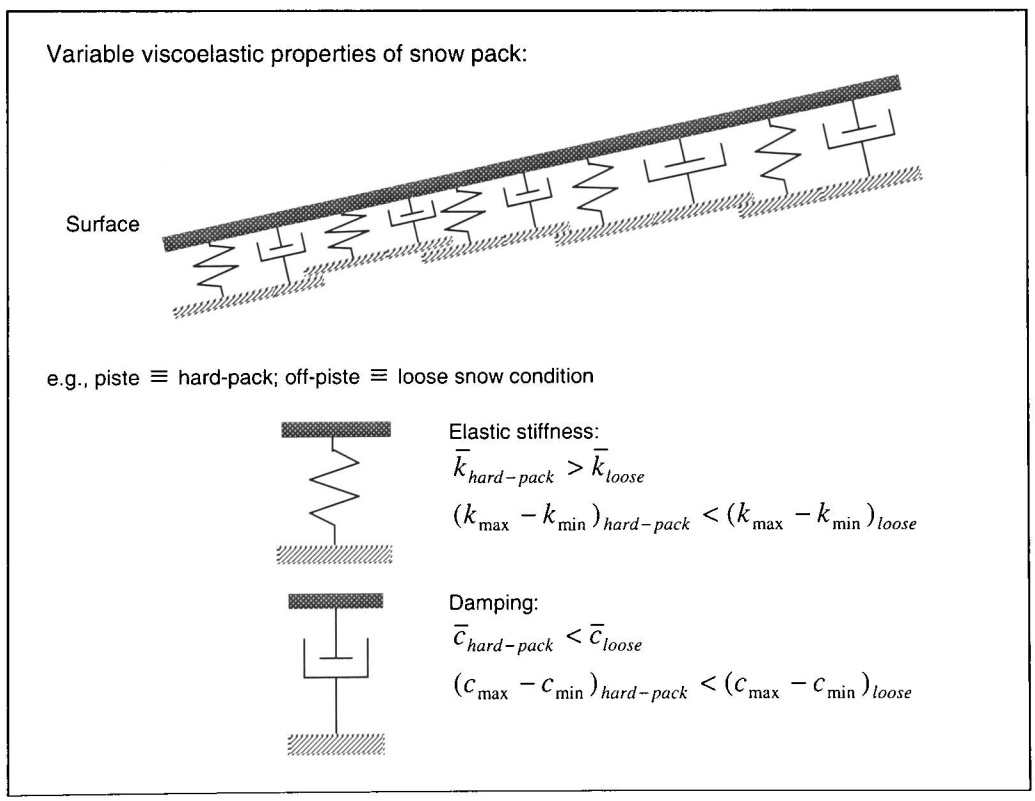

Figure 2-20: Model of the environmental system
(more accurate than the elastic model commonly assumed)

The energy transmitted or absorbed by the surface depends on the speed the ski moves over the surface, the position of the centre of mass of the skier (avoiding detailed biomechanical analysis) and the snow structure (not discussed in detail).

Two scenarios may be considered to help understanding of the response of a ski with regards to its physical characteristics - in terms of longitudinal and torsional stiffness and damping. Compare a loose-packed, irregular surface (e.g., off-piste condition) against a hard-packed snow condition with relatively regular surface (e.g., piste condition). The range of elasticity and damping is greater in loose snow conditions, with less damping and a greater mean elasticity on hard-packed snow expected (see Figure 2-20).

More kinetic energy of the ski-skier system is absorbed in loose snow conditions, compared with hard-packed surface conditions. Off piste, this may be compounded by topographical changes (i.e., uneven surface), which produces system movement with an increase in the component of movement perpendicular to the slope.

The reaction forces on the ski depend on the location of the resultant weight of the skier (see §2.4.1) and on the absorbed kinetic energy (i.e., not contributing to a resultant velocity). The amplitude of vertical deflection generated over a loose-packed snow condition is greater than that generated on a hard-packed (piste) surface, although, the rate of change of deflection amplitude (i.e., velocity) may be greater on-piste. Understanding the dynamic response of the ski over different conditions is important for the adaptive ski concept. Establishing a method for identifying snow condition based on the dynamic response of the ski introduces the potential to use this information as the basis for control of actuators in a smart technology system.

The snow condition (e.g., hard-packed versus loose-packed, or soft) affects the surface reaction forces on the ski that contribute to structural deformation and vibration (investigated through field-testing of instrumented skis – see §3.4). Ski deformation is proportional to flex (the inverse of stiffness) and what is suitable for one snow condition is not necessarily the best for another (e.g., stiff skis that provide good edge control on hard-packed piste conditions may be difficult to edge in softer snow conditions and therefore considered unresponsive). Structural vibration may lead to edge chatter – resulting in skid turns rather than more controlled carving turns. It is the opinion here that the amplitude and frequency of structural vibration in the ski is related to the surface conditions - with relatively higher frequency, lower amplitude vibrations being associated with hard-packed conditions compared with the vibrations experienced over softer snow conditions. This is the premise for the adaptive ski concept and semi-active vibration control of skis (see §3.4.3).

Should the ski be subjected to excitation forces at frequencies close to its natural frequency, resonance will occur and there will be free vibration with a greatly magnified response. The environmental input contributes to the excitation forces that stimulate a response, dependant on the physical properties of the system (see §2.3). Ideally, the system would be engineered to prevent resonance occurring over its operating range, or (frequency) bandwidth. However, if the system is expected to perform over a wide operating bandwidth, it becomes more difficult to engineer a system that can perform consistently. A narrower operating bandwidth is easier to define (through field-test measurements), with relatively fewer variables - reducing the complexity of the system. In this respect, recreational skis may be considered a more complex system than competition race skis that are intended for use over a relatively narrow bandwidth.

Overcoming edge chatter and providing the correct amount of flex requires consideration of a complex dynamic system that demands mutually exclusive physical characteristics (i.e., in terms of longitudinal and torsional stiffness and damping) to satisfy variable environmental conditions.

The challenge is to engineer a ski that has an operating bandwidth that is broad enough to be compatible with the needs of the skier. Incorporating smart technology to adapt the physical characteristics of the skis to their changeable environment introduces the potential to increase the bandwidth, or operating range of the ski.

2.5 Smart skis

A variety of smart materials have been used to provide feedback control in response to environmental changes. A single material may be used as sensor and actuator, in a distributed or continuous network. The concept presented in this work proposes the use of one material (i.e., piezoelectric thin film polymer) as the sensor and another as the actuator (i.e., using a controllable rheological fluid), to provide a physical response based on that monitored by the sensor. Further, it is proposed that a third smart material (i.e., piezo-ceramic located under the skier at the MRS) should be used to generate a power supply for the actuator and control circuit.

Previous attempts at incorporating smart technology in skis have been based around a single smart material used as both sensor and actuator.

Research (Scherrer, von Niederhausern, Gotthardt) at École Polytechnique Fédérale de Lausanne (EPFL), in collaboration with Skifabrik Stöckli AG (i.e., Stöckli skis) and Swissmetal, is investigating the adaptive damping capability of shape memory alloys (SMAs) integrated into the composite structure of alpine skis. It is reported [Fugazza, 2003] that laminated strips of copper-zinc-aluminium (CuZnAl) alloys are used to damp vibrations with the aim of improving ski performance.

The SMA strips have martensitic transformation temperatures above 0°C, so when the ski is in contact with snow, the CuZnAl elements transform into martensite and damp vibrations in the ski.

Despite having relatively slower response times than other smart materials, SMAs are considered less susceptible to environmental operating conditions - other than temperature, which is used to 'activate' the material. Another perceived advantage is the ability to integrate the SMA into the composite – avoiding the necessity to have a shim.

A lead-zirconium-titanate (PZT) piezo-ceramic sensor and actuator unit developed by Active Control eXperts (ACX) and integrated on the K2 Four ski (circa 1995) is the first commercial application of smart technology on skis. The system claims to provide vibration control and improve edge-to-snow contact for better control. The system comprises three stacks of two PZT sheets, each with an embedded control chip and shunt circuitry, with a unit size of approximately 50mm x 150mm.

HEAD skis [www.head.com/ski] claim to have incorporated a smart technology system to control torsional stability based on speed, terrain and snow conditions. The HEAD "Intelligence" system comprises a series of piezoelectric "Intellifibres" that are located in the fore-body of the ski, with the aim of controlling the torsional mode of vibration. The embedded piezoelectric fibres generate a current proportional to the mechanical deformations in the ski and it is claimed that the current is amplified (up to seven times) and fed back into the fibres, so that they produce a mechanical force used to increase the torsional stability of the ski. The system has a claimed response time of 5ms.

Increased torsional stability at speed and in hard-packed snow conditions is the motivation; however, the actual ability of the HEAD system to achieve what is claimed is less clear. Assuming the electrical energy generated by the piezoelectric fibres can be efficiently conserved when not required to produce a counter-force, it still remains unclear how the input may be amplified (up to seven times), without an additional power source. Maintaining an adequate power supply is recognised (see §5.1.2 on technical risk) as a significant technical barrier to the future development of the adaptive ski concept proposed in this work. Any suggestion that the piezoelectric fibres actually twist the fore-body against the application of force infers that the fibres are capable of producing a force capable of overcoming the fore-body torsional stiffness, which is considered here to be implausible. In addition, the fibres would have to produce this force with the power generated from the vibrating ski. The environmental temperature affects the power generated by and required for the piezoelectric fibres, which have a defined pyroelectric response.

The HEAD "Intelligence collection" includes race skis (i.e., the Worldcup i.SL and Worldcup i.Race) and the graphics on the HEAD skis entered in the 2002 winter Olympics (in Salt Lake City) suggest

that those skis also contained the smart technology system. However, it is debatable if the skis used in the Olympics actually had the smart technology system.

The adaptive ski system investigated in this work proposes the use of a magnetorheological (MR) fluid damper to semi-actively control the dynamic movement of the ski. A piezo-system may be able to provide 2% damping over a wide frequency range (e.g., the K2 system aims to target 200Hz vibrations). The MR fluid has a significantly greater resistive force capability (certainly able to achieve amplitude reduction>20%; for a frequency<10Hz), but over a lower frequency range (<40Hz). This work investigates the feasibility of powering a small MR fluid device (see 4.4.2) capable of providing a significant level of adaptive force control to semi-actively damp a ski (see §5).

There is a focus on investigating control of induced vibrations below 40Hz. The relatively higher amplitude of lower frequency (i.e., <40Hz) forced vibrations is considered (here) to generate greater adverse control conditions (than >40Hz). Therefore, vibration control of the lower frequency forced vibrations may be expected to provide tangible control benefits that may be noticeable even to recreational skiers.

3 Ski Dynamic Measurement

This section presents measurement and analytical techniques used to obtain results from static and dynamic tests. The tests provide quantifiable information on modern carving skis that is necessary for developing the adaptive ski concept. Specifically, the tests seek to investigate stiffness and damping in carving skis and identify locations for the adaptive damping system – with initial focus on fore-body vibration control. It is not the intention to reverse engineer a particular ski.

Static tests of skis are carried out with reference to procedures outlined in standards from the American Society for Testing and Materials (ASTM). Dynamic tests show that different skis have a dissimilar response and that they respond differently when edged.

In addition to static analysis to quantify stiffness, two methods of dynamic structural analysis are considered [Døssing, 1, 1988]:

1. System analysis – where the inherent properties of a system are determined so that a dynamic model may be established
2. Signal analysis – where the response of a system to some unknown excitation is determined and presented

System analysis involves studying the response of the system following stimulation with a measurable force. Signal analysis is the study of the system response to operational forces.

The response, or force ratio (i.e., output sensitivity to an input force) is an independent, inherent property (or characteristic) for linear systems, whether excited or at rest. Spectrum analysis of acceleration data in the time domain transforms the data into the frequency domain, so that energy concentrations (as functions of acceleration, velocity, or displacement) may be identified (with respect to frequency) and related to mechanical components of the system. This enables the source vibration and the dynamic compliance of the structure to be considered.

Static and dynamic system analysis is presented of data obtained from laboratory tests performed on a custom-made ski simulator (see §3.2). Techniques for system analysis (see §3.3) can be extended to analyse the signal produced from instrumented skis during field tests. A technique for instrumentation of skis with piezo-polymer sensors is proposed and preliminary test results are appraised (see §3.4). It is proposed that the instrumentation used in field-tests and techniques used for laboratory analysis may be developed for control of the proposed adaptive ski.

3.1 Laboratory procedures

Laboratory testing provides the opportunity to carry out repeatable tests on skis under controlled conditions. It is possible to identify and compare physical characteristics (e.g., stiffness) of skis. Test methods for alpine skis are outlined in ASTM standards and include measurement of:

- Centre spring constant and spring constant balance of alpine skis [ASTM F 498-77 (1998)]
- Lateral toe release of adult alpine ski bindings under impact loading [ASTM F 1017-86 (1994)]
- Linear deformation and breaking strength of alpine skis [ASTM F 780-93a (1998)]
- Mass moment and inertia of alpine skis [ASTM F 1722-96 (1996)]
- Quasi-static release moments of alpine ski bindings [ASTM F 504-94 (1994)]
- Torsion characteristic of alpine skis [ASTM F 779-93 (1998)]
- Verification of ski binding test devices [ASTM F 1062-97 (1997)]

The focus here is on ski dynamic measurement and therefore no detailed analysis of binding forces or ski failure is included. ASTM standards (i.e., ASTM F 498-77 [1998] and ASTM F 779-93 [1998]), relating to measurement of spring constants (i.e., centre, fore-body and aft-body) and torsional stiffness, are used for guidance in static testing.

Flexural and torsional rigidity is measured by Deak et al [1975] and Sakata and Ito [1997], with the latter presenting a compilation of results taken over 22 years - providing a quantifiable comparison of ski development between 1975 and 1996. Piziali and Mote [1972] quantified dynamic characteristics of pre-carving skis using laboratory and field measurements. Static results included measurements of flexural and torsional stiffness, geometry and inertia. Dynamic laboratory measurements sought to identify resonance within a specified frequency spectrum (0-1000Hz) and characterised modal properties of the skis under investigation. Conclusions included acknowledgement that free vibration measures are not meaningful – supporting what has already been presented in this work on the boundary conditions for modelling (see figure 2-15, §2.4). Also, the physical information that is related to straight skiing was found to be independent to that obtained for turning manoeuvres – hence, the motivation in this work for investigating torsional stiffness characteristics. A similar laboratory and field-test analysis (also supported with video) was carried out by Niessen et al [1997], with boundary conditions imposed on the fore-body and aft-body to make laboratory tests more representative. The laboratory load condition excluded the first mode of vibration (at approximately 15Hz) determined from free vibration tests, but there was better correlation with subsequent natural frequencies (i.e., approximately: 35Hz and 53Hz, constrained, and 32Hz and 50Hz, free)

A system for measuring elastic characteristics of skis in straight and curved trajectories was presented by De Cecco and Angrilli [1999]. A mechanical frame with 16 dynamometric (i.e., strain gauged double-cantilever beam) supports was used to measure ski response following a force (i.e., 300-

1600N) produced by a hydraulic cylinder that was representative of the skier. Load position could be changed to simulate force and moment components at the base of a 'boot,' connected to the hydraulic cylinder. Results indicated that ski stiffness increases with ski angulation. Damping characteristics were not investigated.

Laboratory testing of snowboards was presented by Buffington et al [2001] – where computational and field studies were used to determine bending and torsional natural frequencies and damping ratios of a cohort of snowboards. A dynamic test machine (developed at Bucknell University) capable of simulating field tests was reported. Four pneumatic actuators subjected the snowboard to forces representative of those applied by the heel and toe of the rider. Data from strain gauges and accelerometers could be compared with that obtained from field-tests.

3.1.1 Ski stiffness

The centre spring constant (i.e., the stiffness) can be determined by following the ASTM guidelines (i.e., [ASTM F 498-77 (1998)]). The ski is simply supported at the forward and aft control points (i.e., FCP & ACP respectively) and load is placed at the mid-running surface – mid-way between the FCP & ACP (see Figure 3-1). The bending stiffness can be determined using equation [3-1].

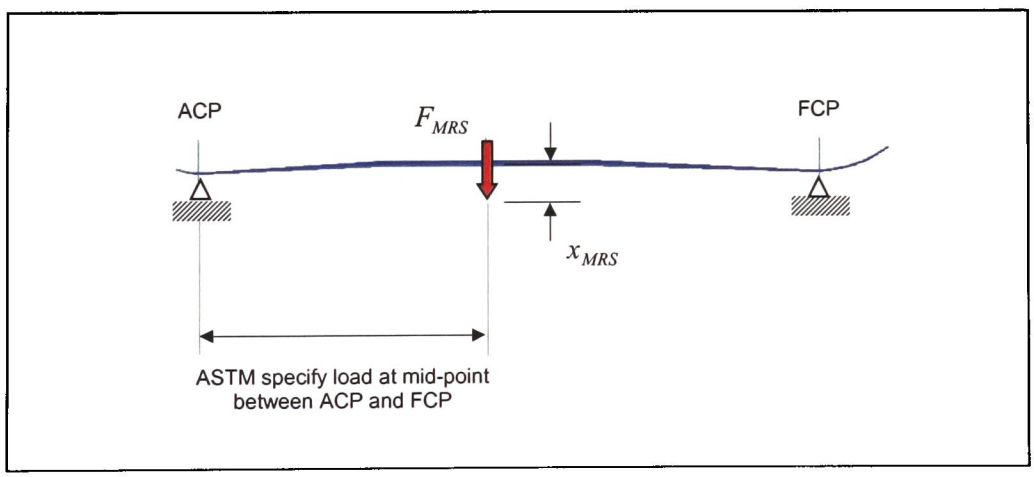

Figure 3-1: Determining overall ski stiffness (based on [ASTM F 498-77 (1998)])

$$B_{centre} = \frac{F_{MRS} \cdot l_{contact}^3}{48 \cdot x_{MRS}} \qquad [3\text{-}1]$$

where, B_{centre} = bending stiffness (at the centre); F_{MRS} = load at the MRS; $l_{contact}$ = contact length (between the FCP and ACP supports); and, x_{MRS} = displacement at the MRS.

Bending stiffness (B) is proportional to the product of the modulus of elasticity (E) and the second moment of area (I) about the neutral axis:

i.e., $$B \propto E \cdot I \qquad [3\text{-}2]$$

Rearranging equation [3-1], the centre spring constant may be defined:

$$k_{centre} = \frac{48 \cdot B_{centre}}{l_{contact}^3} = \frac{F_{MRS}}{x_{MRS}} \qquad [3\text{-}3]$$

3.1.2 Fore and aft-body spring constants

The fore-body (or aft-body) spring constant may be calculated by clamping the ski at the MRS and measuring the deflection at the FCP (or ACP), when loaded (see Figure 3-2) as a cantilever. It is considered here that measurement of the fore-body and aft-body spring constant is more relevant than the overall ski stiffness (i.e., fore and aft body stiffness can be used to predict dynamic response during skiing). The fore-body and aft-body spring constants can be used in the distributed parameter model (advocated earlier – see Figure 2–15, §2.4) and is used to quantify steering forces (referring to equation [2–26], as presented by Glenne et al [1997]).

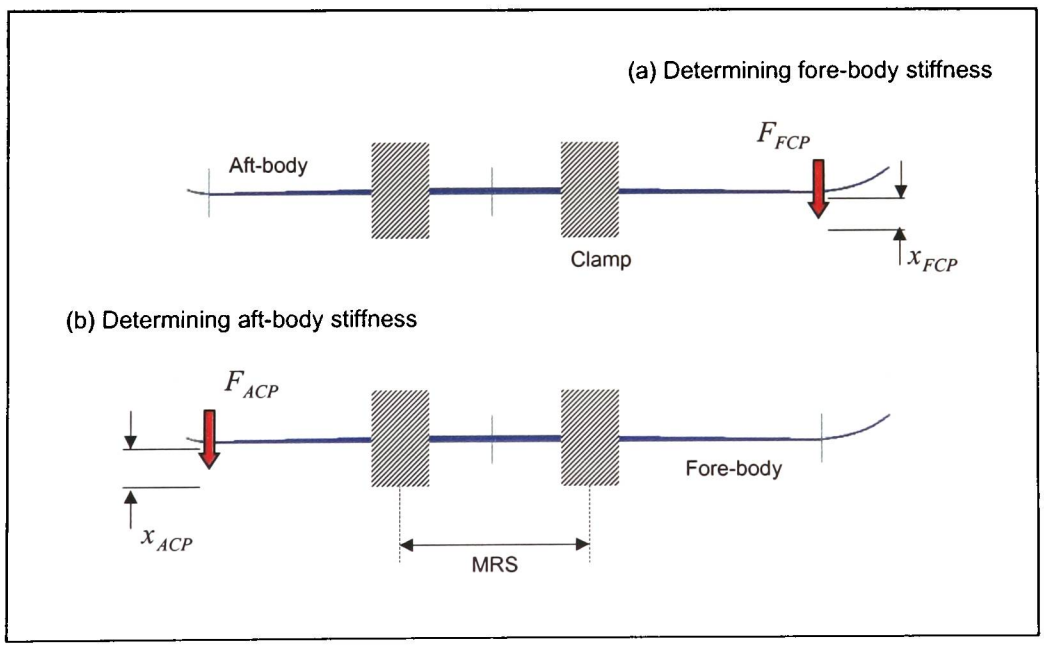

Figure 3-2: Determining fore-body, or aft-body stiffness (an adaptation of [ASTM F498-77 (1998)])

The parameters in the calculation of the fore-body and aft-body bending stiffness are similar to those in equation [3–1]. The fore-body and aft-body are considered as cantilever structures, with the length

being the distance from the clamp at the MRS to the load point at the FCP (i.e., l_{fore}) or ACP (i.e., l_{aft}), respectively.

Therefore,

$$B_{FCP} = \frac{F_{FCP} \cdot l_{fore}^3}{3 \cdot x_{FCP}} \quad [3\text{-}4]$$

$$B_{ACP} = \frac{F_{ACP} \cdot l_{aft}^3}{3 \cdot x_{ACP}} \quad [3\text{-}5]$$

where, B_{FCP} = bending stiffness (in the fore-body) and B_{ACP} = bending stiffness (in the aft-body). Rearranging equations [3–4] and [3–5], the fore-body and aft-body spring constants may be defined:

$$k_{fore} = \frac{3 \cdot B_{FCP}}{l_{fore}^3} = \frac{F_{FCP}}{x_{FCP}} \quad [3\text{-}6]$$

$$k_{aft} = \frac{3 \cdot B_{ACP}}{l_{aft}^3} = \frac{F_{ACP}}{x_{ACP}} \quad [3\text{-}7]$$

3.1.3 Torsional stiffness

Skis should have a high torsional rigidity so that they do not twist during a turn - when the skier "edges" the ski. Torsional stiffness may be measured by clamping the ski at the MRS and measuring the ratio of torque (applied at the FCP or ACP) to angle of twist (see Figure 3-3). Similar to fore-body and aft-body spring constants, torsional stiffness can be used in the distributed parameter model (advocated earlier – see Figure 2–15, §2.4) and can also be used to quantify steering forces (referring to equation [2–26], as presented by Glenne et al [1997]).

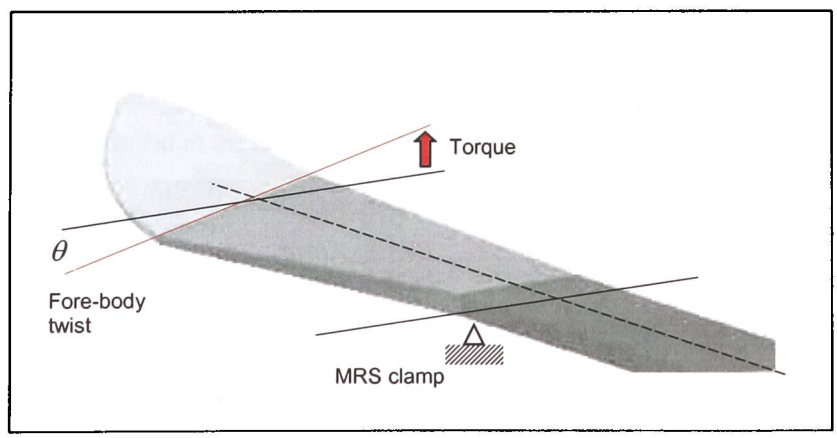

Figure 3-3: Determining fore-body torsional stiffness (based on [ASTM F 779-93 (1998)])

$$GJ = \frac{T \cdot l}{\theta} \qquad [3\text{-}8]$$

where, θ = angle of twist; T = torque; l = length (either l_{fore} or l_{aft}) and GJ = torsional stiffness - i.e., the product of the modulus of rigidity (G) of the ski and the polar second moment of area (J).

Rearranging equation [3-8], the torsional spring constant (k_T) may be defined:

$$k_T = \frac{GJ}{l} = \frac{T}{\theta} \qquad [3\text{-}9]$$

3.2 Ski simulator

Laboratory testing of skis is considered here to generally be a poor representation of the real world situation and is consequently not considered a means to provide anything more than quantification of physical characteristics. Therefore, there is a reliance on field-testing of skis that is traditionally qualitative rather than quantitative. The qualitative approach is subjective and depends very much on the feedback from the test skier – not necessarily representative of the majority of recreational skiers. Changing snow and temperature conditions compromise both approaches and make it more difficult to provide a fair comparison of ski performance (assuming skis of comparable geometry and stiffness are being tested).

The ability to simulate a turn in the laboratory is of particular benefit to this work, with particular interest in fore-body vibration. Analyses of fore-body vibration properties are compared following tests on a range of skis and a control structure (i.e., an aluminium beam), carried-out on a custom built rig (i.e., the ski simulator).

A laboratory set-up that enables some aspects of ski dynamics to be simulated and analysed under controlled and repeatable conditions would be useful to benchmark dynamic aspects of existing commercially available skis and may be used to appraise new concepts. The same motivations for laboratory appraisal, that led to the development of the ski simulator presented here, were identified by De Cecco and Angrilli, [1999].

The fore-body is of particular interest, since it is used to initiate and control a turn - assuming the skier weights the fore-body during the turn (see §2.3.2). Even if the skier is leaning back, with their weight acting on the aft-body, the relative length makes the fore-body more susceptible to vibration than the aft-body – assuming a conventional binding setting, aft of centre. Therefore, the proposed adaptive system is first considered for fore-body vibration control, as is the case on previous and

existing attempts at integrating smart technology (see §2.5) on skis (i.e., K2 and HEAD skis respectively). Consequently analysis is focussed on the fore-body.

The ASTM procedures for carrying out static tests on skis and snowboards can be used to establish a basic requirement (i.e., quantification of physical characteristics - specifically stiffness) from any laboratory rig test, or simulator. Subsequently, by considering ski dynamics, it is possible to develop a system to put the ski under forces representative of those experienced in a turn. Albeit a simplification, it is possible to consistently reproduce boundary conditions characteristic of a turn and compare experimentally derived data from both static and dynamic tests.

The simulator is mounted on a lathe bed and is designed to test skis and snowboards, comprising two moment arms (e.g., acting as fore-body and aft-body supports – see Figure 3-4). Each moment arm is built around a split shaft that is cradled on four roller bearings (i.e., in two support cradles at opposite ends of the split shaft – see Figure 3-5 a). The angle of tilt of the moment arm is measured with a digital inclinometer (FISCO Solatronic, model EN17). Locking the moment arms in a horizontal position (i.e., 0°), they can be located on the lathe bed to simply support the ski at the FCP and ACP so that the MRS may be loaded (i.e., to determine ski stiffness, as outlined in §3.1.1). Alternatively, the moment arms (again, locked in a horizontal position) may be located on the lathe bed to clamp the ski at the MRS so that the FCP or ACP may be loaded (i.e., to determine fore-body or aft-body spring constants - see §3.1.2). To reduce the contact area at the support, the moment arm has a support shaft (see Figure 3-5 a) onto which the ski is positioned.

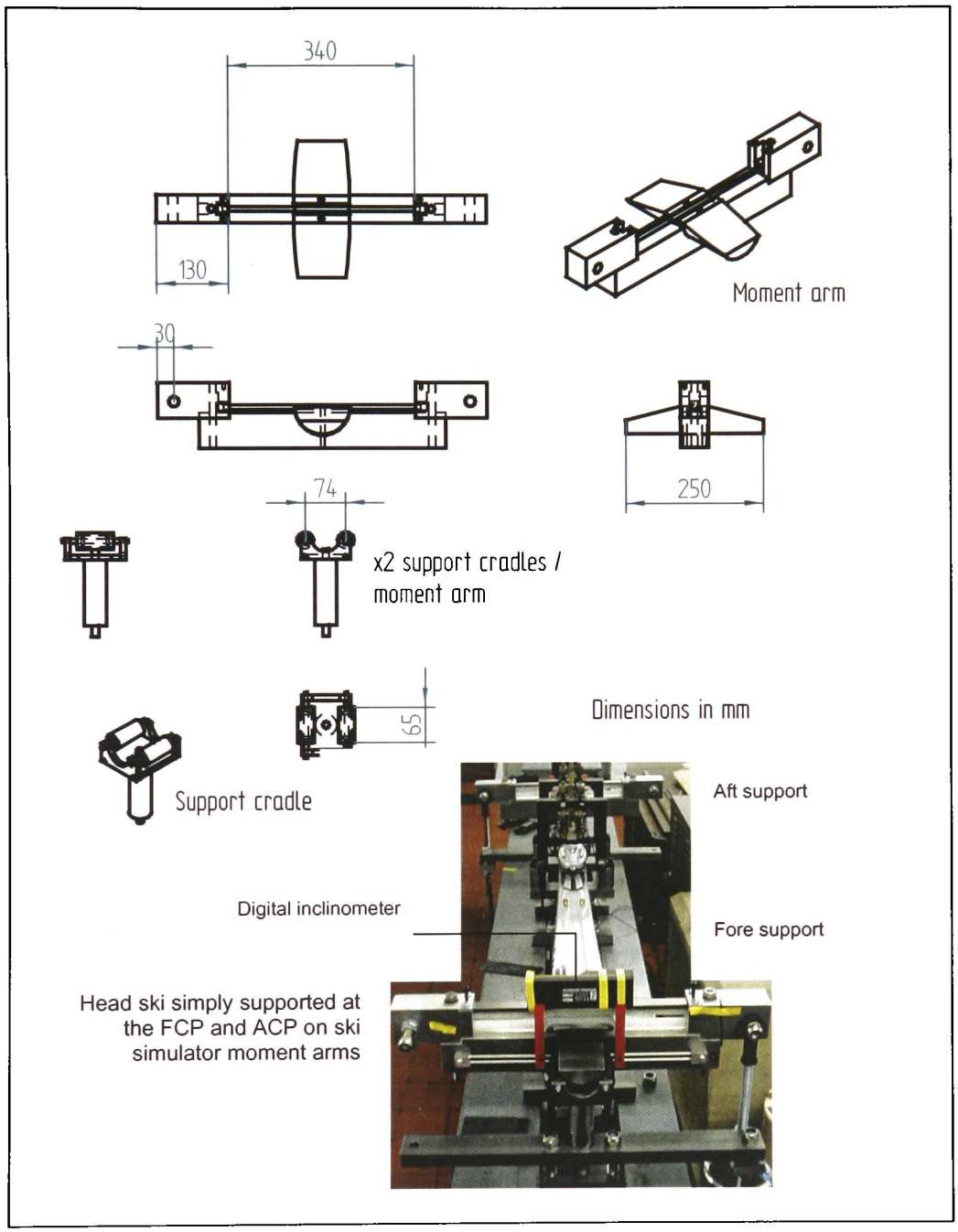

Figure 3-4: Ski simulator moment arm and roller bearing cradle

The split shaft (see Figure 3-5 a) enables the moment arm to rotate on the roller bearing cradle, about the central axis of the shaft. This coincides approximately with the neutral axis of the ski, when the moment arm supports (on the ski support shaft - see Figure 3-5 a) the FCP or ACP of the ski. Therefore, with one of the moment arms positioned to clamp the ski at the MRS, the fore-body (or aft-body) can be twisted (i.e., to determine torsional stiffness, as outlined in §3.1.3) by putting the

second moment arm at an angle (about the split shaft). The angle of the second moment arm is measured with a digital inclinometer.

The position of the split shaft on the roller bearing has to be balanced so that during rotation (over an acceptable range of angular displacement), the centre of gravity of the moment arm acts between the rollers (see Figure 3-5). If the centre of gravity were to act on the rollers, an unequal reaction force would result and, rather than rotate, the moment arm would translate off the corresponding roller. Therefore, the distance between the rollers in the cradle is considered - to provide stability of the moment arm, while enabling an acceptable range of angular displacement.

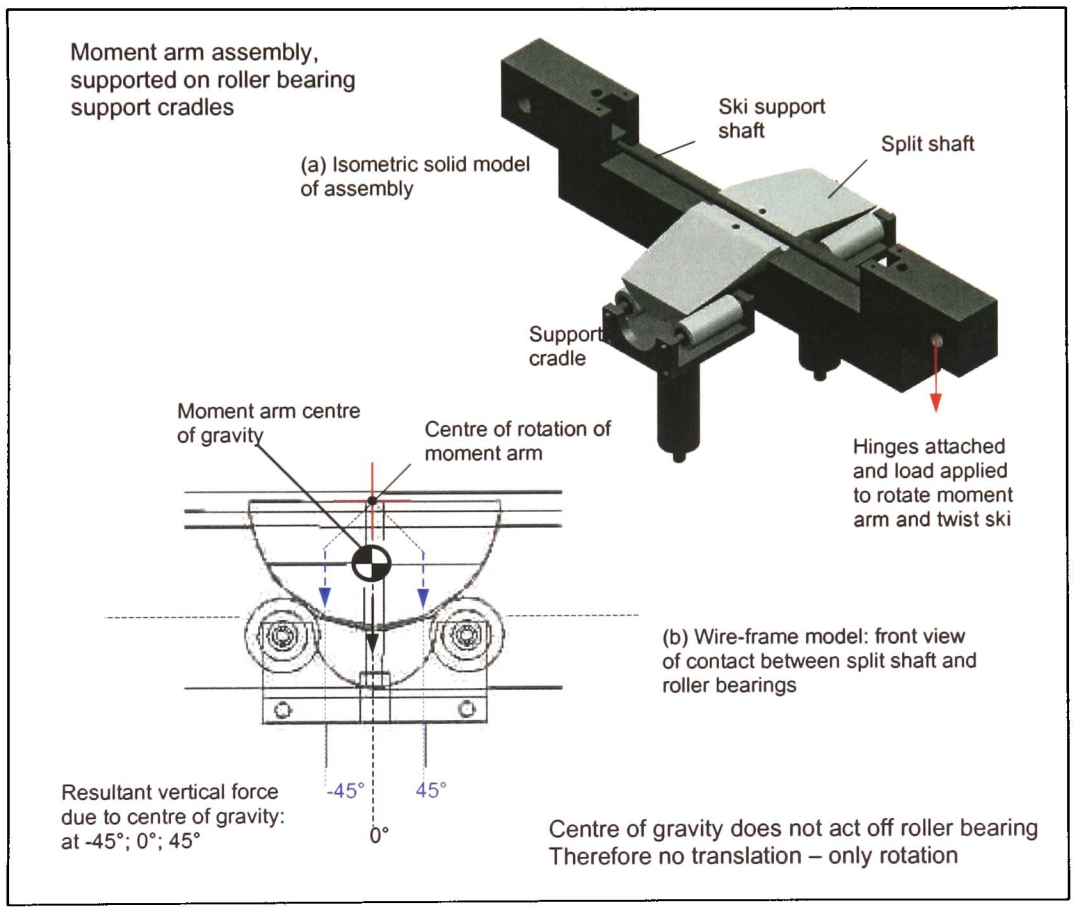

Figure 3-5: Balancing the moment arm

The moment arms are positioned on the lathe bed to produce torsional variation in the fore-body and aft-body. A DERRITRON VP30 electromagnetic vibrator (without link arm suspension) is secured to the floor underneath the lathe bed, with a DERRITRON TA300 solid state power amplifier, to vibrate the ski for dynamic analysis. The variable dynamic input and support conditions can be used to subject the ski to a variety of forces that can be used to simulate those experienced during a turn.

3.2.1 Static tests

Eight alpine skis are tested against each other to investigate ski stiffness, with an aluminium beam acting as a control structure. The cohort comprises skis from six manufacturers (i.e., Atomic, Fischer, Head, Rossignol, Salomon and Völkl), and includes two different models from two manufacturers (i.e., the "Crossmax 8" and "Crossmax 10" from Salomon, and the "Beta-ride 10-20" and "Beta-ride 11-20" from Atomic). The skis are from either the 2001/2002 or 2002/2003 season and are all approximately 1700mm in length (tip to tail).

Data from tests on the (EN 755-2) aluminium beam (1700mm long x 75mm wide x 7mm thick), used as a control structure, are used to derive experimental results that can be compared with theoretically derived values, to give an indication of accuracy.

Room temperature in the laboratory where the tests are conducted varies between 20°C and 24°C, with the ASTM guidelines stating a temperature range of 23°C (±5°C) for tests.

3.2.1.1 Full-body deflection

The overall ski stiffness is determined by simply supporting the ski and measuring vertical deflection of the full-body under loading (i.e., similar to the procedure outlined in §3.1.1). To reduce the contact area at the support, the ski is simply supported by the moment arms on low friction (nylon) rollers (Ø15mm) – located 1445mm apart on the lathe bed. Each ski is loaded in the middle of the binding to simulate the force on the ski during operation.

This procedure diverges from ASTM guidelines, which states that the load should be applied mid-way between the supports. Also, the position of the aft-body support (1445mm from the fore-body support, in-line with the FCP) is, on some skis, only approximately in-line with the ACP (the stated support point in ASTM guidelines). The support condition adopted here provides a more consistent comparison of the skis under investigation, with a variable load condition to accommodate the various settings - with respect to binding location.

The following formula (derived with reference to ROARK: Young (ed.) [1989]) is used to calculate the stiffness (EI):

$$EI = \frac{F \cdot a}{3xl}\left(\frac{l^2 - a^2}{3}\right)^{\frac{3}{2}} \qquad [3\text{-}10]$$

where, F is the applied force; a is the point of application of the force from the FCP (i.e., between 765mm and 800mm, depending on the location of the bindings on the ski); x is the measured deflection average and l is the length of the ski (i.e., 1445mm).

The skis are loaded (i.e., with masses of 1kg, 6kg, 8kg, 10kg and 11kg) in 10-second intervals, with deflection of the top surface of the ski being measured by a Linear Variable Displacement Transformer (LVDT). The LVDT (DCT 3000A, from RDP Group) produces an analogue output that is logged to a computer via a Pico ADC-212 (analogue-digital converter), with a sampling period of 25ms. The mid-point deflection average is calculated and the average stiffness is calculated (with 5s of data, 5s after loading) from the different load conditions. Averages of full-body bending stiffness (calculated using equation [3-10]) are plotted (see Figure 3-6) for a cohort of shaped (carving) skis tested: (1) without bindings; (2) with bindings mounted; (3) with bindings mounted and a boot fitted.

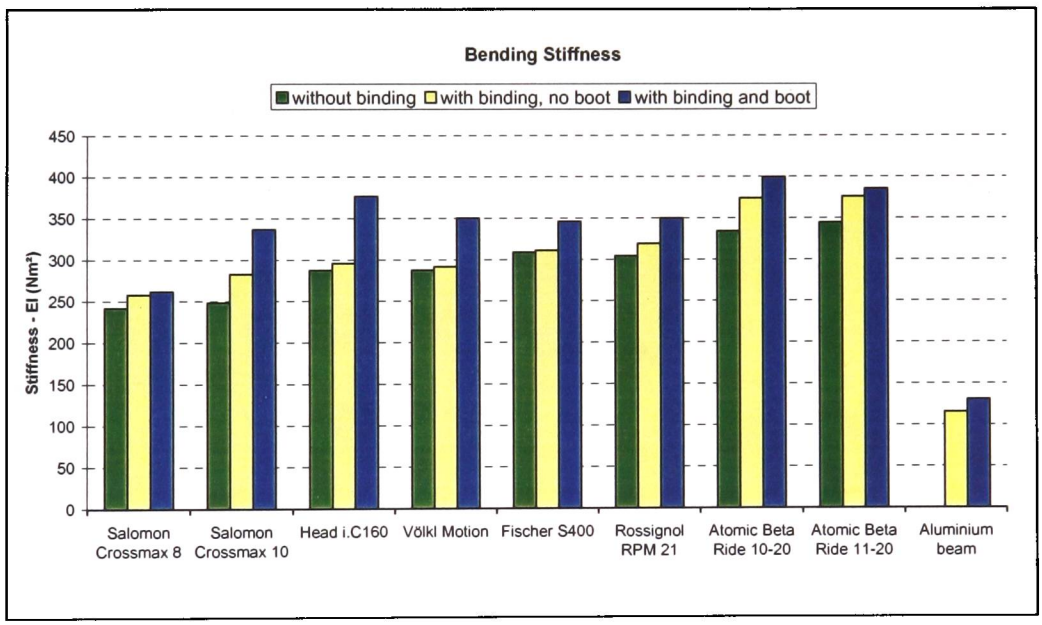

Figure 3-6: Bending stiffness comparison of eight shaped (carving) skis (circa 2001-2003) against an aluminium beam (acting as control)

The stiffness of the aluminium beam is not considered to be altered by the binding, since the toe-piece and heel-piece are separately mounted and are not connected. Therefore, since the measured stiffness is approximately $115 Nm^{-2}$ and the theoretical stiffness is approximately $152 Nm^{-2}$ (given the beam dimensions and a modulus of elasticity of $7.1 \times 10^{9} Nm^{-2}$, for aluminium EN 755-2), this corresponds to an accuracy of approximately 75.7%. This is not insignificant and may be attributed to systematic errors that either affect the boundary conditions, the measurements, or both.

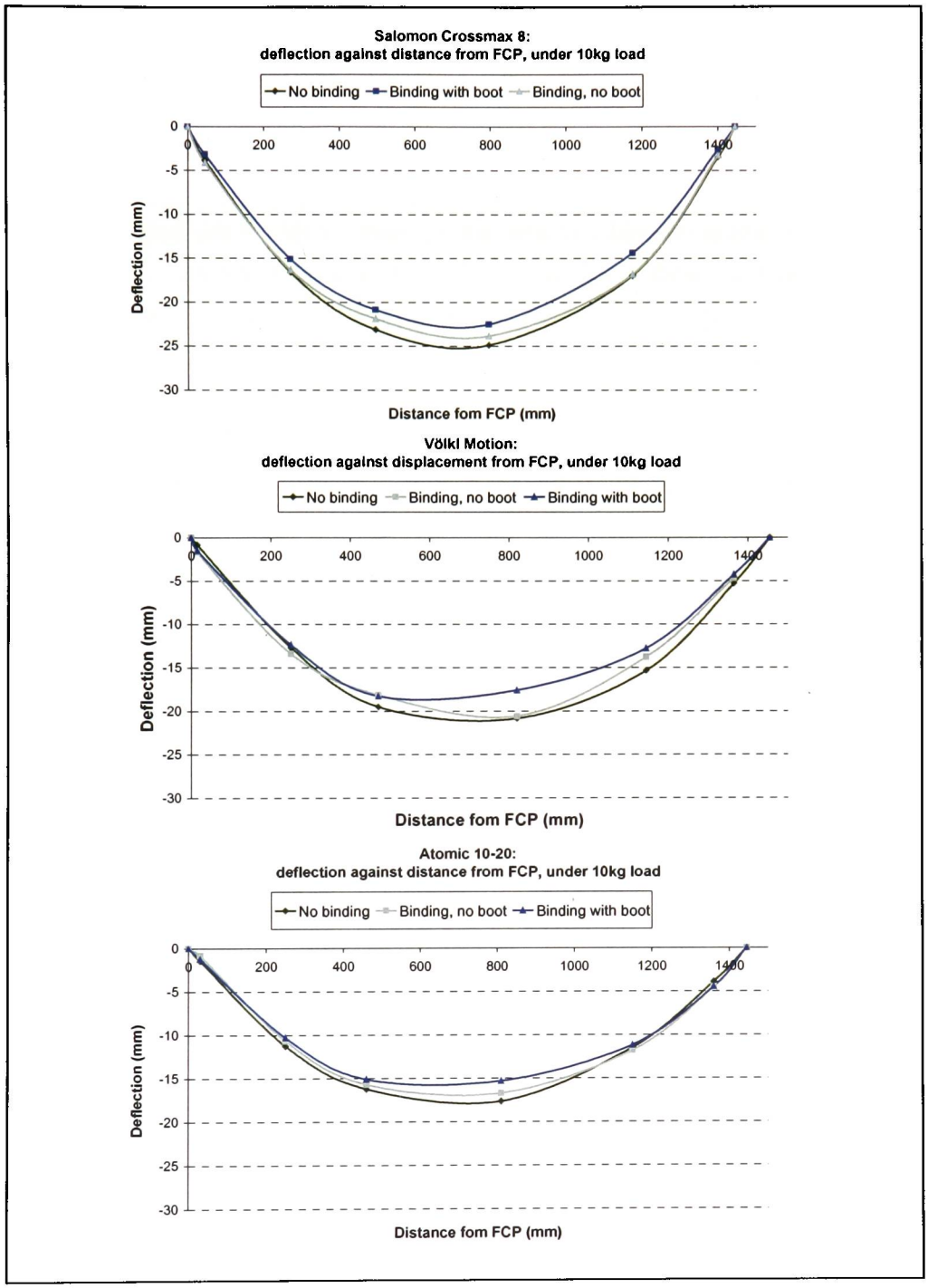

Figure 3-7: Ski deflection shape from three shaped (carving) skis, with and without binding (and boot): comparing the Salomon "Pilot", Völkl "Motion" and a more conventional binding mount from Atomic

The vertical (x) deflection under loading is measured, at six locations along the length of the ski (i.e., three measurements on the fore-body, one at the load point and two on the aft-body). Deflection averages are determined for the load at each measurement location and are plotted against distance

from the FCP. The deflection shapes of three skis with different binding mounting configurations are compared (see Figure 3-7) with and without binding (and boot). The Salomon "Pilot" and Völkl "Motion" binding systems (see Figure 3-8) claim to reduce flattening, so that the ski flexes under the MRS (i.e., so that the flex of the MRS is not restricted when the skier stands in the binding). In the "Pilot" system, the binding toe-piece and heel-piece are mounted on separate axles. In the "Motion" system the binding is hinged between the toe-piece and heel-piece and the assembly is slid onto segmented rails fixed into the MRS. Both systems claim to enable the binding to float over the deflecting ski. However, the results presented here show that there is flattening (more evident on the Völkl ski than on the Salomon ski), comparable with a relatively conventional shim mounted binding (from Atomic).

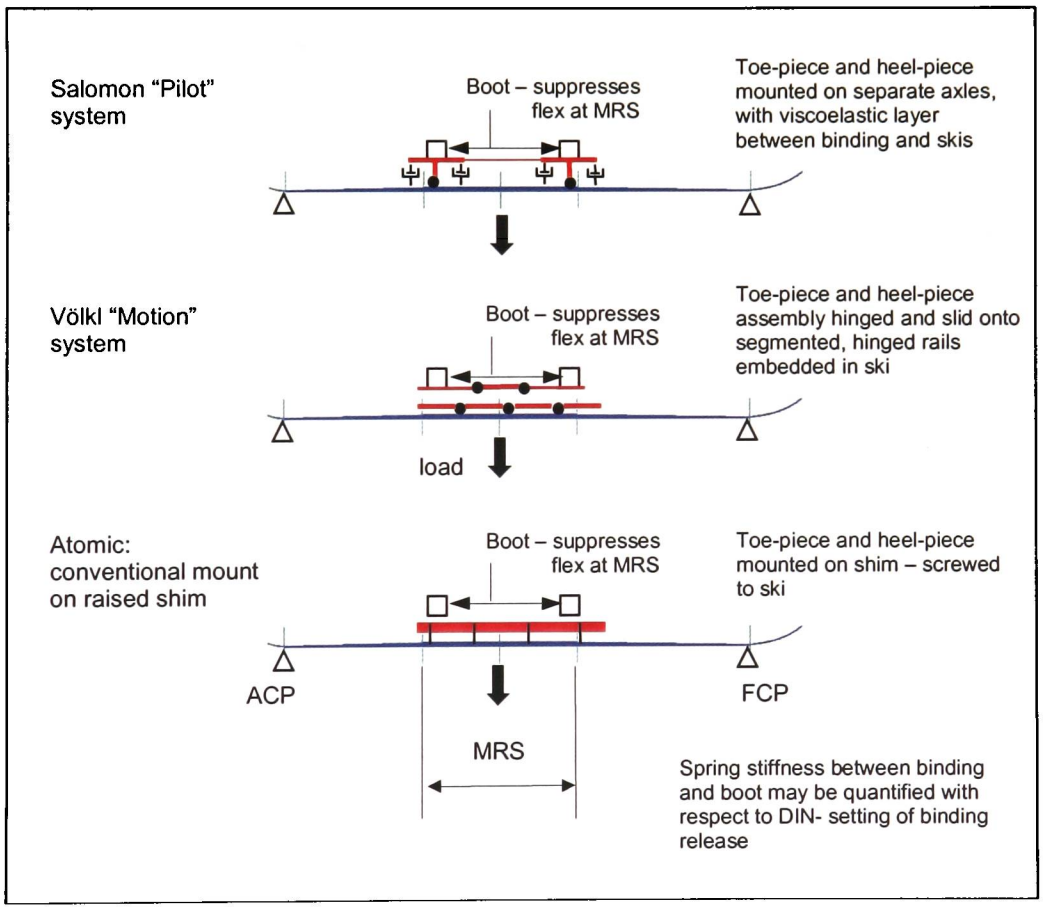

Figure 3-8: Schematic comparison of the Salomon "Pilot" and Völkl "Motion" binding systems, relative to a conventional shim mounted binding from Atomic.

The sprung release (DIN) setting of the bindings has not been recorded and may contribute to a change in deflection under the MRS. Also, the sole size of the boot (EU 38/39) is smaller than that expected for use with the (170cm) skis tested. Increasing the boot size (> EU42) is likely to further increase the MRS stiffness - reducing deflection so that there is more pronounced flattening.

The results presented here from the full-body deflection tests do provide information on the flex pattern of shaped skis, that is not readily available. Looking at the deflection shape under loading does illustrate (see Figure 3-7) the influence of the binding and boot on the dynamic behaviour of the ski. The results show that irrespective of the binding mounting configurations (tested), the MRS is stiffened and the deflection shape flattens. However, the boundary conditions make the results of limited use for dynamic analysis. Tests on the fore-body and aft-body are more relevant (see §3.2.1.2 and §3.2.1.3).

3.2.1.2 Fore and aft-body deflection

The fore-body and aft-body stiffness is determined by clamping the MRS and measuring the respective vertical deflection of the cantilever supported fore-body and aft-body, under loading (i.e., similar to the procedure outlined in §3.1.2). The moment arms are located on the lathe bed to clamp the ski 530mm from the FCP and 320mm from the ACP, so that the fore-body and aft-body may be loaded in turn and the respective deflections measured.

The skis are loaded (i.e., with masses of 1kg, 1.5kg, 2kg, and 3kg hung from zip ties) in intervals of 10s (to allow the ski to stabilise between loads). Deflection of the top surface of the ski is measured by a LVDT, with a sampling rate of 40 Samples/s (i.e., one sample every 25ms). The end-point deflection average (from the sampled measurements) is calculated and the average stiffness is calculated from the different load conditions.

The fore-body and aft-body stiffness is calculated using equations [3–3] and [3–4], respectively (see §3.1.2). The fore-body and aft-body stiffness is plotted (see Figure 3-9) and error bars show the variation between the maximum and minimum measurement with respect to the average.

Since the average measured stiffness of the aluminium (control) beam is approximately $108Nm^{-2}$ and the theoretical stiffness is approximately $152Nm^{-2}$ (given the beam dimensions and a modulus of elasticity of 71GPa), this corresponds to an accuracy of approximately 71.0%. This is not insignificant and may be attributed to systematic errors that either affect the boundary conditions, the measurements, or both.

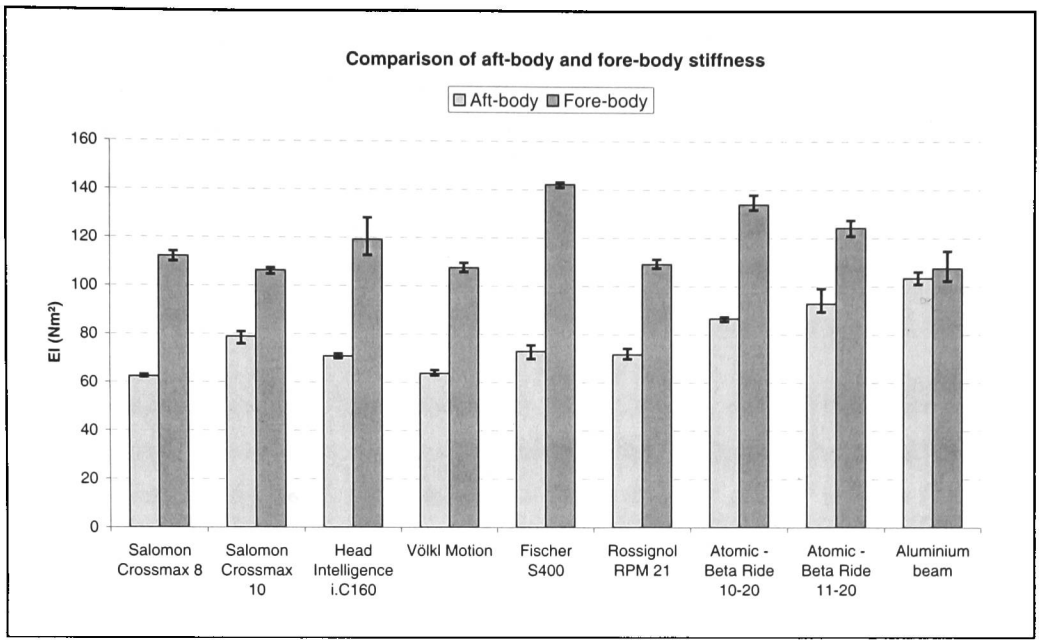

Figure 3-9: Comparison of fore-body and aft-body stiffness from eight shaped (carving) skis (circa 2001-2003) against an aluminium beam (acting as control)

The fore-body is consistently stiffer than the aft-body, with the exception of the aluminium beam – as expected. The Fischer "S400" has the stiffest fore-body, however, it is also the widest with a thickness similar to the other skis. Since stiffness is proportional to width, the relatively high fore-body stiffness of the Fischer "S400" may be attributed to geometry.

In terms of geometry and construction the skis from the same manufacturer provide the most similar comparison. The fore-body and aft-body stiffness of the Atomic skis are most alike and while the fore-body stiffness of the Salomon skis are approximately the same, the aft-body stiffness of the "Crossmax 10" is greater than that of the "Crossmax 8". This difference in aft-body stiffness on the Salomon skis may be attributed to the "Pro-link" damper that is attached to the aft-body of the "Crossmax 10", but is not on the "Crossmax 8". The additional Pro-link damper on the "Crossmax 10" may also account for the difference in bending stiffness (see Figure 3-6).

The fore-body stiffness of the Salomon "Crossmax 8" and Völkl "Motion" are comparable, although non-specialist qualitative feedback seems to indicate a preferable dynamic response from the Völkl ski. Given the similarities in fore-body and aft-body stiffness, the apparent performance difference may be due to geometry, damping (investigated subsequently - see §3.2.2), or torsional stiffness.

3.2.1.3 Fore and aft-body torsion

The torsional stiffness is determined by measuring the angle of twist that is induced by a torque, produced using the moment arms to twist the fore-body and aft-body, respectively. Locating one moment arm on the lathe bed to clamp the FCP, the other moment arm is positioned to clamp the ski 510mm from the FCP – in front of the binding toe-piece. The moment arm at the FCP is used to transmit a torque into the fore-body, with the second moment arm fixed in a horizontal position. The ski is clamped between two low friction (nylon) rollers (Ø15mm), with the upper roller reinforced by a steel bar (cross-section: 8mm x 20mm), fixed to the moment arm.

The moment arm is loaded (i.e., with masses of 1kg, 1.5kg, 2kg, 3kg and 5kg) to produce a torque on the ski, with angle of twist being measured 5s after the torque is applied. The digital inclinometer (FISCO Solatronic, model EN17) has an accuracy of 0.1° at 0° or 90° and 0.2° between 1° and 89°.

The arrangement is similar for determining the aft-body torsional stiffness, with one moment arm located on the lathe bed to clamp the ACP and the other positioned 380mm from the ACP – behind the binding heel-piece. The moment arm at the ACP is used to transmit a torque into the aft-body, with the second moment arm fixed in a horizontal position.

The fore-body and aft-body torsional stiffness is calculated using equation [3–5] (see §3.1.3) and plotted (see Figure 3-10). The average torsional stiffness is calculated from results from the different load conditions. Error bars show the variation between the maximum and minimum measurement with respect to the average.

The torsional stiffness determined from fore-body tests of the aluminium (control) beam is approximately $144Nm^{-2}$ and the theoretical torsional stiffness is approximately $222Nm^{-2}$ (given the beam dimensions and a modulus of rigidity of 25.9GPa), this corresponds to an accuracy of approximately 64.7%.

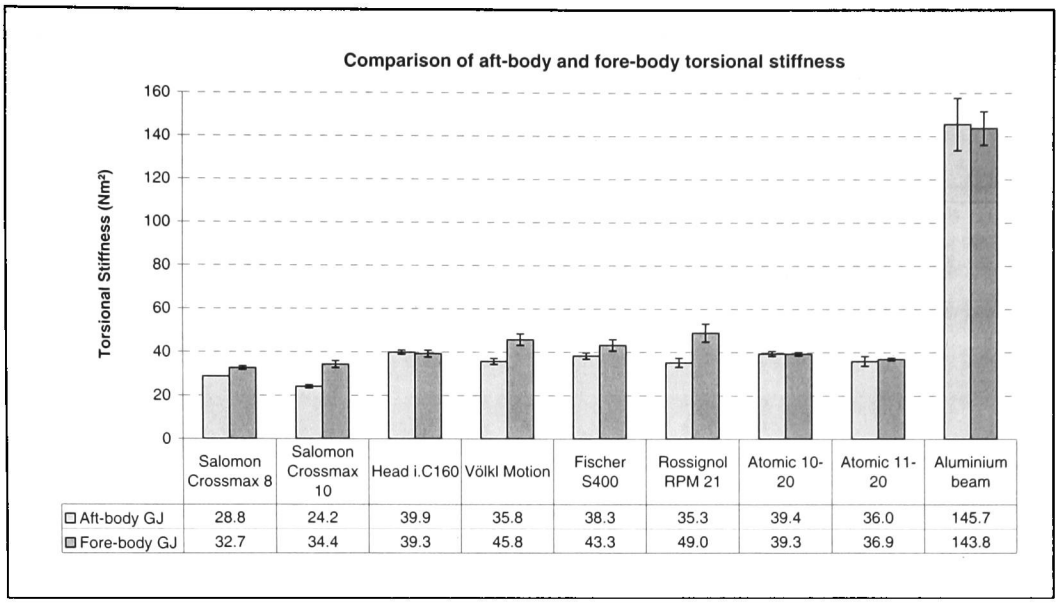

	Salomon Crossmax 8	Salomon Crossmax 10	Head i.C160	Völkl Motion	Fischer S400	Rossignol RPM 21	Atomic 10-20	Atomic 11-20	Aluminium beam
Aft-body GJ	28.8	24.2	39.9	35.8	38.3	35.3	39.4	36.0	145.7
Fore-body GJ	32.7	34.4	39.3	45.8	43.3	49.0	39.3	36.9	143.8

Figure 3-10: Comparison of fore-body and aft-body torsional stiffness from eight shaped (carving) skis (circa 2001-2003) against an aluminium beam (acting as control)

The fore-body torsional stiffness is greater than the aft-body torsional stiffness for most of the skis in the cohort, with the exception of the Atomic skis and the Head ski. Interestingly, the Salomon skis have the lowest fore-body torsional stiffness in the cohort. The Völkl skis have a greater torsional stiffness and this may contribute to the perception reported from non-specialist qualitative feedback that there is a performance advantage over the Salomon skis. The lower torsional stiffness in the Salomon skis may give a perception of reduced performance - more noticeable to heavier or aggressive skiers.

3.2.2 Dynamic tests

Fore-body edge chatter is investigated for low frequencies (i.e., <50Hz) that may contribute to a reduction in edge control and that may be feasibly controlled by the adaptive system. Higher frequencies of vibration have smaller amplitudes and may actually contribute to edge control, by preventing the edge from 'sticking.' Tests are carried out on two carving skis (i.e., Salomon "Crossmax 8" and Völkl "P50 Motion"), a non-shaped (Dynastar) ski and an aluminium beam (acting as a control structure).

Initial dynamic analysis seeks to identify fore-body frequency response (<50Hz) to a sinusoidal forced vibration (at 14Hz, 16Hz, 18Hz, 20Hz and 30Hz), generated by a shaker at the mid-point (800mm from the supported FCP). Single input, single output (i.e., SISO) accelerometer

measurements are collated for five output locations (approximately 100mm apart) down the length of the fore-body. Impulse tests are also carried out to identify fore-body resonant frequencies. The techniques for analysing the time domain data from SISO measurements are subsequently presented (see §3.3 and appendix A–4) along with results of note.

Locating the moment arms on the lathe bed to support test skis near their respective FCP and ACP, each ski is subjected to a controlled vibration (i.e., in terms of frequency and amplitude). A stinger (i.e., a steel wire) connects a floor-mounted shaker to the ski near the binding heel-piece (at a point convenient for clamping) under the MRS (see Figure 3-11). The stinger ensures that the shaker induced force is only along the axis of the stinger (i.e., the vertical x-axis) and it also protects the shaker from lateral reaction forces (i.e., in the y-axis and z-axis).

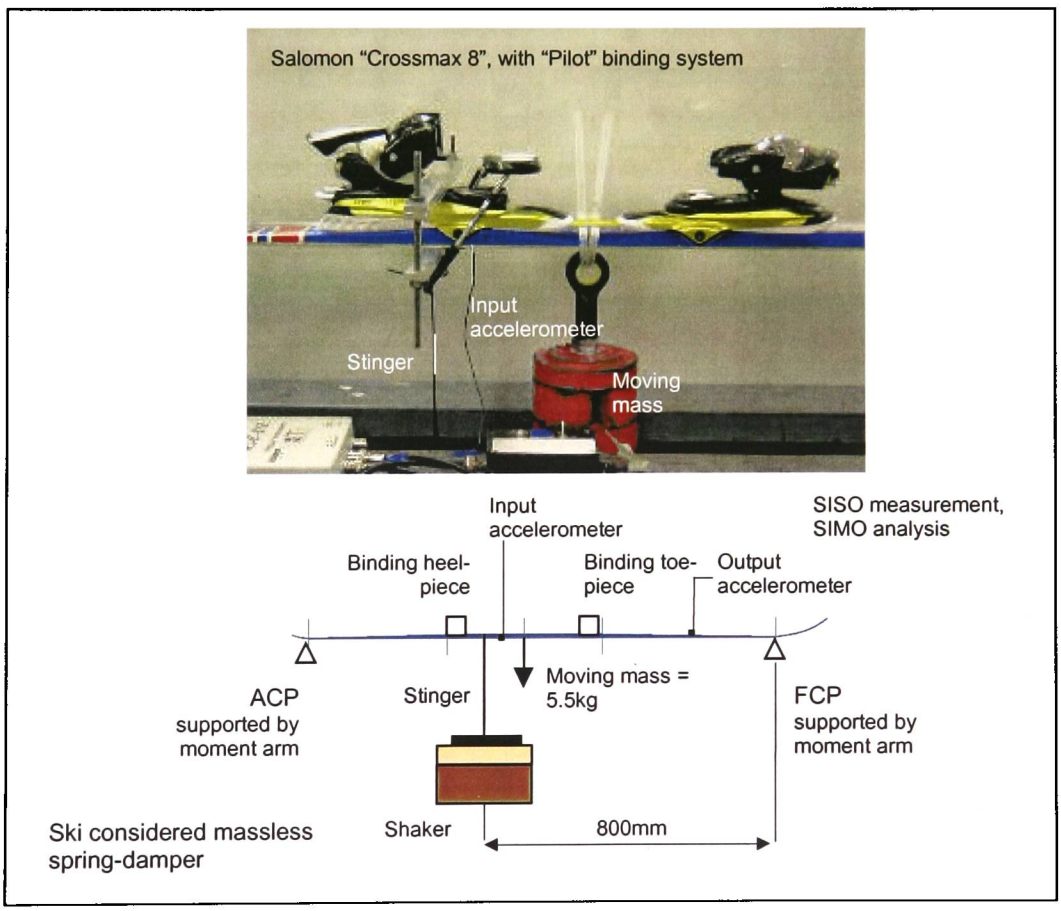

Figure 3-11: Experimental investigation of fore-body dynamic response with the ski simply supported at the FCP and ACP and a controlled vibration at the MRS.

Any camber is removed by loading the ski mid-way between the fore-body and aft-body moment arm supports (i.e., the 5.5kg mass removes camber). The length of the stinger is adjusted depending on the amount of deflection in the ski under loading. The ski is assumed to be a massless spring (and

damper), with the load (5.5kg including the clamp to attach the stinger) being considered the moving mass.

Fore-body edge vibration is investigated by carrying out a single input, single output analysis. The shaker provides a single sinusoidal input vibration, measured by an accelerometer that is attached with thin double-sided tape to the underside of the ski close to the stinger. The force input is calculated as the product of the moving mass and the input accelerometer measurement (i.e., the ski is assumed to be a mass-less, spring-damper system). A second accelerometer is attached at locations between the FCP and binding toe-piece, along the edge of the ski, to measure fore-body vibration output. Single input, multiple output vibration analysis, with multiple accelerometers located on the fore-body edge, would require additional amplifiers for each of the accelerometers and a data logger capable of logging multiple channels at an acceptable rate - determined by calculating the Nyquist sampling rate (see §3.3.2). The sampling rate is normally calculated at 2.5 x the Nyquist frequency, since filter cut-off is not instant (i.e., due to roll-off at the cut-off frequency).

The output accelerometer is located at one of the five points on the fore-body and up to 30 seconds of data is logged (to a PC via a Pico ADC 212/100) for a sinusoidal input force at 14Hz, 16Hz, 18Hz, 20Hz and 30Hz. The amplitude is zeroed before the frequency is increased, to enable the output response to be clearly attributed to the correct input. The output accelerometer is then relocated to the next point and the procedure repeated for the same swept frequencies.

The pre-processed logged data is edited to provide 20 seconds of time domain data for each point and at each frequency. This provides good resolution in the frequency domain and allows data at the beginning and end of each frequency sweep to be excluded. Excluding data at the beginning of a sweep is particularly advantageous, since the system may not have settled. However, this pre-processing step is costly in terms of time.

The data is imported into MATLAB and the accelerometers are calibrated (i.e., 7.5mV/g for the output acceleration and 8.8mV/g, multiplied by the mass for the input force). The input force and output acceleration is then transformed from time domain data into the frequency domain (using FFTs as outlined in §3.3.2).

A mains powered Pico ADC-212/100 (see §3.3.1) dual channel analogue to digital converter (ADC) is used to log data from the input accelerometer and the roving output accelerometer. Single axis piezoelectric polymer film accelerometers (ACH-01-03) are used, with battery powered ACH-01 amplifiers (having fixed x10 gain) – all supplied by Measurement Specialities Inc. (MSI). At room temperature (20-25°C), the sensitivity of the accelerometer is 9mV/g (±2mV/g) and the frequency range is between 2Hz and 20kHz, with resonant frequency at 35kHz.

Piziali & Mote, [1972] presented single input - (moving) single output accelerometer measurements from laboratory tests representative of "straight running" (i.e., where there the ski is flat and there is no angulation), but did not present laboratory tests representative of a turn.

A turn can be simulated with the moment arm near the FCP being used to twist the fore-body until only the edge of the ski at the FCP is in contact with the support shaft (see Figure 3-12). The angle of twist in the ski is measured with a digital inclinometer (FISCO Solatronic, model EN17) and the ski support shaft on the moment arm is instrumented with strain gauges to measure horizontal and vertical forces exerted by the ski at the fore-body support. Results from the instrumented support are not included in this work.

(a) FCP twisted to simulate fore-body-initiated turn

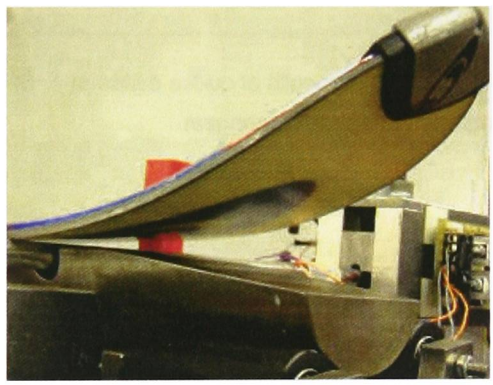

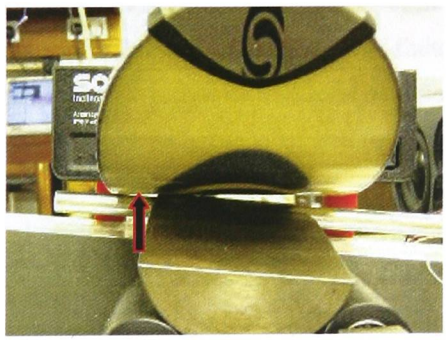

(b) Reaction force of support shaft twists the forebody, with contact area reduced to the edge

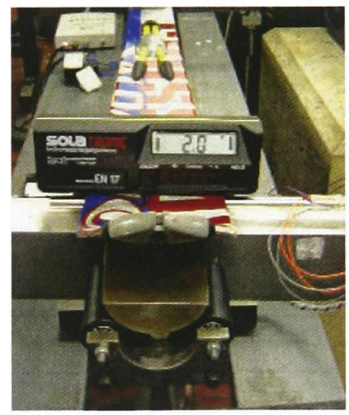

(c) Angle of twist measured with digital inclinometer (at FCP and at five positions down the fore-body in increments of 100mm

Figure 3-12: Investigating dynamic response with the fore-body twisted to simulate turn conditions (using the moment arm support to twist the fore-body at the FCP)

Tests are carried out with the ski simply supported, to enable the fore-body dynamic response to be investigated when twisted (i.e., a situation characteristic of a turn). Clamping the ski at the MRS and attaching the stinger to the FCP (i.e., testing the fore-body as a cantilever – see Figure 3-13) may be a more representative simulation, but it would not be possible to investigate the dynamic response with the FCP edged.

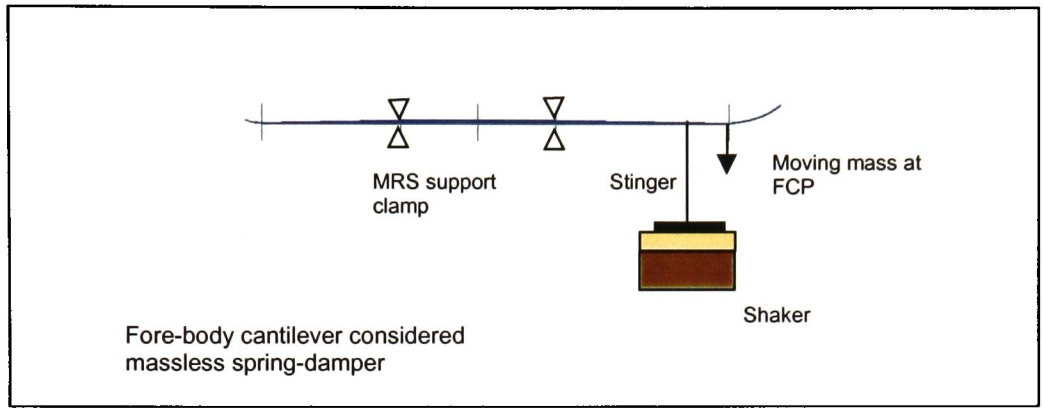

Figure 3-13: Alternative set-up to allow analysis of fore-body cantilever (would not enable dynamic response of fore-body twist to be investigated).

3.3 Modal analysis

Modal analysis [Ewins, 1984] provides test results for:

1. Structural analysis
2. Investigating vibration-related problems – such as noise and fatigue
3. Validation, or refinement of models – e.g., finite element (FE) models
4. Predicting dynamic effects of structural modification
5. Predicting dynamic response to applied loads

Experimental modal analysis provides measurements of the frequency response function of structures under test, with modal parameter (i.e., resonant frequency and damping) estimation and modal visualisation (i.e., mode shapes) and validation (e.g., of FE models). However, it is not easy to use modal analysis to study changes (better investigated by computational modelling) as this requires structural modifications to be made.

Successful modal analysis requires:

1. Clear understanding of the system under investigation
2. Accurate measurements
3. Detailed data analysis

The ski system has been introduced (see §2) and distributed and discrete models presented (see §2.4) focusing on analysis of the fore-body with a view to investigating edge chatter. Testing requires an excitation source (e.g., an impact hammer, or shaker system), transducers (i.e., force transducers, or accelerometers), data acquisition hardware and software for logging and processing results. The aim is to identify modal parameters (i.e., resonant frequencies, damping and mode shapes) and this can be achieved by experimental modal analysis, or by computational (e.g., finite element) modelling.

This work identifies frequencies from single input, single output (SISO) measurements in the laboratory and attempts to quantify damping. The fore-body is analysed as a multi-degree of freedom system by compiling frequency response functions obtained by moving the output accelerometer down the fore-body. Multiple input multiple output (MIMO) measurements from field-testing of skis (see §3.4.2) are used to provide signal analysis of the response to operational forces. This work does not go as far as solving the lumped-parameter model (represented as a series of masses connected by springs and dampers) in the modal-space. In the modal-space the equations of motions in the lumped-parameter model are decoupled and the system is represented as a collection of single degree of freedom models – one for each mode in the multi-degree of freedom system.

3.3.1 Data logging

The Nyquist sampling theorem states that for a particular bandwidth signal with maximum frequency ($f_{\max}$), the equally spaced sampling frequency must be greater than twice the maximum frequency.

i.e., $$f_s > 2 \cdot f_{\max} \qquad [3\text{-}11]$$

where, f_s is the Nyquist sampling rate and $f_{\max}$ is the Nyquist frequency.

The sampling theorem was first recognised by Nyquist [1928] and mathematically proven by Shannon [1949]. Nyquist established that for periodic functions, no information would be lost if the sample rate is at least twice as fast as the signal of interest. A Fourier series (see equation [3–12]) can be used to take any alternating signal and decompose it into a sum of sines and cosines of different frequencies (see Appendix A-3). Therefore, the Nyquist sampling theorem can be used to sample periodic functions without loss of information (up to a specified maximum frequency).

Fourier series: $$P(t) = a_0 + \sum_{n=1}^{\infty} [a_n \sin(2\pi f t) + b_n \cos(2\pi f t)] \qquad [3\text{-}12]$$

where, $P(t)$ is the signal in the time domain, and a_n and b_n are the unknown coefficients of the series. The integer, f , corresponds to the frequency (Hz).

Vibrating mechanical systems have frequencies below 100kHz; therefore, a sampling rate of 200kHz should be satisfactory for most mechanical engineering applications. However, a higher sampling rate produces an increased amount of data that needs to be stored and processed.

Two models of analogue to digital converter are used during the course of this work: the Pico Technology ADC-212/100 and the ADC-11/10. These devices provide a low cost PC based data acquisition capability. Both devices plug into the parallel port of a PC and are used with PicoLog data acquisition software.

The Pico ADC-212/100 is a dual channel analogue to digital converter with 12-bit resolution and is claimed to be capable of taking 50 million samples per second (50MS/s). However, the data sampling rate is limited by the size of the buffer (128kB). Given that there are 8-bits in one Byte, each 12-bit sample equates to 1.5 Bytes. Therefore, the buffer is able to hold a maximum of 85kS, while the transfer speed in the parallel port (i.e., 1MB/s approx.) allows approximately 700kS/s. Consequently, the buffer limits the sample rate of the ADC-212/100 to 85kHz for single channel logging and 42.50kHz for dual channel logging. This equates (using equation [3–11]) to respective Nyquist frequencies of 42.50kHz and 21.25kHz for single and dual channel data logging. The ADC-212 is used to support dynamic tests on the ski simulator and to collect data for demonstration of the feasibility of the adaptive ski concept.

The Pico ADC-11/10 is a compact ADC that interfaces via a D-type connector (female) between the input channels and output to a PC, via the parallel port (i.e., a D-type male connector). It is capable of multiplexing up to 11 channels with 10-bit resolution and has a claimed sampling rate of 10kHz (i.e., 10kS/s). The transfer speed in the parallel port is capable of a sampling rate of 800kHz for a 10-bit sample and therefore does not limit the performance of the ADC-11/10. The 10kHz sampling rate of the ADC-11/10 is divided by the number of channels being used – i.e., if 10 channels are logging data, the sample rate is 1kHz per channel. A sampling rate of 1kHz equates (using equation [3–10]) to a Nyquist frequency of 500Hz (i.e., one sample every 1ms). The input range for the ADC-11 is from 0V to 2.5V and therefore requires a power supply to offset the zero so that negative readings may be recorded. The ADC-11 is used in field tests without a power supply, to log data from skis instrumented with an array of PVDF sensors.

Data acquisition packages (other than those from Pico) such as those from National Instruments, combined with commercial dynamic data analysis packages, would provide a more sophisticated system that could certainly be applied to the laboratory ski simulator.

Theoretically velocity-time data can be obtained by integrating acceleration-time data obtained from accelerometer measurements. However due to accelerometer drift, the practice of obtaining velocity-

time data from accelerometer measurements requires greater consideration. Conventionally, to try and overcome the effect of drift, electronic hardware is used to filter the data. Alternatively, digital filters are now increasingly part of the data acquisition process.

In this work, time domain data is collected unfiltered and post-processed (i.e., logged and then processed). This should allow more flexible use of the data – enabling further analysis in subsequent works. A low pass digital filter with cut-off frequency at 80Hz (i.e., the Nyquist frequency) would be adequate for the frequency bandwidth of interest (i.e., 0-50 Hz). However, it has been decided not to filter the data, to avoid frequency roll-off around the cut-off frequency. Results have been edited to show only the frequency bandwidth less than the Nyquist frequency.

3.3.2 Spectrum analysis

Dynamic analysis begins by taking experimental data in the time domain and manipulating it in the frequency domain (i.e., spectrum analysis). In this work analogue signals are converted to digital sequences of time history, which are stored (on a computer) and processed. The stored time domain data are converted using a Fast Fourier Transform (FFT) into the frequency domain as a complex spectrum. MATLAB (from MathWorks) code for performing a FFT is presented in the appendices (see appendix A-3).

The Frequency Response Function (FRF) represents the complex (i.e., a function defined by a magnitude and phase) ratio between output and input (see Figure 3-14), as a function of frequency. The FRF produces a sinusoidal output motion for a sinusoidal input force (at angular frequency w). The output amplitude and the phase between the output and input are multiples of, respectively, the magnitude and phase of the complex function.

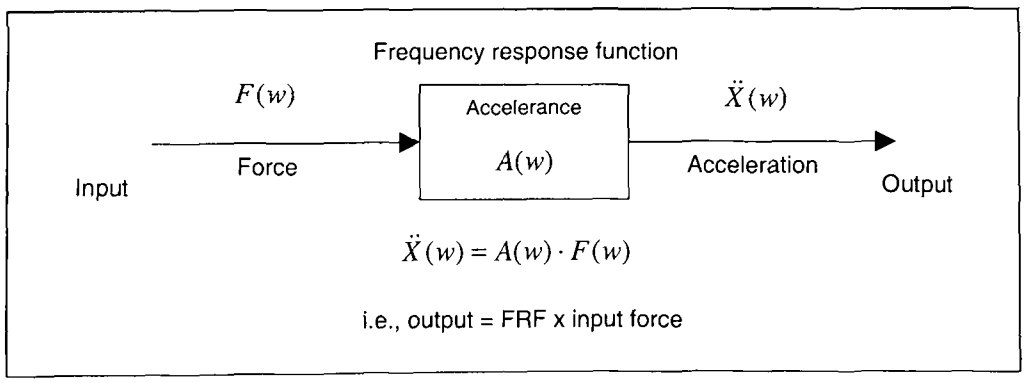

Figure 3-14: Frequency Response Functions (FRFs)

Motion can be described [Døssing, 1, 1988] in terms of acceleration, velocity or displacement – where the corresponding FRF is a measure of accelerance (or inertance), mobility, or compliance (see Figure 3-14). Accelerance is generally obtained directly from measurement, while compliance is commonly used for modelling a system. Accelerance, mobility and compliance are algebraically related:

$$A(w) = \frac{\ddot{X}(w)}{F(w)}\left[\frac{\mathrm{ms}^{-2}}{\mathrm{N}}\right] = \frac{-w^2}{(k - w^2 m) + j(wc)} \qquad [3\text{-}13]$$

$$M(w) = \frac{\dot{X}(w)}{F(w)}\left[\frac{\mathrm{ms}^{-1}}{\mathrm{N}}\right] = \frac{jw}{(k - w^2 m) + j(wc)} \qquad [3\text{-}14]$$

$$H(w) = \frac{X(w)}{F(w)}\left[\frac{\mathrm{m}}{\mathrm{N}}\right] = \frac{1}{(k - w^2 m) + j(wc)} \qquad [3\text{-}15]$$

where, $A(w)$, $M(w)$, $H(w)$ are the respective system descriptors for quantifying accelerance (or inertance), mobility and compliance (or receptance). The inverse of the FRF describes dynamic mass (i.e., accelerance^{-1}), impedance (i.e., mobility^{-1}) and dynamic stiffness (i.e., compliance^{-1}).

Calculation of the FRF enables single input, single output measurements to be compared and, by compiling measurements (of amplitude and phase) from different output sites, an operating deflection shape may be obtained for a multi-degree of freedom system (see §3.3.4). Assuming the same time range is compared (in this case 20s of time domain measurements), the FRF provides a measure of the dynamic output normalised by the force.

Accelerance can be obtained from the FFT of the time-domain measurements at the input and output accelerometers. However, it is advantageous to consider compliance, which (as discussed earlier - see §3.3.1) cannot be determined from the time-domain measurements due to accelerometer drift. The relationship between accelerance and compliance can be seen by comparing equations [3–13] and [3–15], with the practical significance illustrated (see Figure 3-15.) Therefore, instead of calculating compliance from time-domain data, it can be calculated in the frequency domain from accelerance (i.e., the amplitude of the accelerance is scaled by $-w^{-2}$, and there is a phase difference of –180°).

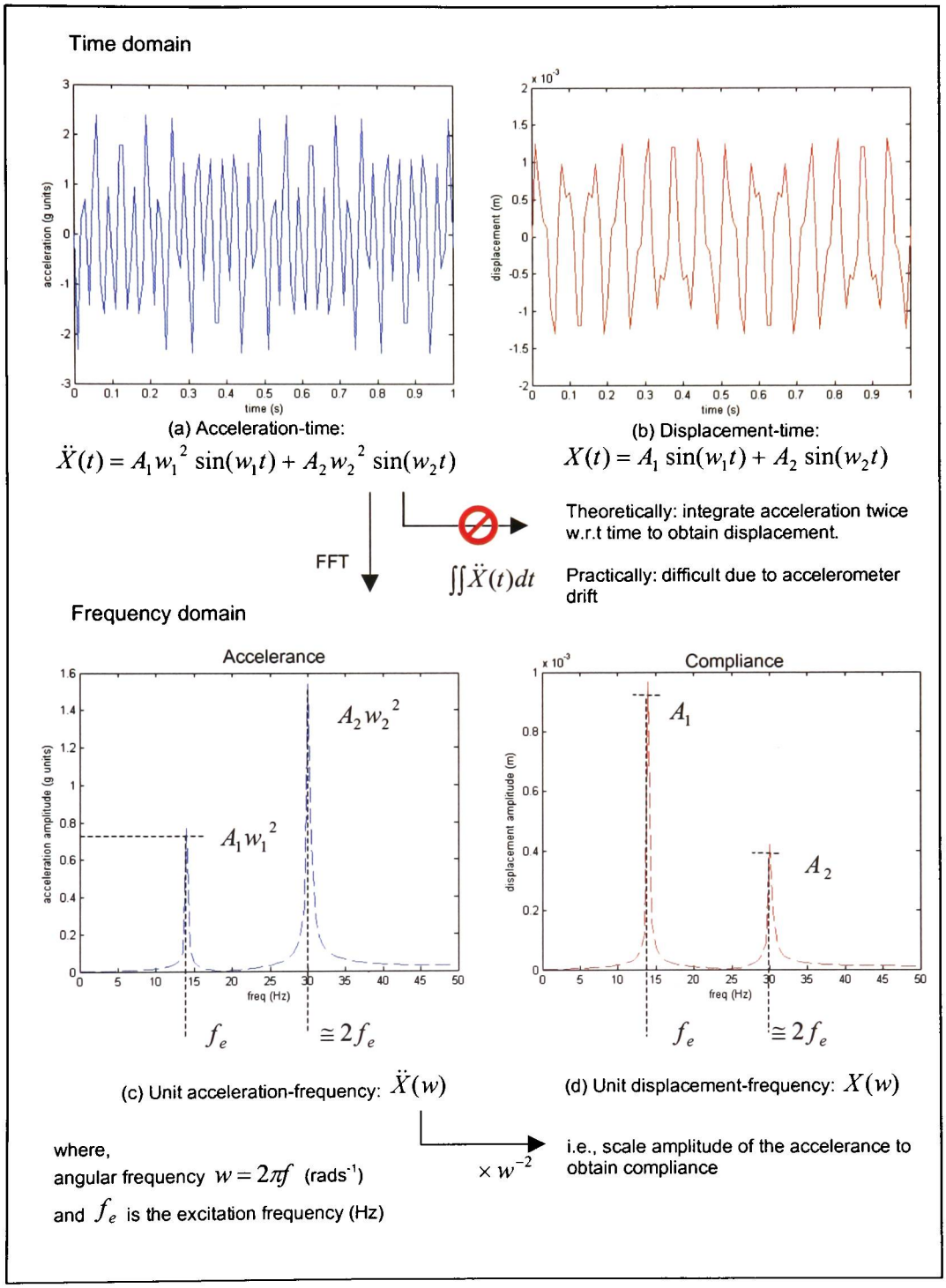

Figure 3-15: Relationship between acceleration in the time-domain and compliance in the frequency domain

Døssing [1, 1988] explains the principles of spectrum analysis:

1. Analogue time domain data (conventionally hardware filtered) are sampled, digitised (digitally filtered) and logged. The sampling rate and record lengths determine the frequency range and resolution of the analysis.
2. Continuous sequences may be multiplied (weighted) by a window function – tapering the data at both the beginning and end of each record. This makes the data more suitable for block analysis and less susceptible to leakage (i.e., where the spectrum is distorted due to lack of periodicity in the transform window).
3. The sequence in the time domain is (Fourier) transformed into the frequency domain as a complex spectrum.
4. Auto-spectrum is calculated by multiplying the spectrum by its complex conjugate
5. Cross-spectrum is obtained by multiplying the complex conjugate of one spectrum by a different spectrum.

The auto-spectra of the input force and the dynamic response, together with the cross-spectrum between the force and response are used to determine FRF estimates (see Figure 3-16).

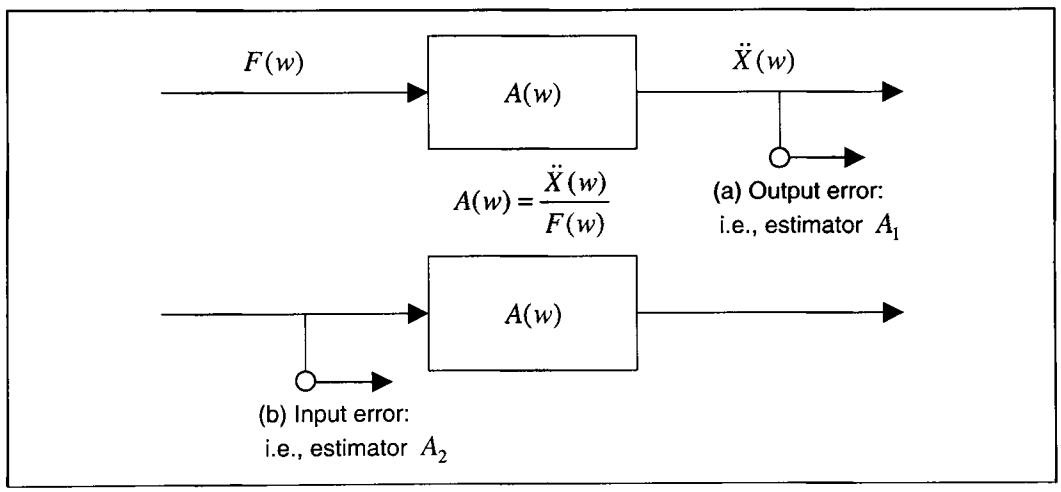

Figure 3-16: FRF estimates (produced with reference to Døssing [1, 1988])

For noise in the output measurement (see Figure 3-16 a), the estimator A_1 (of the accelerance) is equal to the cross-spectrum between the force and the response, divided by the auto-spectrum of the force (see equation [3–16]).

$$A_1(w) = \frac{\sum F^* \cdot \ddot{X}(w)}{\sum F^* \cdot F(w)} \qquad [3\text{-}16]$$

where F^* is the complex conjugate of the force (with respect to frequency).

The dynamic measurements from the ski simulator are more likely to be subject to output noise than input noise. The accelerometer that is used to quantify input force is located on the underside of the ski, next to the stinger, where the force is applied. It can therefore be expected that, aside from some low-level electrical noise, a good measure of the input excitation can be made. This infers that the A_1 estimator is applicable to the dynamic laboratory measurements. Random noise in the output measurement is removed during the averaging process of the cross-spectrum and as the number of averages in increased, A_1 converges to the true A.

Noise in the input measurement (see Figure 3-16 b) may occur if the structure is forced to vibrate at its natural frequency. The structure becomes compliant at its natural frequency and the high vibration amplitudes may not be representative of the input force. The input noise is removed using the A_2 estimator (see equation [3–17]).

$$A_2(w) = \frac{\sum \ddot{X}^* \cdot \ddot{X}(w)}{\sum \ddot{X}^* \cdot F(w)} \qquad [3\text{-}17]$$

where $\ddot{X}^*$ is the complex conjugate of the acceleration (with respect to frequency).

The estimators form the confidence interval (see equation [3–18]) for the FRF if there is noise at both the output and input measurements.

$$A_1(w) \leq A(w) \leq A_2(w) \qquad [3\text{-}18]$$

or for compliance:

$$H_1(w) \leq H(w) \leq H_2(w) \cdot \qquad [3\text{-}19]$$

Schwarz and Richardson [1, 1999] give reference to a third spectrum averaging technique (not used here) for a FRF estimate assuming random noise at both the input and output

Leakage occurs if the time signal is not periodic in the transform window (i.e., the time sample – in this case 20s) transformed into the frequency domain. The FFT assumes that the signal is periodic, with no discontinuities. However, in practice there are discontinuities (particularly with the Pico ADC data logging hardware, which multiplexes the channels) that affect the periodicity – reducing accuracy due to leakage. Windowing the data reduces leakage in its spectrum. In this work windowing is only used in calculation of the estimators (i.e., a Hanning window is added using commands in the signal processing toolbox of MATLAB 6.5, release 13). Despite discontinuity concerns (primarily associated with the use of the Pico hardware), the data is not windowed to avoid compromising efforts to calculate the damping factor from the compliance (see §3.3.3 and appendix C).

3.3.2.1 Frequency response

A procedure (see Figure 3-17) is established (based on the spectrum analysis technique reported previously – see §3.3.2) to process time domain measurements for spectrum analysis (using MATLAB). Time domain data from SISO accelerometer measurements are calibrated, with the input force being calculated as the product of the input acceleration and the moving mass (i.e., the load), with the ski assumed to be a massless spring-damper system (supported by moment arms at the FCP and ACP). The sampling frequency and time range (or window) is specified and the input force and output acceleration are transformed into the frequency domain, using an FFT that quantifies the amplitude (in N and g units respectively - see Figure 3-18 a and b). The FRF (see Figure 3-18 c) is calculated as accelerance (A) from the ratio of the FFT of the output acceleration and the FFT of the input force.

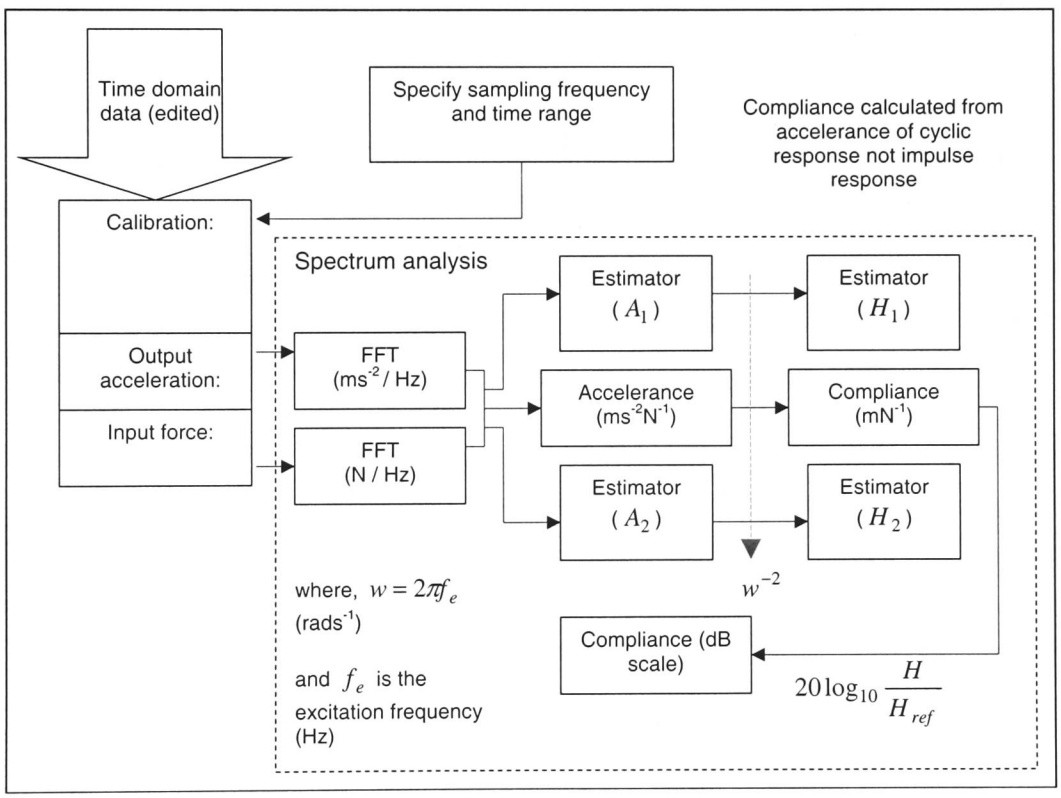

Figure 3-17: Spectrum analysis data processing procedure

The accelerance estimators (i.e., A_1 and A_2 - see equations [3–16] and [3–17]) are calculated from the ratio of the cross-spectral density (i.e., the cross-spectrum) and the power spectral density (i.e., the auto-spectrum). It can be seen (see Figure 3-18 b) that the calculation of the accelerance (A) from the FFT of the input and output measurements without windowing, lies within the confidence interval (see equation [3–18]) determined by the estimators (i.e., A_1 and A_2, which are windowed).

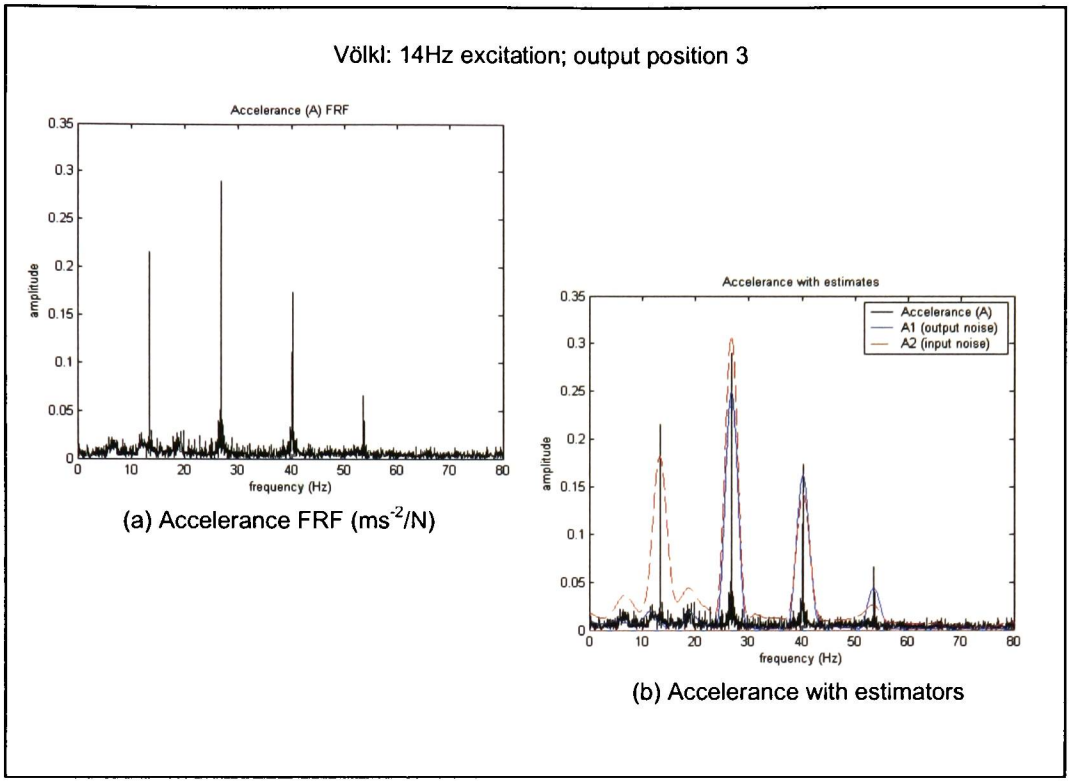

Figure 3-18: Spectrum analysis of processed data (example from SISO measurements of the Völkl "Motion", with output accelerometer 300mm from FCP, for excitation at 14Hz)

The compliance is obtained by scaling the amplitude of the accelerance by the inverse square of the angular frequency (i.e., w^{-2}). Accelerance estimators can be similarly scaled to produce compliance estimators (i.e., H_1 and H_2). The compliance or accelerance can be presented as a displacement to unit sinusoidal force (at the angular excitation frequency) on a decibel scale and used to identify damping characteristics of the structure (see appendix C). The compliance from SISO measurements is used to compile operating deflection shapes of the fore-body structure (see §3.3.4).

The output accelerometer in the SISO measurements is positioned on the fore-body at one of five locations (100mm apart, with the first position 100mm from the FCP) over the right hand edge (viewed looking down the fore-body from the MRS). The output accelerometer is located off-centre to enable measurement of edge movement that may manifest itself as chatter.

The frequency response (of the Salomon "Crossmax 8") is compared for different sinusoidal excitations, at the same output measurement position (see Figure 3-19 a-d). The excitation frequency (f_e) can be identified from the first spike in the plot of accelerance amplitude against frequency. There are secondary responses at approximately twice the excitation frequency (i.e., $2 f_e$) and for the

14Hz and 16Hz excitations (see Figure 3-19 c and d), these secondary responses have considerably greater amplitude than those generated at the excitation frequency. There is greater dynamic activity at shaker excitation frequencies of 14Hz and 16Hz compared with that generated by excitations at 18Hz and 20Hz.

Comparing the response at the third output measurement position (300mm from the FCP) for excitation frequencies at 14Hz and 16Hz, it can be seen (see Figure 3-19 e and f) that the dynamic response changes down the fore-body. The accelerance amplitudes from the measurement 300mm from the FCP are greater than those 500mm from the FCP, despite the vibration source being closer to the latter measurement position (i.e., since the sinusoidal input force is 800mm from the FCP). A similar pattern is obtained from tests on the Völkl ski and a non-shaped (Dynastar) ski (see appendix B-1) – compared against an aluminium beam (cross-section: 75mm x 7mm).

The moment arm of the ski simulator twists the fore-body until the contact surface at the FCP support is reduced to the right hand edge of the ski. The dynamic analysis is repeated with the FCP edged (i.e., the fore-body is twisted 2.5°) and accelerance compared (see appendix B-1) for different sinusoidal excitations (i.e., 14Hz and 16Hz) at the same output measurement position (i.e., 300mm from the FCP). The measured accelerance amplitude with the FCP edged decreases more significantly in the Salomon "Crossmax 8" and the Dynastar than it does in the Völkl.

The results show that there is variable dynamic response between the test structures and that the response amplitude changes with excitation frequency. Further analysis of the fore-body response seeks to better identify potential benefits of a variable vibration control capability. Compliance results are compiled to illustrate operational deflection shapes (see §3.3.4).

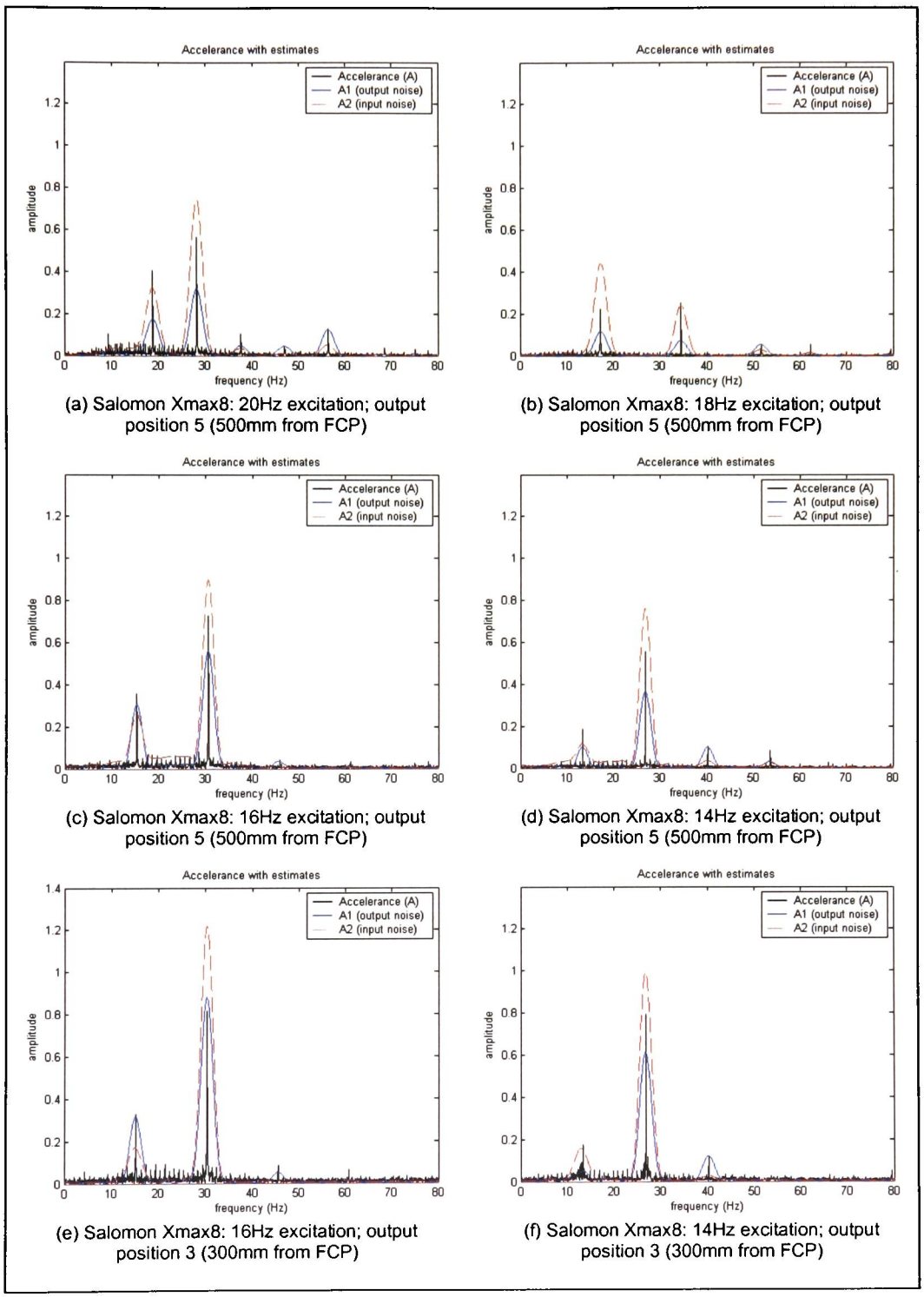

(a) Salomon Xmax8: 20Hz excitation; output position 5 (500mm from FCP)

(b) Salomon Xmax8: 18Hz excitation; output position 5 (500mm from FCP)

(c) Salomon Xmax8: 16Hz excitation; output position 5 (500mm from FCP)

(d) Salomon Xmax8: 14Hz excitation; output position 5 (500mm from FCP)

(e) Salomon Xmax8: 16Hz excitation; output position 3 (300mm from FCP)

(f) Salomon Xmax8: 14Hz excitation; output position 3 (300mm from FCP)

Figure 3-19: Accelerance of the Salomon "Crossmax 8" ski: comparing the response 500mm from the FCP (subject to a sinusoidal excitation at 14Hz, 16Hz, 18Hz and 20Hz) and 300mm from the FCP (subject to excitation at 14Hz and 16Hz)

3.3.2.2 Impulse response

Impulse tests are carried out to identify fore-body resonant frequencies, with the shaker used to generate the impulse. Given the location of the accelerometers on the fore-body, the frequency should correspond to the second mode of the structure being tested (see Figure 3-20). It would be better to determine the impulse response first, to identify the second modal frequency as the excitation frequency for cyclic tests (i.e., the frequency of the sinusoidal excitation). This would enable the second mode to be excited in the cyclic tests and for the operational deflection shape to be determined during resonance.

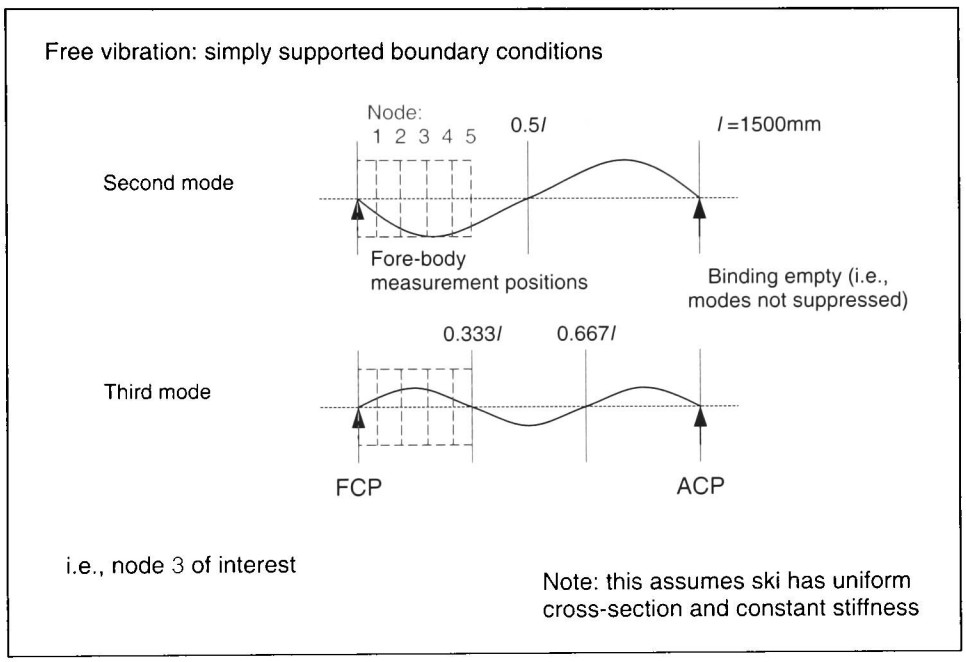

Figure 3-20: Fore-body modal response of simply supported ski

The impulse response functions are clearer for some structures than others (see Figure 3-21). This may be due to a physical problem with the impulse, although using the shaker reduces the risk of a double strike (associated with impact hammers). Schwarz and Richardson [1, 1999] and Døssing [1, 1988] acknowledged that accurate impact test results depend on the skill of the individual using the hammer to avoid bad hits (i.e., double impacts), so to avoid error the shaker is instead used.

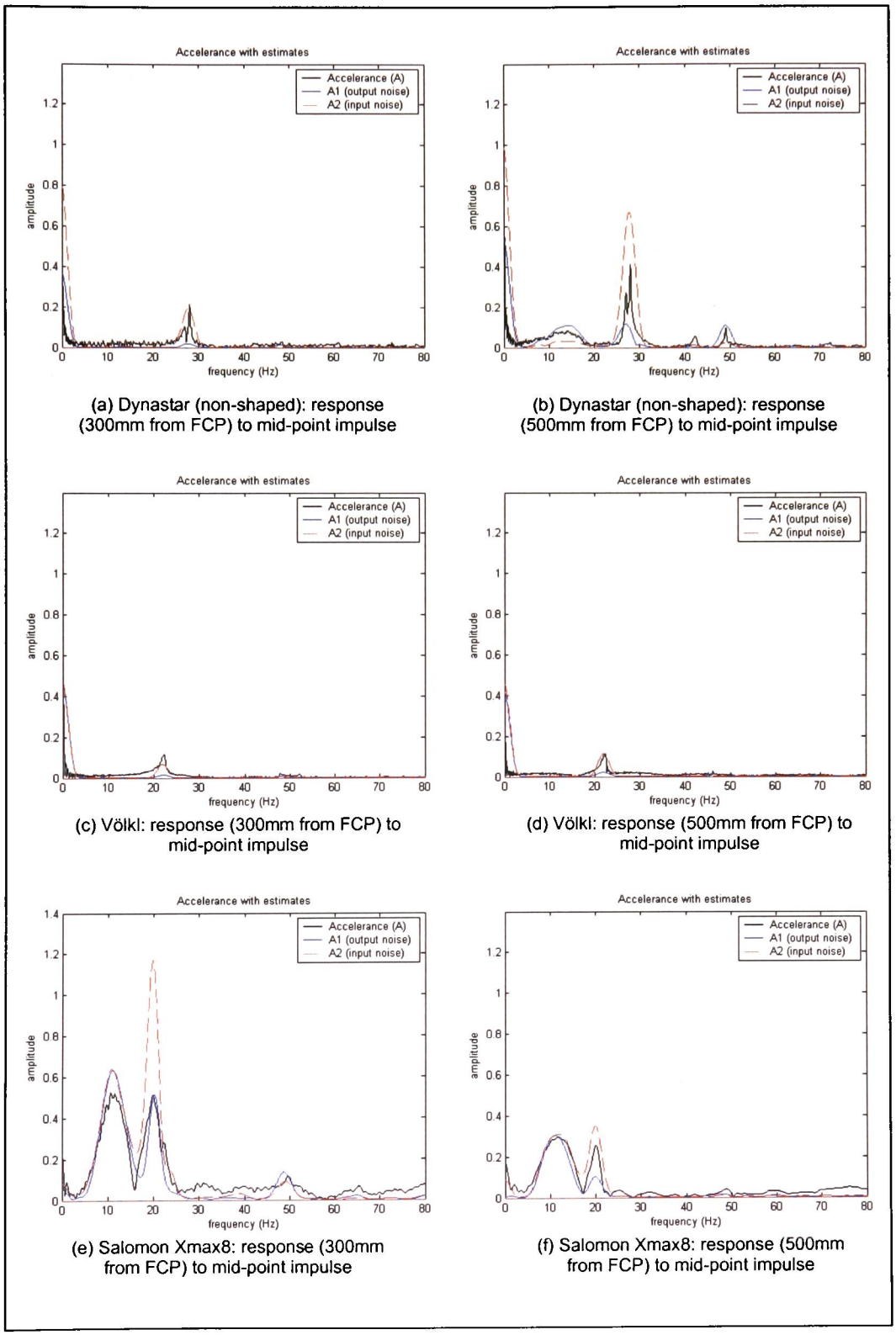

(a) Dynastar (non-shaped): response (300mm from FCP) to mid-point impulse

(b) Dynastar (non-shaped): response (500mm from FCP) to mid-point impulse

(c) Völkl: response (300mm from FCP) to mid-point impulse

(d) Völkl: response (500mm from FCP) to mid-point impulse

(e) Salomon Xmax8: response (300mm from FCP) to mid-point impulse

(f) Salomon Xmax8: response (500mm from FCP) to mid-point impulse

Figure 3-21: Impulse response functions from measurement node 3 (300mm from the FCP) and node 5 (500mm from FCP) for the Dynastar, Völkl and Salomon "Crossmax 8"

The relatively small data set (hundreds of data points over seconds) in the impulse test compared with the cyclic test (where there are a couple of thousand data points over 20s) is a greater source of error. In order to avoid loss of resolution, the impulse data set is made the same size as the cyclic data sets by adding zeroes. An alternative would be to repeat the impulse data set, but this would lead to discontinuities and affect the impulse response function. A better solution is to increase the sampling frequency for impulse response functions (i.e., more points for a shorter time).

The impulse response functions (see Figure 3-21) indicate that the Dynastar resonates at 28Hz, the Völkl at 22Hz and the Salomon at 10Hz (with a secondary response at 20Hz). Analysis of excitations at these respective frequencies for the three structures would have enabled an approximation of the mode shape to be determined from the operational deflection shape (see §3.3.4). The operational deflection shapes obtained using the results of cyclic tests are instead combinations of mode shapes.

3.3.3 Damping

The rate of decay of free oscillation, measured by the logarithmic decrement (see Figure 3-22), can be used to determine the amount of damping in a system. The larger the damping, the greater the rate of decay. The logarithmic decrement (δ) is defined as the natural logarithm of the ratio of any two successive amplitudes (i.e., x_1 and x_2):

i.e., $$\delta = \ln\frac{x_1}{x_2} = \frac{2\pi\zeta}{\sqrt{1-\zeta^2}}. \qquad [3\text{-}20]$$

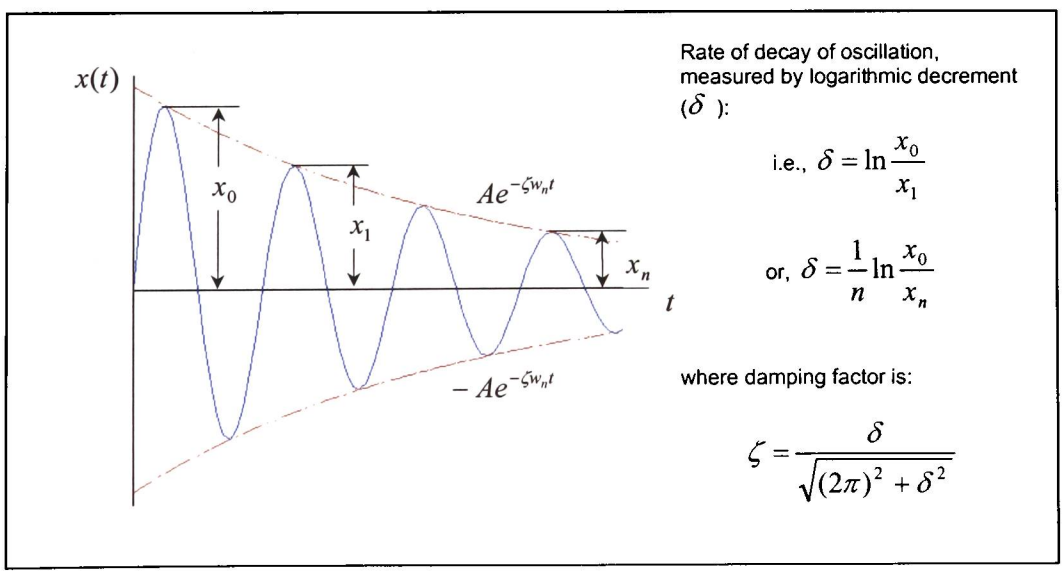

Figure 3-22: Determining the logarithmic decrement from the rate of decay of free oscillation (produced with reference to Meirovitch [2001] and Thomson [1993])

Rearranging equation [3–20] to solve for the damping factor:

$$\zeta = \frac{\delta}{\sqrt{(2\pi)^2 + \delta^2}} \cdot \qquad [3\text{-}21]$$

A more accurate determination of damping factor can be made by measuring the displacements at two different times, separated by a given number of periods (i.e., peak displacements x_1 and x_{n+1} corresponding to times t_1 and t_{n+1}, where n is an integer). So, the logarithmic decrement becomes:

$$\delta = \frac{2\pi\zeta}{\sqrt{1-\zeta^2}} = \frac{1}{n}\ln\frac{x_1}{x_{n+1}} \cdot \qquad [3\text{-}22]$$

Equation [3–22] can be substituted into equation [3–21] to obtain the damping factor.

Accuracy can be further improved by determining the logarithmic decrement from more than two measurements. Rearranging equation [3–22]:

$$\ln x_n = \ln x_1 - \delta(n-1) \cdot \qquad [3\text{-}23]$$

A semi-log plot of $\ln x_n$ against n, based on equation [3–23] has the form of a straight line with gradient $-\delta$. Quantifying the logarithmic decrement from the plot of multiple measurements increases the accuracy of the damping factor that can be determined using equation [3–21].

The logarithmic decrement is determined from time-domain data obtained from impulse tests and the damping factor is derived for the non-shaped Dynastar ski and the shaped Völkl ski (see Figure 3-23). The results for the shaped Völkl ski are slightly higher than those obtained for the non-shaped Dynastar ski. The damping factor indicates that both skis are underdamped and that there is greater damping in the MRS (from measurements taken at the mid-point) than in the fore-body (comparing measurements taken 500mm from the FCP). These results suggest that simply adding viscoelastic layers (see §2.1.3.2) is inadequate for damping skis.

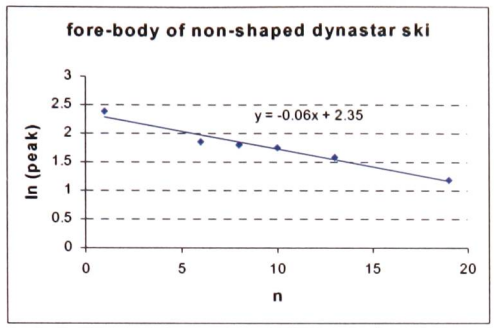

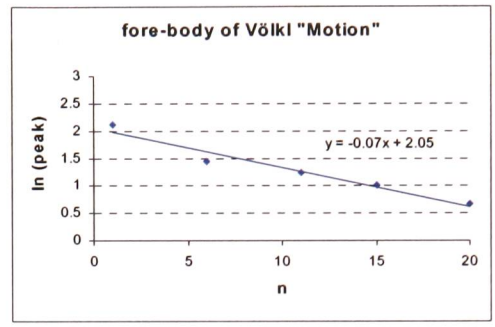

(a) Determining logarithmic decrement from decaying oscillation (from time-domain data)

Ski	logarithmic decrement		Damping factor	
	mid	fore (500mm from FCP	mid	fore (500mm from FCP
Dynastar	0.074	0.062	0.012	0.010
Völkl	0.090	0.072	0.014	0.011

(b) Results: comparing mid-point and fore-body (500mm from FCP)

$\zeta << 1$ i.e., system is underdamped

Damping is greater in the MRS than in fore-body

Figure 3-23: Damping factor quantified from analysis of the rate of decay of oscillation from impact tests (comparing the Völkl "Motion" and non-shaped Dynastar ski)

As described by Gade et al [1994], frequency response functions on a decibel (dB) scale can be used to determine an estimate of the fore-body damping characteristics of the ski (see appendix C). The resolution is insufficient to do so here, due to the sampling frequency. An increased sampling frequency is recommended for future impact analysis

3.3.4 Operating deflection shape

The operating deflection shape represents the actual (measured) motion of one point relative to others. The output is normalised and quantified as compliance – defined by a magnitude and phase. The operating deflection shape of the fore-body during the dynamic tests on the ski simulator can be illustrated by compiling the compliance results for different output sites. Although mode shapes and operating deflection shapes are related, they are different (as discussed by Schwarz and Richardson [2, 1999]):

1. Each mode is defined for a specific natural frequency, whereas operational deflection shape can be defined at any frequency.
2. Modes are defined for linear, stationary structures (i.e., at resonance). Operational deflection shape can be defined for non-linear and non-stationary structures.
3. Modes are used to characterise resonant vibration, while operational deflection shape can characterise resonant and non-resonant vibration.
4. Modes only change if the material properties or boundary conditions change and do not depend on forces or loads, but operational deflection shape will change if the load changes.

Operating deflection shapes approximate mode shapes near the natural frequencies of the structure and away from the natural frequencies, they are combinations of the mode shapes.

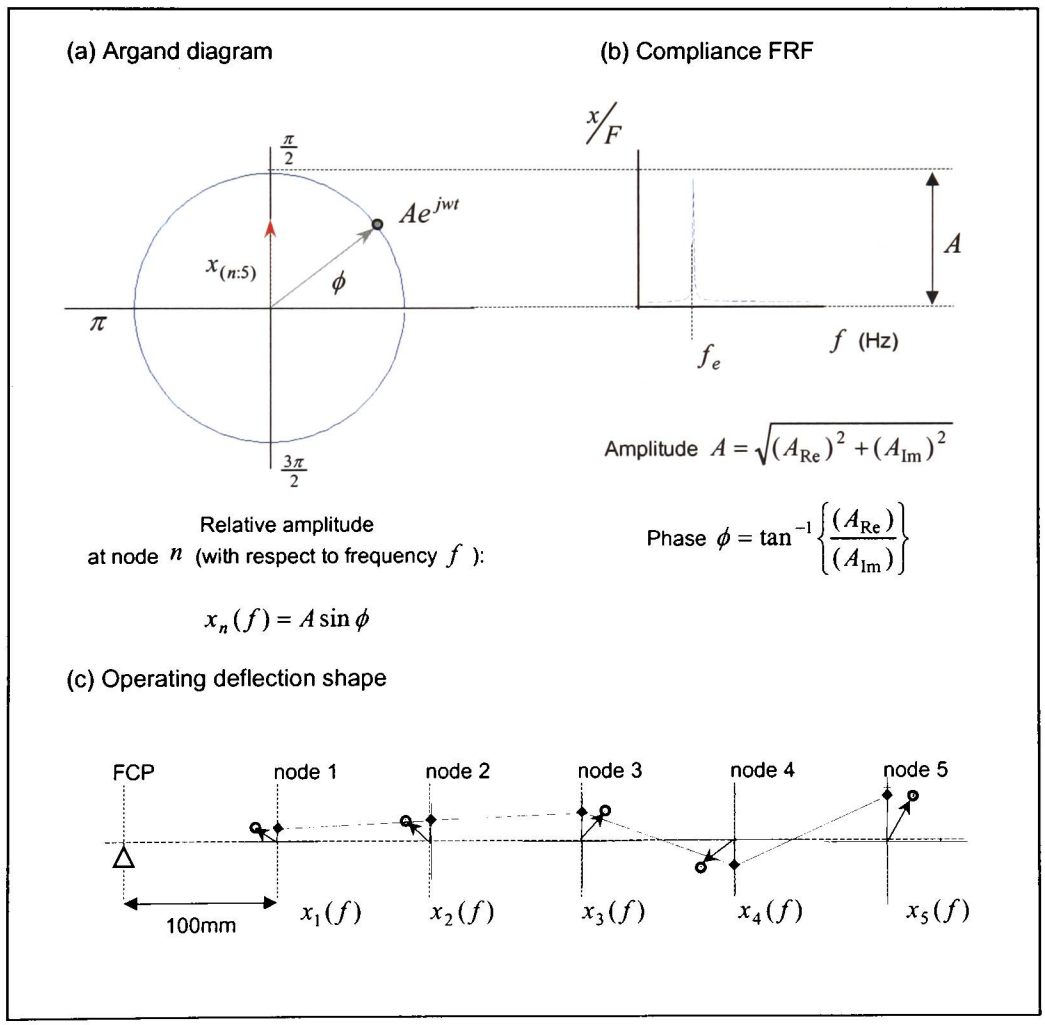

Figure 3-24: Determining operational deflection shape from frequency response functions

Referring to an Argand diagram, the peak amplitude can be quantified from the FRF for a particular frequency (see Figure 3-24 a and b). Compliance amplitude is obtained by dividing the accelerance amplitude by the angular frequency squared (see Figure 3-15). Quantifying the phase at a specific frequency enables the relative amplitude of the node to be determined. Compared with other nodes, the relative amplitude can be plotted to provide an operational deflection shape (see Figure 3-24 c).

The single-axis accelerometer is mounted over the edge of the ski. The compliance (mm/N) at the nodal measurement positions is in the vertical x-axis when the ski is not twisted. However, when the ski is twisted by the moment arms at the FCP, the compliance has components in two axes (x and z). In order to compare the compliance in the vertical x-axis, it is necessary to resolve the measured acceleration with respect to the angle of twist at the nodal measurement position (see Figure 3-25).

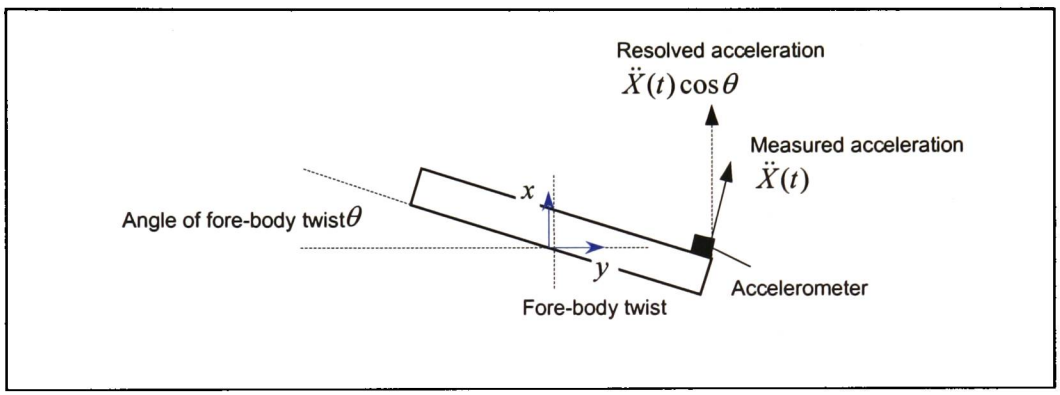

Figure 3-25: Resolved acceleration from that measured with the fore-body twisted

Compiling information from the frequency response functions from SISO measurements at each node, the operational deflection shape of the edge may be illustrated with respect to shaker excitation and with the FCP twisted (to simulate turn conditions). Results are presented, from tests on the Salomon "Crossmax 8," comparing the edge response at the nodal measurement positions at 14Hz and 16Hz shaker excitation with and without the FCP twisted (see Figure 3-26). Further results (presented in appendix B-2) compare the edge response of the shaped Völkl "Motion," the non-shaped Dynastar ski and an aluminium beam (not included in twist tests).

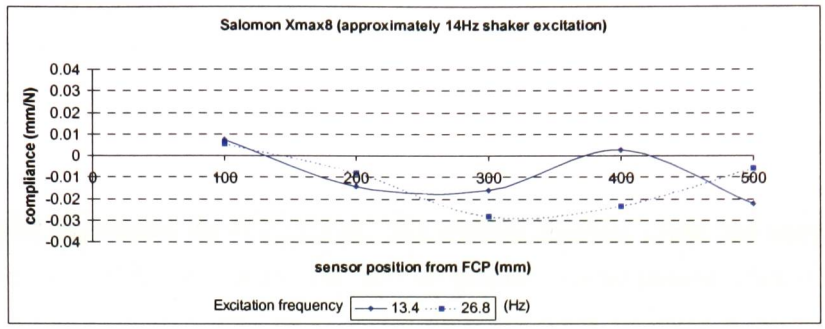

(a) Salomon Crossmax 8; 14Hz shaker excitation

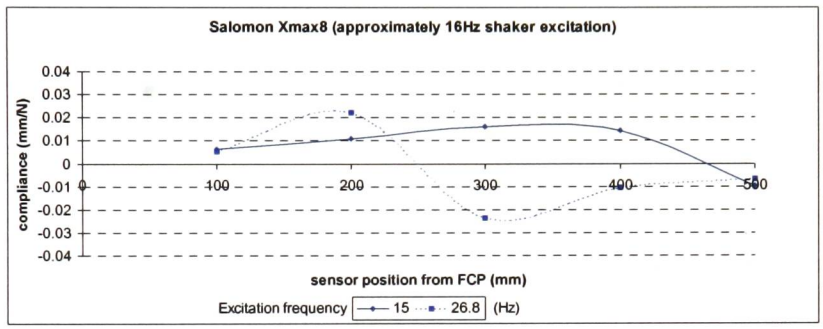

(b) Salomon Crossmax 8; 16Hz shaker excitation

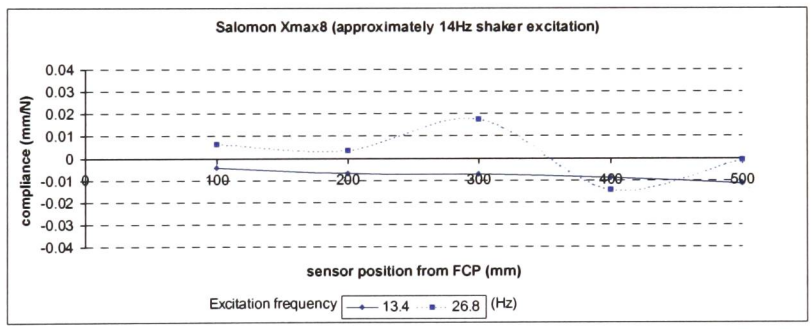

(c) Salomon Crossmax 8; FCP twisted; 14Hz shaker excitation

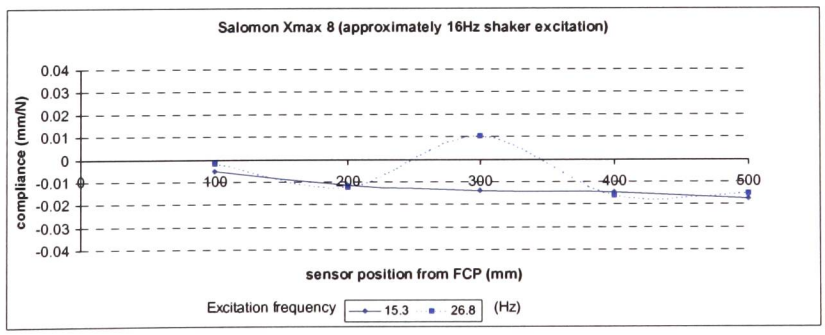

(d) Salomon Crossmax 8; FCP edged; 16Hz shaker excitation

Figure 3-26: Salomon "Crossmax 8" fore-body operational deflection shapes (at 14Hz and 16Hz shaker excitation) with and without the FCP twisted

It is important that the operational deflection shape is not confused with the modal shape (unless the operational deflection shape is presented at a modal frequency). The operational deflection shapes presented here (see also appendix B-2) are combinations of the mode shapes at a specific excitation frequency (i.e., approximately 14Hz, or 16Hz), with a secondary response at twice the excitation frequency. Therefore, the results provide a comparison of the edge response at these specific frequencies - with and without the FCP twisted. The dynamic response of the fore-body, 300mm from the FCP, on the carving skis is interesting and may indicate a modal frequency below 50Hz. A more conclusive statement and comparison of the structures could be made if the operational deflection shapes were to be plotted at modal frequencies.

The ability to calculate and present operating deflection shape is useful in analysing the response of the ski to the simulated conditions and comparing with results obtained from field-tests. This may enable laboratory simulations to be developed so that they are closer representations of the real system. A representative physical simulator can complement computational modelling and is of benefit to ski development. The results from tests on the simulator have provided considerable information on the behaviour of modern alpine skis that is not readily obtainable. This information enables conjecture on how the proposed smart technology system may benefit skiing.

3.4 Instrumented ski

Skis are instrumented with piezo-polymer sensors with the aim of investigating dynamic-mechanical behaviour (see §3.4.1). The motivation for field-testing instrumented skis is to identify characteristic signal response to defined dynamic behaviour and conditions (e.g., vibration response during straight-run; carving turn; sliding turn, with respect to on-slope conditions). Results from preliminary field tests are appraised (see §3.4.2).

The feasibility is discussed for using an integrated sensor array to provide feedback for control of the proposed adaptive ski (see §3.4.3). It is envisaged that actuator response would be controlled based on identification of a characteristic signal in the time domain, so that force-control would be proportional to an observed feedback signal.

3.4.1 Piezoelectric sensors

A non-invasive sensor is required that will measure the deformation of a ski during dynamic operating conditions, without altering the response of the ski. A consistent signal output is required in a low temperature environment (i.e., –20°C to 20°C). The piezoelectric polymer – polyvinylidene fluoride (PVDF) is considered suitable for measuring the dynamic behaviour of a ski, with benefits

over foil resistive strain gauges and opportunity for use in the adaptive ski concept. Laminated DT Series Elements (LDT1-028K/L with rivets and wire leads) from Measurement Specialities Inc. (MSI) have been selected to retrofit a non-invasive sensor array to skis for field-testing.

Polyvinylidene fluoride is a crystalline polymer with piezoelectric properties that can be exploited in electromechanical transducers. The piezoelectric effect for use of PVDF as an actuator is discussed by Bailey and Hubbard [1985], with the converse piezoelectric effect being used in this work. The PVDF sensors generate a current proportional to rate of change of strain that can be measured as a voltage when passed through an operational amplifier.

It is acknowledged that the PVDF sensors have a defined pyroelectric response (i.e., a current change proportional to change in temperature). Sirohi and Chiopra [2000] compared characteristics of PVDF and the piezoelectric ceramic – lead zirconate titanate (PZT). PVDF has greater temperature dependence (i.e., pyroelectric) and the piezoelectric coefficient is approximately 10% of PZT. Despite this, as a sensor PVDF is said to be more suitable – since the value of the modulus of elasticity is an order of magnitude smaller (e.g., 71GPa for PZT and 4–6GPa for PVDF), therefore, having much less influence on the host structure.

Compared to conventional (foil) resistive strain gauges, use of PVDF has several advantages for this application. PVDF sensors do not require a power source, whereas a battery pack (subject to thermal affects) would be required for carrying out field-tests with strain gauges. Calibrated piezo-polymer accelerometers are considered, but a battery pack is required to power amplifiers. As with PVDF sensors, output voltage from strain gauges will decrease with temperature. In the case of strain gauges this may be overcome by using a full-bridge network and physically re-calibrating at the required operating temperature – hence, four sensors are required to take one strain reading (at least two are required if a half-bridge is used). A single non-strained PVDF sensor exposed to the same environmental temperature as the strain measuring sensor array can be used to log the pyroelectric response and the results used to re-calibrate all sensors in the array. Therefore, compared with conventional strain gauges it can be seen that monitoring ski deflection with PVDF sensors requires less bulk (i.e., no battery pack) and less complexity (i.e., one sensor provides a strain reading with calibration for thermal changes based on the pyroelectric response of a single non-stressed sensor).

A network of laminated PVDF sensors are bonded to the surface of the ski, in a 2x5-grid array down the length of the ski (i.e., 2x4 down the fore-body and 2x2 down the aft-body). The PVDF sensors produce a current, measured as a voltage output (V_1) that is proportional to their rate of change of strain ($d\varepsilon / dt$), acting over the area of the sensor, and produced by the vibrating ski. The voltage output is converted (using a Pico ADC-11, multi-channel data logger, with 10-bit resolution – see §3.3.1) from an analogue to digital signal and is recorded (using Pico software) on a laptop computer

carried by the skier. Theoretically, integrating the voltage output with respect to time should give a voltage (V_2) that is proportional to strain (ε).

i.e., $$V_1 \propto \frac{d\varepsilon}{dt}; \quad [3\text{-}24]$$

$$\int_1^2 V_2 \cdot dt \propto \int_1^2 \varepsilon \cdot dt; \quad [3\text{-}25]$$

so, $$V_2 \propto \varepsilon \quad [3\text{-}26]$$

However, as with accelerometers, the signal from PVDF sensors is subject to drift that requires filtering to make integration of time-domain data successful. Alternatively, the signal can be analysed in the frequency domain (see §3.3.2) to give a measure of the mobility (i.e., $\dot{\varepsilon}_{PVDF} \propto \dot{x}_{ski}$) of the ski at the distributed sensor locations.

3.4.2 Field-tests

A variety of field-test procedures for measurement of ski dynamics have been reported. Pressure and frequency response of pre-carving skis were measured by Piziali and Mote [1972], using nine semi-conductive pressure transducers located along the ski length and one piezo-resistive accelerometer (with a ±20g range), located on the central-axis, near the tip. Radio telemetry of analogue data was supported by video. A jump was used to initiate each test and synchronise all the measurement systems.

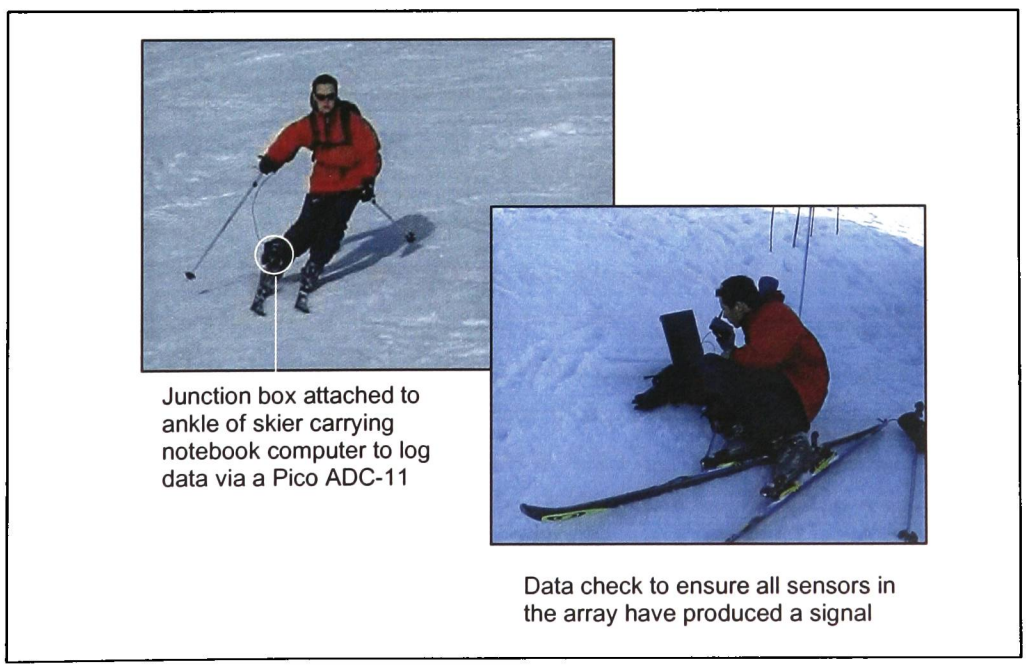

Figure 3-27: Field-testing of instrumented skis

Analysis of data from field-testing (see Figure 3-27) aims to identify characteristic signals that define a particular dynamic movement (e.g., vibration response during straight-run; carving turn; sliding turn). The instrumented skis are used to investigate deformation experienced during prescribed motions (e.g., a series of turns). Data are logged (with respect to time), from the PVDF sensor array bonded to the surface of the ski, onto a laptop carried in a backpack on the skier (see Figure 3-27). Data analysis is supported by video records, with processed data being compared to digital video footage taken during the test run. Synchronising the clocks on the video camera and computer (see Figure 3-28) make it possible to relate logged signals to observed motions. However, to produce quantified motion analysis from video requires more than one camcorder and time-consuming analysis. Therefore, given the resources available and scope of the work, video is limited to providing a record of the tests as they are carried out.

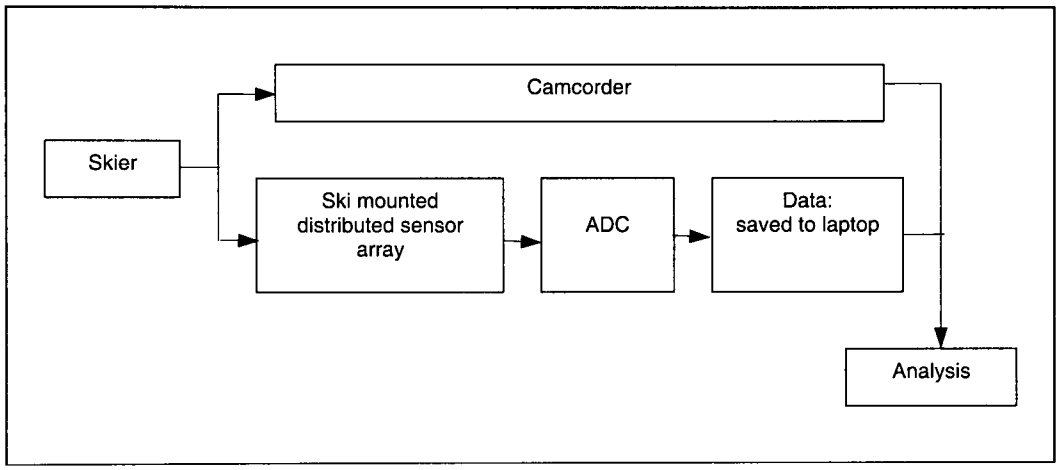

Figure 3-28: Field-test schematic [Watson and Blackford, 2001]

Analysis of time domain data from preliminary field tests presents results (see Figure 3-29) that highlight initial failings in the data logging procedure. The Pico ADC-11 is saturated by the signal produced by the sensors. Therefore, the PVDF sensors are generating current proportional to rate of change of ski deflection that results in voltage outside the 0-2.5V range of the ADC. Also, the 50Hz sampling frequency (i.e., readings every 20ms) is inadequate – allowing analysis over a frequency range of 25Hz at best (assuming a Nyquist frequency of half the sampling frequency). Although not presented here, better results have been produced at increased sampling frequency (i.e., 200Hz, equivalent to a reading every 5ms) and with resistors in-place to overcome saturation by reducing the voltage through the ADC. Despite these revisions there remain problems associated with use of the Pico ADC-11 (see §3.3.1) for this application. The 0-2.5V range only allows positive voltages to be recorded, with a power source required to offset the zero to enable negative values to be recorded. If a power source is to be used, alternative devices may be considered with higher specifications.

Nevertheless, further work to produce signal analysis of field-test data using the ADC-11 is recommended. The limitations of the ADC-11 are comparable to the constraints that must be faced in the development of feedback control for the adaptive ski (see §3.4.3).

Measured response from PVDF instrumented Salomon "Crossmax 8"

$(V \propto \dot{\varepsilon} \propto \dot{x})$

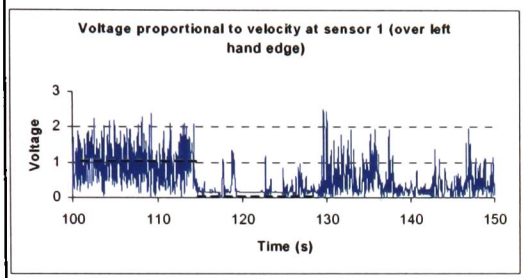

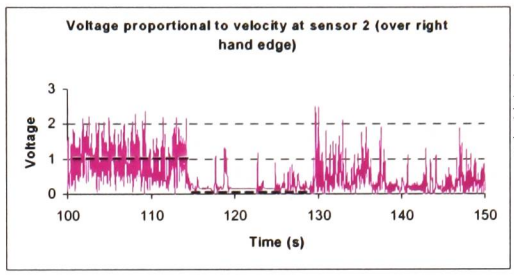

- Zero drift: from 1V between 100s and 115s, to 0V during turning (i.e., 115s to 130s)

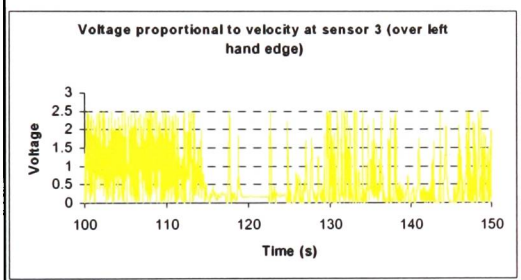

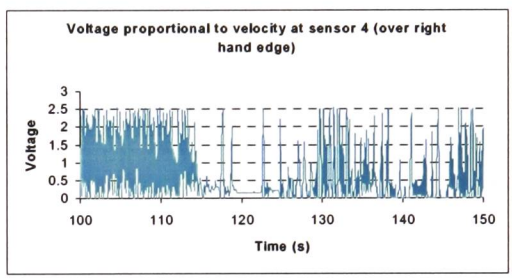

- ADC saturation: signal > 2.5V range

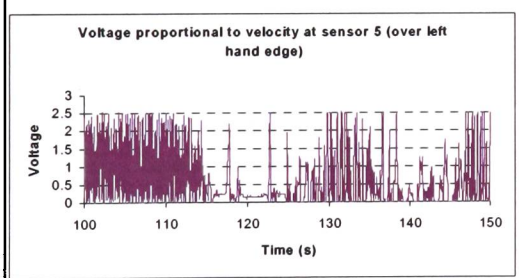

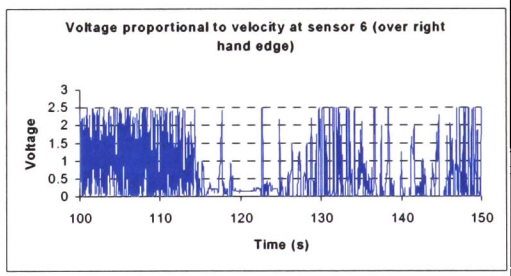

- No difference between sensor over left hand edge and that over right hand edge during turn (i.e., 115s to 130s). Turn can not be distinguished (i.e., left or right), but can be identified (i.e., by a reduction in mobility).

Increased sampling frequency required (i.e., from 50Hz to 200Hz) and resistors required in order to prevent saturation of the Pico ADC-11

Figure 3-29: Time domain results from field tests of PVDF piezo-polymer instrumented ski

Observations of time domain results from fore-body sensors on an instrumented Salomon "Crossmax 8" illustrate the issues with saturation, drift and low sampling rate (see Figure 3-29). The results correspond to a straight flat run followed by a left then right turn. There does not appear to be significant difference between the output from sensors located over the left and right edge. The amplitude is reduced during turning – suggesting that torsional deformation increases longitudinal stiffness.

3.4.3 Control feedback

The ultimate aim for the proposed adaptive ski is an integrated system that will provide semi-active vibration control – to increase the performance by enhancing the handling characteristics. The system actuator should act in a specific way to counter vibration, proportional to the amplitude and rate of change of amplitude. This may be achieved with a control algorithm (see Figure 3-30) using sensor input provided by a distributed array of embedded PVDF sensors.

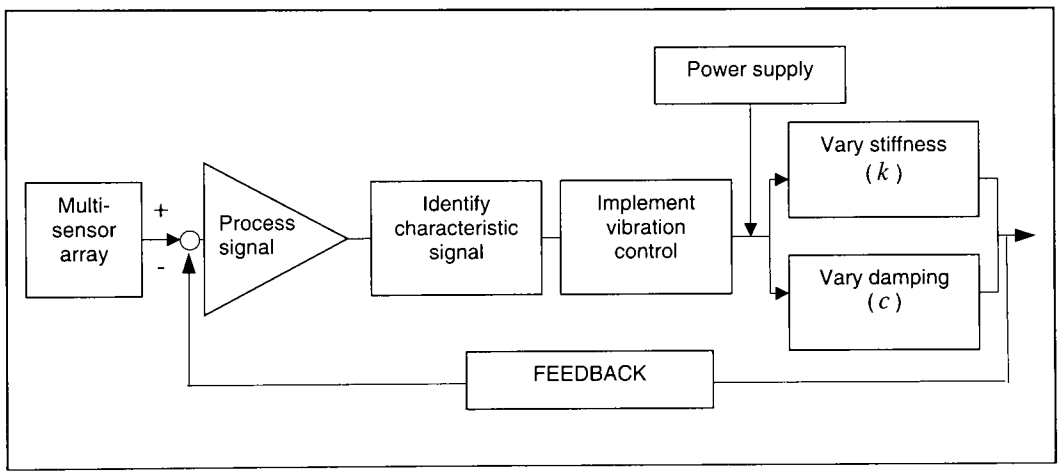

Figure 3-30: Conceptual control schematic [Watson and Blackford, 2001]

Work on a distributed-parameter control system to actively control a PVDF dampener has been presented by Bailey and Hubbard [1985], with a similar experimental set-up being used by Gaudenzi et al [2000], to demonstrate a single-input single-output closed loop feedback control system for active damping with piezoelectric patches. This work provides a good reference point for developing the necessary control to support the adaptive ski concept. Control considerations for MR fluid devices are discussed later (see §4.3.6).

3.5 Précis (§2 & §3)

Before going on to introduce magnetorheological fluid (§4) and its application in semi-active damping of an adaptive ski (§5), it is worth summarising the main points from this chapter (§3) and the previous one (§2).

The assignment of boundary conditions in the modelling of skis (computationally and in the laboratory) is discussed (see §2.4), with a view to establishing constraints for simulations (virtual and physical) that yield data of practical significance (i.e., so that results are representative of the real world situation). Specifically, it is recommended in this work that it is better to consider the MRS as being clamped (as it is constrained between the skier's boot and the snow surface) and model the fore-body and aft-body as cantilevers.

The response of the ski and its dynamic stability will depend on torsional and longitudinal characteristics (i.e., mass, stiffness and damping) of the fore-body and aft-body cantilevers. Therefore, it is of interest to investigate these characteristics and quantify the dynamic response – subject to controlled stimulus (i.e., system analysis in the laboratory) and during skiing (i.e., signal analysis from field tests).

Full body ski stiffness (i.e., with the ski simply supported at the FCP and ACP) has been quantified and is used to compare a cohort of skis (see §3.2.1.1). Observations on full-body flex have lead to the conclusion (here) that there is a flat spot under the MRS proportional to the length of the skier's boot. It follows, that a variety of systems (such as the Salomon "Pilot" and Völkl "Motion") that claim to reduce the flat spot and increase full body flex fail to do so. It is considered here that increasing full body flex may in fact reduce ski stability. It is therefore the opinion that fitting a shim (such as that offered on the Atomic 10-20 and 11-20) provides better ski stability, by reinforcing the MRS and providing a structure that can be used to improve isolation of fore-body and aft-body vibrations. These qualitative observation based conclusions add further support to the use of the boundary conditions advocated here (referring again to §2.4).

Full body ski stiffness is considered here to be of little practical significance, despite the ASTM guidelines [ASTM F 498-77 (1998)]. Although full body ski stiffness is investigated (see §3.2.1.1), the boundary conditions are not considered representative of the real world situation. Investigation of fore-body and aft-body, longitudinal and torsional, stiffness and damping is of greater practical significance. Particularly, the ability to quantify characteristics that influence the dynamic stability of a ski and use this information to specify parameters for the adaptive ski. Fore-body and aft-body longitudinal and torsional ski stiffness has been quantified (i.e., with the MRS clamped) and is used to compare a cohort of skis (see §3.2.1.2 and §3.2.1.3 respectively). Considering anecdotal feedback

(from non-specialist skiers) on the perceived dynamic stability of the skis following field-tests, the results suggest that torsional stiffness may provide the difference in performance. Despite this observation, subsequent work on the adaptive ski (see §5) focuses on longitudinal vibration control to simplify concept demonstration (see §5.2).

The ability to investigate dynamic response under controlled, repeatable conditions in the laboratory is shown (see §3.2.2). Apparatus has been developed (see §3.2) and a system analysis procedure is established (see §3.3) and used to investigate full-body dynamic response (i.e., frequency response from cyclic excitations and impulse response from impact excitations). Operating deflection shapes compare (see §3.3.4 and appendix B-2) full-body response of skis with the FCP twisted (onto an edge), based on the compilation of frequency response functions from SISO (single input, single output) accelerometer measurements. Mode shapes could be better investigated by identifying resonant frequencies (<50Hz) from impact excitations and then determining the frequency response from cyclic excitations at resonant frequencies.

The excitation frequencies experienced during skiing must be identified from signal analysis of field test data. The system analysis techniques can be adapted for signal analysis of data from field tests of instrumented skis. Skis have been instrumented with piezo-polymer (PVDF) sensors and field-tested (see §3.4). However, the data presented here has not been sampled at high enough frequency and the capability of the data acquisition hardware (i.e., the Pico ADC 11, used here) is questioned.

Further work is required to apply the techniques established here and better quantify torsional and longitudinal characteristics of skis and their dynamic response. This information is required so that the performance of the MR fluid damper can be specified. The following chapters present research on MR fluid (specifically its use in devices for semi-active damping – see §4) and its proposed application in an adaptive ski (see §5). Despite not having data on skis to support a specification for a MR fluid damper, it became necessary to demonstrate the feasibility of the concept (see §5.2) for commercial reasons.

4 Magnetorheological (MR) Fluid

This section provides a background to MR fluid and its application. An introduction to the physics, chemistry and application of controllable rheological fluids is presented with emphasis on magnetorheological (MR) fluid (see §4.1 and §4.2). Considerations are discussed for MR fluid device design - including an introduction to an analysis of magnetic field systems and with references to the control of rheological fluids (see §4.3). Clarification is provided of what is meant by passive, variable, active and semi-active damping.

The design of a diaphragm sealed, fixed core MR fluid damper is presented and results from experiments on a prototype are analysed to appraise its performance (see §4.4). The force-displacement characteristics of the prototype damper are modelled and parameters quantified from analysis of results from low frequency cyclic tests.

4.1 Controllable rheological fluids

Rheo is Greek for flow [Yanyo, 2003] and rheology is the study of the flow of fluids (i.e., liquids, gases and "solids"). Electrorheological (ER) and magnetorheological (MR) fluids are suspensions of micron sized particles that can be polarised in the presence of a field (electric or magnetic, respectively). MR fluids should not be confused with colloidal ferro-fluids, where the particle size is 1000 times smaller than the micron-sized particles in MR fluid, so, exhibiting significant Brownian motion.

Willis Winslow and Jacob Rabinow are considered [Carlson et al, 1996], respectively, the pioneers of research into electrorheological (ER) and magnetorheological (MR) fluid. Research by Rabinow on MR fluids in the late 1940s and early 1950s ran parallel to research by Winslow on ER fluids in the 1940s.

Rabinow's early MR fluids, as described by Carlson [2001], consisted 9 parts by weight of carbonyl iron with one part silicone oil, petroleum oil, or kerosene. Grease or another thixotropic additive was added to improve the settling stability of the suspension. Winslow also developed MR fluids, consisting 10 parts by weight carbonyl iron suspended in mineral oil, with ferrous naphthenate or ferrous oleate acting as a dispersant and a metal soap (such as lithium stearate or sodium stearate) as a thixotropic additive.

Controllable rheological fluids undergo an apparent change in viscosity in the presence of an applied field. The change in rheometry (i.e., the on state) results from the alignment of particles in an applied

field. Chains form and can be used in a variety of modes (i.e., direct shear, pressure and squeeze – see §4.3.2, Figure 4-5) to restrict fluid flow, proportional to the applied field. Rheological properties of controllable fluids (i.e., in the off-state and on-state) depend [Jolly et al, 1999] on concentration and density of particles, particle size, particle shape distribution, properties of the carrier fluid and additional additives, applied field, temperature, and other environmental factors. To be able to optimise controllable fluids for a particular application, understanding of the interdependent factors is required.

A review of the understanding of the behaviour of ER and MR fluids is presented by Rankin et al [1998], who concluded that better understanding of the rheology under application conditions is required. MR fluid rheometry has been carried out in a number of studies [Jolly et al, 1996; Tang and Conrad, 2000; Genç and Phulé, 2002], quantifying shear stress in the fluid with respect to the magnetisable particles (i.e., the percentage of carbonyl iron by volume). Magnetic properties of MR fluids with different carbonyl iron content (i.e., 10%, 20% and 30% iron by volume) have been investigated experimentally by Jolly et al [1996] and used to verify a mathematical model based on the dipolar interaction of particles. Rheological measurements [Genç and Phulé, 2002], supported with SEM analysis, x-ray spectroscopy and x-ray diffraction (XRD), compare MR fluids with different carbonyl iron content (i.e., 33% and 40% iron by volume) and different particle size distribution (i.e., 0.5μm-5μm and 1μm-9μm). The saturation magnetisation for MR fluids with coarser powders was found to be greater than for MR fluids with finer powders. The dynamic yield stress (or shear stress with respect to shear strain rate - see §4.1.2, Figure 4-1) was shown to increase with increasing volume fraction of magnetic particles.

The rheological behaviour of ferro-fluids is investigated by Lemaire and Bossis [1991], who recognised the significance of wall effects on yield stress – specifically, with respect to the surface roughness of the wall (i.e., a rough wall surface is required in MR fluid devices). A reduction in surface roughness at the wall interface with the fluid causes the fibres (produced by the alignment of particles parallel to the field) to slip. Tang and Conrad [2000] acknowledged that magnetic interaction between particles can be stronger than that between the particles and walls, with wall surface condition influencing the measured fluid shear stress. A similar observation has been made during practical investigations carried out in this research, although nothing on this has been quantified. MR fluid devices with wall interfaces that have a smoother surface finish produce relatively smaller on-state forces. At rougher wall interfaces, the particles are pushed against the wall, where they become embedded and act as anchors for aligned-particle fibres. However, the embedding of particles at wall interfaces causes a problem for sealing of MR, ER and ferro-fluid devices (see §4.3.3). The walls of MR fluid devices engineered to support this research are ribbed. A thread (1mm pitch) is rough machined inside the steel cylinder that acts as the flux return sleeve and on the cylindrical surface of the electromagnet – see §4.3.1, §4.4.1 and §4.4.2.

Li et al [1999] made reference to three methods for measuring the linear viscoelastic properties of ER and MR fluids:

1. Sinusoidal oscillatory flow;
2. Steady flow in a concentric cylinder or disk rheometer;
3. Dynamic methods, such as vibrating sandwich beam.

Subsequent research [Li et al, 2002] used a three parameter viscoelastic model (i.e., a spring in series with a Voigt model) to represent MR fluid behaviour, and indicates that the elastic component of MR fluids increases with field strength, though decreases with temperature.

4.1.1 Comparing MR, ER & Ferro-fluids

Electrostatic polarisation is the basis for the ER response and is described by Rankin et al [1998]. In an electric field, the particles polarise and appear as electric dipoles, attracting and forming chains in the direction of the field, to produce a fibrous structure (analogous to that of a MR fluid in the presence of a magnetic field). Work is required to break the fibrous structure and make the fluid flow, thereby changing the apparent rheological properties.

Three regimes of applied field strength and interparticle forces have been identified [Rankin et al, 1998] as being relevant in MR fluids:

1. Low fields (almost irrelevant in many devices), where particle magnetisation is linear and can be treated using techniques developed to describe electrostatics of ER fluids.
2. Intermediate fields (of practical use in MR devices), where a magnetically saturated region grows from the polar regions (see §4.3.2, Figure 4-5).
3. Large fields, where particle magnetisation completely saturates and the particles can be treated as a simple dipole of fixed strength.

Colloidal ferro-fluids are similar to MR fluids, however, differences in particle size and composition results in distinctions in their performance [Carlson and Jolly, 2000]. MR fluids similar to ferro-fluids have been created by BASF, with ferrite-based particles on the order of 30nm in diameter coated with long chain polymer molecules. These fluids are reported [Carlson and Jolly, 2000] to have good stability and abrasion properties. However, ferro-fluids exhibit an order of magnitude less yield strength than iron-based MR fluids – as a result of inferior magnetic properties of the ferrite and the predominance of thermal particle forces (see §4.1.2, equation [4–8]).

The larger yield strengths of MR fluids compared to ER fluids enables MR fluid devices to be substantially smaller than ER fluid devices capable of similar performance. Power requirements for ER and MR fluid devices are approximately equal for devices of comparable performance. The

difference [Carlson et al, 1996] is that the power supply for ER fluid devices must provide high voltage at low current, while the power supply for MR fluid devices generally provide higher current at a low voltage.

The performance of ER and MR fluids is compared below (see Table 4-1):

Property	ER Fluid	MR Fluid
Yield Strength (Field)	2 – 5 kPa (3 – 5 kV/mm) Electric field limited by break down	50 – 100 kPa (150 – 250 A/mm) Magnetic field limited by saturation
Viscosity (no field)	0.2 – 0.3 Pa-s at 25°C	0.2 – 0.3 Pa-s at 25°C
Operating temperature range	+10°C to +90°C (ionic, DC) -25°C to +125°C (non-ionic, AC)	-40°C to +150°C (limited by carrier fluid)
Current density	0.02 – 0.15mA/mm^2 (4kV/mm, 25°C) (x10 – x 100 at 90°C)	Not necessarily required. Can energise with permanent magnets
Density (gcm^{-3})	1 – 2.5	3 – 4
Constituent particle material	Any (conductive surface)	Iron / Steel

Table 4-1: Comparing ER and MR fluids (with reference to Carlson et al [1996])

Yield strength of MR fluids is limited by magnetic saturation, which compares favourably to ER fluids, which are generally limited by the electric field breakdown strength of the fluid [Carlson et al, 1996]. MR fluids are capable of operating over a temperature range of between -40°C and 150°C, with the range being limited by the properties of the carrier fluid. Since electro-chemistry does not influence the magneto-polarisation mechanism [Spencer et al, 1997], a wider range of additives (e.g., surfactants, dispersants, friction modifiers, anti-wear agents – see §4.2) can be added to the carrier fluid to make MR fluids with enhanced stability and increased seal and bearing life. According to Carlson et al [1996] dissipative currents and joule energy loss is not a concern for MR fluids – with permanent magnets able to activate MR fluids with no steady-state power requirement.

Since ER fluids depend on the movement of ions or electric charge, they are sensitive to temperature and to the presence of contaminants. According to Carlson et al [1996] low conductivity, DC, ER fluids polarised by an ionic conduction mechanism are capable of operating over a temperature range of between 10°C and 90°C. ER fluids require around 0.05mA/mm^2 in an electric field of 3kV/mm to

activate them. Non-ionic ER fluids are generally capable of operating over a broader temperature range of between -25°C and 125°C. Non-ionic fluids are often used with high-frequency AC fields (to minimise electrophoretic effects – detrimental to the electro-rheology of the fluid). To support this as much as 0.01-0.02mA/mm^2 at 3kV/mm (RMS) must be provided (due to relatively large device capacitance).

Non-linear conduction in ER fluids, particularly at high field-strengths, is identified [Rankin et al, 1998] as phenomena requiring better understanding of the physical chemistry of the fluid. Rankin et al [1998] also provided a review of information on ER fluid rheology, structure formation and constituent materials.

Despite much research into ER fluids and control of ER fluid devices, there are few commercial applications. Sims et al [1999] used commercially available ER fluid from Bayer (i.e., Rheobay 3565) in low frequency feedback control experiments. There has been greater commercial application of MR fluid research. BASF Group is a producer of carbonyl iron powders (see §4.2) and research has been carried out to engineer MR fluids. Rheonetic™ is the trade name given to MR fluid developed by Lord Corporation. A considerable amount of information is available on MR fluid from the Rheonetic™ section of the Lord Corporation web site (i.e., www.rheonetic.com).

4.1.2 Modelling MR fluid behaviour

The behaviour of controllable fluids is often [Carlson and Jolly, 2000; Zipser et al, 2001; Genç and Phulé, 2002] represented as a Bingham plastic (see equation [4–1]).

$$\tau = \tau_o + \eta\dot{\gamma} \qquad [4\text{-}1]$$

where, τ = total shear stress (Nm^{-2}); τ_o = yield stress (Nm^{-2}); $\dot{\gamma}$ = shear strain rate (s^{-1}); η is the dynamic viscosity (Pa s) – a temperature dependent constant of the fluid,

or, using a Herschel-Bulkley power law model [Wang and Gordaninejad, 2001; Yanyo, 2003]:

$$\tau = \tau_o + K\dot{\gamma}^n \qquad [4\text{-}2]$$

where, K = consistency (Pa s^n); n = power value index.

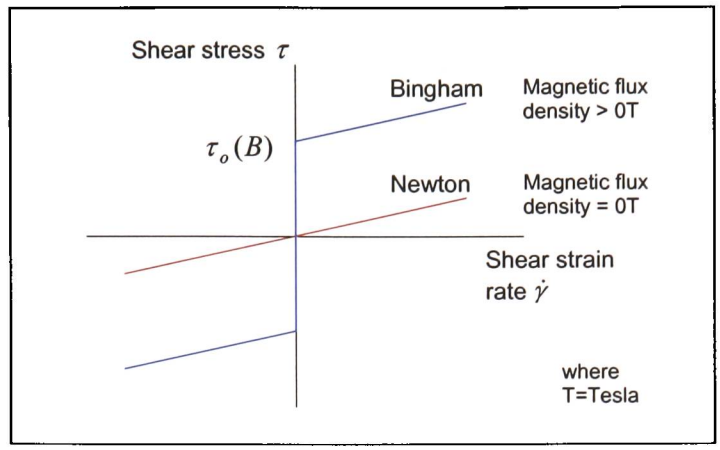

Figure 4-1: Graphical comparison of Bingham and Newton fluids (produced with reference to Zipser et al [2001] and Yang et al [2002])

In the Bingham plasticity model, the yield stress is dependent on the applied magnetic field (B), while the slope of the measured shear stress against shear strain rate defines the field-independent consistency (see Figure 4-1, comparing a Bingham plastic with a Newtonian fluid). Therefore, the Bingham model can be rewritten [Rankin et al, 1998; Zipser et al, 2001; Yang et al, 2002] to more accurately represent MR fluid behaviour:

$$\tau = \tau_o(B) + \eta\dot{\gamma} \cdot \qquad [4\text{-}3]$$

Since the yield stress in the Bingham model is field dependent, without a magnetic field MR fluid is therefore assumed to behave as a linear viscous liquid and is modelled as a Newtonian fluid:

i.e., $$\tau = \eta\dot{\gamma} \cdot \qquad [4\text{-}4]$$

The Herschel-Bulkley model simplifies similarly (i.e., to equation [4–4]) for the non-field condition.

Bingham plasticity can be represented [Spencer et al, 1997] as an idealised mechanical model comprising a Coulomb friction element in parallel with a viscous damper (see Figure 4-2).

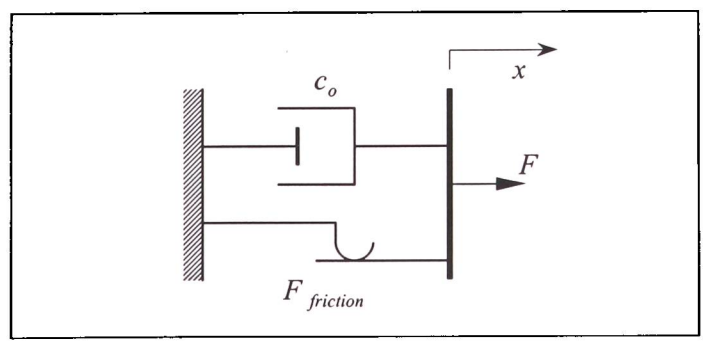

Figure 4-2: Mechanical representation of Bingham model (produced with reference to Spencer et al [1997])

However, according to Jolly et al [1999], while the Bingham plastic model has proved useful in the design and characterisation of MR fluid devices, the true behaviour of MR fluid exhibits some significant departures – particularly, the non-Newtonian behaviour of MR fluid in the absence of a magnetic field. Therefore, the MR fluid may be better represented by equations [4–5], [4–6] and [4–7].

Flow rate;
$$Q = \left(\frac{n}{3n+1}\right) \cdot \pi \cdot r^3 \cdot \left(\frac{r \cdot \Delta P}{2 \cdot l \cdot K}\right)^{\frac{1}{n}} \qquad [4\text{-}5]$$

Pressure drop;
$$\Delta P = \left(\frac{3n+1}{n}\right)^n \left(\frac{Q}{\pi \cdot r^3}\right)^n \cdot \left(\frac{2 \cdot l \cdot K}{r}\right) \qquad [4\text{-}6]$$

Wall shear rate;
$$\dot{\gamma}_w = \left(\frac{3n+1}{n}\right)\left(\frac{Q}{\pi \cdot r^3}\right) \qquad [4\text{-}7]$$

where, Q = flow rate (m^3s^{-1}); r = tube radius (m); ΔP = pressure drop (Pa); n = flow behaviour index; K = consistency (Pa s^n); l = tube length (m); $\dot{\gamma}_w$ = wall shear rate (s^{-1}).

Temperature sensitivity is considered by Carlson et al [1996] to be more significant for ER fluids than MR fluids. The mechanical properties of MR fluid are considered by Spencer et al [1997] to vary less than 10% in the range of -40°C and 150°C. However, research by Zipser et al [2001] indicated that MR fluid has a strong temperature dependency. Experimental investigations lead to a definition of a temperature dependent regression line.

$$\tau_o(B) = aB + bBT \qquad [4\text{-}8]$$

where, τ_o is the field dependent yield stress (where B is the flux density), decreasing proportional to the absolute temperature (T), with experimentally derived constants a and b dependent on the chemical composition of the MR fluid (particularly the carbonyl iron content by volume).

Thermal sensitivity of MR fluid has potentially significant implications for the adaptive ski. The thermal dependence of the MR fluid viscosity at low temperatures must be considered. Used in a damper, MR fluid is expected to dissipate energy that will result in an increase in fluid temperature. Applying the magnetic field will also increase the fluid temperature, with the activated electromagnet acting as a heating element. Therefore, unless the device is cooled, the MR fluid cannot be expected to remain at a constant temperature – resulting in changing viscoelastic properties and an increase in the complexity of the required control algorithm. Thermodynamics of MR fluid are not investigated here, but temperature increases are observed during operation of MR fluid devices. For successful development of the adaptive ski system, appraisal is recommended of MR fluid device performance with respect to temperature.

4.2 Composition of MR fluids

Typically, MR fluids comprise micron sized particles (i.e., between 0.1μm and 10μm) of hard and soft carbonyl iron particles (see Table 4-2) in a non-magnetic medium. Choosing a particle material [Carlson & Jolly, 2000] with high saturation magnetization (J_s) increases maximum interparticle attraction (i.e., maximising the magnetorheological effect). Iron has the highest saturation magnetization of known elements, with J_s=2.1Tesla. Alloys of iron and cobalt have slightly higher saturation magnetization (i.e., typically J_s=2.4Tesla) and have also been used in MR fluids.

BASF Group is a producer of carbonyl iron powders – obtained from the thermal decomposition of iron pentacarbonyl ($Fe(CO)_5$), which reacts to give iron (Fe) and carbon monoxide (CO) in an endothermic reaction when heated above its boiling product. Carbonyl iron particles have an onion-like structure grown around a central core. The mechanical hardness of the carbonyl iron particles is determined by the tension between the onion-like layers. Hard grades of carbonyl iron have a Vickers hardness of around 850 (Hv 0.025). Soft grades of carbonyl iron are produced by reduction with hydrogen, which destroys the onion-like layer structure of the mechanically hard particles and reduces its carbon, nitrogen and oxygen content. Carbon content is an indicator of the degree of reduction:

Secondary constituents of BASF carbonyl iron powders		
Constituents	Hard grades	Soft grades
Carbon	0.7 - 0.8 %	0.005 - 0.05 %
Nitrogen	0.7 - 1.0 %	0.01 % max.
Oxygen	0.2 - 0.3 %	0.2% max.

Table 4-2: Secondary constituents of carbonyl iron powders

An image (see Figure 4-3) taken with a scanning electron microscope (SEM) shows the particles in a sample of water based MR fluid after the carrier liquid has been evaporated from the sample. The larger spheres are hard carbonyl iron (3μm<Ø<6μm) and the smaller particles are soft carbonyl iron (0.8μm<Ø<3μm). Further details about MR fluid composition are presented later (see §4.2.1), with emphasis on the carrier fluid chemistry.

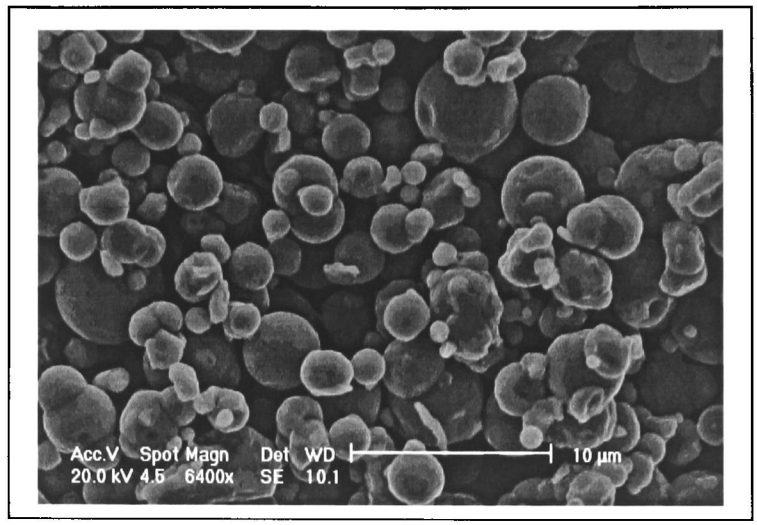

Figure 4-3: SEM image – carbonyl iron particles from water based MR fluid

The broad particle size distribution observed here (see Figure 4-3) is supported by SEM work carried out by Genç and Phulé [2002]. A SEM image of the alignment of particles in an applied magnetic field is presented by Jolly et al [1996].

The composition of some early MR fluids, developed by Rabinow and Winslow, has been described earlier (see §4.1). Commercially viable MR fluids must overcome concerns of settling (where the fluid stratifies and the particles separate from the carrier fluid - see §4.2.1) and "In-Use-Thickening" (IUT, as described by Carlson [2001] - see §4.2.2).

Typical carrier fluids include [Carlson & Jolly, 2000]: petroleum based oils, silicone, mineral oils, polyesters, polyethers, water, and synthetic hydrocarbon oils. There are a number of benefits associated with water based MR fluids [Jolly et al, 1999]. Water based MR fluids are more compatible for use with natural rubber diaphragms than hydrocarbon oil based fluids. Also, the wide choice of water-soluble stabilisers and surfactants, can enable water based MR fluids to be more stable and less viscous (i.e., exhibiting a lower off-state potential). However, water based fluids have a limited temperature range and may only be used in a completely sealed system to prevent evaporation.

Engineering MR fluid with high yield strength in the on-state (when the device is activated) should not mean sacrificing a low off-state viscosity. The range (i.e., the difference between the on-state and the off-state) of the fluid makes it attractive for use in semi-active vibration control devices. It is important that additives do not adversely affect the off-state viscosity and therefore the operating range of the MR fluid for a particular application.

4.2.1 Non-settling

Settling in MR fluids is dictated by the rheology of the suspending medium and the surface properties of the magnetic particles – plus any additional surface active agents. Settling can be further influenced by the presence of remnant fields, device operating temperature and other environmental factors to which the MR fluid is subjected. Experimental work by Jolly et al [1999] showed that higher viscosity MR fluids exhibit a lower initial settling rate. Therefore, higher viscosity fluids are more able to hold the micron-sized particles in suspension.

Examples of additives that can be added to inhibit sedimentation and agglomeration [Carlson & Jolly, 2000] include thixotropic agents and surfactants such as xantham gum, silica gel, stearates and carboxylic acids. The thixotropic network disrupts flow at very low shear rates, but thins as the shear rate is increased. Stearates form a network of swollen strands when used in conjunction with mineral oil and synthetic esters – trapping and immobilising particles.

An alternative to overcoming sedimentation with an increase in the viscosity of the carrier fluid is included in a review by Rankin et al [1998]. MR fluid stability can also be improved by reducing the particle size (i.e., to ~30nm) so that the particles can be "held" by a less viscous carrier fluid. Tests of MR fluid with sub-micron sized particles seem to indicate good long-term stability (with Brownian motion in the absence of a field – a characteristic associated with ferro-fluids).

The practical significance of sedimentation is queried, with Carlson [2001] describing the effect of the piston moving in a MR fluid filled damper - suggesting that stroking the damper is enough to overcome fluid settling. The movement of the piston inside the cylinder (with larger inside diameter than the piston diameter) causes the MR fluid to jet through the orifice (resulting from the difference in piston and cylinder diameters). Even at low piston speeds, the fluid jet produces swirl and eddies in the non-active region of the cylinder. Therefore it is claimed that normal motion of the MR fluid device is sufficient to generate flow that is able to remix any stratified MR fluid. As an example, two or three strokes (of the MotionMaster ^{TM} RD-1005 MR fluid damper, from Lord Corporation) is said to be sufficient to remix the fluid after months of inactivity.

4.2.2 In-Use-Thickening (IUT)

In-use-thickening (IUT) describes [Carlson, 2001] what happens to MR fluids subjected to high stress and shear rate over a period of time – resulting in thickening of the fluid. An increase in the off-state viscosity is symptomatic of IUT and results from spalling of the surface layer of the carbonyl iron particles that comprise the MR fluid.

Carbonyl iron particles (see §4.2) have a brittle surface layer (of iron oxides, carbides and nitrides) that fractures, breaks and separates when subjected to high inter-particle stresses. The resulting nanometer-sized secondary particles have a large surface area to weight ratio – capable of significantly affecting the overall rheology of the MR fluid.

The IUT problem was not identified until long-term life testing was undertaken on commercial MR fluid truck seat dampers (developed by Lord Corporation). MR fluid deterioration depends on:

1. Shear rate
2. Temperature
3. Duration

The lifetime dissipated energy (LDE, [Carlson, 2001]) can be used to estimate the expected life of an MR fluid, with respect to the instantaneous mechanical power (being converted to heat) per unit volume of fluid, over the life of the fluid.

$$\text{LDE} = \frac{1}{V}\int_0^{life} P \cdot dt \qquad [4\text{-}9]$$

where, V = volume (m^3); P = power (Watts); t = time (s).

4.3 MR fluid device design

Rotary brakes and linear vibration dampers employing MR fluid technology have found a number of commercial applications [Chrzan & Carlson, 2001]. A MR fluid rotary brake has been integrated into exercise equipment (e.g., aerobic stair-climbers and cycling machines) to provide computer controlled variable resistance. The MR fluid brake originally designed for Nautilus exercise equipment has since been incorporated in a satellite to study the Aurora Borealis on behalf of NASA. The MR fluid brake and a feedback control system are used in the deployment of wire antennas (2 x 7m) from rotary drums.

A potentially large volume, though cost sensitive [Chrzan & Carlson, 2001] application for MR fluid rotary brakes is force-feedback (haptic) input devices for computers (e.g., joysticks, steering wheels and mice). A steer-by-wire system for electric forklifts (engineered by Linde) is an example [Carlson, 2003] of MR fluid rotary brakes being used in an industrial haptics application. The MR brake provides real-time force feedback to the operator, with resistance varying as a function of wheel orientation and vehicle speed. Such a system may also be applied in simulators (e.g., industrial, medical, military).

MR fluid shock absorbers (from Bostrom seating and Lord Corporation) were first used for truck-seat damping in 1998. Adjustable shock absorbers using MR fluid (i.e., the MagneShock system from

Carrera) were introduced in 1999 for stock car and drag race vehicles, with further automotive applications of MR fluid following. The use of MR fluid in semi-active seismic dampers is investigated by Yang et al [2002] and this application is the motivation for the modelling of MR fluid devices carried out by Spencer et al [1997].

The role of the MR fluid device (e.g., damper, clutch, or brake) should lead to a decision on the required operational mode, followed by some estimates of device specification to meet the desired performance output. Detailed design considerations, such as seal specification, may be used to refine a device for a particular application. Design of the electromagnet that applies the magnetic field and the control system that controls the power-supply to the electromagnet are individually as (if not more) important as the design of the MR fluid device. The development of a MR fluid system ultimately requires a multidisciplinary engineering skills-set.

Significant costs associated with MR fluid devices include [Chrzan and Carlson, 2001]: seals, shaft surface finish, precision mechanical tolerances, electromagnet assembly, control electronics and volume of MR fluid. The diaphragm sealed damper developed here (see §4.4.2) overcomes many of these costs by negating the requirement for a shaft to pass through a seal.

4.3.1 Axis-symmetric damper

The cross-section of a relatively conventional axis-symmetric MR fluid linear damper is illustrated (see Figure 4-4). The damper comprises an outer cylinder (1) and inner shaft with an electromagnet (2) mounted on it. The electromagnet (2) generates a magnetic field that is applied to an annular control volume of MR fluid. The annular control volume completes a magnetic circuit between the piston-like ends (3) of the electromagnet and a steel sleeve (4) that provides a return path for the magnetic flux (5). The electromagnet is mounted on the shaft and moves relative to the outer cylinder. Wires supplying power to the electromagnet may be contained inside the shaft (6). MR fluid surrounds (7) the electromagnet and shaft and is contained inside the cylinder by sliding seals (8). An accumulator (10) allows for thermal expansion of the fluid and [Spencer et al, 1997] helps prevent cavitation in the fluid during operation.

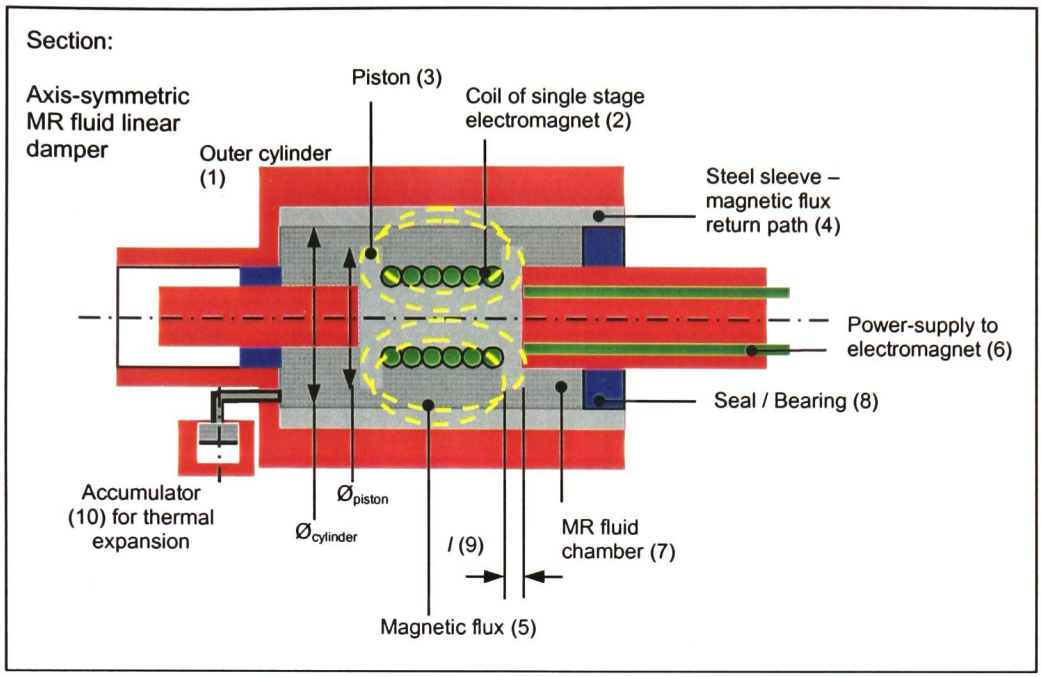

Figure 4-4: Axis-symmetric MR fluid linear damper

As the inner shaft and electromagnet move inside the cylinder, MR fluid is forced through the annular region between the electromagnet and steel sleeve. Although there is shear mode (i.e., with moving poles) associated with the movement of the piston relative to the sleeve, valve mode (i.e., with fixed poles and particle alignment perpendicular to pressure driven flow) is the primary control mode (see §4.3.2). The fluid dynamics that result from moving the electromagnet overcome [Carlson, 2001] any settling of the particles inside the MR fluid (see §4.2.1).

Applying a magnetic field produces an apparent change in the viscosity of the MR fluid in the control region of the annular volume. The apparent change in viscosity is the result of spherical carbonyl iron particles aligning along magnetic field lines - trapping fluid and restricting flow around the electromagnet through the annular region. The MR fluid in the control region acts like a valve controlled by the electromagnet.

The relationship between controllable force and dynamic range (i.e., the difference between the maximum on-state and off-state resistive force) is discussed by Yang et al [2002]. The controllable force range is inversely proportional to gap size (i.e., between the piston and inside of the steel cylinder). A small gap size equates to a large controllable (on-state) force. However, a small gap size decreases the dynamic range, by increasing the off-state resistive force (i.e., the minimum force that must be applied to move the damper). The dynamic range of the damper must be compatible

with the operating range of the ski. This implies a large gap width is required to accommodate a low off-state force.

4.3.2 Operational modes

There are a number of defined operational (stress) modes [Carlson et al, 1996; Jolly et al, 1999; Zipser et al, 2001] that classify the design of controllable fluid devices:

1. Direct-shear mode – with relatively moveable poles; has been developed for a variety of applications – e.g., clutches, brakes, chucking, locking devices (see Figure 4-5 a).
2. Valve or pressure driven flow mode – with fixed poles; has been developed for a variety of applications, such as servo-valves, dampers, and shock absorbers (see Figure 4-5 b).
3. Squeeze mode – where the poles move parallel to the magnetic field, acting against aligned columns of particles, considered suitable for vibration dampers of mounts where there are small motions and high forces (see Figure 4-5 c).
4. Combinations of the above modes.

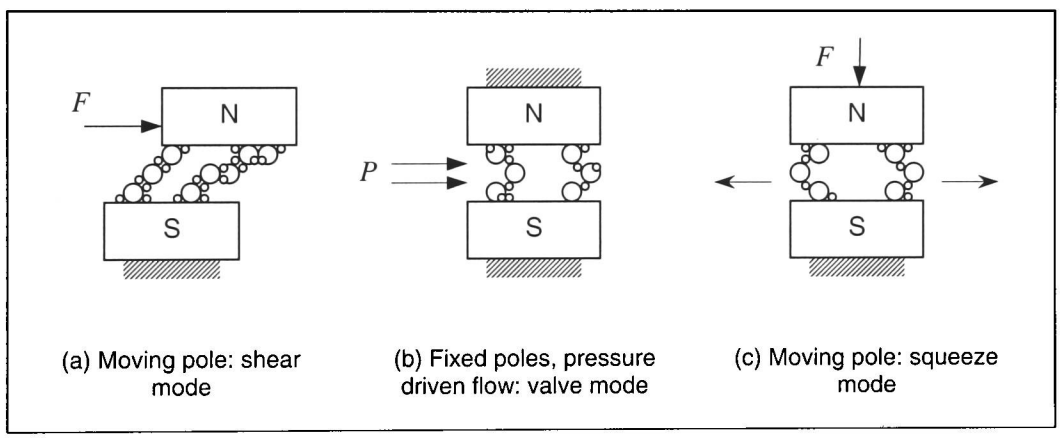

Figure 4-5: Operational modes with MR fluid particle alignment in presence of magnetic field

In the shear mode, the off-state viscous component can be defined [Carlson et al, 1996] with respect the apparent fluid viscosity (see equation [4–10], while the on-state can be defined with respect to the field induced shear stress (see equation [4–11].

Viscous force: $$F_\eta = \frac{\eta \cdot S \cdot l \cdot w}{g} \quad [4\text{-}10]$$

Shear force: $$F_\tau = \tau \cdot l \cdot w \quad [4\text{-}11]$$

where, η is the apparent fluid viscosity; τ is the field induced shear stress; S is the speed of one pole relative to the other; l is the duct length (m); g is the annular gap (m) and w the annular width (m).

From [4–10] and [4–11], the minimum fluid volume ($V_{\min} = l \cdot w \cdot g$) can be derived:

i.e., $$V_{\min} = \left(\frac{\eta}{\tau^2}\right)\left(\frac{F_\tau}{F_\eta}\right) \cdot F_\tau \cdot S \cdot \qquad [4\text{-}12]$$

In the valve mode (predominant in the axis-symmetric device – see Figure 4-4), the off-state viscous component can be defined [Carlson et al, 1996] with respect the apparent fluid viscosity (see equation [4–13]. The on-state of the MR fluid can be defined with respect to the field induced shear stress (see equation [4–14].

Viscous component: $$\Delta P_\eta = \frac{12 \cdot \eta \cdot Q \cdot l}{g^3 \cdot w} \qquad [4\text{-}13]$$

where, ΔP is the pressure drop (Nm^{-2}); η is the apparent fluid viscosity (Pa s); Q is the flow rate (m^3s^{-1}); l is the duct length (m); g is the annular gap (m) and w the annular width (m).

Shear component: $$\Delta P_\tau = \frac{c \cdot \tau \cdot l}{g} \qquad [4\text{-}14]$$

where, τ is the field induced shear stress (Nm^{-2}) and $c \equiv 2$ = constant for MR fluid.

From [4–13] and [4–14], the minimum fluid volume ($V_{\min} = l \cdot w \cdot g$) can be derived:

i.e., $$V_{\min} = \frac{12}{c^2}\left(\frac{\eta}{\tau^2}\right)\left(\frac{\Delta P_\tau}{\Delta P_\eta}\right) \cdot Q \cdot \Delta P_\tau \cdot \qquad [4\text{-}15]$$

The resisting force of the axis-symmetric MR fluid damper (see Figure 4-4, §4.3.1) can be broken-down [Yang et al, 2002] into a controllable, field induced, on-state shear component and an uncontrollable, off-state viscous and friction component (see Figure 4-6).

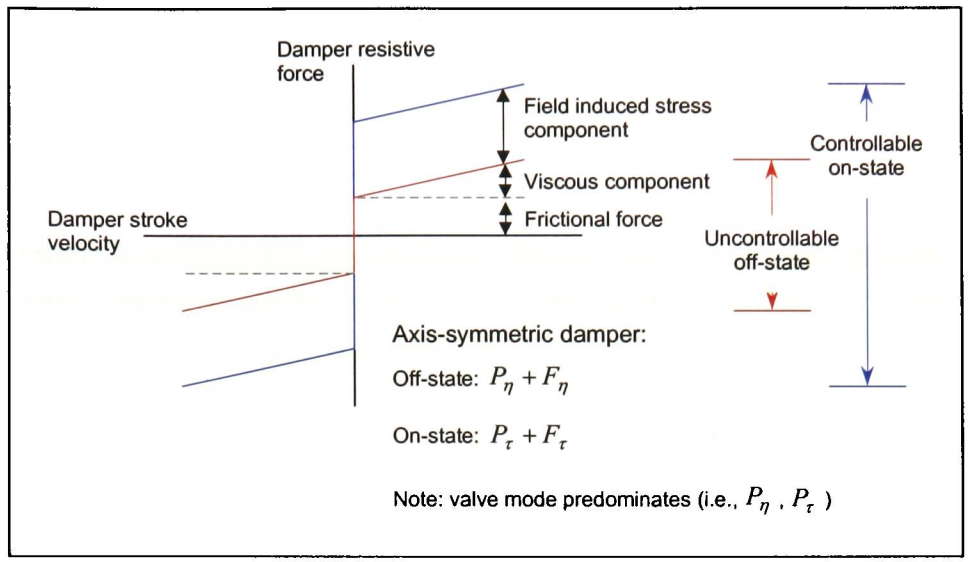

Figure 4-6: Decomposition of resisting force of axis-symmetric MR fluid damper (produced with reference to Yang et al [2002])

The valve mode predominates in the axis-symmetric damper (i.e., there is greater force control provided by ΔP_τ than ΔF_τ). Therefore, for a greater on state, the valve mode should be optimised. Also, to achieve a high on-state capability, the annular gap should be small. However, to be compatible with the operating range of the ski, a low off-state force is required and the gap must be increased (at the expense of the on-state capability).

4.3.3 Seal specification

Sealing MR fluid inside a device requires practical consideration and understanding of the consequences with respect to the operating bandwidth (i.e., the difference between the on-state and off-state forces and the required stroke velocity). Compared with hydraulic fluids, MR fluid is inherently abrasive because of the particle content.

As an example, consider sealing MR fluid in a relatively conventional cylinder damper with a piston moving inside a cylinder (see Figure 4-4). The shaft of the piston must be hard enough to resist MR fluid particles becoming embedded on its surface and dragged through the sliding seal. To further ensure particles are not dragged through the seal, the shaft of the piston is often polished to reduce the tendency for the particles in the MR fluid to embed in the surface of the shaft. The seal may additionally incorporate a wiper to remove fluid from the shaft as the piston is withdrawn from the cylinder. Critically, the friction between the seal and shaft often results in a raised off-state force (i.e., the off-state force becomes the minimum force required to overcome seal friction).

An alternative to a dynamic, sliding seal may be considered for small amplitude reciprocating devices (such as dampers). Elastomeric rubber diaphragm seals [Carlson et al, 1996; Jolly et al, 1999] may be employed on small stroke damper devices with a view to maintaining an off-state force that is the minimum force required to overcome the MR fluid viscosity (with no magnetic field applied).

A diaphragm sealed damper overcomes evaporation concerns associated with water based MR fluids – presenting a number of benefits (see §4.4.2). A further opportunity [Carlson et al, 1996] is the possibility for stiffness to be added to the elastomeric elements (i.e., the diaphragm seals), so that the damper may act as a controllable mount.

4.3.4 Low cost solutions

Damping of washing machines using a MR fluid sponge (i.e., an open-celled, polyurethane (PU) foam saturated with MR fluid) damper is presented by Chrzan and Carlson [2001] as an example of how low-cost semi-active vibration control can be successfully achieved with MR fluid systems. Low-cost, controllable MR sponge dampers are said to be appropriate for moderate-force vibration control applications.

MR fluid foam devices [Carlson and Jolly, 2000] constrain MR fluid by capillary action in an absorbent matrix (e.g., felt, fabric, sponge, or open-celled foam). The absorbent matrix keeps the MR fluid located in the active control region (i.e., where the magnetic field is applied) – therefore, requiring a minimum volume of MR fluid that operates in the direct shear mode. There is no need for seals, bearings or precision mechanical tolerances (considered by Chrzan and Carlson [2001] to be significant costs associated with MR fluid devices) and MR fluid foam devices may be applied in both linear and rotary devices.

However, degradation of the absorbent matrix presents a problem and an obstacle to commercial acceptance. Consider a relatively simple MR fluid "sponge" damper, with PU foam surrounding an electromagnetic coil wound around a steel core that forms a piston located at the end of a shaft inside a steel cylinder. As power to the electromagnet is applied, the shear forces increase between the MR fluid soaked PU foam and steel cylinder with applied magnetic field. Stroking the damper (i.e., moving the piston in and out of the cylinder) may cause the MR fluid soaked foam to wear (depending on stroke, stroke-rate and applied magnetic field).

Research by Chrzan and Carlson [2001] does not accept that there is significant wear of the sponge. They claim that the stresses are primarily carried by the iron particle structure established within the MR fluid and that performance is not significantly affected as long as the sponge is able to hold the

MR fluid in the working gap. Data from fatigue tests on a MR fluid sponge damper are used to support the claims. Subjected to a 20mm stroke at 2Hz with the magnetic field applied for 5 seconds every 30 seconds, the MR fluid sponge damper maintains an on-state damping force in excess of 60N after two million cycles. This corresponds to a reduction in performance of approximately 9% after one million cycles and 22% after one and a half million cycles (assuming an initial on-state damping force of 85N).

However, a further complication is the potential for the electromagnet to ignite the sponge from heat generated by the electromagnet. Therefore, the thermodynamics of the device need to be considered.

An alternative low cost solution may be realised with the development of MR elastomers [Rankin et al, 1998] comprising silicone gels filled with carbonyl iron particles. MR fluid elastomers, applying the squeeze mode, are considered suitable for use in tuneable mounts, bushings, or vibration absorbers. MR fluid elastomers may be applied to the adaptive ski, but the lack of commercial availability has excluded MR fluid elastomers from this investigation.

4.3.5 Electromagnet design considerations

The objective of magnetic circuit design for MR fluid devices [Carlson, 2003, lecture 4], is to guide and focus magnetic flux onto MR fluid in a control volume (i.e., the volume in the gap that comprises the MR valve). This work does not focus on sophisticated electromagnet design, nevertheless an understanding of the fundamentals is required to be able to produce working MR fluid devices.

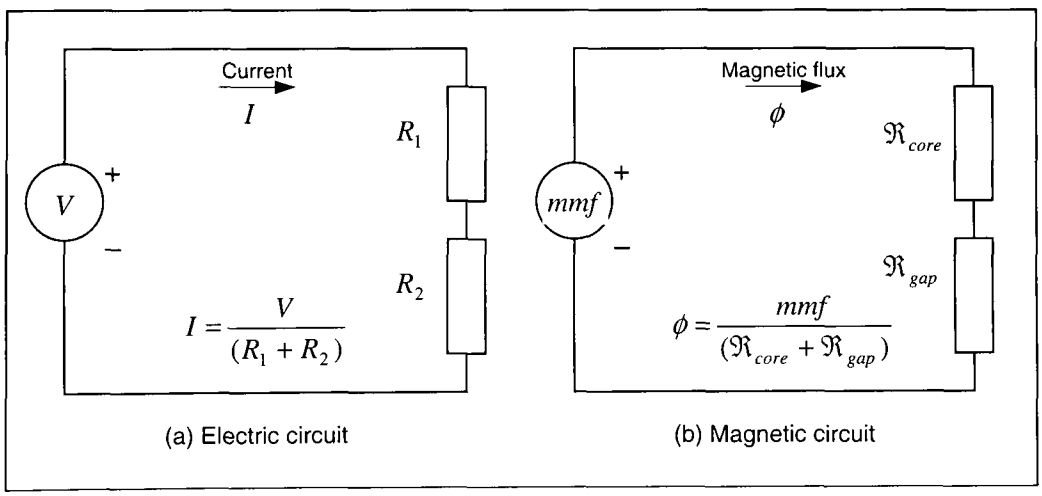

Figure 4-7: Electric: magnetic circuit analogues (produced with reference to Fitzgerald et al [2003])

The basic tools for analysis of magnetic field systems, relevant to MR fluid device design, are presented here - with reference to Fitzgerald et al [2003]. The relationships in magnetic circuits are

analogous to those in electric circuits (see Figure 4-7). The relationship between electric current and magnetic field can be described with reference to Maxwell's equations and Ampere's law:

$$I = \oint H \cdot dl \qquad [4\text{-}16]$$

or,

$$\frac{I}{2 \cdot \pi \cdot r} = H \qquad [4\text{-}17]$$

where, H = magnetic field intensity (Am^{-1}); I = current (A); l = length (m); r = radius (m) of the wire.

The magnetic field in the core is the ampere-turn product - i.e., the magnetomotive force:

$$mmf = N \cdot I \qquad [4\text{-}18]$$

where, mmf = magnetomotive force (Amp-turns); N = number of turns of coil on the electromagnet; I = current (A).

Losses in the coil of the electromagnet used to activate MR fluid will vary depending on the specification of the coil and how it is wound (i.e., the type of wire, gauge and coil geometry).

Magnetic flux density;

$$B = \mu \cdot H \qquad [4\text{-}19]$$

where, B = magnetic flux density (Tesla); μ_o = permeability of free space ($4\pi \times 10^{-7}\ Hm^{-1}$); μ_r = relative permeability; $\mu = \mu_o \cdot \mu_r$ (where μ the permeability and is between 7 and 8 for MR fluid).

Note: magnetic field intensity (H / Am^{-1}) depends on current and is independent of the medium, while magnetic flux density (B / Tesla) depends on properties of the medium. Low carbon steels (i.e., with a carbon content < 0.15%) have a higher magnetic permeability. Grades of steel suitable for manufacturing the electromagnetic core and flux pathway include AISI-12L14 (an alloy with lead) and AISA-12T14 (an alloy with tin).

Magnetic flux;

$$\phi = \int_S B \cdot dS \qquad [4\text{-}20]$$

or,

$$\phi = B \cdot A \qquad [4\text{-}21]$$

where, ϕ = magnetic flux (weber); A = cross-section area (m^{-2}).

Note: magnetic flux is continuous around a loop.

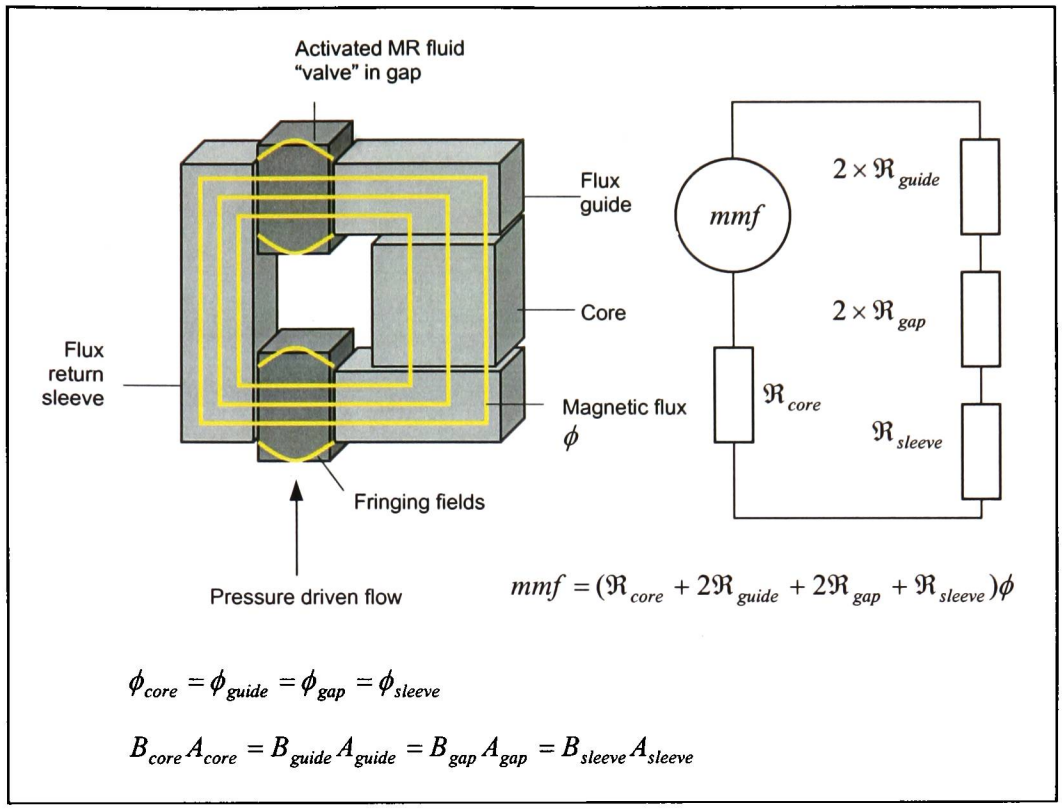

Figure 4-8: Equivalent magnetic circuit for axis-symmetric MR fluid device

The theoretical magnetic performance of a MR fluid device can be calculated by considering an equivalent magnetic circuit (e.g., see Figure 4-8 for an axis-symmetric device, as illustrated in Figure 4-4). It is important that there is sufficient cross section of steel in the core to generate the required magnetic field and that the cross-section in the guide and return sleeve does not restrict the magnetic flux.

The MR fluid within a device may represent the largest magnetic reluctance within the magnetic circuit.

Reluctance; $$\Re = \frac{mmf}{\phi} = \frac{N \cdot I}{\phi}. \qquad [4\text{-}22]$$

The response time (measured in milliseconds) of MR fluid devices can be quantified [Spencer et al, 1997] from the ratio of magnetic inductance of the MR filled gap (L_{gap}) and the resistance of the electromagnetic coil (R_{EM}):

i.e., MR fluid response time constant is $$\frac{L_{gap}}{R_{EM}} \qquad [4\text{-}23]$$

where,

$$L_{gap} = \frac{N\phi}{I} \qquad [4\text{-}24]$$

Stanway [2002] recommends the formal design of electromagnets for MR dampers, specifically the need to minimise time lag associated with the inductive circuit. Also recommended is the design of multiple electrode arrangements, the shaping of electrodes and the use of novel materials.

4.3.6 Semi-active vibration control

Vibration control techniques can be categorised as passive, semi-active and active, with MR fluid damping providing a semi-active control capability. Conventionally, passive systems have a fixed control capability that may not be optimal when the system or operating condition changes. Active systems can adapt for system variations, with actuators providing force or torque control based on feedback measurements from integrated sensors. Semi-active systems are considered [Spencer et al, 1997] those that allow real-time adjustment, but do not input energy– the distinguishing difference between semi-active and active systems. Semi-active systems suppress vibration with passive energy dissipation mechanisms and are considered more stable (according to Oh and Onoda [2002]) and more power efficient (according to Liao and Lai [2002]) than active systems.

The disadvantages of passive vibration control of helicopter main rotors are identified by Gandhi et al [2001], as the motivation for their investigation of semi-active MR fluid damping based on a linear feedback control law. Fixed damping that may be required for a limited fraction of the flight regime produces excessively large periodic loads over other portions of the flight regime – decreasing component fatigue life. Semi-active MR fluid damping is considered as a method to produce the required level of damping without an increase in periodic loads.

Delphi Automotive Systems has developed a linear semi-active, MR fluid primary suspension system (i.e., MagneRide) for General Motors [Stanway, 2002; Carlson, 2003]. The system has been introduced as standard equipment on the 2002 Cadillac Seville (STS), 50th anniversary Chevrolet Corvette and 2003 Cadillac SRX Sports Utility Vehicle and XLR Roadster.

The success of semi-active vibration control for automotive applications is relevant to the development of the adaptive ski system. The capability of achieving complex vibration control with a MR fluid system is demonstrated. The control algorithm for achieving semi-active damping of car suspension systems may be applicable to the adaptive ski.

The control necessary to support a MR fluid device depends to a large extent on the application. Often, the control system and algorithms are specific to the application, with some being considerably

more complex than others. Generally, the controller is an interface between the power supply to the MR fluid device and transducers that monitor one or more environmental aspects of the system. The power supply to the electromagnet is controlled (normally current controlled for faster response times) so that the MR fluid device is made to act based on some sensory input (e.g., semi-active vibration control of a structural element based on monitored vibration – the premise behind the adaptive ski concept).

Gandhi et al [2001] investigated linear feedback control of MR fluid dampers for stability augmentation of helicopter rotor blades, based on an assumed damper model (i.e., where damper force is the product of the damper stroke velocity and an equivalent linear viscous damping coefficient). The results of the study indicated that despite the simplicity of the MR fluid damper model, it is possible to achieve good damping stability.

Better control can be achieved with clearer understanding of MR fluid behaviour (see §4.1.2) and characterisation of the MR fluid device. MR fluid devices can be represented as mechanical models (see §2.1.3.2), with parameters that define response with regard to displacement, velocity and magnetic field. A phenomenological model of a MR fluid damper has been described by Spencer et al [1997], based on a Bouc-Wen hysteresis model (see Figure 4-9).

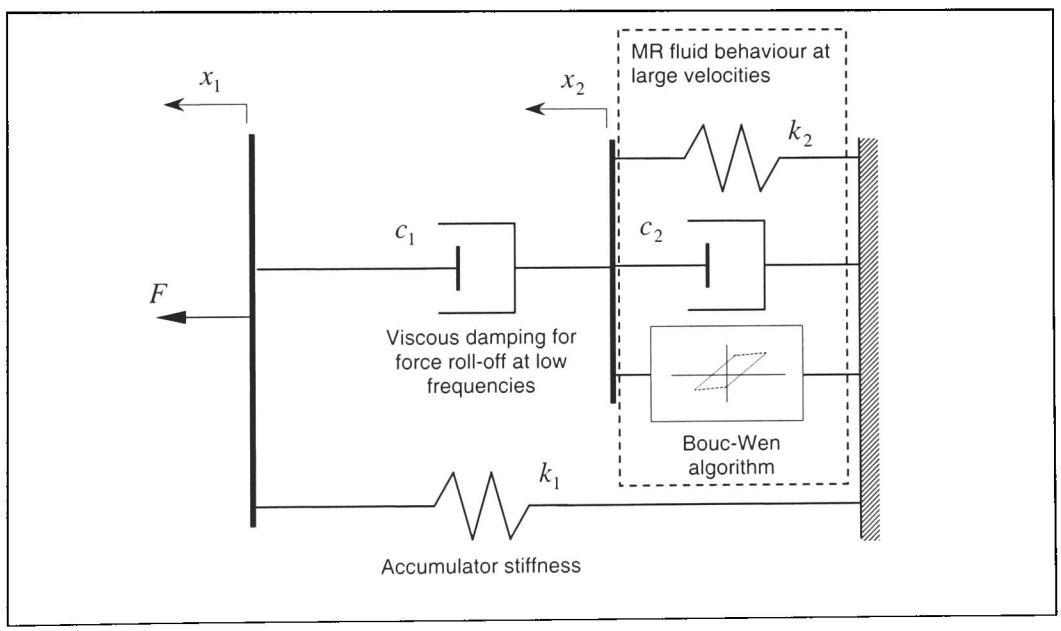

Figure 4-9: Mechanical model of MR fluid damper behaviour [Spencer et al, 1997]

Comparison of measured response and that predicted using the Bouc-Wen model shows a good correlation of the force-displacement behaviour and a close resemblance of the force-velocity behaviour (with divergence at low velocities). The Bouc-Wen model was considered [Spencer et al,

1997] effective for control algorithm development and system evaluation and was used [Yang et al, 2002] to model the behaviour of a large-scale (20-ton) seismic MR fluid damper.

4.4 MR fluid damping

Initial tests with a MR fluid dashpot damper (see §4.4.1) investigates damping as a percentage of vibration amplitude with increasing power to the electromagnet. Tests are carried out to quantify on-state and off-state performance without having to address practical issues - such as sealing, which is likely to compromise the off-state. The MR fluid dashpot damper is scaled down to demonstrate the adaptive ski concept: controlling fore-body vibration relative to a raised shim on a ski-like structure (see §5.2).

Tests of a prototype diaphragm sealed, fixed coil, MR fluid damper (see §4.4.2) seek to quantify the energy absorbed by the damper and assess its performance, with suggestions for modifications prior to any subsequent test and appraisal. Performance analysis of the prototype damper is made with reference to work by Oh and Onoda [2001], and Liao and Lai [2002]. Oh and Onoda [2001] investigated the performance characteristics of a bellows sealed, valve mode, MR fluid damper. Liao and Lai [2002] investigated the energy dissipated and equivalent damping coefficient of a commercially available valve mode MR fluid damper, in terms of input voltage, displacement amplitude and frequency.

The rheology of the MR fluid is controlled by the magnetic field, however, results are consistently presented with respect to the power supplied to the electromagnet (that generates the magnetic field). Ultimately the device will be current controlled – although, without the electronic hardware to support current control, voltage control is used in this work to ensure the electromagnet stabilises. Therefore, because the power supply has more practical significance it is referred to. It would be advantageous to measure the magnetic field generated by the electromagnet (e.g., with a Gauss meter) and calculate its efficiency with respect to the theoretical value.

4.4.1 Dash-pot damper

A simply supported vibrating beam is used for initial tests of a MR fluid dashpot damper (see Figure 4-10) filled with oil based Rheonetic MRF-132LD (from Lord Corporation). An unbalanced rotor is mounted at the mid-point of a simply supported steel beam (see appendix A-1 for dynamic analysis). Resonance of the beam may be observed by altering the rotation speed of the unbalanced rotor. The MR fluid dashpot damper is located under the steel beam and vibration amplitude is measured with respect to the power supplied to the electromagnet.

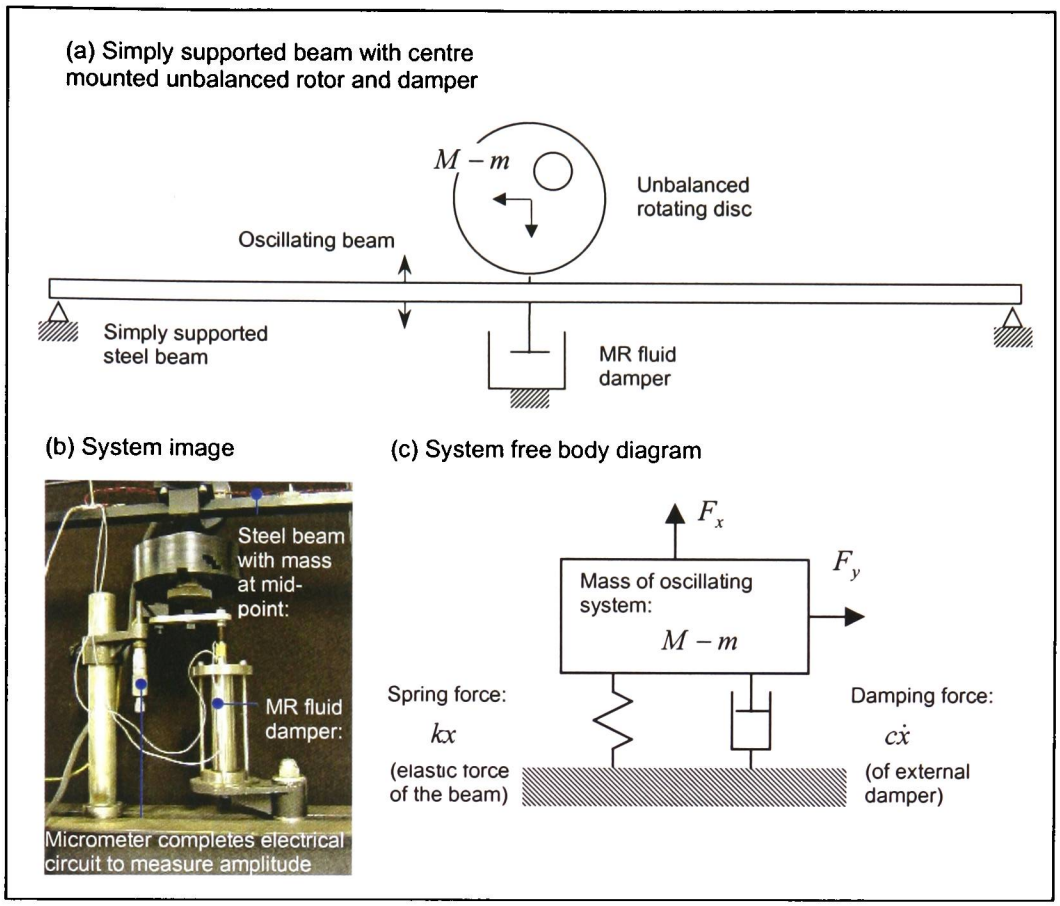

Figure 4-10: Simply supported oscillating beam: MR fluid damping of single degree of freedom system

As the steel beam vibrates, the electromagnet at the end of the input shaft moves inside the cylinder containing the MR fluid (see Figure 4-11). The magnetic flux pathway between the electromagnet and steel cylinder is illustrated (see Figure 4-12) and shows that there are effectively two annular control volumes of MR fluid between the cylinder and electromagnet (i.e., at the top and bottom of the electromagnet). These control volumes act like valves (see §4.3.2 on operational modes) when the electromagnet is activated – resisting flow around the electromagnet as the carbonyl iron particles in the control volume align. Therefore, the dash-pot is applying the pressure driven flow (or valve) mode of MR fluid – common with most MR fluid dampers.

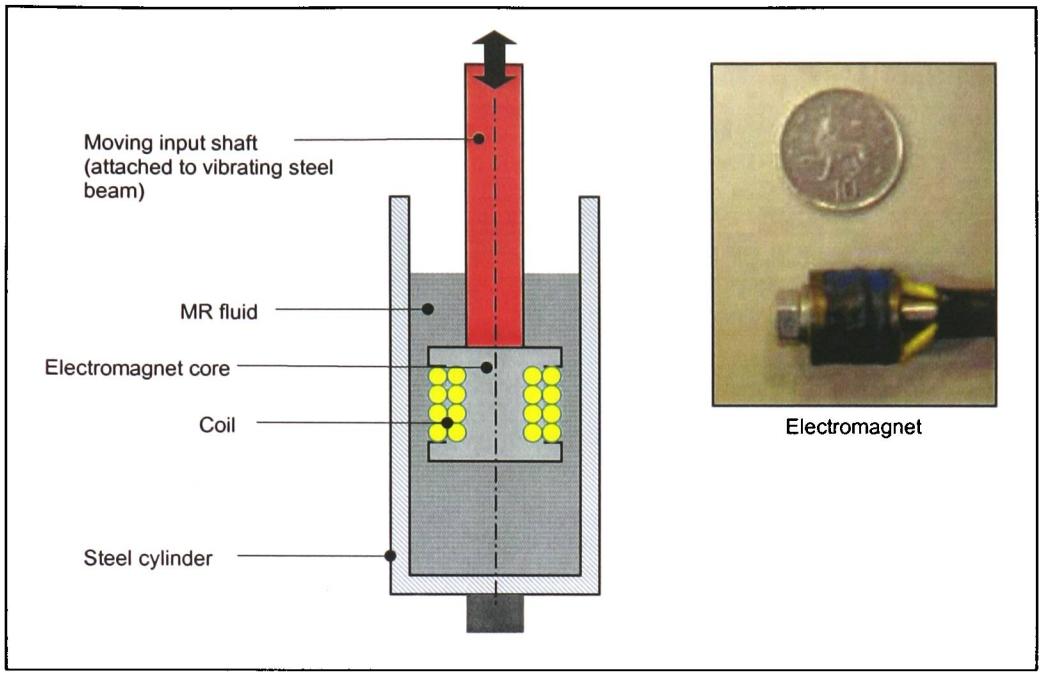

Figure 4-11: MR fluid dash-pot damper

The electromagnet (see Figure 4-12) has approximately 600 turns of 0.2mm copper wire, wound on a 10mm diameter mild steel bobbin over a 10mm length. The piston-like ends have an 18mm diameter and are 3mm thick. The inside diameter of the steel cylinder is 21mm, therefore the annular gap width is 2mm. The outside diameter of the cylinder is approximately 25mm.

The performance of the electromagnet is not a focus in this work, although there is a practical interest in understanding the expected power requirement of the device. Techniques for calculating theoretical performance of the electromagnet are presented (see Figure 4-12 and §4.3.5). Measurements of magnetic field are recommended in future work, to understand the actual efficiency of the electromagnet.

Annular magnetic model:

Core field intensity:

$$H_{core} = \frac{mmf}{2\pi r_{av.}}$$

where,

$r_{av.}$ = average coil radius
= 14 mm

$mmf = NI$
$= 600I$

Magnetic flux density:

$$B_{core} = \mu_o \mu_s H_{core}$$

and magnetic flux in core:

$$\phi_{core} = B_{core} A_{core}$$

where,

μ_s = relative permeability of steel core

A_{core} = equivalent annular cross-section of core
$= \pi \cdot d^2_{coil}$
$= \pi(10)^2$ mm.

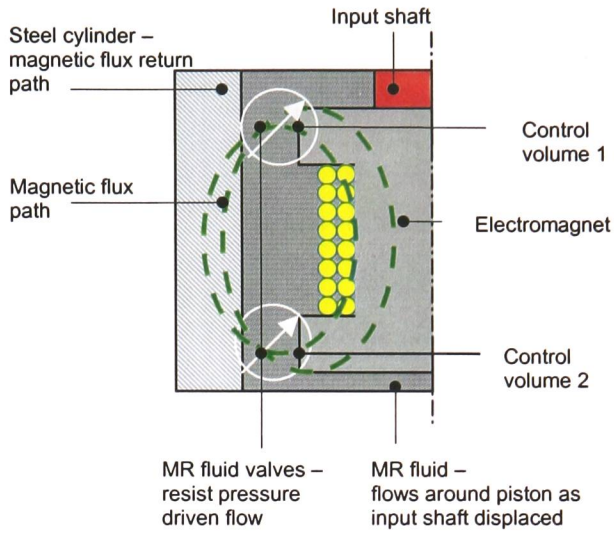

Magnetic flux of MR fluid in annular control region:

$$\phi_{gap} = B_{gap} A_{gap}$$

where A_{gap} = equivalent annular cross-section of gap
$= 2\pi \cdot r_{piston} \cdot l_{piston}$
$= 2\pi(9) \cdot (3)$ mm.

and $B_{gap} = \mu_o \mu_{MR} H_{MR}$

Since $\phi_{core} = \phi_{gap}$;

i.e., $\mu_s H_{core} A_{core} = \mu_{MR} H_{MR} A_{gap}$

Figure 4-12: Annular control regions with derivation for quantifying magnetic field strength

The capability of the MR fluid dashpot damper is demonstrated in the control of the resonating steel beam. As power to the electromagnet is increased, the vibration amplitude at the resonant frequency is decreased (see Figure 4-13), with the reduction in amplitude being quantified relative to the damper off-state (i.e., with no power to the electromagnet and therefore no applied magnetic field).

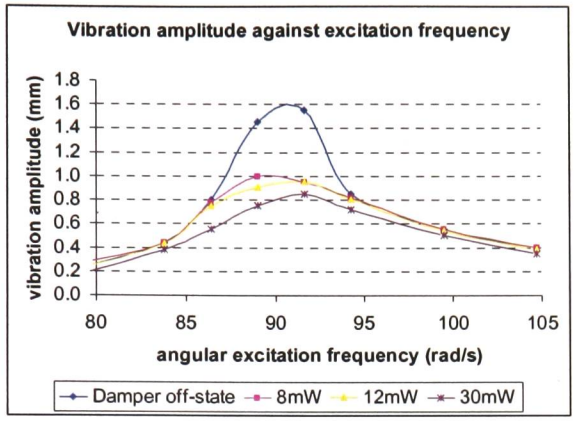

Electromagnet Power (to)	Electromagnet Resistance (of)	amplitude reduction
8mW	0.20Ω	37.5%
12mW	0.13Ω	40.6%
30mW	0.12Ω	46.9%

Figure 4-13: Results from forced vibration of simply supported steel beam with MR fluid damping

The concept demonstrator (presented in detail in §5.2) is a simplified model of the ski system, with a MR fluid damper controlling forced vibration of a cantilever, representative of the ski fore-body. The MR fluid damper in the concept demonstrator is a scaled version of the variable dash-pot damper used on the oscillating beam.

4.4.2 Diaphragm sealed damper

The diaphragm sealed MR fluid damper (see Figure 4-14) is designed to operate with a low off-state force. The device is actuated by moving the input shaft, which moves the diaphragm seals (1) and forces the MR fluid (Rheonetic MRF-132LD) through the annular control region. The annular control region is bounded by a fixed electromagnet (i.e., the electromagnet is not attached to the shaft) and the magnetic flux return sleeve, on the inside of the cylinder. The seals are reinforced with a washer (3) to ensure a more consistent "piston" area, but are considered compliant enough to allow for any thermal expansion of the fluid – removing the need for an accumulator. A shaft (4) runs through the fixed electromagnetic core to connect the diaphragm seals, at either end of the device, to each other (i.e., so that the fluid is pushed through the annular control region from one side or the other).

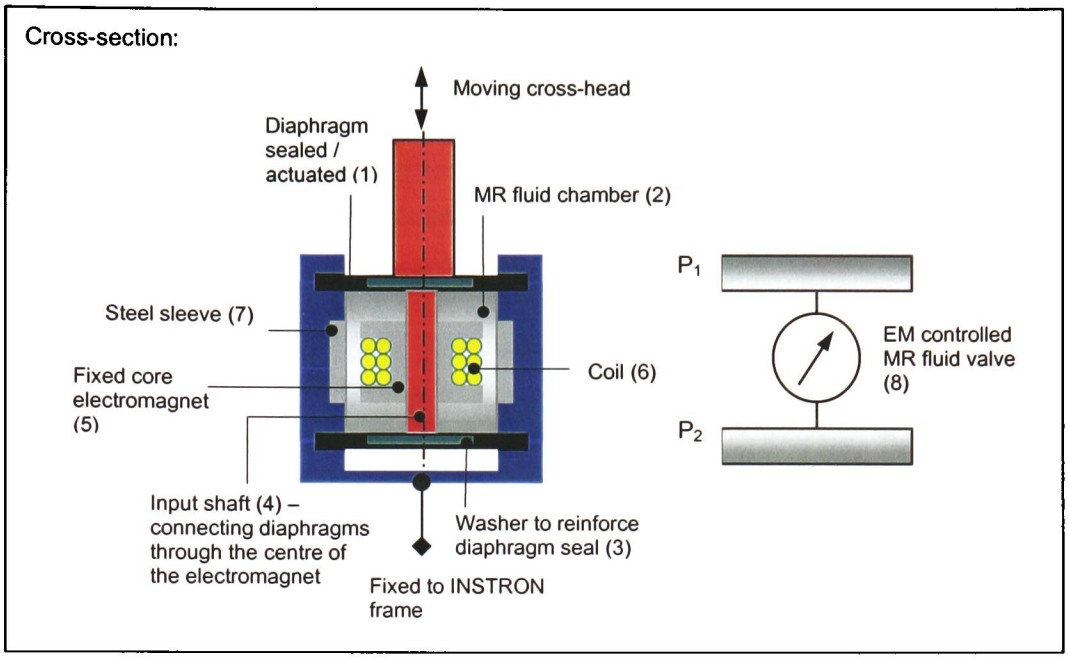

Figure 4-14: Diaphragm sealed, fixed coil, MR fluid damper (with 1mm stroke)

The electromagnetic (EM) core (5) comprises a coil (6) wound around a mild steel bobbin. The EM core is fixed (on a magnetically inert mounting bracket) in the middle of the cylinder, relative to a steel sleeve (7) that completes the magnetic circuit (i.e., acting as the return path for the magnetic flux). Fixing the core relative to the magnetic flux return sleeve enables the height of the sleeve to be minimised (thereby minimising the volume of steel in the device). The fixed core also reduces the number of moving parts and contributes to maintaining a low off-state force. Additionally, the fixed core ensures that the wires supplying power to the electromagnet do not have to move and can be fixed – making the system more robust.

The copper coil is wound around a steel bobbin placed in the middle of the cylinder to maximise the ratio of magnetic field to electrical power. This arrangement is considered novel over a patented diaphragm sealed MR fluid system ([US 2,575,360] – relating to the design of the Rheonetic ™ MRD-1004 damper [Carlson, 1996] from Lord Corporation). The Lord damper has the electromagnetic coil wound around the outside of the cylinder – requiring greater electrical power to generate the same magnetic field.

The annular region between the core and the steel sleeve acts as a valve that can be used to control the flow of MR fluid from one side to the other by changing the amount of electrical power supplied and, therefore, the magnetic field generated by the electromagnet. Activating the electromagnet causes the iron particles in the MR fluid to align (in the direction of the magnetic field) inside the

annular control region – trapping fluid and increasing the apparent viscosity. The effectiveness of the electromagnet controlled MR fluid valve (with respect to the amount of electrical power) depends on the gap width and length of the annular control region. Decreasing the gap width increases the on-state force, but also increases the off-state force. A compromise is required to provide a suitable operating range (i.e., the difference between the on-state and off-state forces) that enables the MR fluid device to contribute to the vibration control of the system to which it is to be applied.

The design of the diaphragm sealed damper is the subject of a patent application [Watson, 2004], filed on behalf of ReacTec Ltd. The patent relates to a variety of proposed applications of the damper beyond the initial adaptive ski concept (e.g., see Figure 4-15). The application of MR fluid devices for vibration control of hand-held power tools has been carried out with ReacTec. The motivation is the reduction of hand-arm vibration (<20Hz) that may result in operators of powered hand tools (such as drills and grinders) contracting Raynaud's disease (also known as vibration white-finger).

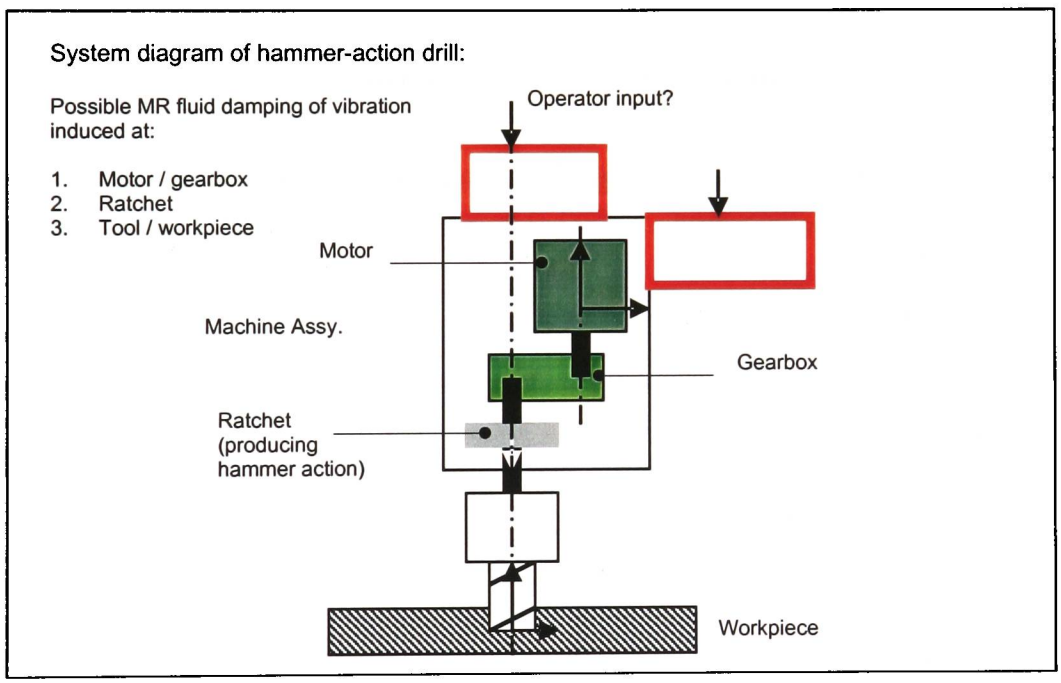

Figure 4-15: Diversification of research on the diaphragm sealed, fixed coil, MR fluid damper for applications outside skiing (e.g., the proposed use in hand-held power tools to reduce hand-arm vibration that may lead to nerve damage)

An INSTRON test machine has been used for tests on a prototype of the diaphragm sealed, fixed coil, MR fluid damper. The damper is loaded between clamps (one fixed, one moving – see Figure 4-16) at the bottom of its 1mm stroke and the cycle speed is set (with measurements accurate up to a maximum of 4mm/s). The force-extension-time measurements from two cycles (i.e., two up-strokes and two down-strokes) are compared and analysed. For clarity, analysis is focussed on two cycles

(i.e., four strokes) of the damper. Subsequent strokes are similar to those in the second cycle. It should be possible to predict the response of the damper (not carried out), however the actual measured performance is of greater interest here. The compilation of a mechanical model to represent the actual measured performance of the damper can be used to identify weaknesses (such as air in the system), so that problems may be addressed and the device developed.

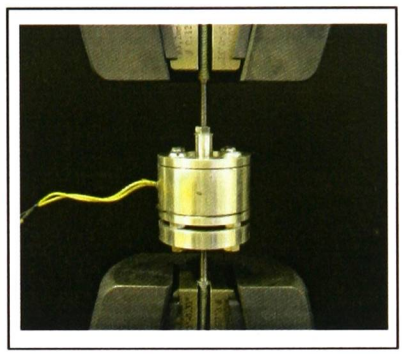

Figure 4-16: Prototype, diaphragm sealed, MR fluid damper clamped on INSTRON test machine – with the wires supplying power to a fixed coil electromagnet (EM)

The tests seek to quantify the energy absorbed by the damper and assess its performance. Plotting the force-displacement relationship of the damper subject to cyclic oscillations produces a curve with an enclosed area (i.e., a hysteresis loop – see Figure 4-17) that is proportional to the energy lost per cycle:

i.e., $$W_d = \oint F_d dx \qquad [4\text{-}25]$$

where, F_d is the damping force (i.e., $F_d = c\dot{x}$) and W_d is the energy lost per cycle

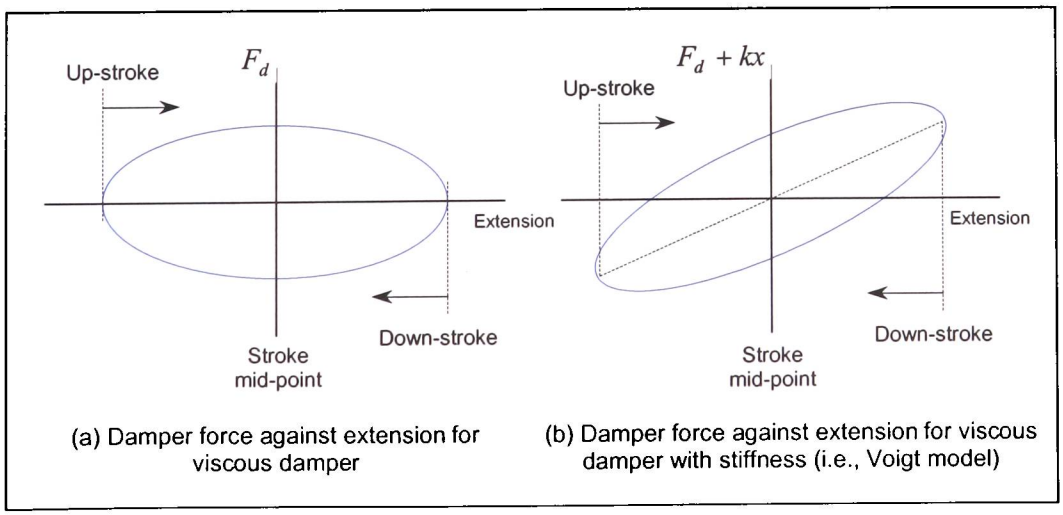

(a) Damper force against extension for viscous damper

(b) Damper force against extension for viscous damper with stiffness (i.e., Voigt model)

Figure 4-17: Energy dissipated by viscous damping (produced with reference to Thomson [1993])

The energy dissipated per cycle by a viscous damper is the area enclosed by the ellipse (see Figure 4-17 a) and is dependent on factors such as temperature, frequency, or amplitude. The hysteresis loop is rotated (see Figure 4-17 b) if a spring force (kx) is added to the damping force ($c\dot{x}$). This conforms to a viscoelastic Voigt model - consisting of a dashpot in parallel with a spring (this representation of viscoelastic, or rheological, properties as simple mechanical devices is introduced in §2.1.3.2 – see Figure 2–11). The change in the hysteresis loop illustrates the change in the viscoelastic properties of the MR fluid device.

The energy dissipated in one cycle (W_d) by a MR fluid damper (i.e., a RD-1005-1, manufactured by Lord Corporation) is described by Liao and Lai [2002]:

i.e., $$W_d = \int_0^{2\pi/w} F_{MR} dx = \int_0^{2\pi/w} c_{eq} \dot{x} dx \qquad [4\text{-}26]$$

where, F_{MR} is the damping force attributed to valve mode control of MR fluid; w is the excitation frequency ($rads^{-1}$); $\dot{x}$ is the relative velocity of the damper; c_{eq} is the equivalent damping coefficient.

The (RD-1005-1) MR fluid damper (capable of a 50mm stroke) primarily exhibits pure damping (i.e., there is no significant elastic component) during tests to characterise its performance, where the stroke is varied below 20mm. Equation [4-26] does not include a spring component that needs to be included to adequately describe the diaphragm sealed damper (see Figure 4-18) being investigated here.

An equivalent mechanical model of the prototype diaphragm sealed MR fluid damper is compiled with reference to work by Oh and Onoda [2002], based on observations of experimental (force-displacement) results from low frequency cyclic tests. The mechanical model of the prototype damper comprises spring elements, a variable viscous damping element and a variable Coulomb-friction element (see Figure 4-18). The spring constant k_1 represents the stiffness of the diaphragm seal. The spring constant k_2 represents the compressibility of the fluid in the chamber, between the diaphragm seal and the annular control region. The viscous damping (c) and Coulomb-friction (F_C) is attributed to the MR fluid (assuming a Bingham model) and is variable with respect to the power supplied to the electromagnet. Oh and Onoda [2002] used test results to estimate the values of stiffness, damping and Coulomb-friction in their equivalent model.

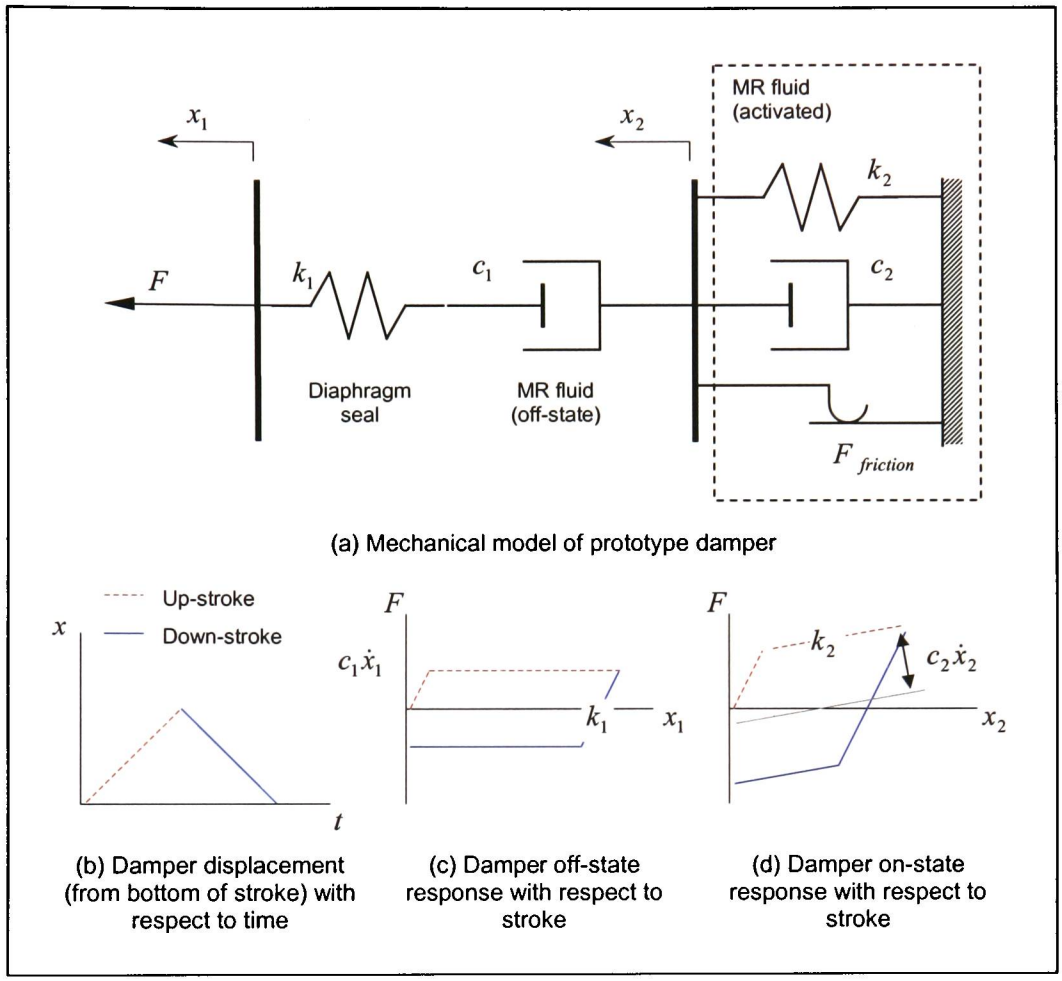

Figure 4-18: Equivalent mechanical model of the diaphragm sealed MR fluid damper at low frequencies

Quantification of the physical characteristics in the equivalent model (see Figure 4-18) of the prototype damper are estimated based on analysis of the results from low frequency cyclic tests. The off-state damping can be estimated from analysis of measurements revealing the force-stroke relationship (see Figure 4-18 c). The force-extension loop (see Figure 4-19) progresses along a clockwise path with increasing time. The force-displacement relationship is approximately elliptical with no magnetic field applied (i.e., primarily exhibiting characteristics of a viscous device). The damping coefficient c_1 is estimated to be 20000kgs^{-1} with no magnetic field applied. This magnitude for off-state damping coefficient is comparable with results presented by Spencer et al [1997].

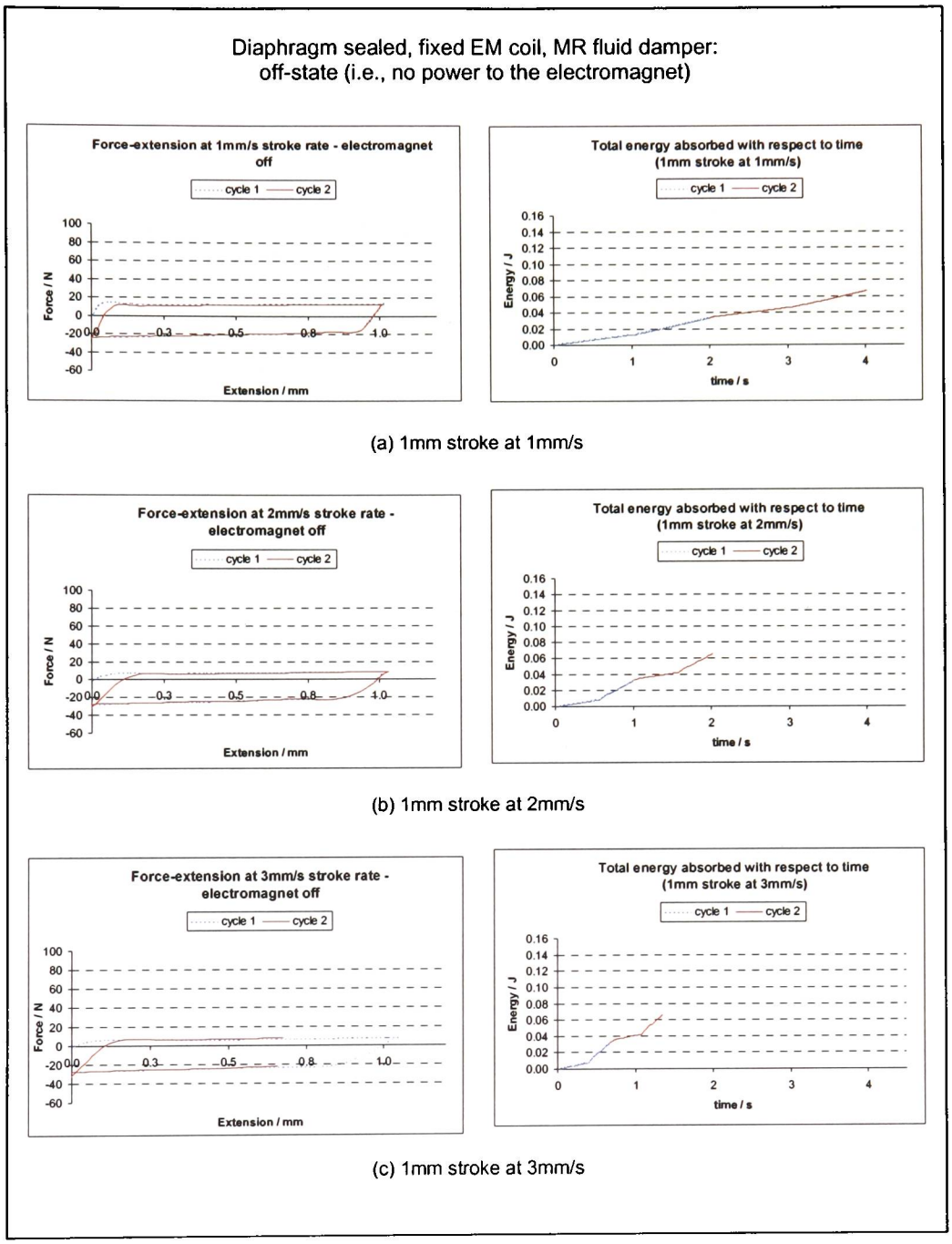

Figure 4-19: Results from cyclic tests of prototype MR fluid damper on INSTRON test machine, comparing off-state damped force and dissipated energy for different stroke rates

The performance of the up-stroke and down-stroke is not equal and it can be seen (comparing Figure 4-19 a, b and c) that the energy dissipated by the damper on the up-stroke is less than that on the down-stroke, with the performance discrepancy more pronounced at higher stroke rates. It is suggested that the unequal performance may be due to air in the system that compromises one stroke

more than the other. The hysteresis loop of the damped force with respect to extension shows (see Figure 4-19) that the damper exhibits predominantly viscous characteristics (referring back to Figure 4-17 a, presenting understanding on the energy dissipated by viscous damping).

Comparing the damped force at a fixed stroke rate (i.e., 1mm/s) for different amounts of power to the electromagnet, it can be seen (see Figure 4-20) that the hysteresis loop rotates with increasing power (referring now to Figure 4-17 b and Figure 4-18 d). Therefore, the spring-like properties of the viscoelastic system increase with power. This observation is supported by Li et al [1999], who indicated that relative to the current in the coil that produces the magnetic field, the spring component increases more than the damping component of the MR fluid.

The on-state damping coefficient (c_2) and spring constant (k_2) can be estimated (see Figure 4-18 d) from analysis of measurements revealing the force-stroke relationship in the presence of a magnetic field (see Figure 4-20). The estimates (see Table 4-3) are used to define the on-state behaviour of the prototype damper for finite element analysis (see §5.3.2), using a simplified Voigt model. A finite element model is used to predict the response of a simplified ski-structure controlled with the prototype damper.

Power supply to prototype MR fluid damper			Resistance	Measured	
				Damping coefficient c_2	Spring constant k_2
Current (A)	Voltage (V)	(Watts)	(ohms)	(kgs^{-1})	(kNm^{-1})
0.15	2.10	0.32	14.0	26600	13.4
0.20	3.00	0.60	15.0	33300	33.3
0.25	3.90	0.98	15.6	25000	53.0
0.30	4.80	1.44	16.0	25000	100
0.40	6.50	2.60	16.3	21900	75.0
0.50	8.30	4.15	16.6	21900	65.6

Table 4-3: Measured characteristics of prototype MR fluid damper, subject to 1mm/s stroke rate

The relationship between damping coefficient, spring constant and power supply has been quantified (see Table 4-3) and can be qualitatively appraised with regard to the force-extension relationships. The force-extension relationships initially indicate predominantly viscous behaviour (i.e., it is approximately elliptical up to 0.6W – see Figure 4-20 a and b). Elastic behaviour develops with increase in power (i.e., the ellipse rotates – see Figure 4-20 c and d). However, the viscoelastic performance appears to drop off (see Figure 4-20 e and f), with noticeable reduction in the viscous behaviour (i.e., since the ellipse narrows).

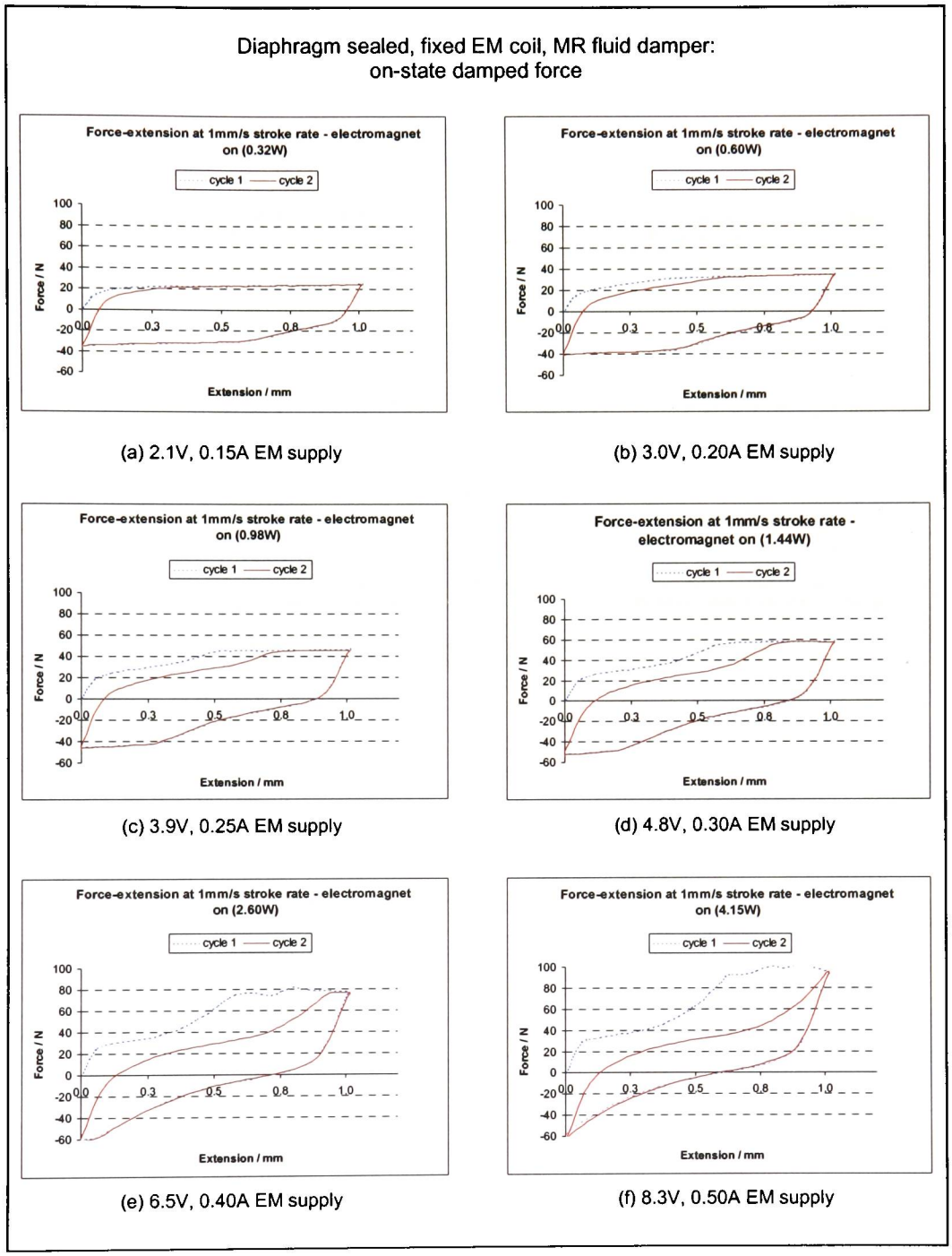

Figure 4-20: Results from cyclic tests of prototype MR fluid damper on INSTRON test machine, comparing damped force with respect to extension for different amounts of power to the electromagnet

The corresponding comparison of dissipated energy for different amounts of power shows (see Figure 4-21), again, unequal performance between strokes. Also, the initial stroke dissipates a greater amount of energy with increased power to the electromagnet. The discrepancy between strokes may

be explained by the air in the system that increases the elastic properties at the expense of the viscous properties. Since the stroke is small, a small volume of air in the system is significant.

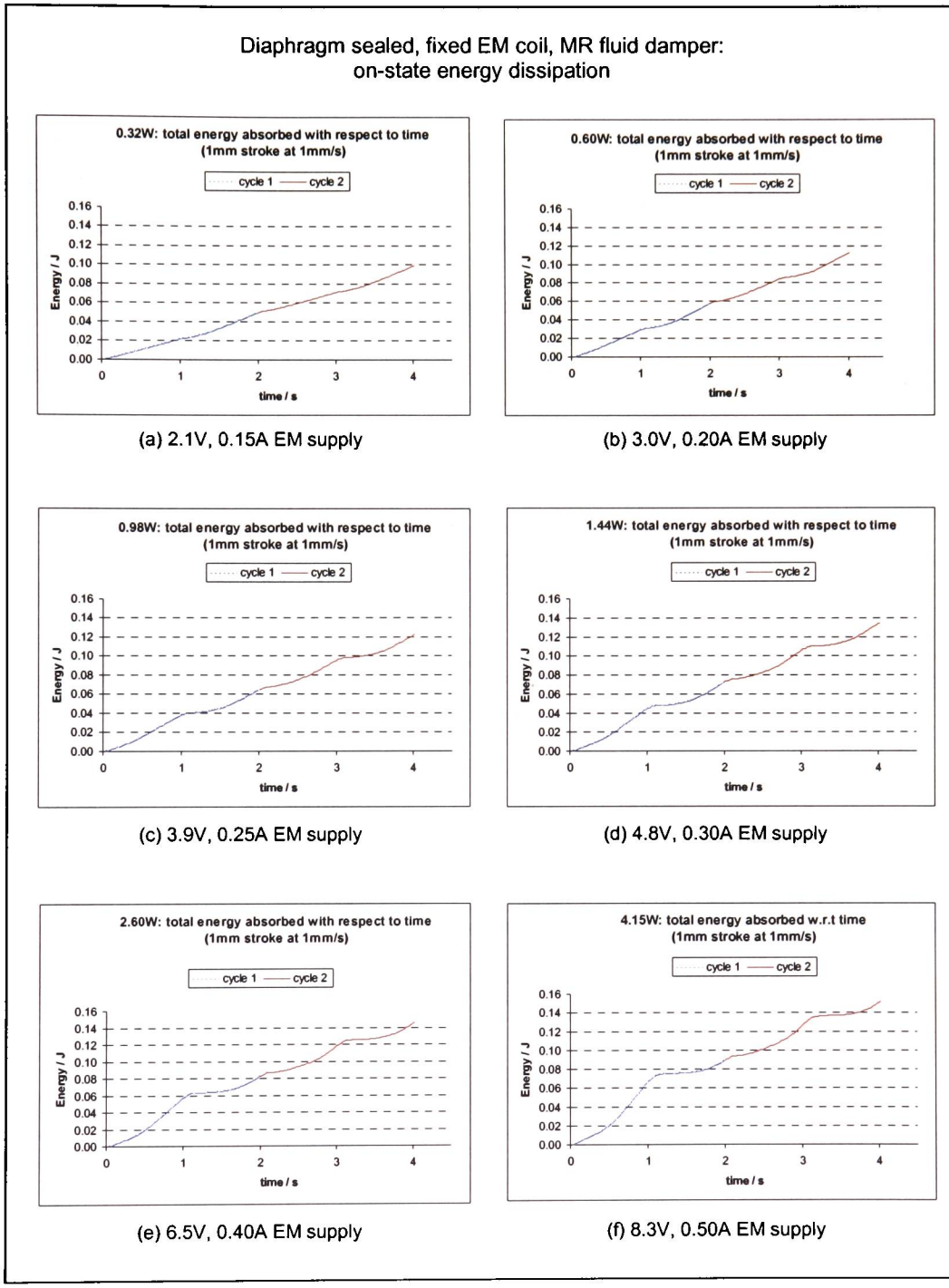

Figure 4-21: Results from cyclic tests of prototype MR fluid damper on INSTRON test machine, comparing dissipated energy with respect to extension for different amounts of power to the electromagnet

Prior to analysing these tests, the lack in performance was not defined. Nevertheless, it was suspected that there would be a problem with air in the system, due to the viscosity of the MR fluid and the small annular control region making it difficult to fill the damper and eliminate air - even under pressure.

Compiling the results from on-state and off-state cyclic tests (i.e., Figure 4-20, Figure 4-21 and Figure 4-19) enables the stroke performance to be compared. The damped force from both cycles are comparable (see Figure 4-22 a and c) - initially with greater performance in the down-stroke, but ultimately with greater performance in the up-stroke (with the switch in performance coinciding with a power supply of approximately 1.2W).

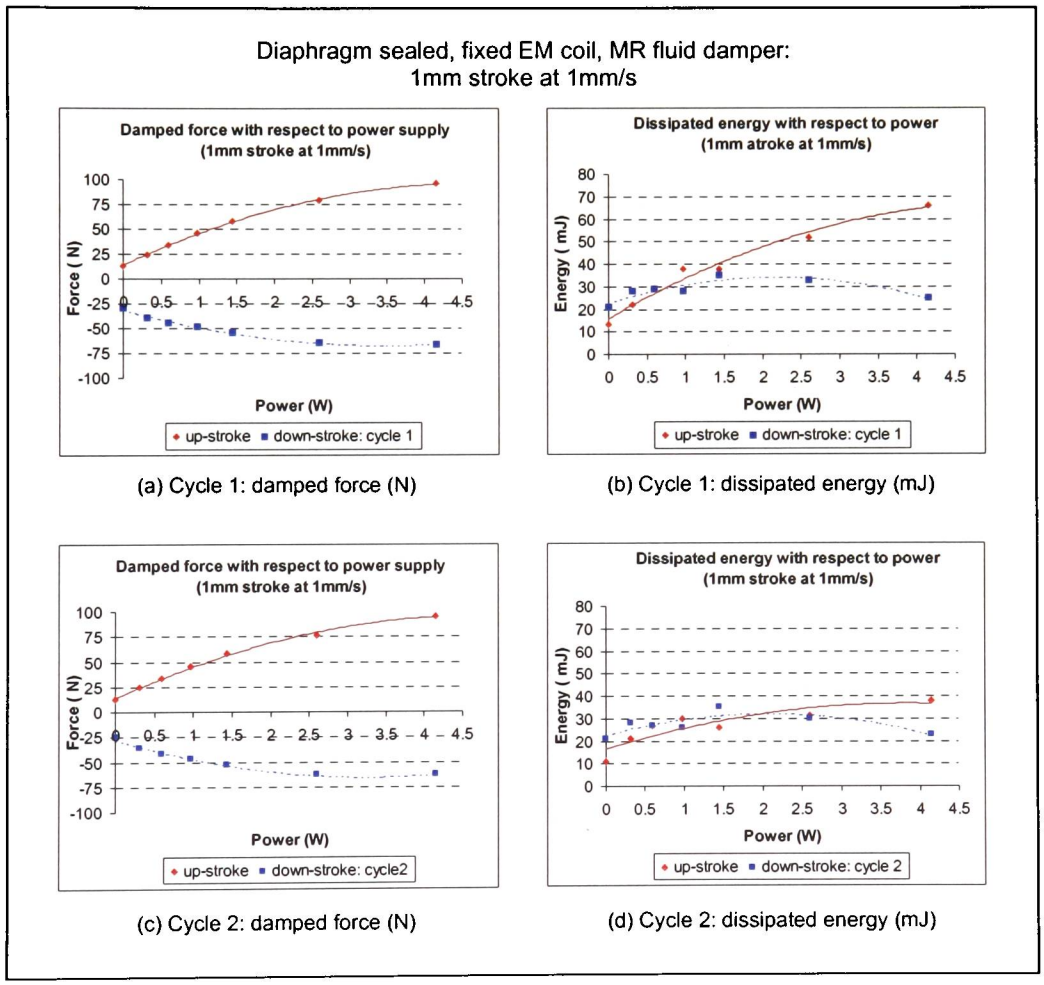

(a) Cycle 1: damped force (N)

(b) Cycle 1: dissipated energy (mJ)

(c) Cycle 2: damped force (N)

(d) Cycle 2: dissipated energy (mJ)

Figure 4-22: Analysis of damped force and dissipated energy from cyclic tests of prototype MR fluid damper (with 1mm stroke) on INSTRON test machine (cycled at 1mm/s)

As already discussed, the difference in performance is attributed to air in the system. Movement of air is considered here to explain the switch in performance (i.e., between down-stroke and up-stroke),

possibly caused by the increased resistance at increased power. The dissipated energy in the first cycle is relatively consistent with the damped force (see Figure 4-22 b) – again, with greater initial performance in the down-stroke switching to significantly better performance in the up-stroke. The dissipated energy in the second cycle shows a drop in performance in both strokes (see Figure 4-22 d). The dissipated energy decreases, because the area under the hysteresis loop decreases (see Figure 4-20). Despite the reduction in dissipated energy between cycles (particularly in the up-stroke – see Figure 4-22 b and d), the damped force between cycles is similar (see Figure 4-22 a and b). This infers that the damper behaves more spring-like, with reduced damping characteristics.

The discrepancy in performance between strokes (i.e., up and down) is more pronounced with increased stroke rate and the discrepancy increases with increased power to the electromagnet. This discrepancy in performance is attributed to air in the system. Attention is required to ensure that air does not compromise the system before any further tests to more accurately quantify the viscoelastic properties of the damper, with respect to power to the electromagnet.

Although the equivalent mechanical model (see Figure 4-18) appears to represent the force-displacement behaviour, it may not characterise the force-velocity relationship (not investigated here). Subsequent work to characterise the performance of the MR fluid damper at higher frequencies may be better carried out with the damper mounted between a rigid structure and a shaker (Figure 4-23). A shaker enables a greater dynamic range to be investigated than is possible with the INSTRON, which cannot cycle accurately above 4mm/s (i.e., 4Hz on a damper with 1mm stroke). The damper can be instrumented with a dynamic load cell to quantify the damped force and with an accelerometer to confirm the stroke, so that the dissipated energy may be calculated.

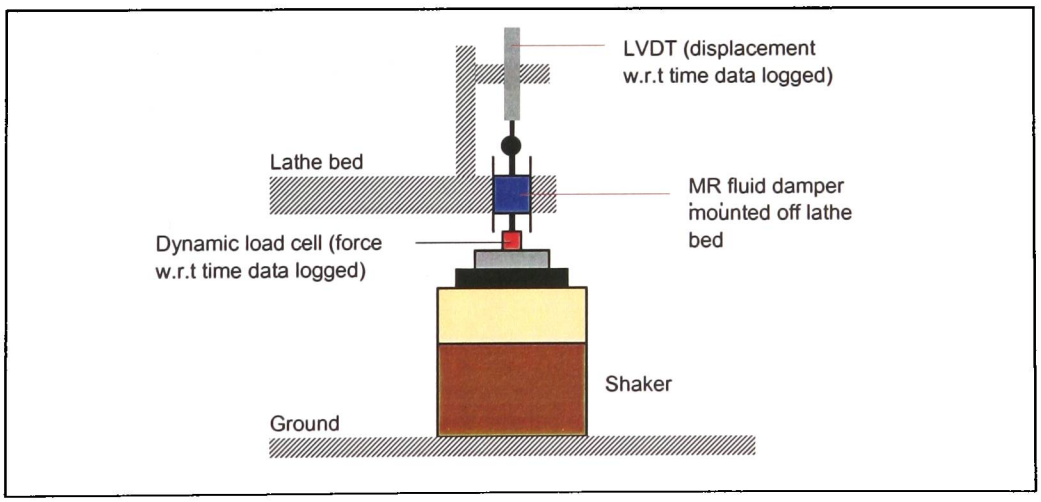

Figure 4-23: Proposed arrangement to experimentally characterise damper performance at higher vibration frequencies (>4Hz)

Further work is required to investigate the scalability of the diaphragm sealed damper. Development of the device is particularly recommended for vibration control applications with a low off-state requirement. Also (referring back to §4.1.2), it is acknowledged that temperature will influence MR fluid response (not investigated here) and greater consideration of thermodynamics in MR fluid device control is recommended (see §6.2 on further work).

5 Adaptive Ski

This section presents the motivation behind the adaptive ski concept (see §5.1), with a description of the system that is the subject of a patent application [Watson, 2001]. The choice of materials is explained and the contribution of this research in the development of the adaptive ski system is reviewed. The technical objectives and system constraints are presented alongside a brief summary of the commercial effort to-date.

Commercial efforts to market the adaptive ski concept to manufacturers within the European ski industry part-influenced the development of a concept demonstrator on a ski-like structure (see §5.2). The concept demonstrator aims to show the potential for vibration control of skis with MR fluid damping. Results from experimental analysis of the concept demonstrator quantify damping with respect to the amount of (electrical) power supplied to a MR fluid dashpot that controls vibrations in the ski-like structure when it is excited by a rotating out-of-balance mass.

The geometric layout of the concept demonstrator is appraised (see §5.3) following field-tests of an extended shim (i.e., one that extends down the fore-body, in front of the binding toe-piece) and using preliminary results from finite element analysis. Experimental results from the prototype diaphragm sealed damper (see §4.4.2) and static testing of skis are used to define physical parameters in a finite element (FE) model of the ski-like structure and predict response. The concept demonstrator is appraised and implications for the prototype damper are discussed.

5.1 Concept

The dynamic response of a ski depends on its physical characteristics and on the environmental conditions (including skier position and snow condition) to which it is exposed. Skiing on changeable snow conditions (e.g., skiing hard-pack verses soft or loose snow) induces vibration with different amplitudes and excitation frequencies. Adapting physical characteristics to control vibration in response to changing conditions offers the possibility of increasing the performance range of the ski, so that it may provide the skier with greater dynamic stability and enhanced control.

This research establishes a concept for adaptive vibration control of skis, using a combination of smart materials technologies. Fundamentally, it is perceived that semi-active damping with a MR fluid device can be adapted by varying the power supply to an electromagnet (inside the MR fluid device), with control based on the monitored vibration response of the ski. The adaptive ski system (see Figure 5-1) comprises an integrated sensor array that provides information to a microprocessor – controlling the power supply to a MR fluid device that semi-actively damps the ski (specifically the

fore-body, though initial proposals also aimed to provide aft-body control). The system is to be powered from a battery, charged by piezo-ceramic elements that convert mechanical energy from the movements of the skier into electrical energy.

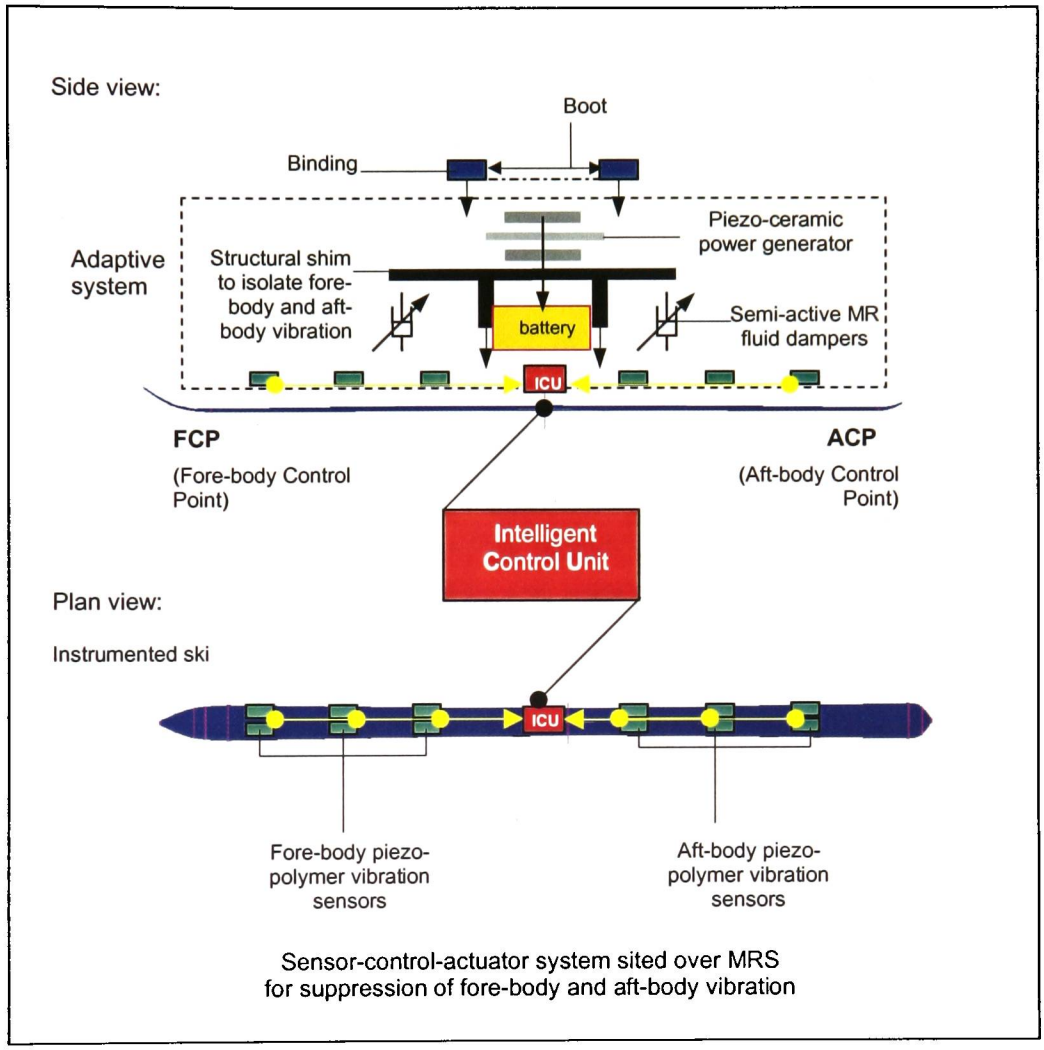

Figure 5-1: Schematic of the adaptive ski system

Integrating a distributed array of piezo-polymer (PVDF) sensors in the composite structure should enable the dynamic response to be monitored and used as the basis for semi-active vibration control. The information from the integrated piezo-sensors would be processed by a microprocessor that would control the power supplied to the electromagnet. There are anecdotal differences of opinion (from contacts made within the ski industry) on how the monitored dynamic response may be interpreted and used to influence adaptive force control.

The premise for the adaptive ski concept is that the vibration control characteristics can be changed to better suit conditions and thereby enhance control. Incorporating a MR fluid device provides the potential for controllable, semi-active damping with greater force control than is possible with piezo-systems (e.g., such as those marketed by K2 and HEAD – see §2.5). The viscoelastic properties of a semi-active damper can be changed, enabling the resistive force and the dissipated energy to be adapted. It is proposed here that the amount of semi-active damping be adapted based on the amplitude and frequency of vibration in the ski. It is suggested that hard-pack conditions induce higher frequency, lower amplitude vibrations compared with those generated when skiing over soft or loose snow (e.g., off-piste). This presents the opportunity to characterise the environmental conditions from the monitored vibration response and control the MR fluid device accordingly. Specifically, it is suggested here that damping be increased to suppress higher frequency (i.e., 10Hz< f <50Hz), lower amplitude vibrations (i.e., characteristic of those induced over hard-pack conditions) and pulsed to increase the decay of higher amplitude, lower frequency (i.e., f <10Hz) vibrations (associated with skiing over soft or loose snow conditions). The reasoning: to achieve a reduction in edge chatter over hard-packed conditions, while enhancing vibration control over loose conditions - without sacrificing flex. Feedback suggests that this control concept may be over-complicated and the system may only require semi-active damping based on vibration amplitude. However, it is the view here that maintaining softer flex over loose conditions is advantageous and therefore the semi-active MR fluid damper should be controlled to avoid compromising this flex characteristic. The research and development of the control algorithm is not included in this work.

The whole system (i.e., the electromagnet and the control unit) is to be powered from a battery charged with current generated from the straining of piezo-ceramic wafers. The piezo-ceramic wafers are to be located under the skier and housed with the battery in the shim. Research [Hooper, 2001] to integrate a piezo-ceramic power generator in the heel of a desert boot, claimed that 200mJ of energy can be "parasitically harvested" per step (charging a mobile phone battery). It is proposed that such a piezo-ceramic system could be arranged in a ski, so that current may be generated from skier movement (i.e., when the skier shifts weight forward, back and between skis – see §2.4.1). Further research is required to better investigate the feasibility of the power supply aspects of the system.

This research establishes a concept and begins to address the force-control capability and requirements for a MR fluid device. Ski dynamics are researched, relevant to the development of specifications for the adaptive ski system. The vibration monitoring capability is investigated through field-tests of skis instrumented with piezo-polymer sensors. A prototype diaphragm sealed MR fluid damper has been developed and its initial performance appraised (see §4.5.2).

Recommendations for further work are based on understanding and acknowledging the technical issues that need to be addressed.

5.1.1 Specifications

The ultimate aim is to semi-actively damp the fore-body of a ski using a MR fluid damper, with autonomous control based on the monitored vibration response. Power is to be supplied from a battery, charged by piezo-ceramic elements that convert mechanical energy to electrical energy. The mechanical energy is to be harvested from the movement of the skier, rather than from the vibrating ski. The adaptive ski is a sensor-control-actuator system with integrated power supply.

- Sensor

Piezo-polymer (PVDF) sensors provide a self-powered capability to monitor the dynamic response of skis. The piezo-polymer sensors convert the mechanical energy of the vibrating ski into a current that may be measured as a voltage when the sensor is loaded. Skis have been instrumented with distributed arrays of piezo-polymer sensors to provide data for signal analysis of field-tests. The piezo-polymer sensors do not require power (as oppose to strain gauges) and are cheap, even in prototype quantities (i.e., less than $2 per laminated PVDF sensor, from Measurement Specialities Inc.). Laminated piezo-polymer sensors may be considered for integration in the composite structure, with confirmation required to ensure compatibility between the laminate and press temperatures (i.e., during the manufacture of the ski).

- Control

A microprocessor is required to process information (i.e., with respect to amplitude and frequency) from a multi-sensor array and control power supply to an electromagnet in a MR fluid device. Assuming the battery supplies a constant voltage, power supply to the electromagnet should be current and time controlled. ReacTec is developing a generic (i.e., for applications outside skiing) microprocessor control unit with funding from a DTI sponsored SMART award. The cost of the microprocessor is not considered prohibitive to commercial development of the adaptive ski system. There are greater financial and technical risks associated with the power supply aspects of the system. Development of a control algorithm is not included in this work.

- Actuator (i.e., semi-active damper)

Fore-body vibrations are to be semi-actively damped by a MR fluid device and isolated through a shim. The dynamic compliance is small (fractions of 1mm), requiring a short-stroke MR fluid damper with as few moving parts as possible to ensure as much of the compliance as possible can be subjected to the control of the damper. Extending the shim in front of the binding toe-piece, so that it overhangs the fore-body, presents an opportunity to increase the stroke in the MR fluid device, by

exposing it to a greater compliance. However, issues with extending the shim have been identified (see §5.3.1).

The vibration control requirements of the ski should overlap with the control capability afforded by the MR fluid device. The difference between the on-state and off-state of the MR fluid device defines its operating range and must be compatible for use on the ski. It is acknowledged that the damping requirements for the ski are yet to be quantified (i.e., further field testing is required - see §3.4.2)

- Power supply

Power is to be stored on a battery that is charged by piezo-ceramic elements, located in the MRS such that strain induced by skier movement can be concentrated on the elements. Pressure and flex induced straining of piezo-ceramic elements can be used to generate a current that can be used to charge the battery. There is precedence [Hooper, 2001] for such a power generating system, although further research is required to verify the amount of power that may be expected. The design of how the boot interfaces with the proposed power generator needs to be considered. Also, the cost and weight implications need to be identified.

- Integration

The bulk of the adaptive ski system may be assembled onto the shim, with the control unit, battery and piezo-ceramic power generator housed over the MRS. There is opportunity to retrofit the entire system onto a ski, reducing the impact of integrating the system into production. Clear understanding of the dynamic response of the ski is required to ensure the adaptive system provides performance benefits – with particular reference to the location of the damper relative to operational deflection shape (or mode shape, if the ski is likely to be excited at a resonant frequency).

5.1.2 Technical risk

If the off-state force is too high, the useful operating range of the device will be reduced. The on-state force is limited by the available power that can be supplied (i.e., the current that can be generated and stored) to the electromagnet. It is acknowledged that a permanent magnet could be used, but an electromagnet provides greater control capability.

Reducing seal friction contributes to minimising the off-state force, without compromising the operating range (i.e., the difference between on-state and off-state forces). Lowering the off-state of a direct shear mode MR fluid device by increasing the gap width of the annular control region will reduce the on-state to power ratio. Similarly, lowering the off state viscosity of the MR fluid by reducing the carbonyl iron content will reduce the on-state to power ratio – assuming that in doing so,

the stability of the MR fluid remains acceptable (i.e., the life-time performance of the MR fluid is not reduced – see §4.2.2).

The kinematics of the system may require a hinged interface between the MR fluid damper and the ski. It is important that loss of dynamic movement at mechanical interfaces is reduced to ensure that the small compliance of the fore-body relative to the shim contributes to as large a stroke (of the damper) as possible. The aim is to ensure mechanical energy from the vibrating ski contributes to movement in the damper that may then be controlled.

Efforts to reduce loss of compliance and lower the off-state without compromising on-state have lead to the development of a prototype diaphragm sealed, short-stroke MR fluid damper, with fixed electromagnetic core.

This research contributes most to understanding the issues associated with the MR fluid damper, so that they may be addressed. It is acknowledged that the force control capability depends entirely on the availability of sufficient electrical power for the electromagnet in the MR fluid device and the microprocessor control unit. The cold operating environment (i.e., 0°C to –30°C) imposes a significant system constraint that further compromises the available power.

Power-supply remains a considerable source of technical risk and more research is required. The amount of power generated and available for use by the electromagnet (i.e., less the power required for the microprocessor control interface) needs to be better ascertained so that the expected on-state force can be more accurately quantified. Initial assumptions are based on research [Hooper, 2001] that indicated 200mJ can be supplied per flex (or compression) of a piezo-ceramic transducer. Tests have been carried out to investigate damping of a ski-like structure with less than 200mW supplied to the electromagnet of a MR fluid dashpot damper. Assuming that 200mJ can be generated from skier movement and efficiently stored, the power available for the electromagnet is likely to be considerably lower (i.e., <<200mW).

The cold operating temperature will reduce the performance of the system. Reducing temperature is likely to reduce the charge generating capability of the piezo-ceramic transducer and reduce the capability of a battery to efficiently store energy. Although, MR fluid can perform at -40°C, the on-state and off-state forces are likely to be affected – changing the operating range of the MR fluid device. Operating at low temperature is likely to elevate the off-state status and reduce the on-state to power ratio (resulting in an increased demand for power).

5.1.3 Commercialisation

ReacTec was founded to realise the commercial potential of this research and efforts have been made to protect the IPR generated, by filing patent applications. An initial patent application was filed [Watson, 2001], relating to all aspects of the adaptive ski concept. A subsequent patent application [Watson, 2004] was filed relating to the diaphragm sealed damper and derivatives of it. The patent applications were filed with advice and assistance from Kennedys Group (based in Glasgow) and Murgitroyd and Company.

A Scottish Company Innovation Support (SCIS) award has provided financial support for the development of the concept and Scottish Enterprise has provided additional financial support to enable industrial contact to be made. Contact has been made with significant names within the European ski industry, with demonstration (i.e., MR fluid damping of a ski-like structure) to a select few. Assistance in making ready the concept demonstrator (see Figure 5-2 and Figure 5-3) was provided by Edinburgh based consultants, Innovation Architechs (IA). Specifically, IA helped construct the ski-like test structure and produced the control box. Analysis of the performance of the concept demonstrator, carried out in this research (see §5.2) was presented in commercial presentations.

Having established the concept and with the IPR secured, interest within the ski industry was sought. The commercial strategy was to add value to the concept and develop better understanding of the technology before returning with a demonstration of the technology to lever a collaboration agreement with a ski manufacturer. However, having identified interest and returned with a demonstration, it was made clear that the full costs of developing the technology would need to be considered before any funding could be released. Advice was sought and costs, including royalties were estimated based on a forecast of resources and the size of the market. The entire development cost of the system was assigned to the ski application, despite opportunities to develop derivatives of the system for other applications.

An industrial collaborator should be aware of the technical uncertainty and commercial constraints imposed by FIS specifications (i.e., B 1.2.6.1 a - for alpine competition equipment) that would seem to prevent use of the technology in competition. If the system can be made to operate from a self contained power supply (i.e., the proposed parasitic piezo-power generator), it may be possible to argue that the system does not make use of "foreign energy" and is therefore acceptable for use in competition. A ban on competition use does not necessarily mean that adaptive skis could not be commercially successful in the recreational market.

Costs and technical risk are barriers to development of the concept. Allowing the initial development costs to be spread across applications would enable the cost of the adaptive ski to be reduced. Should

a manufacturer be interested in the concept, despite the acknowledged concerns, ReacTec should carefully evaluate its commercialisation strategy – balancing the expected return on developing the adaptive system for skis, while valuing the development experience that may provide spin-off opportunities in other applications.

This work is considered a starting point for removing the technical risk associated with dynamic monitoring (through work with the instrumented ski) and force control (through work on the diaphragm sealed MR fluid damper). It is acknowledged that more work needs to be done in both these areas for the system to be considered technically viable. However, the power supply has been identified as the source of greatest technical risk. Fundamentally, further research into power supply and storage is required to ascertain the viability of the system for skis. NOLIAC (piezo-ceramic specialists, based in Denmark) has been contacted with a view to sub-contracting research and development of the power generating aspect of the system.

5.2 Concept demonstrator

Skis are complex composite structures – made with a variety of materials and a number of construction methods (see §2.1.3 and §2.1.4). Engineering a demonstration of the concept on a ski requires an understanding of the ski to which the MR fluid system would be retrofitted. In particular, understanding of how the ski responds to a dynamic input (i.e., the modal, or operational deflection shape), so that the change in response can be quantified with respect to the MR fluid system.

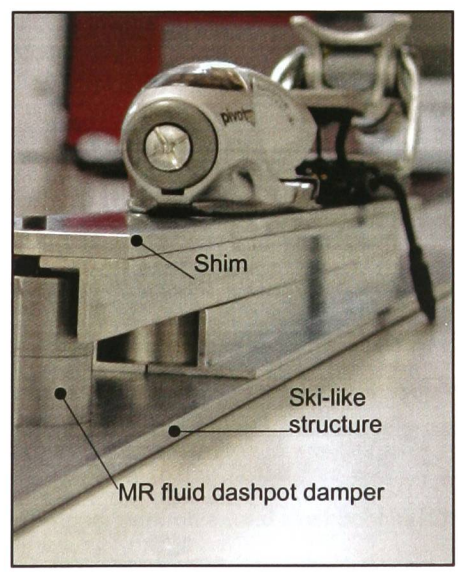

Figure 5-2: Adaptive ski concept demonstrator on aluminium ski-like structure

The ski-like structure (see figure 5–2) is designed to provide a stand-alone commercial demonstration of the concept. The demonstrator is not prejudiced by any brands (i.e., there is no apparent allegiance to a particular manufacturer) and the system facilitates analysis (see Figure 5-3) of what the MR fluid system is able to achieve.

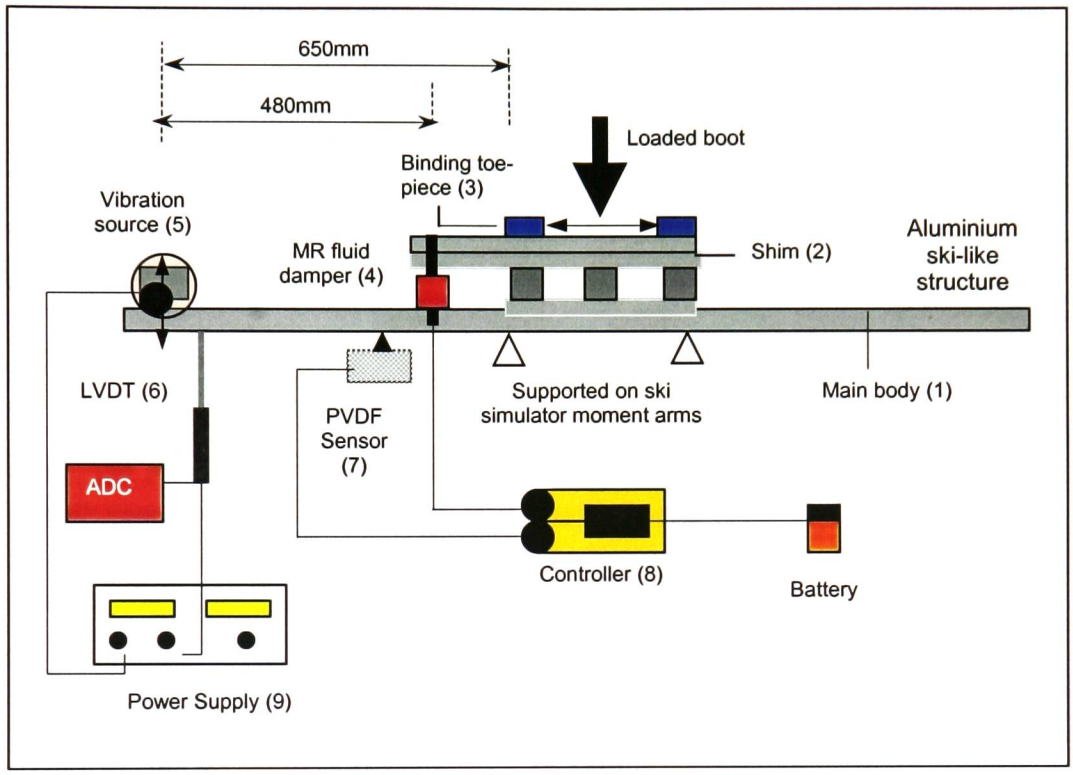

Figure 5-3: Schematic arrangement of ski-like structure used to demonstrate adaptive ski concept

The ski-like structure comprises an aluminium beam that represents the main body of the ski (1), with a raised aluminium structure representative of a shim (2). The shim extends in front of the toe-piece of the binding (3), over the fore-body structure that is to be controlled by (primarily) the valve mode of a MR fluid damper (4). The shim comprises a single beam reinforced by two aluminium T-sections and is considerably more rigid than the main body, so that the induced vibrations can be isolated through the more rigid shim. The MR fluid dashpot damper is located between the overhanging shim and fore-body (480mm from the tip) – effectively controlling the movement of a (650mm) cantilever beam with a vibration source at the free end. The MR fluid dashpot damper comprises 400 turns of (Ø0.2mm) copper wire on a mild steel bobbin (6mm x Ø10mm) with Ø25mm (piston-like) ends and an annular gap width of 2mm. The whole ski-like structure is simply supported on the moment arms of the ski simulator, below and in-line with the toe piece and heel-piece of the binding (see Figure 5-4).

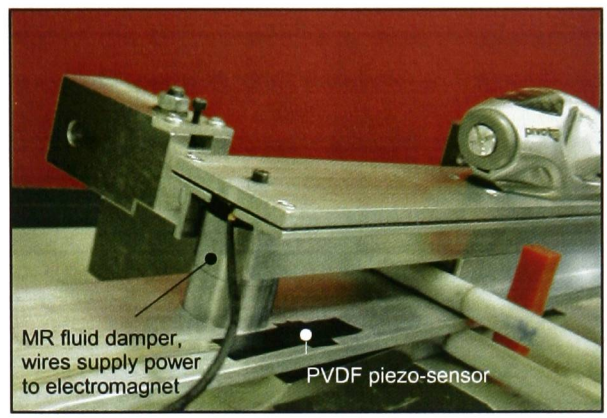

Figure 5-4: Concept verification, with MR fluid damping of (aluminium) ski-like fore-body structure on ski simulator moment arms

Attached to the tip of the fore-body structure (see Figure 5-3), a rotating out-of-balance mass on an electric motor provides a vibration source (5) that represents ski vibration about the FCP. The ability of the MR fluid damper to control vibration is investigated by measuring the vertical displacement of the fore-body with respect to power supplied to the electromagnet inside the MR fluid damper. Using (6) a LVDT (Linear Variable Displacement Transformer), vertical displacement of the fore-body is measured (i) alongside the MR fluid damper and (ii) at the tip, alongside the out-of-balance rotor.

The commercial demonstrator also includes (supplied by Measurement Specialities Inc.) a PVDF piezo-polymer vibration sensor (7), attached to the vibrating structure and connected to a prototype microprocessor control box (8). The control box can switch on the electromagnet inside the MR fluid damper after the PVDF sensor has detected a pre-programmed vibration level. There is a manual on/off control – all (i.e., controller and electromagnet) powered from a 9V PP3 battery. Design and appraisal of the controller is not included in this work.

The control circuit may be bypassed and the MR fluid damper can be connected directly to a variable power supply (9). Damping performance is quantified with respect to the power supplied to the MR fluid damper and the vibration source (i.e., in terms of excitation frequency). Fore-body displacement is measured by a LVDT (6) with data logged to a computer via an analogue digital converter (Pico ADC 212).

The vibration amplitude at the tip of the fore-body (alongside the excitation source) and 480mm from the tip (alongside the damper) is compared (see Figure 5-5) with the MR fluid damper off and on (i.e., with 200mW supplied to the electromagnet). The results show the off-state and on-state damping at different excitation frequencies (<10Hz). The vibration amplitude at the tip is

considerably bigger than that measured alongside the damper (by up to a factor of five, at 7Hz, or 44rads^{-1}). The dashpot damper is not sealed or guided, so the damping can be entirely attributed to the MR fluid rheology.

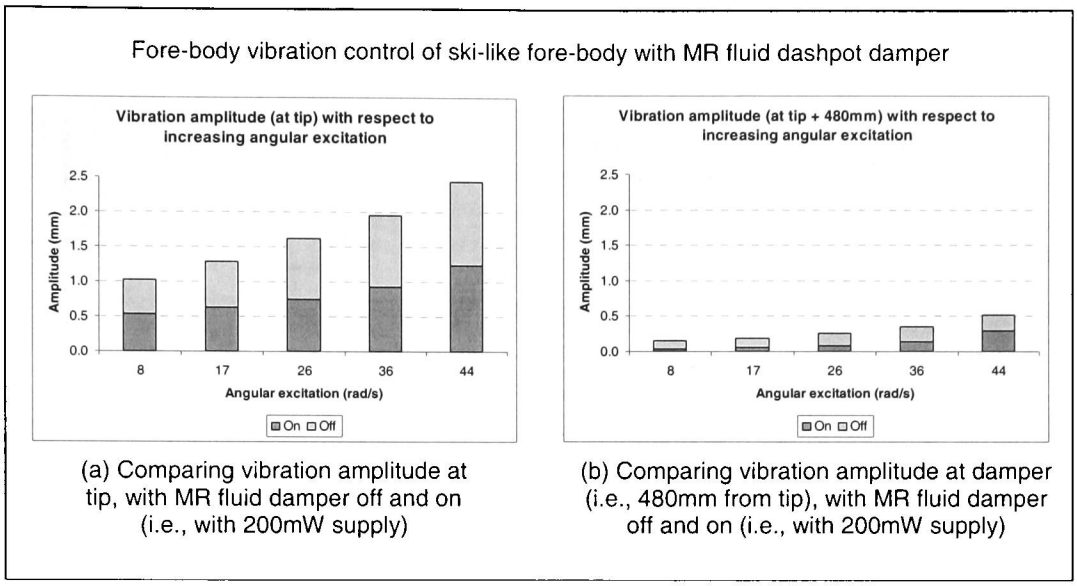

(a) Comparing vibration amplitude at tip, with MR fluid damper off and on (i.e., with 200mW supply)

(b) Comparing vibration amplitude at damper (i.e., 480mm from tip), with MR fluid damper off and on (i.e., with 200mW supply)

Figure 5-5: Comparing off-state and on-state (i.e., with 200mW) MR fluid damping of ski-like structure, with increasing out-of-balance excitation measured at tip (alongside vibration source) and 480mm from tip (alongside damper)

The semi-active damping capability is due to the controllable rheology of the MR fluid (i.e., controlled by the magnetic field generated with respect to the power supplied to an electromagnet). The (650mm) fore-body cantilever is subject to a 7Hz excitation at the tip and the semi-active damping is compared (see Figure 5-6) at the tip and 480mm from the tip (alongside the damper). Increasing power to the damper decreases the absolute vibration amplitude at the tip more than that alongside the damper (see Figure 5-6 a). Comparing the relative amplitude at the tip and alongside the damper (i.e., 480mm from the tip) it can be seen (see Figure 5-6 b) that the performance is better alongside the damper. It is not possible to fully control the moving mass of the fore-body vibration with a damper located 170mm from the support.

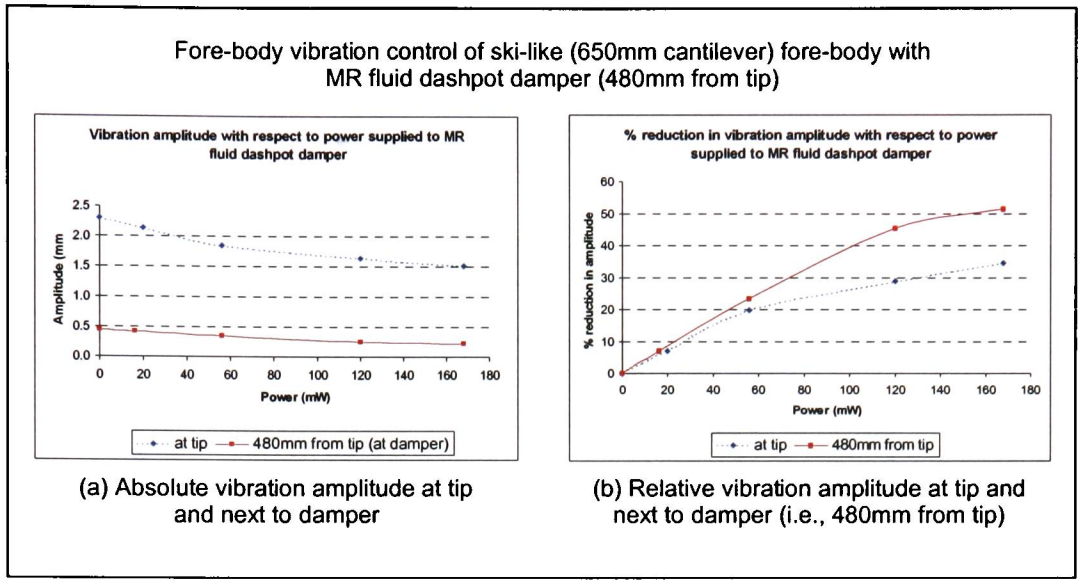

Figure 5-6: Absolute and relative vibration control (with MR fluid dashpot damper) of (aluminium) ski-like fore-body, subject to an out-of-balance excitation (w = 44rads^{-1})

The best that may be expected would be for the vibration to be completely suppressed at the damper. The theoretical deflection of a 650mm cantilever beam can be calculated, subject to a variety of forces, and compared (see Figure 5-7) with the theoretical deflection of a 480mm cantilever beam (i.e., considering the MR fluid damper acts as a built-in support through the shim).

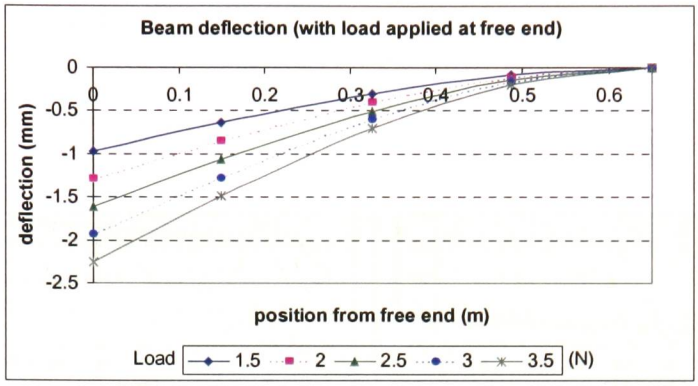

(a) Fore-body (i.e., 650mm aluminium beam) deflection under loading

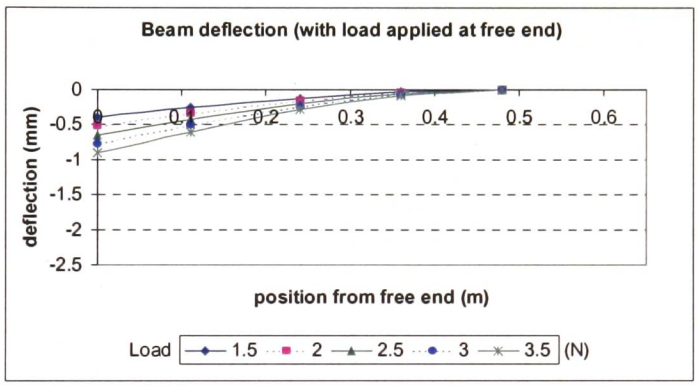

(b) Fore-body (i.e., 480mm aluminium beam) deflection under loading - assuming complete suppression at damper

Figure 5-7: Calculated deflection of aluminium ($E = 71 \text{Nmm}^{-2}$) cantilever beam

Comparing the absolute and relative vibration amplitudes at the tip and alongside the damper with power increased then decreased, the MR fluid memory effect can be observed (see Figure 5-8). Applying an initial magnetic field produces damping that may be subsequently maintained by a smaller magnetic field. For example, approximately 35% damping at the tip, initiated with a 160mW supply, can be maintained with a 90mW supply (see Figure 5-8 c). The MR fluid memory effect may be used to conserve energy by powering up and then down.

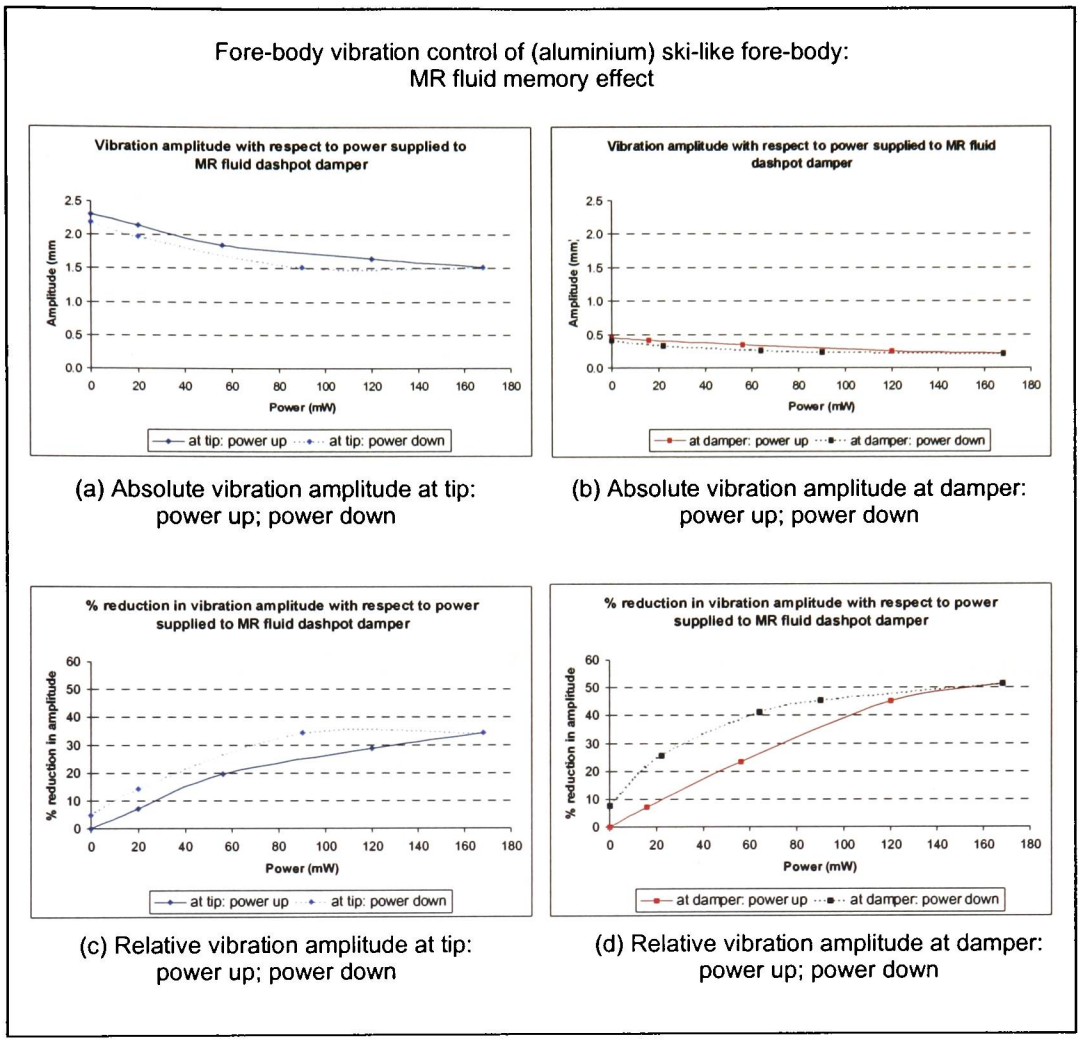

Figure 5-8: MR fluid memory effect, compared at tip (alongside vibration source) and 480mm from tip (alongside damper), on ski-like structure subject to an out-of-balance excitation (w = 44rads^{-1})

The concept demonstrator is a simplification of ski structure and ski vibratory forces. Skis are subject to a combination of pulses (i.e., forces with a finite duration) and excitation forces with complex waveforms and no precise periodicity. The out-of-balance rotor produces a harmonic force (i.e., varying sinusoidally at a given frequency – see appendix A-2) that is the simplest form of vibratory force. Adaptive damping of a ski is a significantly more complex system than the model presented. However, the results show the capability of a MR fluid damper and the demonstrator provides a system to test and develop the control interface. Development of the control interface has the potential to enable the adaptive damping of more complex time-variant vibratory forces, which may be simulated by connecting the ski-like structure to a computer controlled shaker (e.g., on the ski simulator) instead of the out-of-balance rotor.

Work on the concept demonstrator has highlighted a number of important points to be considered in any further development of the system. The small stroke produced in the MR fluid device is used to control dynamic compliance down the fore-body. A high proportion of the dynamic compliance of the fore-body relative to the shim should contribute to the stroke in the damper. It is important that dynamic compliance at the damper is not absorbed by the seal or at mechanical interfaces (i.e., hinges, or guides). Therefore, a low-off state MR fluid device must be specified and the kinematics of the damper relative to the fore-body and shim needs greater consideration.

There is opportunity to conserve power by making use of the MR fluid memory effect. Further research is required to investigate the complexity required to include a control algorithm on the microprocessor that takes advantage of the MR fluid memory effect.

5.3 Design appraisal

The location of the MR fluid damper between an overhanging shim and the fore-body of the ski is appraised. The failure of an overhanging shim in field tests (see §5.3.1) is supported with finite element analysis of the concept demonstrator system (see §5.3.3), suggesting that an alternate arrangement is required to isolate vibration. Subsequently, the suitability of the prototype diaphragm sealed MR fluid damper is discussed (see §5.3.2).

5.3.1 Shim

Following field-tests of a custom-built shim there are concerns with the overhanging shim that is advocated in the concept demonstrator (see §5.2). An aluminium shim (6mm thick, BS1470, EN755-2) was fitted with a releasable Telemark binding and mounted to a ski (170cm, Line "Maverick") on pre-inserted threads (a feature on Line skis taken from the snowboard industry). Natural rubber (6mm thick) was inserted between the shim and ski and a viscoelastic rubber end-stop was fitted at the end of the shim, over the fore-body and under the barrel containing the spring for the release kit. The location of the viscoelastic end-stop corresponds to the proposed placement of the MR fluid damper. On-piste tests lead to permanent plastic deformation of the shim, indicating that greater consideration of the shim design is required (see Figure 5-9).

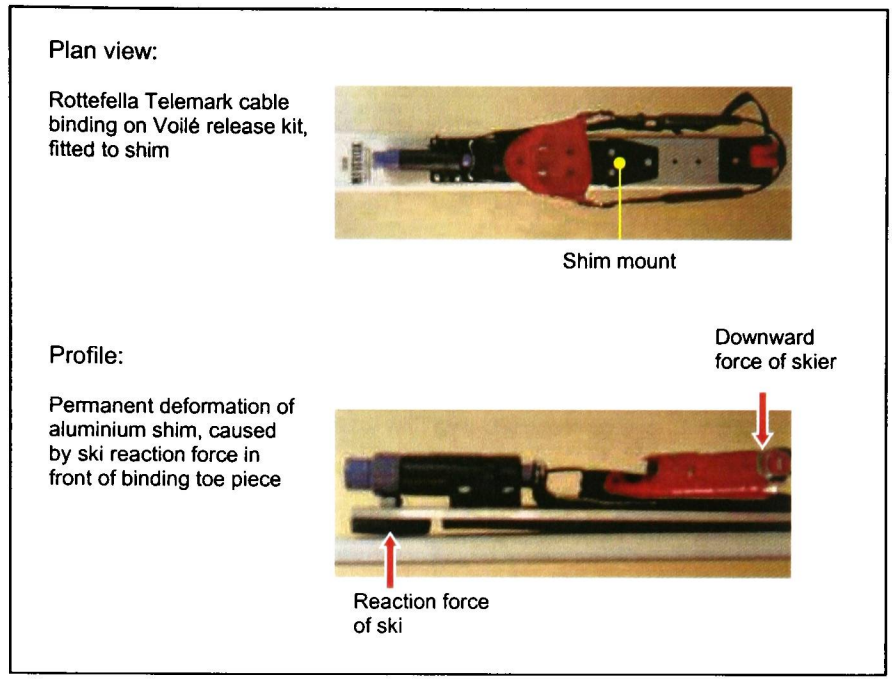

Figure 5-9: Failure of centrally mounted, overhanging shim fitted with Telemark binding, field-tested on Line ski (with pre-inserted threads to mount shim)

The original motivation for testing the shim is to investigate if bindings can be mounted to the ski without the need for multiple screws down the length of the binding – allowing the skis to flex more freely. Line claim to have achieved this with their own alpine binding, as do Salomon with their "Pilot" system (where the binding toe-piece and heel-piece are mounted on separate axles) and Völkl with their "Motion" system (where the binding is mounted on segmented rails). However, following analysis of static deflection tests (see §3.2.1.1), it is the opinion based on this research that MRS deflection is limited when the boot is in the bindings and the weight of the skier is acting down on the ski.

There is a significant difference between the Line alpine binding (a system that works - see Figure 5-10 a) and the test shim (see Figure 5-9). That difference is the position of the toe piece and force exerted by the skier, relative to the reaction force of the ski fore-body on the shim. The test shim is extended in front of the binding toe-piece to accommodate the barrel containing the spring for the release kit. Therefore, the viscoelastic end-stop is sandwiched between what may be considered two cantilever structures – comparable to the situation proposed for integration of the MR fluid damper in the concept demonstrator (see Figure 5-10 b). The fore-body acts as a lever, amplifying the force that is to be isolated through the extended shim.

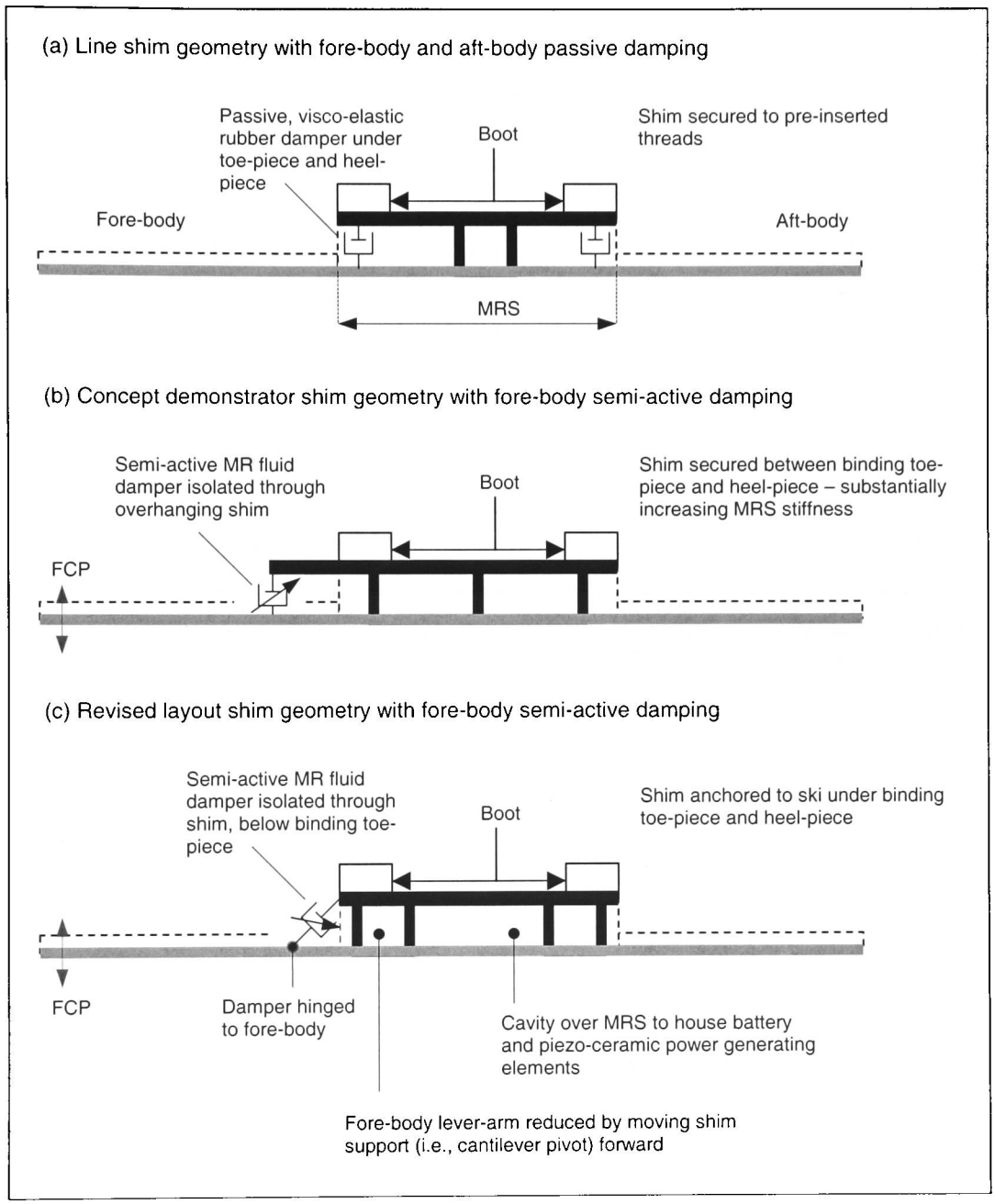

Figure 5-10: Comparison of shim geometry of (a) Line alpine binding, (b) concept demonstrator and (c) suggested revised layout for adaptive ski

A revised layout is proposed (see Figure 5-10 c) to remove the overhanging shim that is susceptible to high strain concentration. The damper is instead angled and isolated through the shim under the toe-piece. However, reducing the distance of the damper from the fore-body pivot reduces the dynamic compliance that is available to stroke the damper and thereby decreases the ability to control the moving mass of the fore-body.

5.3.2 Diaphragm sealed MR fluid damper

The diaphragm sealed prototype damper is specified to achieve a low-off state and the electromagnetic core is fixed to reduce the number of moving parts. Assuming the damper can be made to perform equally in both stroke directions, for the diaphragm sealed damper to be feasible for use on a ski it would have to be scaled down – particularly the diameter. Reducing the diameter of the damper, while maintaining the annular gap width means that the diameter of the electromagnetic core will be reduced. Therefore, the ratio of magnetic field to electrical power may be expected to be reduced, so that more power is required to achieve comparable on-state damping (comparing the prototype damper tested relative to a scaled derivative).

The kinematic relationship between the damper, fore-body and shim requires greater consideration. The dashpot damper in the concept demonstrator is unguided (i.e., there is no axial constraint) and although most of the dynamic compliance of the fore-body relative to the shim is in the vertical x-axis, there is also y-axis movement. The stroke of the diaphragm sealed damper is guided to primarily control vibration in the x-axis. A shaft runs through the fixed electromagnet core, connecting the opposing diaphragm seals that are reinforced with a washer to better act as pistons – forcing the fluid through the annular control region. The damper must allow a small amount of movement in the y-axis, or it must be hinged to the fore-body (to allow an extra degree of freedom). Any absorption of dynamic compliance at a mechanical interface may reduce the stroke in the damper and therefore compromise the ability of the damper to control fore-body vibration.

The work carried out on the concept demonstrator and with dashpot dampers is considered a proof of concept of the force control that may be provided by an MR fluid device with a view to fore-body vibration control of a ski. This research has lead to the development of a prototype diaphragm sealed, fixed core MR fluid damper.

5.3.3 Finite element modelling

A finite element model of the aluminium ski-like structure is compiled (using ABAQUS CAE) with boundary conditions modelling support of the mid-surface, constraining deflection in all axes. The response of the structure is modelled subject to a concentrated 3.5N load at the tip and an (x-axis) axial constraint between the fore-body and shim (see Figure 5-11). The axial constraint is defined by damping coefficient and elastic spring constant to model the measured characteristics of the prototype, diaphragm sealed MR fluid damper. A quadratic mesh is used for finite element analysis as this gives an unconstrained response most similar to that calculated for a cantilever beam equivalent to the fore-body.

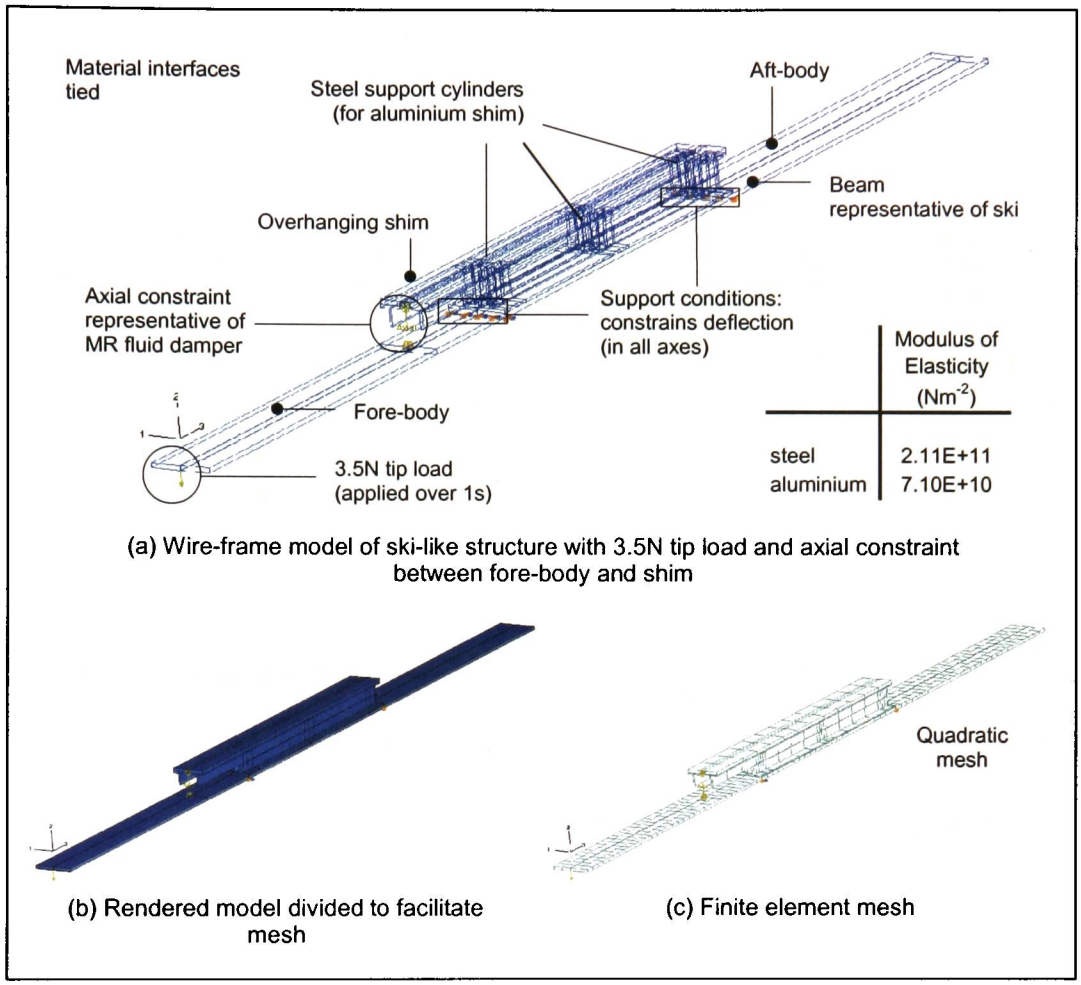

Figure 5-11: Finite element model of concept demonstrator, using ABAQUS CAE

Finite element analysis of the aluminium ski-like structure is used to predict deflection at the tip and at the axial constraint (i.e., representing the prototype MR fluid damper as a Voigt model). The static analysis carried out provides an indication of the amplitude of vibration with a concentrated force magnitude of 3.5N. The results (see Table 5-1) for MR fluid damper characteristics at four different power supplies are compared with the model of the damper off-state (i.e., where the Voigt model is defined by a damping coefficient of $20000 kgs^{-1}$). As expected (see Figure 5-7), despite a capability to reduce deflection by almost 50% at the damper location, there is considerably less reduction at the tip (<20%).

Prototype MR fluid damper characteristics		Aluminium ski-like structure			
Damping coefficient	Elastic spring constant	E=7.1E10Nm^{-2}			
kgs^{-1}	kNm^{-1}	deflection (mm)		reduction	
		at tip	at damper	at tip	at damper
20000	-	3.05	0.21	-	-
26600	13.4	2.86	0.18	6%	14%
33300	33.3	2.69	0.15	12%	29%
25000	53.0	2.64	0.14	13%	33%
25000	100	2.49	0.11	18%	48%

Table 5-1: Predicted deflection at tip and damper from finite element model of aluminium ski-like structure, with axial constraint between fore-body and shim (equivalent to measured characteristics of prototype MR fluid damper)

The results from the finite element analysis can be illustrated with the initial (unloaded) condition (e.g., see Figure 5-12 a), or as a displacement gradient (e.g., see Figure 5-12 b). It can be seen more clearly from the illustration comparing the shape of the unloaded and loaded structure that deflection of the overhanging shim may be expected (see Figure 5-12 a).

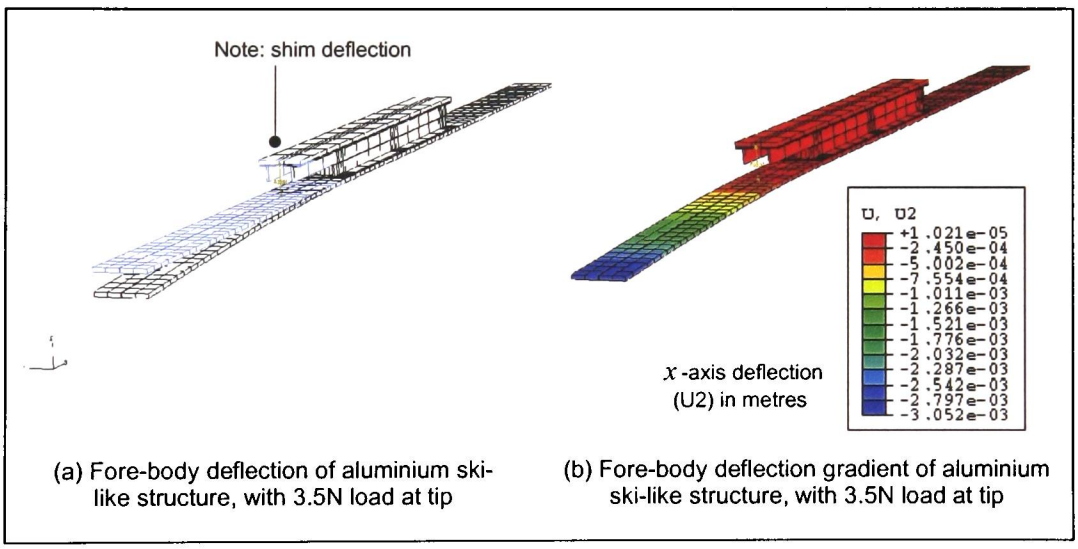

(a) Fore-body deflection of aluminium ski-like structure, with 3.5N load at tip

(b) Fore-body deflection gradient of aluminium ski-like structure, with 3.5N load at tip

Figure 5-12: Finite element analysis of fore-body deflection subject to a 3.5N load at the tip with axial constraint representative of a Voigt model (c =25000kgs^{-1}, k =100kNm^{-1}) defined from measured results from a prototype, diaphragm sealed MR fluid damper

Comparing Von Mises stress (see equation [5–1]) with zero axial constraint and that representative of the activated MR fluid damper (i.e., c =25000kgs^{-1}, k =100kNm^{-1}), it can be seen (see Figure 5-13) that the axial constraint produces stress concentration at the fore-body end of the axial constraint and the overhanging shim. The stress concentration at the fore-body end of the axial constraint is not a

concern, since the reaction force from the damper would be distributed over a greater area than that modelled. However, the evidence of stress on the overhanging shim at relatively small loads (i.e., 3.5N) is significant, particularly given the failure of the shim for the releasable Telemark binding (see §5.3.1).

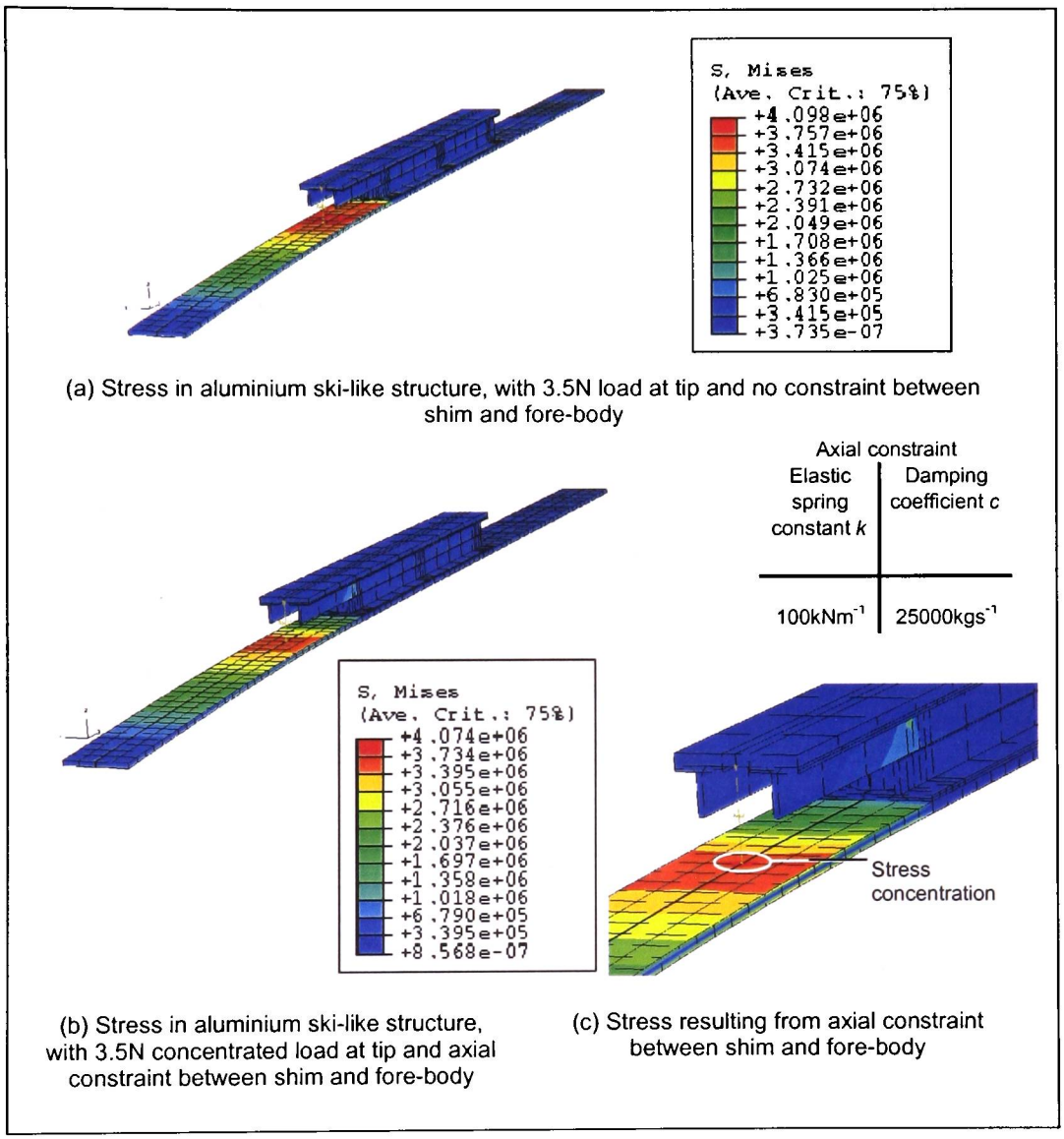

(a) Stress in aluminium ski-like structure, with 3.5N load at tip and no constraint between shim and fore-body

(b) Stress in aluminium ski-like structure, with 3.5N concentrated load at tip and axial constraint between shim and fore-body

(c) Stress resulting from axial constraint between shim and fore-body

Figure 5-13: Finite element analysis of Von Mises stress with and without axial constraint between fore-body and shim of aluminium ski-like structure

Yielding occurs when Von Mises stress (σ_V) exceeds the yield strength in tension (i.e., σ_V is a measure of surface stress):

$$\sigma_V = \sqrt{\frac{(\sigma_1 - \sigma_2)^2 + (\sigma_2 - \sigma_3)^2 + (\sigma_1 - \sigma_3)^2}{2}} \qquad [5\text{-}1]$$

where $\sigma_1, \sigma_2, \sigma_3$ are principal stresses (in orthogonal axes 1, 2 and 3).

The finite element model of the ski-like structure is used to provide a prediction of ski response. The constraint and load conditions are maintained, but the properties of the beam are changed to model the measured fore-body properties of the Salomon "Crossmax 8" and Völkl "Motion" (see Table 5-2).

The measured stiffness from fore-body deflection tests (i.e., $(EI)_{fore}$) is divided by the second moment of area of the beam (in the ski-like structure) to give an equivalent modulus of elasticity that is used to define the material property in the finite element model. There is a similar response from the Salomon and Völkl skis, as predicted from static tests (see §3.2.1.2) and given the similarity in equivalent modulus.

Prototype MR fluid damper characteristics		Salomon Xmax8				Völkl Motion			
Damping coefficient	Elastic spring constant	$E_{equivalent}$=8.32E10Nm^{-2}				$E_{equivalent}$=8.04E10Nm^{-2}			
kgs^{-1}	kNm^{-1}	deflection (mm)		reduction		deflection (mm)		reduction	
		at tip	at damper	at tip	at damper	at tip	at damper	at tip	at damper
20000	-	2.64	0.19	-	-	2.72	0.19	-	-
26600	13.4	2.49	0.16	6%	16%	2.56	0.16	6%	16%
33300	33.3	2.35	0.14	11%	26%	2.42	0.14	11%	26%
25000	53.0	2.30	0.13	13%	32%	2.37	0.13	13%	32%
25000	100	2.17	0.10	18%	47%	2.24	0.11	18%	42%

Table 5-2: Predicted deflection at tip and damper from finite element model of ski-like structure, with axial constraint between fore-body and shim (equivalent to characteristics of prototype MR fluid damper) and modulus of elasticity equivalent to measured fore-body stiffness of Salomon "Crossmax 8" and Völkl "Motion"

Significantly more work can be done to model the effects of integrating semi-active damping in a ski. The capability to predict response using measured values to define model parameters is demonstrated. This work provides measurements from static and dynamic tests from a cohort of carving skis and from analysis of a prototype, diaphragm sealed MR fluid damper. These measurements can be used to define finite element models more representative of the smart ski system and to assign boundary conditions for dynamic analysis. The structure can be remodelled to better represent ski geometry and the geometric relationship between ski, shim and damper.

6 Further Work

The aim of this section is to highlight aspects of this research that may be continued. Experimental investigation into dynamic factors of shaped (carving) skis has enabled static and dynamic analysis to be made and should provide a good foundation for further analytical work (see §6.1). A prototype short-stroke, diaphragm sealed, MR fluid damper with a fixed electromagnetic core can be developed further (see §6.2) to suit vibration control systems for diverse applications. Development of the adaptive ski concept would benefit from further analysis of ski dynamics and more research into low-off state MR fluid damping. The most significant technical issue in realising a working prototype of the adaptive ski is power supply (see §6.3). The feasibility of self-contained power generation for the system (i.e., for the electromagnet and control interface) requires further research into parasitic power generation. The cold operating environment compounds the power management problem and changes the viscoelastic properties of the MR fluid - increasing the complexity of the required control algorithm.

6.1 Ski dynamics

Information on dynamic response of skis enables conjecture on the performance of the proposed adaptive ski system. Specifications for the performance of the adaptive ski are not fully defined. The experimental and analytical techniques presented here may be extended:

1. To provide quantitative data that may be used to better support computational finite element modelling
2. To better model the ski with improved boundary conditions
3. To replicate the conditions representative of a run, on a ski in the laboratory, based on results from on slope measurements.

Torsional stiffness is identified as an important characteristic in the qualitative feel of modern alpine skis. Torsional damping may also contribute to reduced edge chatter, although there is no quantitative information in this research to support this. Further work is required to identify the performance benefits of torsional stiffness and damping. The diaphragm sealed damper is less suited to the control of torsional vibrations. Experimental results and non-specialist qualitative feedback from field-tests seem to indicate that perceived performance advantages may be linked to fore-body torsional stiffness (more so than longitudinal flex). The perceived performance advantage, due to difference in torsional stiffness, is considered to be more obvious to heavier or more aggressive skiers. A medium term future objective should be to carry out experimental and computational analysis focussed on analysis and simulation of fore-body and aft-body response. Models focussed

on fore-body and aft-body response are considered here to be of significant value to the development of skis with enhanced dynamic stability (i.e., with greater resistance to edge chatter).

Computational modelling of the ski response with information on materials and construction from the manufacturer would greatly accelerate the ability to simulate and analyse different scenarios. However, ski manufacturers are generally reluctant to release such information.

Quantitative data can be obtained using the techniques presented here (see §3), with impulse response functions being used to identify modal frequencies prior to analysis to determine frequency response functions and operational deflection shapes. This objective may be realised in the short term and would enable dynamic structural analysis to be focussed at modal frequencies. Increased sampling rates would improve the accuracy in obtaining damping coefficients.

The validity of simulations with computational models is heavily dependent on the assignment of boundary conditions. The work carried out here provides guidance on the assignment of boundary conditions, based on the experience gained in developing and using a physical simulator. Specifically it is recommended that, rather than simple support conditions at the FCP and ACP, in future more representative boundary conditions should be used.

Computational simulation would benefit from more representative modelling of the ski-snow interface. In order to model the difference between hard and soft packed snow, it is recommended here that a Voigt model be used to represent the ski-snow interface, rather than an elastic model (as used by Pärsinnen and Lehtovaara [1991], Clerc et al [1989], Devaux and Trompette [1980]). Research into the characteristics of snow may provide quantification of the elasticity and damping of hard and soft packed conditions. Equally, biomechanics research may enable better models of the skier to be incorporated into computational simulations of skis.

Improved analysis of field test data sampled at higher frequencies would also provide more information on ski-slope interaction. Extending system analysis and signal analysis to investigate discrete models with nodes along and across the fore-body would benefit understanding of ski dynamic response. A long-term future objective should be to develop laboratory test equipment to subject skis in the laboratory to forces identified following signal analysis from field testing of instrumented skis.

6.2 MR fluid damping

There is a significant body of research on engineering MR fluid devices with a large stoke for applications where there is a relatively large dynamic compliance - often with reasonably high input

forces. There is an opportunity to develop MR fluid devices for applications that require control of relatively small dynamic compliance with significant, but low input forces.

Further research is recommended to investigate the feasibility of engineering a short-stroke MR fluid device with low off-state and multi-degrees of freedom – perhaps with multi-degrees of control (to control both longitudinal and torsional vibration). It is recommended that the squeeze mode of MR fluid be considered, with a view to integrating a short stroke (<0.5mm) semi-active damper with low off state viscous force. Further research and experimentation with MR fluid filled foams and gels is recommended, with a view to producing results that may be used in finite element modelling of the adaptive ski system.

Analysis is presented from tests of a prototype short stroke, diaphragm sealed MR fluid damper with a fixed electromagnetic core. Diaphragm seals are used as an alternative to friction seals in an effort to reduce the off-state of the MR fluid device (i.e., the energy absorbed by the device without any power supplied to the electromagnet). Lowering the off-state allows greater dynamic compliance to be controlled by the MR fluid device. If the dynamic movement is small (as is the case between the fore-body and shim), any dynamic compliance that is absorbed will reduce the stroke that can be controlled by the device.

More work can be done to appraise the performance of the prototype device and develop it for low off-state applications:

1 Investigate the force-velocity relationship (>5Hz) and qualitatively and quantitatively define equivalent mechanical parameters that define the behaviour of the damper
2 Research seal designs and materials that will reduce the elasticity of the device
3 Investigate the use of MR fluids, which have a less viscous off-state consistency
4 Quantify and appraise electromagnet performance with a view to engineering an electromagnetic core that more efficiently concentrates magnetic field on the control volume of MR fluid.

Identification of the force-velocity relationship may be realised in the short term using the alternative experimental procedure presented (see §5) to enable analysis at higher frequencies. It is likely that decrease in temperature will result in an elevated fluid viscosity (i.e., off-state) and more power will be required to achieve the same apparent change in shear stress (i.e., on-state). Investigating the energy absorbed by a MR fluid device should enable the viscoelastic characteristics to be defined with respect to a number of factors - such as stroke, cycle frequency, temperature, and with respect to the power supplied to generate the magnetic field. Performance of the device should be quantified in terms of the damper-force and spring-force with respect to stroke displacement and velocity.

Changing the consistency of the fluid will have an influence on the performance of the device. Reducing iron content is likely to decrease the on-state potential and require more power to achieve the same apparent viscous change. Reducing chemical additives may reduce the long-term stability of the fluid.

More research is required to quantify efficiency of electromagnets and their performance in cold operating environments. The theoretical performance of the electromagnets wound to support this work should be compared with measured values to enable the efficiency (i.e., electrical-power: magnetic flux) to be quantified. Greater efficiency may be expected from manufactured electromagnets and therefore less power may be required to achieve the desired control with the MR fluid device. Greater power efficiency may also be achieved by considering designs to better concentrate the magnetic flux in the control regions of the device (i.e., focussing the generated magnetic flux on small volumes of MR fluid). Research into the electromagnetism of MR fluid devices has been identified as being a significant future direction – and therefore requires a longer-term commitment.

6.3 Adaptive ski

There are technical uncertainties with the proposed adaptive ski system, aside from the issue of developing a suitable MR fluid damper - discussed in the previous section. The primary concerns are associated with the power supply required by the electromagnet in the MR fluid damper.

It is proposed that piezo-ceramic elements be located over the MRS of the ski to parasitically generate power, proportional to the rate of change of strain – induced by skier movement. More research is required to verify the viability of this aspect of the concept. Specifically, to confirm if it is feasible to generate sufficient power from piezo-ceramic wafers, for the electromagnet and the control interface. If sufficient power can be generated to provide an adequate response from the system, a method to harvest the power must be developed. It is suggested here that locating the piezo-ceramic elements in the MRS may enable the ceramic to be stressed by the movement of the skier. The constraints imposed by the cold operating environment also require careful consideration for power management and efficient power storage. Losses will further reduce the power available to the electromagnet.

A micro-processor control interface (not presented in this work) has been developed by ReacTec and there are a variety of control algorithms that have been used with MR fluid devices. Development of a control algorithm suitable for application on skis requires understanding of ski dynamics and system constraints – including temperature and power supply.

7 Conclusions

1. A concept for an adaptive ski system has been proposed. The adaptive system involves a mixture of different technologies not conventionally associated with this application. Development of smart systems (in sports equipment, including skis) indicates that there is potential to integrate such technology with a view to enhancing dynamic performance (although with dubious success in the case of piezo-systems).

2. The concept is investigated, with particular focus on identifying implications for MR fluid damping. Measurements are analysed of fore-body deflection of a MR fluid damped ski-like structure. A finite element model of the ski-like system is predicts fore-body response damped with a prototype MR fluid damper.

3. A prototype short-stroke, diaphragm sealed MR fluid damper with a fixed electromagnetic core has been developed. The device is suitable for low-off state applications, where there is small but significant dynamic compliance that requires control with respect to vibration amplitude or frequency.

4. An equivalent force-displacement model of the prototype MR fluid damper is proposed based on qualitative and quantitative analysis from low frequency cyclic tests.

5. Procedures are established for quantifying physical characteristics and carrying-out dynamic analysis of skis from measurements on custom-built laboratory test equipment, enabling tests to be carried out that provide information more relevant to the real-world situation.

6. Following field-tests skiers report differences in the "feel" of skis that have measured similarities in flex. The qualitative difference may be explained by measured differences in torsional stiffness. The binding and boot significantly reduces full body flex.

7. Field-testing of skis instrumented with piezo-polymer PVDF sensors provides data that can be used to analyse the vibratory signal produced from a moving ski. PVDF sensors are considered the basis for feedback control of the adaptive ski.

8 References

Aichner N, 1978: Bodendruckverteilung und Formänderungswiderstand beim Gleitenden Ski; PhD dissertation, Technische Universität Graz, Graz

American Society of Testing and Materials (ASTM), 1994: Lateral toe release of adult alpine ski bindings under impact loading; F 1017-86

American Society of Testing and Materials (ASTM), 1994: Quasi-static release moments of alpine ski bindings; F 504-94

American Society of Testing and Materials (ASTM), 1996: Mass moment and inertia of alpine skis; F 1722-96

American Society of Testing and Materials (ASTM), 1997: Verification of ski binding test devices; F 1062-97

American Society of Testing and Materials (ASTM), 1998: Centre spring constant and spring constant balance of alpine skis; F 478-77

American Society of Testing and Materials (ASTM), 1998: Linear deformation and breaking strength of alpine skis; F 780-93a

American Society of Testing and Materials (ASTM), 1998: Standard terminology for geometry of alpine skis; F 472-92

American Society of Testing and Materials (ASTM), 1998: Torsion characteristic of alpine skis; F 779-93

Babiel S, Hartmann U, Spitzenpfeil P, Mester J, 1997: Ground-reaction forces in alpine skiing, cross-country skiing and ski jumping; *Science and skiing*; Müller E, Schwameder H, Kornexl E, Raschner C (Eds.); First International Congress on Skiing and Science, Austria; Chapman & Hall; 18; pp 200-207

Bailey T, Hubbard J E (Jr.), 1985: Distributed piezoelectric-polymer active vibration control of a cantilever beam; *AIAA Journal of Guidance and Control*; Vol. 8 (5), pp. 605-611

Broch JT, 1984: *Mechanical vibration and shock measurements*; Brüel & Kjær A/S (Denmark)

Buffington KW, Shooter SB, Thorpe IJ, Krywicki JJ, 2001: Laboratory, computational, and field study of snowboard dynamics; *Materials and science in sports*; Froes FH, Haake SJ (Eds.); The Minerals, Metals & Materials Society (TMS); pp 172-183

Carlson J D, 2003: MR device basics; *MR Technology Workshop (Strasbourg, June)*; lecture 3 pp 1-50

Carlson J D, 2003: Magnetic design; *MR Technology Workshop (Strasbourg, June)*; lecture **4** pp 1-35

Carlson J D, 2001: What makes a good MR Fluid?; *Conf. Electrorheological (ER) Fluids and Magneto-rheological (MR) Suspensions (Nice, July 9-13)*

Carlson J D, Catanzarite D M, St. Clair K A, 1996: Commercial magneto-rheological fluid devices; *Proc. 1996 Int. Conf. ER Fluids, MR Suspensions & Associated Technology (Singapore)*; pp 20-28

Carlson J D, Jolly M R, 2000: MR fluid foam and elastomer devices; *Mechatronics*; 10 pp 555-569

Chrzan M J, Carlson J D, 2001: MR fluid sponge devices and their use in vibration control of washing machines; *Proc., Annual Symposium on Smart Structures and Materials (Newport Beach, CA., March)*

Clerc C, Gaertner R, Trompette P, 1989: Computer aided design of skis; *Finite elements in analysis and design*; 5; pp 1-14

Deak A, Jorgensen J, Vagners J, 1975: The engineering characteristics of snow skis part 1: static bending and torsional characteristics; *Journal of Engineering for Industry*; pp 131-137

De Cecco M, Angrilli F, 1999: Testing ski stability; *Meas. Sci. Technol.*, 10, pp N38-N43

Devaux P, Trompette P, 1980: Modal analysis of a ski by the finite element method; *Journal of sound and vibration*; 73 (4); pp 597-600

Døssing O, 1988: Mechanical mobility measurements; *Structural testing*, part 1; Brüel & Kjær A/S; pp 1-47

Døssing O, 1988: Modal analysis and simulation; *Structural testing*, part 2; Brüel & Kjær A/S; pp 1-54

Ewins D J, 1984: Modal testing: theory and practice; *Letchworth: Research Studies Press Ltd.; Mechanical engineering research studies; Engineering dynamics series; John Wiley & Sons Inc.*

Federation Internationale de Ski, 2003/2004: *Specifications for competition equipment and commercial markings*; Oberhofen, Thunersee, Switzerland

Fitzgerald A E, Kingsley C K, Umans S D, 2003: Magnetic Circuits and Magnetic Materials; *Electric Machinery*; *McGraw-Hill series in electrical engineering. Power and Energy*; Chapter 1 pp 1-56

Fugazza D, 2003: Shape-memory alloy devices in earthquake engineering: mechanical properties, constitutive modelling and numerical simulations; *Master degree thesis: Earthquake Engineering*; European School of Advanced Studies in reduction of Seismic Risk; University of Pavia; 1; pp 5-7

Gade S, Herlufsen H, 1994: The use of impulse response function for modal parameter estimation; *Damping part 2; Technical Review;* No.2; Zaveri K (Ed.); Brüel & Kjær A/S; pp 1-27

Gade S, Zaveri K, Konstantin-Hansen H, Herlufsen H, 1994: Complex modulus and damping measurements using resonant and non-resonant methods; *Damping part 2; Technical Review* No.2; Zaveri K (Ed.); Brüel & Kjær A/S; pp 28-44

Gamma K, 1981: Ski equipment / skis; *The handbook of skiing*; Dorling Kindersley (Ed.); Pelham Books Ltd.; pp 22-26; pp 178-187

Gandhi F, Wang K W, Xia L, 2001: Magnetorheological fluid damper feedback linearisation control for helicopter rotor application; *J. of Smart Materials & Structures*; 10 pp 96-103

Genç S, Phulé P P, 2002: Rheological properties of magnetorheological fluids; *J. of Smart Materials & Structures*; 11 pp 140-146

Glenne B, 1981: Mechanics of skis; *Handbook of snow*; Gray DM, Male DH (Eds.); Pergamon Press, London 20; pp 741-765

Glenne B, DeRocco A, Vandergrift J, 1997: The modern alpine ski; *Cold Regions Science and Technology*; 26; pp 35-38

Hooper A, 2001: Smart technology: research and development at QinetiQ; *IOP Conference Proc., Smart Technology Demonstrators and Devices (Edinburgh, 12 December);* session 2, 3; pp 1-13

Hosokawa K, Kawai S, Sakata T, 2002: Improvement of damping property of skis; *Journal of Sports Engineering*; 5; pp 107-112

Howe J, 1983: *Skiing mechanics*; Poudre Press, Laporte, Colorado, USA

Hull D, Clyne TW, 1996: Elastic deformation of long-fibre composites; *An introduction to composite materials*, second edition; Clarke DR, Suresh S, Ward IM (Eds.); Cambridge solid state science series, Cambridge University Press; 4; pp 60-77

Jolly M R, Bender J W, Carlson J D, 1999: Properties and applications of commercial magnetorheological fluids; *J. of Intelligent Material Systems & Structures*; 10 pp 5-13

Jolly M R, Carlson J D, Muñoz B C, 1996: A model of the behaviour of magnetorheological materials; *J. of Smart Materials & Structures*; 5 pp 607-614

Lemaire E, Bossis G, 1991: Yield stress and wall effects in magnetic colloidal suspensions; *J. of Physics D: Applied Physics*; 24 pp 1473-1477

Li W H, Chen G, Yeo S H, 1999: Viscoelastic properties of MR fluids; *J. of Smart Materials & Structures*; 8 pp 460-468

Li W H, Du H, Chen G, Yeo S H, Guo N Q, 2002: Non-linear rheological behaviour of magnetorheological fluids: step-strain experiments; *J. of Smart Materials & Structures*; 11 pp 209-217

Liao W H, Lai C Y, 2002: Harmonic analysis of a magnetorheological damper for vibration control; *J. of Smart Materials & Structures*; 11 pp 288-296

Lind D, Sanders SP, 1996: *The physics of skiing: skiing at the triple point*; Springer-Verlag New York, Inc., USA

Meirovitch, L, 2001: *Fundamentals of vibrations*; McGraw-Hill Companies, Inc., USA

Niessen W, Müller E, Raschner C, Schwameder H, 1997: Structural dynamic analysis of alpine skis during turns; *Science and skiing*; Müller E, Schwameder H, Kornexl E, Raschner C (Eds.); First International Congress on Skiing and Science, Austria; Chapman & Hall; 20, pp 216-225

Nordt AA, Springer GS, Kollár P, 1999: Computing the mechanical properties of alpine skis; *Journal of Sports Engineering*; 2; pp 65-84

Nyquist H, 1924: Certain factors affecting telegraph speed; *Bell System Technical Journal*; 3, pp 324-346

Oh H-U, Onoda J, 2002: An experimental study of a semi-active magneto-rheological fluid variable damper for vibration suppression of truss structures; *J. of Smart Materials & Structures*; 11 pp 156-162

Pärsinnen K, Lehtovaara A, 1991: Finite element method for the calculation of nominal pressure distribution between ski and track; *Finite elements in analysis and design*; 10; pp 1-8

Piziali RL, Mote CD, 1972: The snow ski as a dynamic system; *Journal of Dynamic Systems, Measurement, and Control*; pp 133-138

Rankin P J, Ginder J M, Klingenberg D J, 1998: Electro- and magneto-rheology; *Current Opinion in Colloid and Interface Science*; 3, 4, pp 373-381

Renshaw AA, Mote CD, 1991: A model for the turning snow ski; *Skiing trauma and safety: Eighth International Symposium*, ASTM STP 1104; Mote CD, Johnson RJ (Eds.); American Society for Testing and Materials, Philadelphia, pp.217-238

Sahashi T, Ichino S, 2001: Carving-turn and edging angle of skis; *Journal of Sports Engineering*; 4; pp 135-145

Sakata T, Ito T, 1997: Considerations on mechanical properties and shape of skis; *Proc. 5th Japan International SAMP Symposium*; pp 1335-1340

Schwarz BJ, Richardson MH, 1999: Experimental modal analysis; *Proc. Computational Systems Inc., Reliability Week, Orlando, Florida*; 1, pp 1-12

Schwarz BJ, Richardson MH, 1999: Introduction to operating deflection shapes; *Proc. Computational Systems Inc., Reliability Week, Orlando, Florida*; 2, pp 1-7

Shackelford JF, 2000: Composites; *Introduction to materials science for engineers,* fifth edition; Prentice-Hall, Inc., USA; 14; pp 497-545

Sims N D, Stanway R, Peel D J, Bullough W A, Johnson A R, 1999: Controllable viscous damping: An experimental study of an electrorheological long-stroke damper under proportional feedback control; *J. Smart Materials & Structures*; 8 pp 601-615

Sirohi J, Chopra I, 2000: Fundamental understanding of piezoelectric strain sensors; *Journal of Intelligent Material Systems and Structures*; Vol. 11 (4), pp 246-257

Spencer (Jr.) B F, Dyke S J, Sain M K, Carlson J D, 1997: Phenomenological model of magnetorheological damper; *ASCE J. of Engineering Mechanics*; 123, 3, pp 230-238

Stanway R, 2002: Smart fluids – the shock of the new; *Materials World, February*; pp 10-12

Strong AB, 2000: *Plastics: materials and processing*, second edition; Prentice-Hall, Inc., USA

Tang X, Conrad H, 2000: An analytical model for magnetorheological fluids; *J. of Physics D: Applied Physics*; 33 pp 3026-3032

Thomson WT, 1993: *Theory of vibration with applications*, fourth edition; Prentice-Hall, Inc., USA

Wang X, Gordaninejad F, 2001: Dynamic modelling of semi-active ER/MR fluid dampers; *Damping and Isolation, Proceedings of SPIE Conference on Smart Materials and Structures*; Vol. 4331, pp 82-91

Watson P, 2001: Improvements in or relating to skis; *British patent application: GB0129588; European patent application: PCT/GB02/05551; International patent application: PCT/GB2002/005551*

Watson P, 2004: Improvements in or relating to vibration control; *International patent application: PCT/GB2004/003595*

Watson P, Blackford J, 2001: Smart technology – smart skis; *Proc. Smart Technology Demonstrators and Devices IOP Conference, Edinburgh*; 4, pp 1-15

Yang G, Spencer (Jr.) B F, Carlson J D, Sain M K, 2002: Large-scale MR fluid dampers: modelling and dynamic performance considerations; *Engineering Structures*; 24 pp 309-323

Yanyo L C, 2003: Introduction to rheology; *MR Technology Workshop (Strasbourg, June)*; lecture 1 pp 1-25

Yoneyama T, Kagawa H, Okamoto A, Sawada M, 2000: Joint motion and reacting forces in the carving ski turn compared with the conventional ski turn; *Journal of Sports Engineering*; 3; pp 161-176

Young WC, 1989: ROARK's formulas for stress and strain; sixth edition; *McGraw-Hill International Editions*

Zipser L, Richter L, Lange U, 2001: Magnetorheologic fluids for actuators; *Sensors and Actuators A*; 92 pp 318-325

Appendix A

Forced Damped Vibration

System characteristics, that influence dynamic response to a vibratory force, are introduced (see §A-1). Equations are derived for amplitude and phase of a system subject to a single harmonic forced damped vibration (see §A–2). The relationship between displacement amplitude with respect to frequency is considered. Subsequently, a vibrating system subject to multiple harmonic forces is represented mathematically (see §A–3). Finally, techniques are presented for analysing experimental data from such vibrating systems (see §A–4).

A-1 System characteristics

Characteristics of the system contribute to dynamic stability (or lack of). Subjected to a vibratory force ($F(t)$ – i.e., one that is time dependent), the dynamic response of the system will depend on its mass (m), stiffness (k) and damping (c) characteristics (see equation [A-1]).

$$F(t) = m\ddot{x} + c\dot{x} + kx \qquad \text{[A-1]}$$

Mass (m) controls the amount of acceleration ($\ddot{x}$), stiffness (k) controls the amount of displacement (x) and damping (c) controls the amount of velocity ($\dot{x}$ – i.e., rate of change of displacement) in the system. Stiffness (see §A-1.1) and damping (see §A-1.2) are of interest in this work – specifically the ability to adapt these characteristics using a semi-active MR fluid damper, for enhanced dynamic control.

A-1.1 Stiffness

An undamped (spring-mass) system that is excited (i.e., with an initial displacement) will undergo free vibration and oscillate at its natural frequency (f_o : a property of the system).

Consider a harmonic excitation (in terms of displacement) as a function of time (see Figure A 1):

i.e., $$x(t) = A_{\mathrm{Re}} \cos wt + A_{\mathrm{Im}} \sin wt = A\cos(wt - \phi) \qquad \text{[A-2]}$$

Comprising real (A_{Re}) and imaginary parts (A_{Im}) and with angular frequency w (measured in rad/s), the harmonic function has:

amplitude $$A = \sqrt{A_{\text{Re}}^2 + A_{\text{Im}}^2} \quad \text{[A-3]}$$

and phase angle $$\phi = \tan^{-1} \frac{A_{\text{Re}}}{A_{\text{Im}}} \quad \text{[A-4]}$$

Rewriting the trigonometric function (equation [A-2]) in exponential form (illustrated in an Argand diagram – see Figure A 1 a):

$$x(t) = A_{\text{Re}} e^{jwt} \quad \text{[A-5]}$$

where $j = \sqrt{-1}$

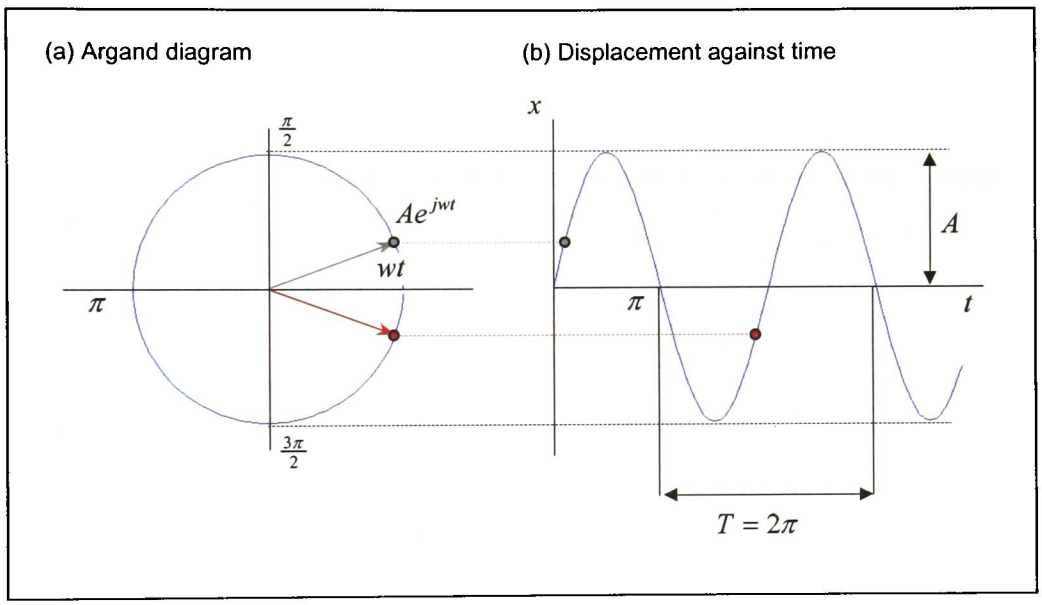

Figure A 1: Harmonic motion (produced with reference to Meirovitch [2001] and Thomson [1993])

The period of oscillation is: $$T = \frac{2\pi}{w} \quad \text{[A-6]}$$

Since the natural frequency (measured in Hz) is the reciprocal of the period:

$$f_o = \frac{1}{T_o} \quad \text{[A-7]}$$

Therefore, $$w_o = 2\pi \cdot f_o \quad \text{[A-8]}$$

Derivations of harmonic excitations are presented subsequently (see appendix A-2) and show that the angular frequency is:

$$w_o = \sqrt{\frac{k}{m}} \qquad [A\text{-}9]$$

where k is the spring constant (see §2.1.3.2) and m is the mass of the system.

Therefore, increasing mass will decrease the natural frequency, while increasing stiffness will increase the natural frequency. Smart materials may enable the stiffness to be adapted so that the natural frequency is increased beyond the upper frequency that may be expected to excite the ski over its operating range.

A-1.2 Damping

Conventionally, viscoelastic materials (see §2.1.3.2) are included in the ski composite to damp vibrations.

A damped system will dissipate energy in order to control motion. For an underdamped system, the angular resonant frequency of damped oscillation (w_d) is:

$$w_d = \frac{2\pi}{T_d} = w_o\sqrt{1-\zeta^2} \qquad [A\text{-}10]$$

where, T_d is the damped period of motion (in seconds) and ζ is the non-dimensional damping ratio (or viscous damping factor) - investigated experimentally (see §3.3.3 and appendix C).

$$\zeta = \frac{c}{c_c} \qquad [A\text{-}11]$$

where, c_c is the critical damping between oscillatory and non-oscillatory motion:

$$c_c = 2m\sqrt{\frac{k}{m}} = 2mw_o = 2\sqrt{km} \qquad [A\text{-}12]$$

The system is underdamped if $c < c_c$ and overdamped if $c > c_c$. Therefore, in the underdamped case ($0 < \zeta < 1.0$), there is oscillatory motion and in the overdamped case $\zeta > 1.0$, the motion is non-oscillatory (see Figure A 2).

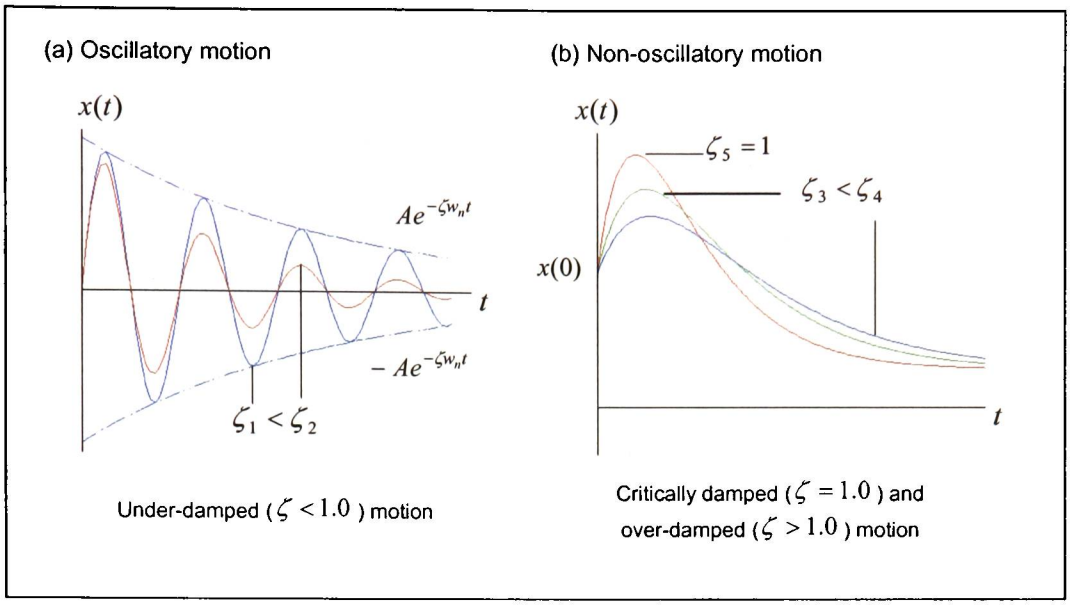

Figure A 2: Damped motion (produced with reference to Meirovitch [2001] and Thomson [1993])

Therefore, dividing through by m, equation [A-1] can be rewritten (rearranging and substituting equations [A-10], [A-11] and [A-12]) for a viscously damped single-degree-of-freedom system:

$$\frac{F(t)}{m} = \ddot{x} + 2\zeta w_o \dot{x} + w_o^2 x \qquad \text{[A-13]}$$

Smart materials, in addition to adapting stiffness and raising the value of the natural frequency (see appendix A-1.1), may be used to vary the damping characteristic to efficiently dissipate energy proportional to the velocity (see §2.1.3.2, equation [2-22]).

A-2 Single harmonic force

For concept verification, a single harmonic force is used (1) on a simply supported steel beam (as described below) and (2) on a ski-like structure to model fore-body vibration in a ski (i.e., the concept demonstrator). A single harmonic force is relatively easy to produce and enables analysis of experiments on a simplified prototype system to be compared with theory.

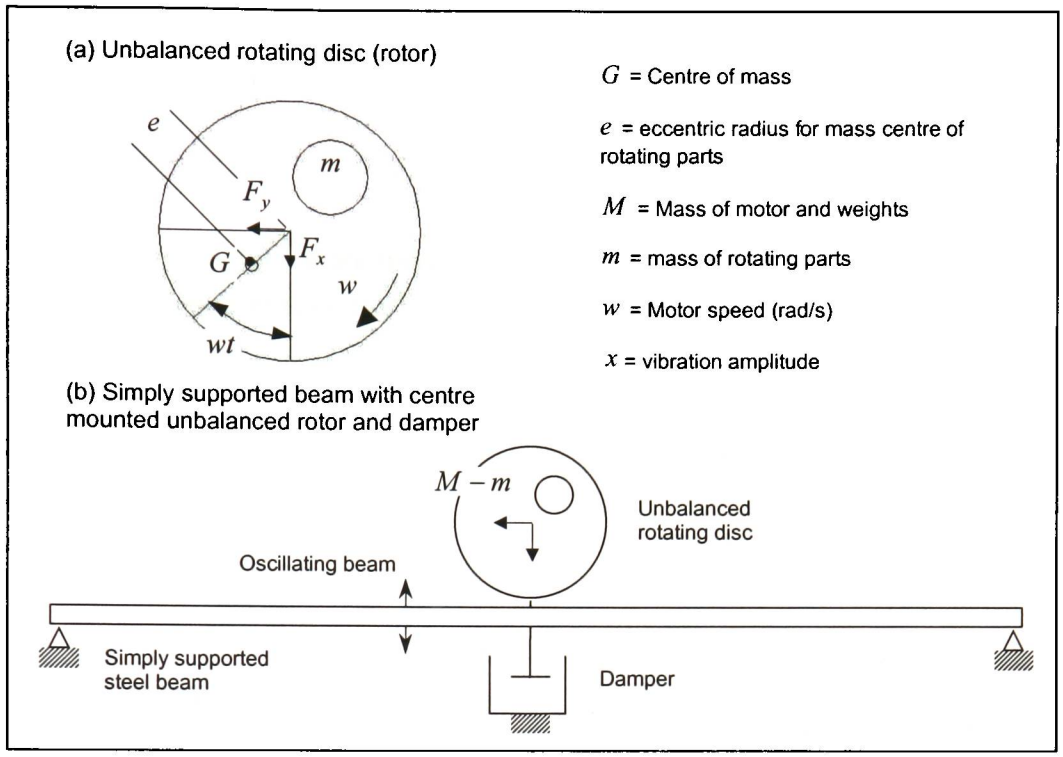

Figure A 3: System schematic

Consider an unbalanced rotating disc driving an electric motor mounted at the mid-point of a simply supported beam (see Figure A 3). When rotated at constant speed, the unbalanced disc induces a harmonic force that excites bending vibration of the motor-beam system.

Modelling as a single degree of freedom system (see Figure A 4), an equation of motion can be derived using Newtonian mechanics.

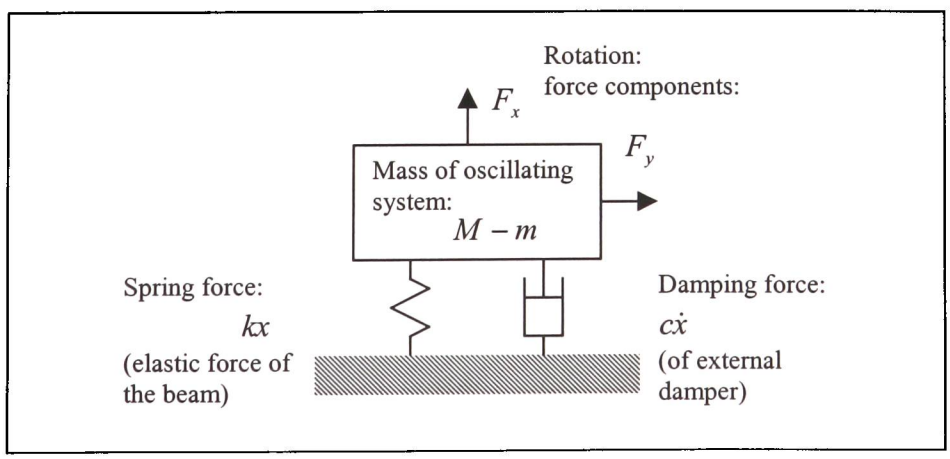

Figure A 4: System free body diagram

The resolved component of the force induced by the rotating disc in the x-direction is:

$$F_x = m(\ddot{x} - ew^2 \cos wt) \quad \text{[A-14]}$$

and the mechanical equation of the oscillating system is:

$$(M - m)\ddot{x} = -F_x - kx - c\dot{x} \quad \text{[A-15]}$$

where M is the total mass of the system and m is the mass of the rotating part (removed from the disc), subject to elastic restoring force (kx) of the beam and damping force ($c\dot{x}$) of the damper.

Combining equations [A-14] and [A-15] gives the differential equation of motion:

$$M\ddot{x} + c\dot{x} + kx = mew^2 \cos wt \quad \text{[A-16]}$$

The disturbing force is harmonic at a circular frequency (w) corresponding to motor speed.

A solution representing steady forced vibration at the same frequency is obtained by assuming a solution of the form:

$$x(t) = A\cos wt + B\sin wt \quad \text{[A-17]}$$

Therefore,

$$\dot{x}(t) = -Aw\sin wt + Bw\cos wt \quad \text{[A-18]}$$

$$\ddot{x}(t) = -Aw^2 \cos wt - Bw^2 \sin wt \quad \text{[A-19]}$$

Substituting equations [A-17], [A-18] and [A-19] in equation [A-16]:

$$\begin{aligned} &M(-Aw^2 \cos wt - Bw^2 \sin wt) \\ &+c(-Aw\sin wt + Bw\cos wt) \\ &+k(A\cos wt + B\sin wt) = mew^2 \cos wt \end{aligned} \quad \text{[A-20]}$$

and factorising coefficients of $\cos(wt)$ and $\sin(wt)$:

$$\begin{aligned} &(-MAw^2 + cBw + kA)\cos wt \\ &-(MBw^2 + cAw - kB)\sin wt = mew^2 \cos wt \end{aligned} \quad \text{[A-21]}$$

Equating coefficients of sine and cosine:

$$-MAw^2 + cBw + kA = mew^2 \quad \text{[A-22]}$$

$$-(MBw^2 + cAw - kB) = 0 \quad \text{[A-23]}$$

Therefore, solving for unknowns A and B:

From equation [A-23]: $$A = \frac{B(k - Mw^2)}{cw} \quad \text{[A-24]}$$

Substituting equation [A-24] in equation [A-22]:

$$B \cdot \left[- Mw^2 \left(\frac{k - Mw^2}{cw} \right) + cw + k \left(\frac{k - Mw^2}{cw} \right) \right] = mew^2 \quad \text{[A-25]}$$

So, $$B = \frac{mew^2(cw)}{-Mw^2(k - Mw^2) + (cw)^2 + k(k - Mw^2)} \quad \text{[A-26]}$$

and $$A = \frac{mew^2(k - Mw^2)}{-Mw^2(k - Mw^2) + (cw)^2 + k(k - Mw^2)} \quad \text{[A-27]}$$

Considering the system in terms of a phase angle (ϕ) - i.e., allowing the wave to be shifted along the time axis and enabling the system to be represented by a cosine function:

$$x(t) = x_o \cos(wt - \phi) \quad \text{[A-28]}$$

Using trigonometric identities, equation [A-28] can be rewritten:

$$x(t) = (x_o \cos\phi)\cos wt - (x_o \sin\phi)\sin wt \quad \text{[A-29]}$$

Equating the coefficients of $\cos(wt)$ and $\sin(wt)$ in equations [A-26] and [A-29] in terms of unknowns A and B:

$$A = (x_o \cos\phi) \quad \text{[A-30]}$$

$$B = (x_o \sin\phi) \quad \text{[A-31]}$$

Therefore, since:

$$\text{Phase angle } \phi = \tan^{-1}\left(\frac{x_o \sin\phi}{x_o \cos\phi} \right) \quad \text{[A-32]}$$

and $$\text{Amplitude } x_o = \left(x_o^2 \sin^2\phi + x_o^2 \cos^2\phi \right)^{\frac{1}{2}} \quad \text{[A-33]}$$

Substituting values of A & B (from equations [A-26] and [A-27]) into equations [A-30] and [A-31] and using equation [A-32]:

Phase angle $$\phi = \tan^{-1}\left(\frac{cw}{k - Mw^2}\right) \quad \text{[A-34]}$$

Similarly, simplifying the denominator in equations [A-26] and [A-27] and substituting equations [A-30] and [A-31] in equation [A-33]:

Amplitude $$x_o = \left\{\frac{\left[mew^2(cw)\right]^2 + \left[mew^2(k - Mw^2)\right]^2}{\left[(k - Mw^2)^2 + (cw)^2\right]^2}\right\}^{\frac{1}{2}} \quad \text{[A-35]}$$

Factorising [A-35] $$x_o = \left\{\frac{(mew^2)^2\left[(k - Mw^2)^2 + (cw)^2\right]}{\left[(k - Mw^2)^2 + (cw)^2\right]^2}\right\}^{\frac{1}{2}} \quad \text{[A-36]}$$

So, $$x_o = \frac{(mew^2)}{\sqrt{(k - Mw^2)^2 + (cw)^2}} \quad \text{[A-37]}$$

It can be seen from equation [A-37], that the amplitude of vibration is large when the natural frequency of vibration (w_o) is:

$$w = w_o = \sqrt{\frac{k}{m}} \quad \text{[A-38]}$$

Therefore, at $w = w_o$ the denominator in equation [A-37] is minimised. So, for the resonance condition (substituting equation [A-38] in equation [A-37]), the peak amplitude is:

$$x_o = \frac{me}{c} \cdot \sqrt{\frac{k}{m}} \quad \text{[A-39]}$$

Estimates of vibration amplitude at high and low frequency may also be made (substituting values of w in equation [A-37]):

$$w \to 0;\ x_o \to 0 \quad \text{[A-40]}$$

$$w \to \infty;\ x_o \to \frac{me}{M} \quad \text{[A-41]}$$

The relationship between equations [A-38], [A-39], [A-40] and [A-41] is illustrated (see Figure A 5).

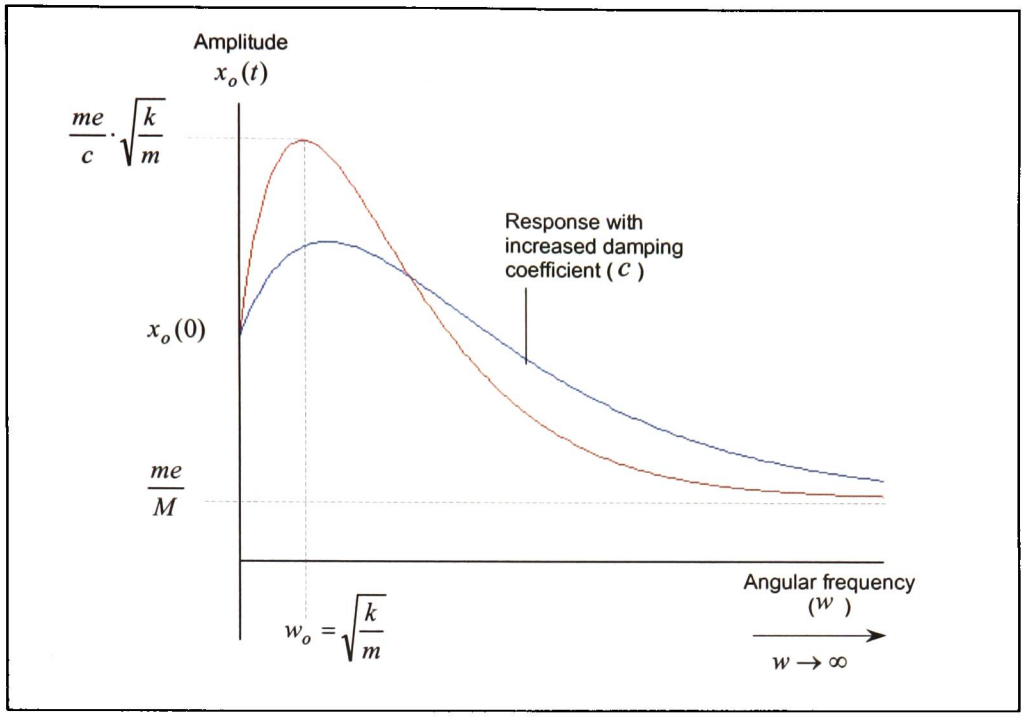

Figure A 5: Variation of vibration amplitude to exciting frequency

Phase angle is also frequency dependant (substituting values of w in equation [A-34] and with reference to Figure A 6):

$$w \to 0;\ \phi \to 0 \qquad \text{[A-42]}$$

$$w \to w_o;\ \phi \to \frac{\pi}{2} \qquad \text{[A-43]}$$

$$w \to \infty;\ \phi \to 0 \qquad \text{[A-44]}$$

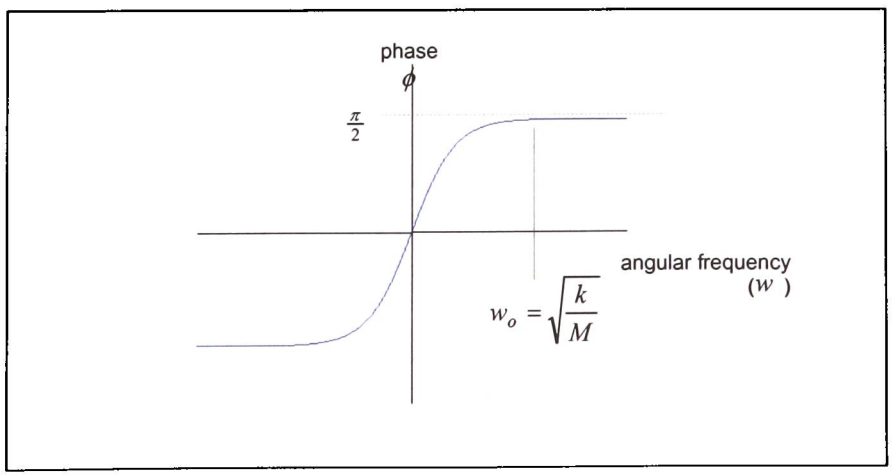

Figure A 6: Phase angle with respect to frequency

A-3 Multiple harmonic forces

Considering a system subjected to multiple harmonic forces, (with reference to equation [A-28]) the displacement may be represented by:

$$x(t) = X_1 \cos(w_1 t - \phi_1) + X_2 \cos(w_2 t - \phi_2) + ... + X_n \cos(w_n t - \phi_n) \qquad [A\text{-}45]$$

where X_n is the displacement amplitude; w_n is the angular frequency (i.e., $w = 2\pi \cdot f$) and ϕ_n is the phase angle produced by the n^{th} harmonic force.

For example, the displacement of a system subjected to two harmonic forces may be represented by:

$$x(t) = X_1 \cos(w_1 t - \phi_1) + X_2 \cos(w_2 t - \phi_2) \qquad [A\text{-}46]$$

Corresponding to the motion illustrated (see Figure A 7).

The MATLAB code used to generate Figure A 7 c is presented below, where "h1" and "h2" are functions (of time) used to produce a data set for two separate and distinct harmonics.

```
t=0:0.005:0.5;                          %% specify: time difference and period                1
        h1=5*sin(2*pi*7*t);             %% first harmonic (generates data set w.r.t time)     2
        h2=2*sin(2*pi*14*t+45*pi/180);  %% second harmonic                                     3
plot(t,h1+h2,'g'); axis ([0 0.5 -8 8]); %% plot (in green) specified axes                       4
```

The vibrating system comprises two harmonics: the first (produced by the function "h1") has amplitude of 5mm and a frequency of 7Hz; the second (produced by the function "h2") has amplitude of 2mm and a frequency of 14Hz, with a phase of 45°.

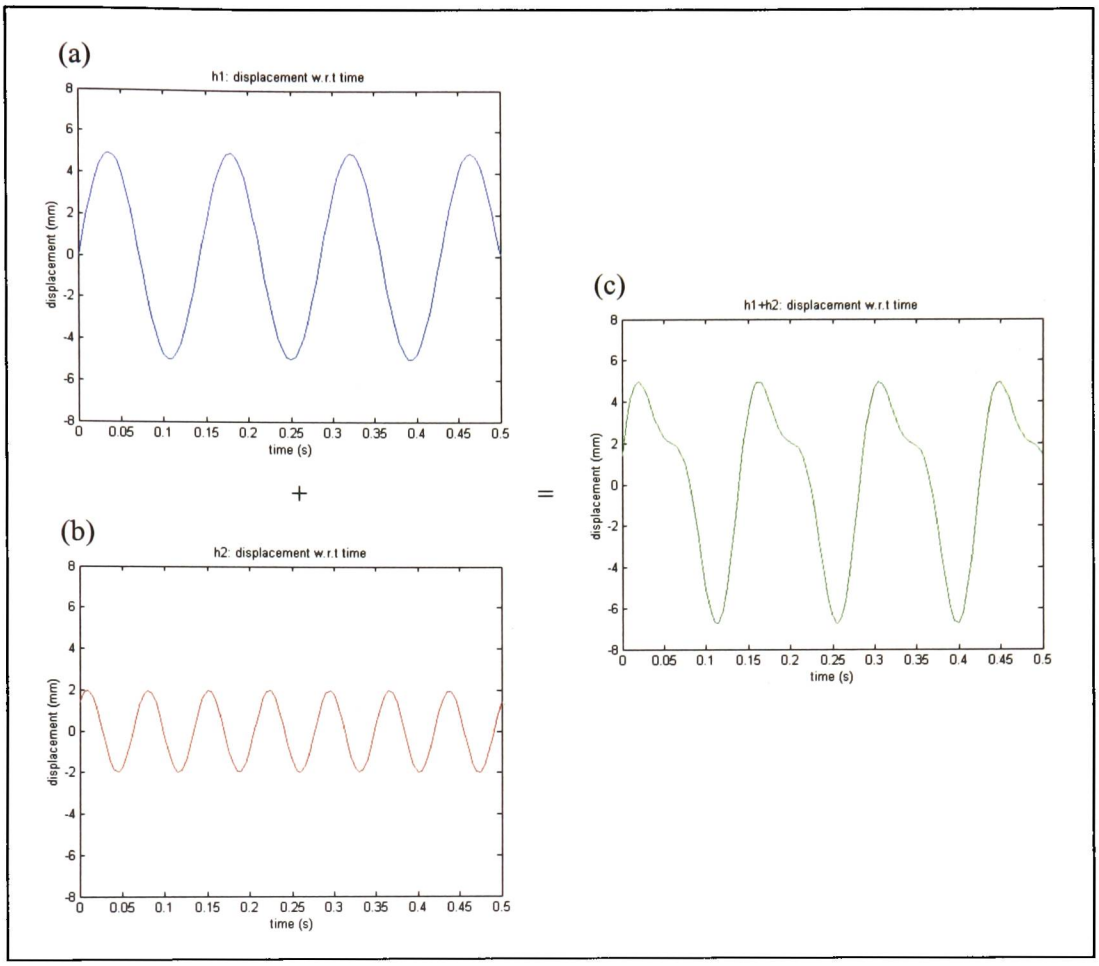

Figure A 7: Displacement (induced by two harmonic forces) with respect to time

A-4 Vibration analysis

Fourier series enable an alternative representation of data to be presented that is useful for analysis. Instead of representing the signal amplitude in the time domain, a Fourier analysis can be performed to transform data into the frequency domain.

A Fourier series takes a signal and decomposes it into a sum of sines and cosines of different frequencies.

$$f(t) = a_0 + \sum_{n=1}^{\infty}[a_n \sin(2\pi nt) + b_n \cos(2\pi nt)] \qquad \text{[A-47]}$$

$f(t)$ is the signal in the time domain, where a_n and b_n are the unknown coefficients of the series. The integer, n, corresponds to the frequency (Hz).

Techniques are presented for analysing time-domain data so that a function may be derived and used to represent the vibration in the measured system. Examples demonstrate the validity of the techniques, with output values from the processing of defined functions being compared with the function coefficients.

A-4.1 Amplitude with respect to frequency

The Fast Fourier Transform (FFT) algorithm is commonly used to compute discrete data and is built into MATLAB. Referring back to the example presented in the previous section (appendix A-3), a MATLAB code for FFT analysis of a vibrating system (i.e., modelled by "h1" and "h2") is presented below:

```
T=2;                                %% define time period                          1
t=0:0.01:2;                         %% define time difference & period              2
N=201;                              %% define number of samples                     3
freq=[0:N/2-1]/T;                   %% define frequency (range w.r.t T)             4

        h1=5*sin(2*pi*7*t);         %% first harmonic (generates data set w.r.t time) 5
        h2=2*sin(2*pi*14*t+45*pi/180); %% second harmonic                           6
        ht=h1+h2;                   %% total (sum of first and second harmonics)    7
f=fft(ht);                          %% fft (ht)                                     8
  f=f(1:100);                       %% excluding -ive frequencies (half the data set) 9
 a=2/N*imag(f);                     %% imaginary coefficients (of fft)              10
 b=2/N*real(f);                     %% real coefficients (of fft)                   11
  ampl=(a.^2+b.^2).^0.5;            %% ampl (ht)                                    12
plot(freq,ampl);                    %% plot (ampl against freq)                     13
```

Parameters are defined on lines 1-4 and will be kept the same in subsequent examples. The FFT of a data set created by the function "ht" is carried out on line 8:

The plot generated by the above code is presented in Figure A 8, showing displacement amplitude against frequency. The frequency and amplitude correlate to the input equations (i.e., amplitude of 5mm with a frequency of 7Hz for "h1" and amplitude of 2mm with a frequency of 14Hz for "h2"), demonstrating the effectiveness of the code.

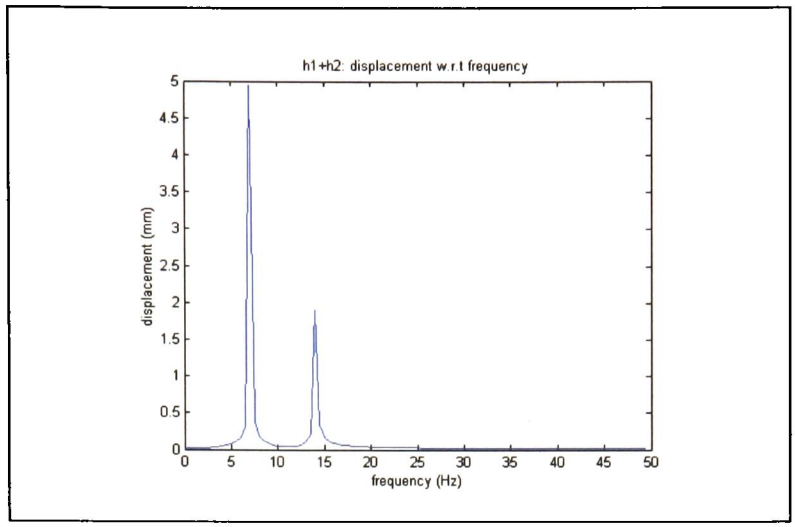

Figure A 8: Quantifying amplitude in the frequency domain

The MATLAB code computes the real and imaginary parts of the FFT and then calculates the absolute value – enabling the frequency and amplitude to be quantified. The real part of the FFT corresponds to the cosine series and the imaginary part corresponds to the sine series.

The MATLAB FFT returns data that is divided by N/2 to obtain the coefficients used in the sine and cosine series (equation [A-47]). The coefficients are returned in reverse-wrap-around order, with the positive frequencies in the first half of the list and the negative frequencies in the second half. The positive and negative frequencies are complex conjugates (see equations [A-48] and [A-49]) and therefore, since they add no information, the negative frequencies are ignored in the code (line 9) presented above.

i.e., the coefficient of the frequency = 1 is the complex conjugate of the frequency = -1, where, the complex number, c, is:

$$c = a + bj \qquad \text{[A-48]}$$

and the complex conjugate is:

$$\bar{c} = (a - bj) \qquad \text{[A-49]}$$

where the imaginary number (i.e., $\sqrt{1}$) is represented by j

A-4.2 Phase

MATLAB can be used to compute the phase angle (in radians) of the complex matrix. For example, consider the second harmonic (i.e., "h2") in the previous example (see §A-4.1), assuming the same

defined parameters (lines 1-4). Plotted against frequency between 13Hz and 15Hz (see Figure A 9), the phase (in degrees) can be identified when compared to the same harmonic function without phase (i.e., "h2p": "h2" with the phase term removed). Lines 11 and 12 in the code below are used to calculate the phase angle (of "h2" and "h2p" respectively), as the inverse tangent (recalling equation [A-32] from §A-2) of the real over the imaginary parts of the FFT.

```
        h2p=2*sin(2*pi*14*t);                  %% h2 with phase removed (derived)                  5
        h2=2*sin(2*pi*14*t+45*pi/180);         %% h2 data set (phase in radians)                    6
f2p=fft(h2p);                                  %% fft of h2p                                        7
f2p=f2p(1:N/2);                                %% complex conjugate ignored                         8
f2=fft(h2);                                    %% fft of h2                                         9
f2=f2(1:N/2);                                  %% complex conjugate ignored                         10
        phase=(angle(f2).*180/pi);             %% inverse tangent of real/imaginary parts of fft    11
        phase0=(angle(f2p).*180/pi);           %% as above (in degrees)                             12
plot(freq,phase);                              %% plot phase (h2) against frequency                 13
grid on, axis([13 15 -180 180]);               %% specify grid and axes dimensions                  14
hold;                                          %% hold plot                                         15
plot(freq,phase0,'r--');                       %% plot phase (h2p) against frequency (red, dashed)  16
axis([13 15 -180 180]);                        %% axes dimensions                                   17
```

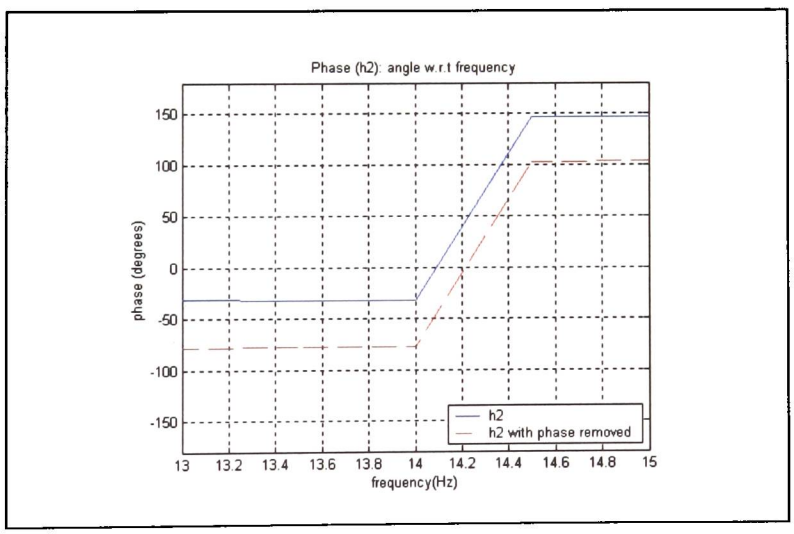

Figure A 9: Quantifying phase with respect to frequency

The difference between the horizontal lines in the plot (of "h2" and "h2p" in Figure A 9) corresponds to the phase (i.e., phase of "h2" is 45°). The frequency range is identified beforehand (i.e., 13-15Hz since the frequency of "h2" is known to be approximately 14Hz), along with the amplitude (see §A-4.1).

The practical significance is the ability to identify the phase from a discrete data set, having already determined the frequency and amplitude using the technique presented in the previous section (see §A-4.1). If "h2" represents a discrete data set, the amplitude method (presented in §A-4.1) can be used to derive h2p (i.e., "h2" without phase). The MATLAB code presented in this section (above) shows how the phase angle (of a FFT) may be obtained. Comparing the phase-frequency relationship of the discrete data set (i.e., "h2") with the derived data set (i.e., "h2p") enables the phase of the discrete data set (i.e., "h2") to be identified.

Combined, the code presented in this section and the previous section (§A-4.1) make it possible to derive the components of an oscillation and represent it as a function (comparable to equation [A-45], §A-3). This may be used to process accelerometer data that is subject to drift, so that a function may be derived that can be manipulated to obtain velocity and displacement estimates.

A-4.3 Filtering noise

The Fourier transform is useful for extracting information from a signal with a noisy background. For example, adding random noise to the signal shown in figure Figure A 7 c (i.e., produced by "h1" and "h2") will result in the plot illustrated (see Figure A 10).

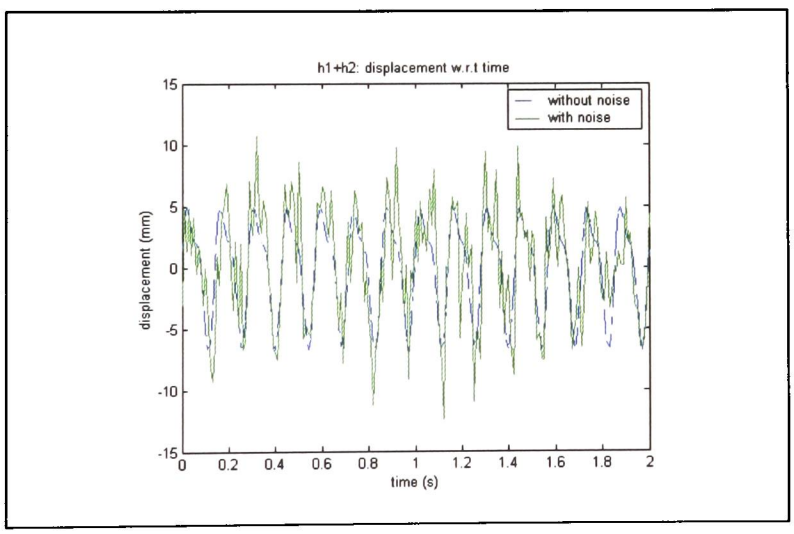

Figure A 10: Signal hidden by background noise

The MATLAB code used to plot Figure A 10 appears below. The code on line 5 adds a random number that overwhelms the signal. The random number producing the noise has amplitude of 3.

```
t=0:0.01:2;                          %% time difference & period                    1
    h1=5*sin(2*pi*7*t);              %% first harmonic (generates data set w.r.t time)  2
```

```
h2=2*sin(2*pi*14*t+45*pi/180);   %% second harmonic                    3
ht=h1+h2;                        %% vibration (sum of harmonics)       4
htr=ht+3*randn(1,N);             %% vibration with noise (ampl:3)       5
plot(t,ht,'--');                 %% plot vibration / time (dashed)      6
hold                             %% hold current plot                  7
plot(t,htr,'g')                  %% plot vibration with noise / time (in green)  8
```

The power spectrum can be used to filter a noisy signal so that the frequencies associated with "h1" and "h2" may be identified. The MATLAB code to filter the signal using the power spectrum is presented below - assuming the same parameters and functions in the code above, up to and including line 5 (i.e., continuing to number from 5). The post-filtered output of the time-domain signal (see Figure A 10) is illustrated in the frequency-domain (see Figure A 11).

```
T=2;                             %% time period                        6
N=201;                           %% number of samples                  7
p=abs(fft(htr))/(N/2);           %% absolute values of fft (htr)       8
p=p(1:N/2).^2;                   %% power                               9
freq=[0:N/2-1]/T;                %% frequency                           10
plot(freq,p);                    %% plot fft power ratio against freq   11
```

The complex conjugate is again ignored, by dividing by N/2 in line 8 and including only half the data set (in line 9).

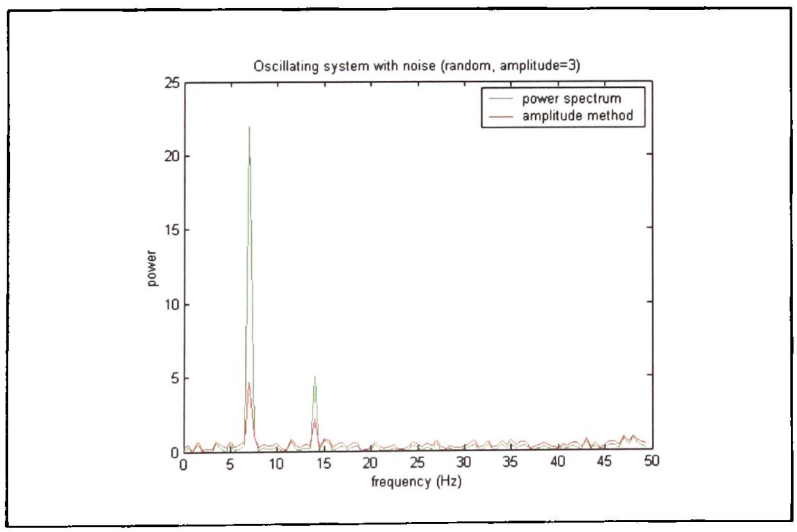

Figure A 11: Comparing the power spectrum with the amplitude method for analysis of an oscillation (h1+h2 + random noise of amplitude 3)

The code presented earlier (in §A-4.1) compares well with the result from the power spectrum (see Figure A 11), with the added advantage of providing a quantifiable estimate of the amplitude. However, if the system is subject to greater noise, the power spectrum provides clearer identification of the frequencies of interest. A comparison is shown (Figure A 12) of the two methods used to analyse the same vibration (i.e., "ht"=h1+h2), with random noise of amplitude 5 (i.e., changing line 5 of the code above). Therefore, when analysing data subject to noise (e.g., field-test data) it is advisable to start by looking at the output from the power spectrum and compare it with results from the amplitude method.

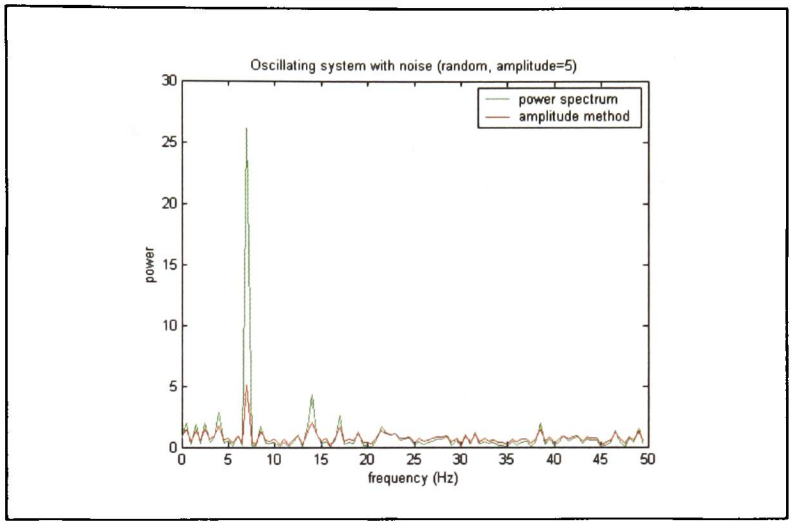

Figure A 12: Comparing the power spectrum with the amplitude method for analysis of an oscillation (h1+h2 + random noise of amplitude 5)

The concepts presented here are used to process data from tests on skis using the ski simulator and from field-testing of instrumented skis.

Appendix B

Supplementary Ski Measurements

Results from tests supplementary to those presented in the text. Frequency response functions (as accelerance against frequency) of different skis are compared at one nodal measurement position at different frequencies (i.e., 14Hz and 16Hz). The frequency response is similarly compared with the fore-body of the skis twisted and the FCP edged to simulate conditions representative of a turn, to investigate chatter.

The frequency response functions (as compliance against frequency) at different measurement nodes can be compiled and the results used to illustrate operational deflection shape. Operational deflection shapes of different skis are compared at 14Hz and 16Hz excitation frequencies. The operational deflection shape with the FCP edged is similarly compared.

The operational deflection shape will give mode shape if the frequency response functions are compiled at resonant frequencies. Therefore, it would be worthwhile to identify resonant frequencies from impulse response measurements prior to investigating frequency response. Alternatively, frequency response measurement may be based on frequencies identified from signal analysis (e.g., from field-testing).

B-1 Frequency response

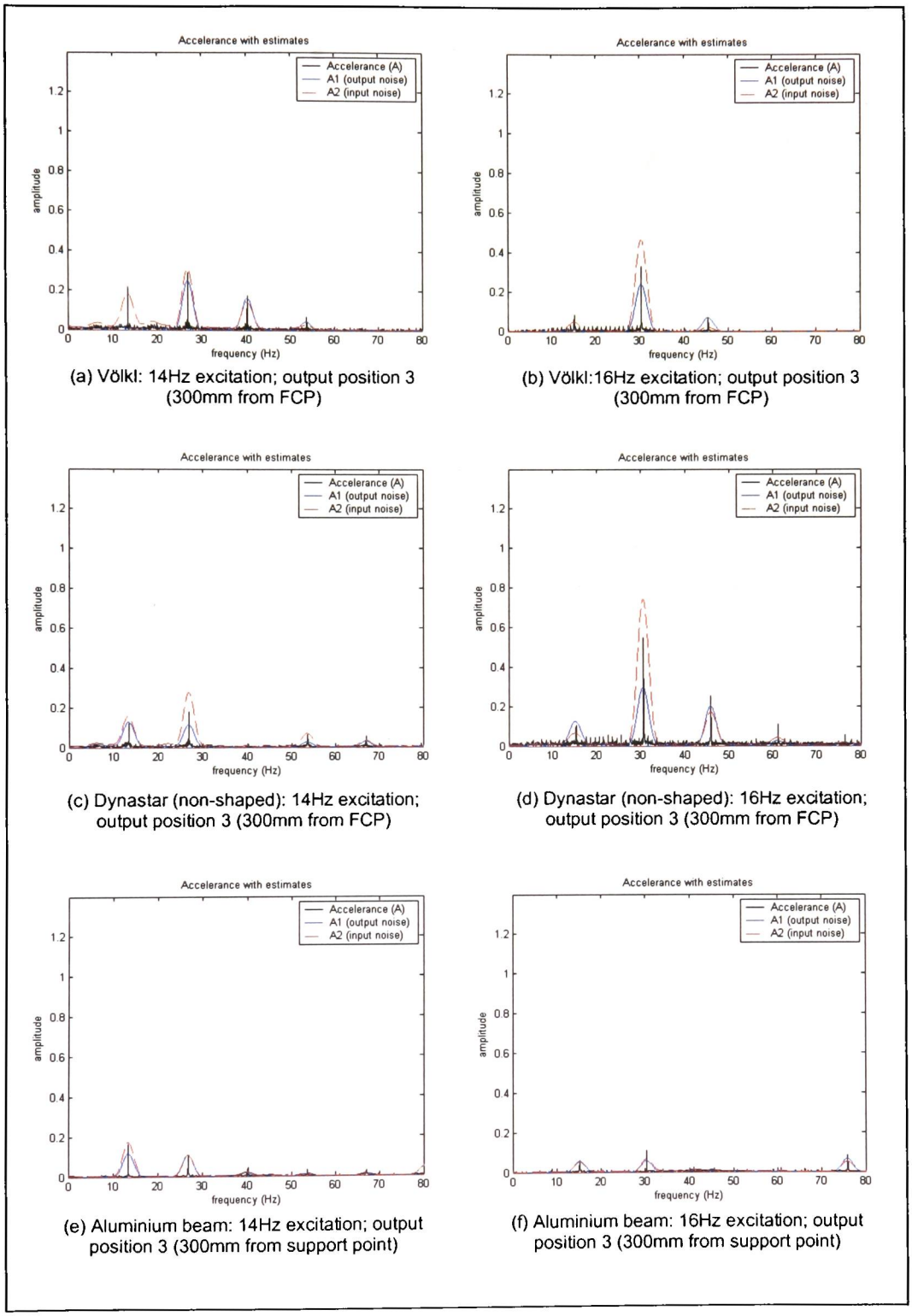

(a) Völkl: 14Hz excitation; output position 3 (300mm from FCP)

(b) Völkl:16Hz excitation; output position 3 (300mm from FCP)

(c) Dynastar (non-shaped): 14Hz excitation; output position 3 (300mm from FCP)

(d) Dynastar (non-shaped): 16Hz excitation; output position 3 (300mm from FCP)

(e) Aluminium beam: 14Hz excitation; output position 3 (300mm from support point)

(f) Aluminium beam: 16Hz excitation; output position 3 (300mm from support point)

Figure B 1: Accelerance (at 14Hz and 16Hz excitation frequencies) 300mm from the FCP: comparing the response of the Völkl "P50 Motion" , a non-shaped (Dynastar) ski and an aluminium beam

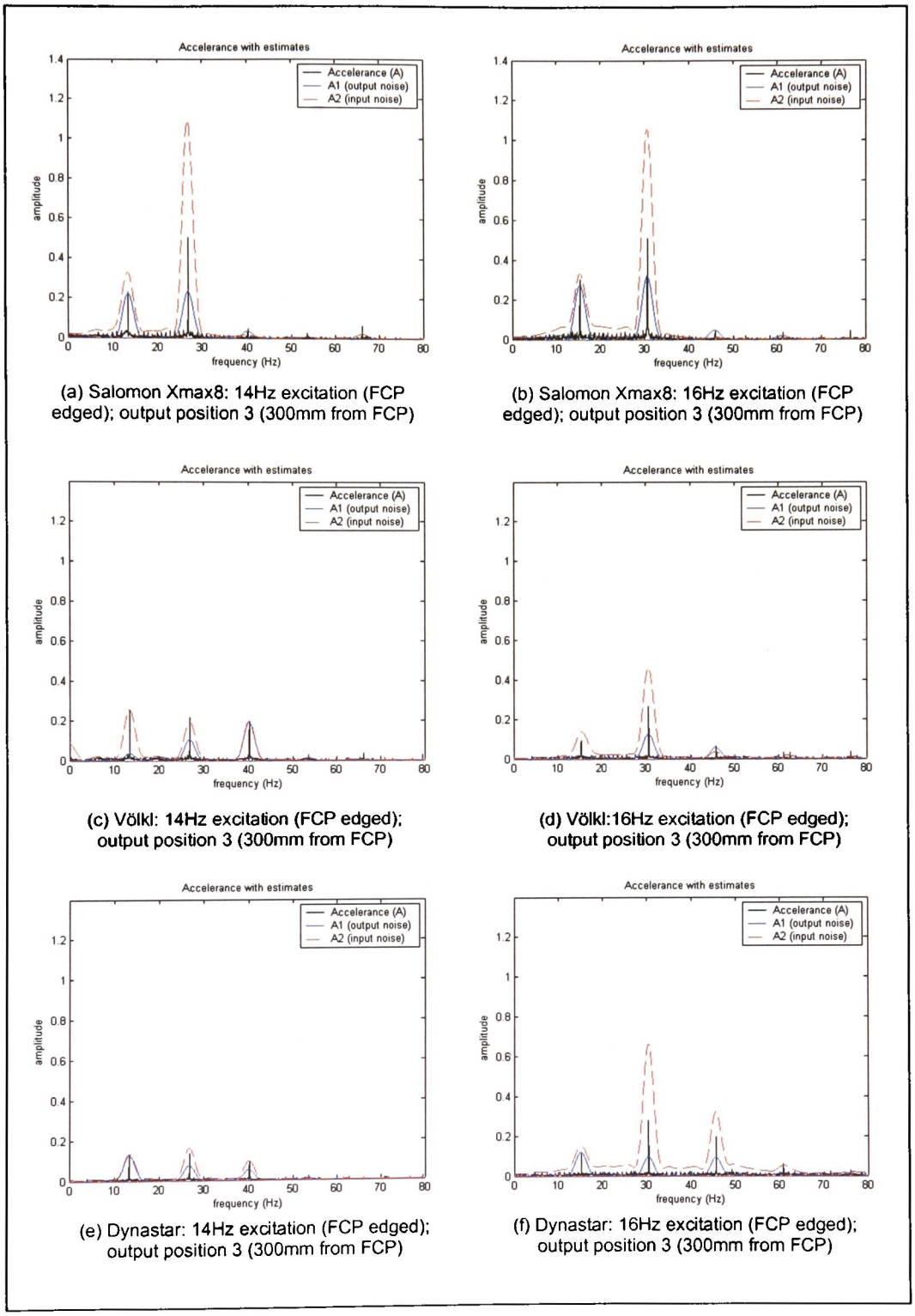

(a) Salomon Xmax8: 14Hz excitation (FCP edged); output position 3 (300mm from FCP)

(b) Salomon Xmax8: 16Hz excitation (FCP edged); output position 3 (300mm from FCP)

(c) Völkl: 14Hz excitation (FCP edged); output position 3 (300mm from FCP)

(d) Völkl:16Hz excitation (FCP edged); output position 3 (300mm from FCP)

(e) Dynastar: 14Hz excitation (FCP edged); output position 3 (300mm from FCP)

(f) Dynastar: 16Hz excitation (FCP edged); output position 3 (300mm from FCP)

Figure B 2: Accelerance (at 14Hz and 16Hz excitation frequencies), 300mm from the FCP - subject to fore-body twist (i.e., at the FCP): comparing the response from the Salomon "Crossmax 8", Völkl "Motion", and non-shaped Dynastar skis

B-2 Operational deflection shape

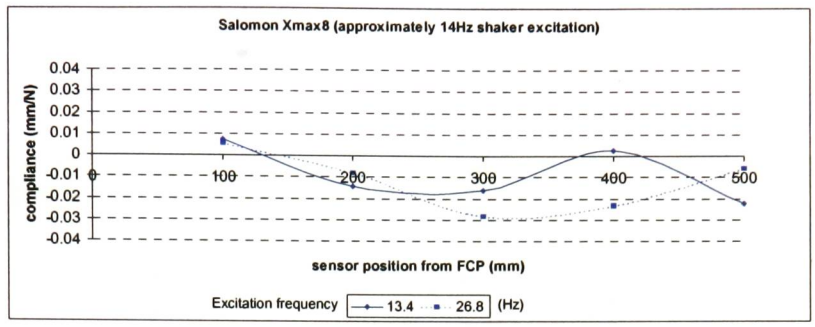

(a) Salomon Crossmax 8; 14Hz shaker excitation

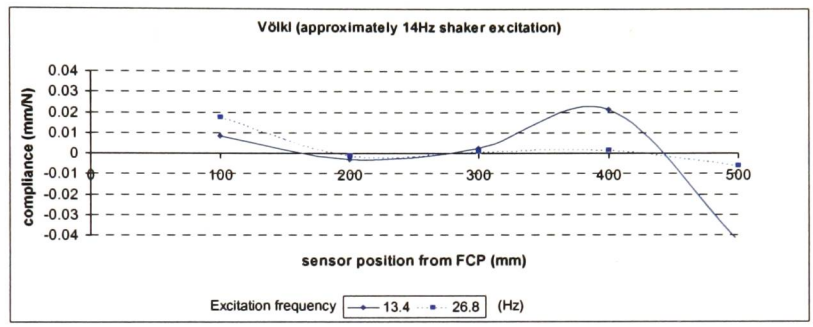

(b) Völkl Motion; 14Hz shaker excitation

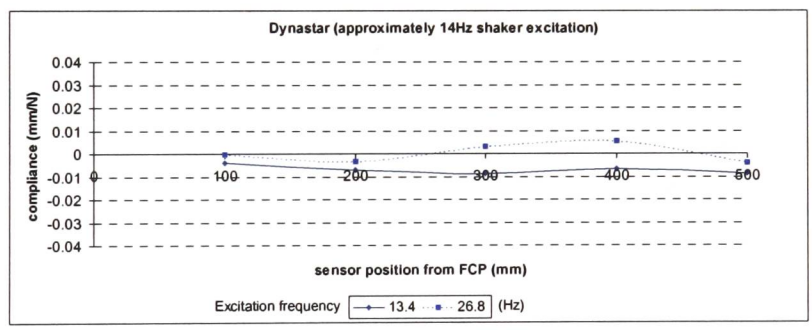

(c) non-shaped Dynastar; 14Hz shaker excitation

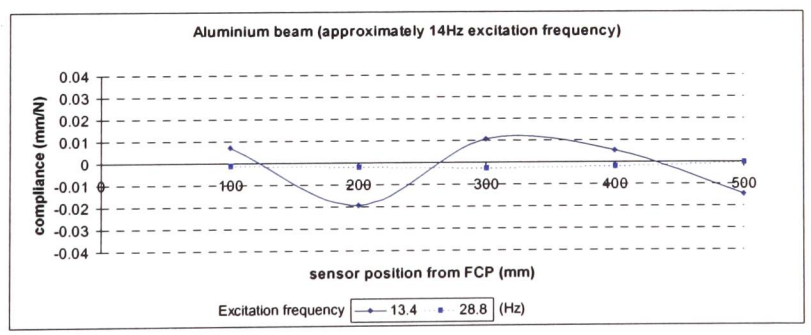

(d) Aluminium beam (cross-section: 70mm x 7mm); 14Hz shaker excitation

Figure B 3: Fore-body operational deflection shapes at excitation frequency of approximately 14Hz – comparing the response of the Salomon "Crossmax 8" and Völkl "Motion" against a non-shaped Dynastar ski and an aluminium beam

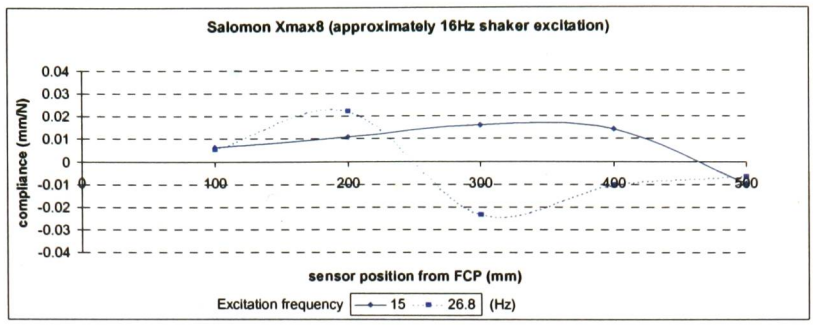

(a) Salomon Crossmax 8

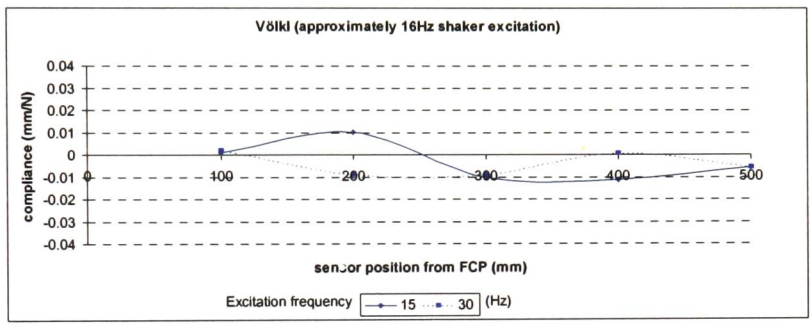

(b) Völkl Motion

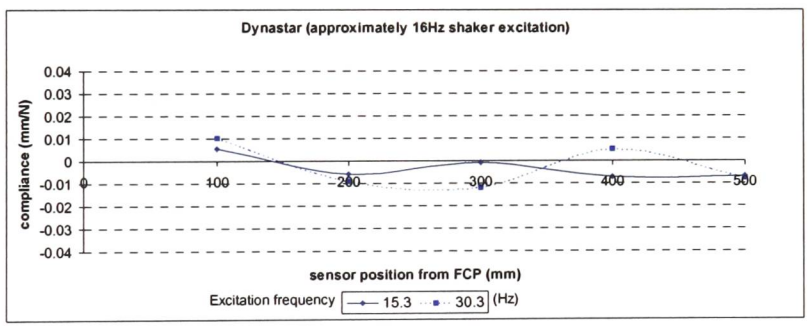

(c) non-shaped Dynastar

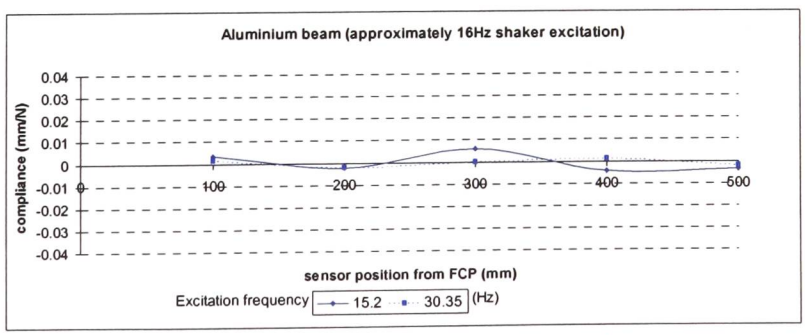

(d) Aluminium beam (cross-section: 70mm x 7mm)

Figure B 4: Fore-body operational deflection shapes at excitation frequency of approximately 16Hz – comparing the response of the Salomon "Crossmax 8" and Völkl "Motion" against a non-shaped Dynastar ski and an aluminium beam

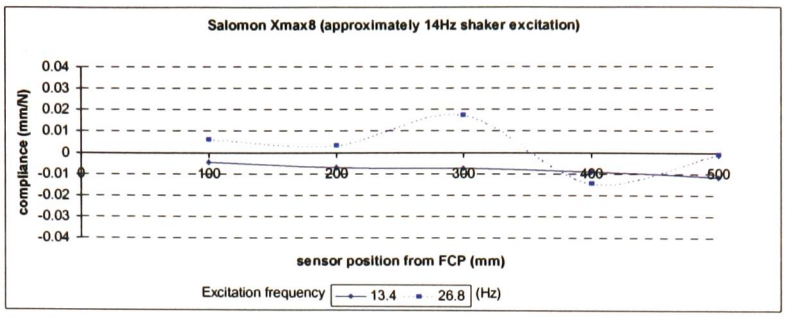

(a) Salomon Crossmax 8; FCP twisted; 14Hz shaker excitation

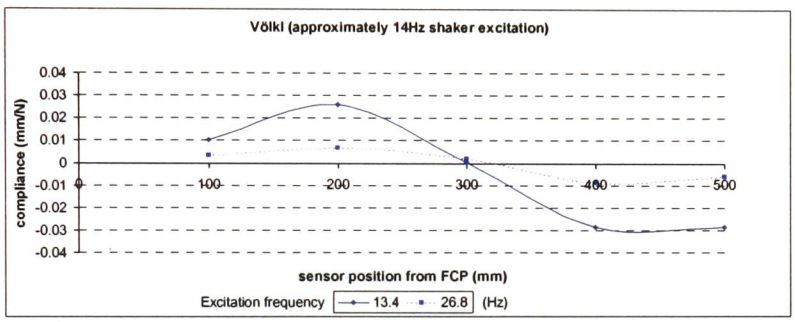

(b) Völkl Motion; FCP twisted; 14Hz shaker excitation

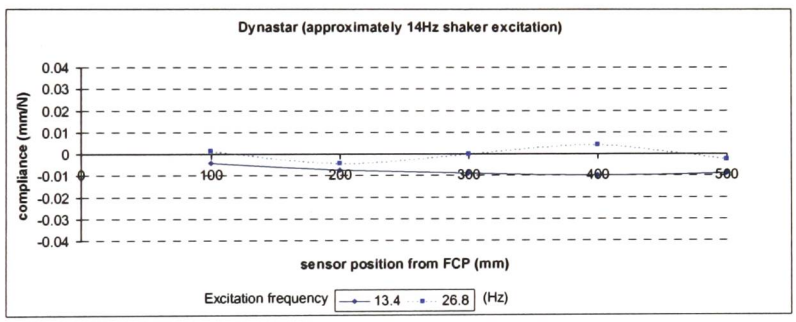

(c) non-shaped Dynastar; FCP twisted; 14Hz shaker excitation

Figure B 5: Fore-body operational deflection shapes at excitation frequency of approximately 14Hz, with the fore-body twisted and the FCP edged – comparing the response of the Salomon "Crossmax 8" and Völkl "Motion" against a non-shaped Dynastar ski

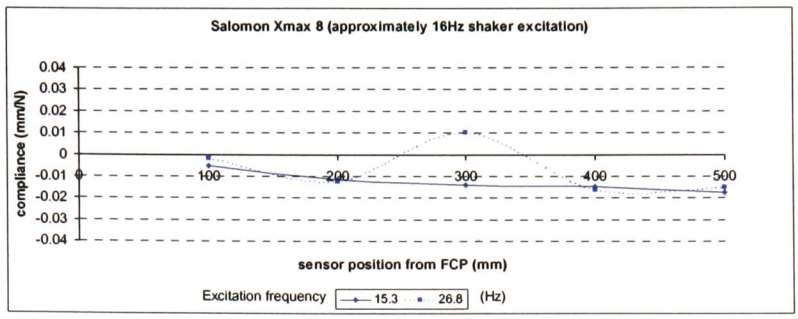

(a) Salomon Crossmax 8; FCP edged; 16Hz shaker excitation

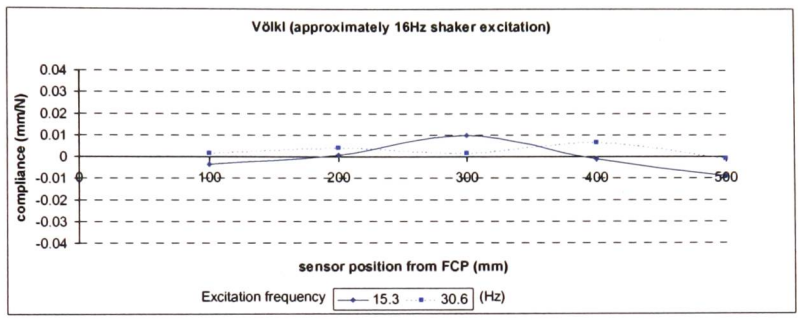

(b) Völkl Motion; FCP edged; 16Hz shaker excitation

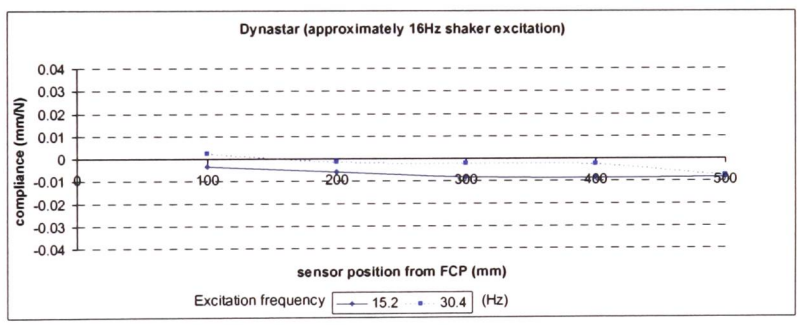

(c) non-shaped Dynastar: FCP edged; 16Hz shaker excitation

Figure B 5: Fore-body operational deflection shapes at excitation frequency of approximately 16Hz, with the fore-body twisted and the FCP edged – comparing the response of the Salomon "Crossmax 8" and Völkl "Motion" against a non-shaped Dynastar ski

Appendix C

Quantifying Damping in the Frequency Domain

The decibel is a relative magnitude between a quantity and a reference quantity of the same type (i.e., the ratio of displacement to a reference displacement) that can be used to present results on a logarithmic scale [Broch 1984]:

i.e., $$N(dB) = 20\log_{10}(\frac{X}{X_{ref}}) \qquad [C\text{-}1]$$

where, N is the number of decibels, X is the measured (displacement) level and X_{ref} is the reference level.

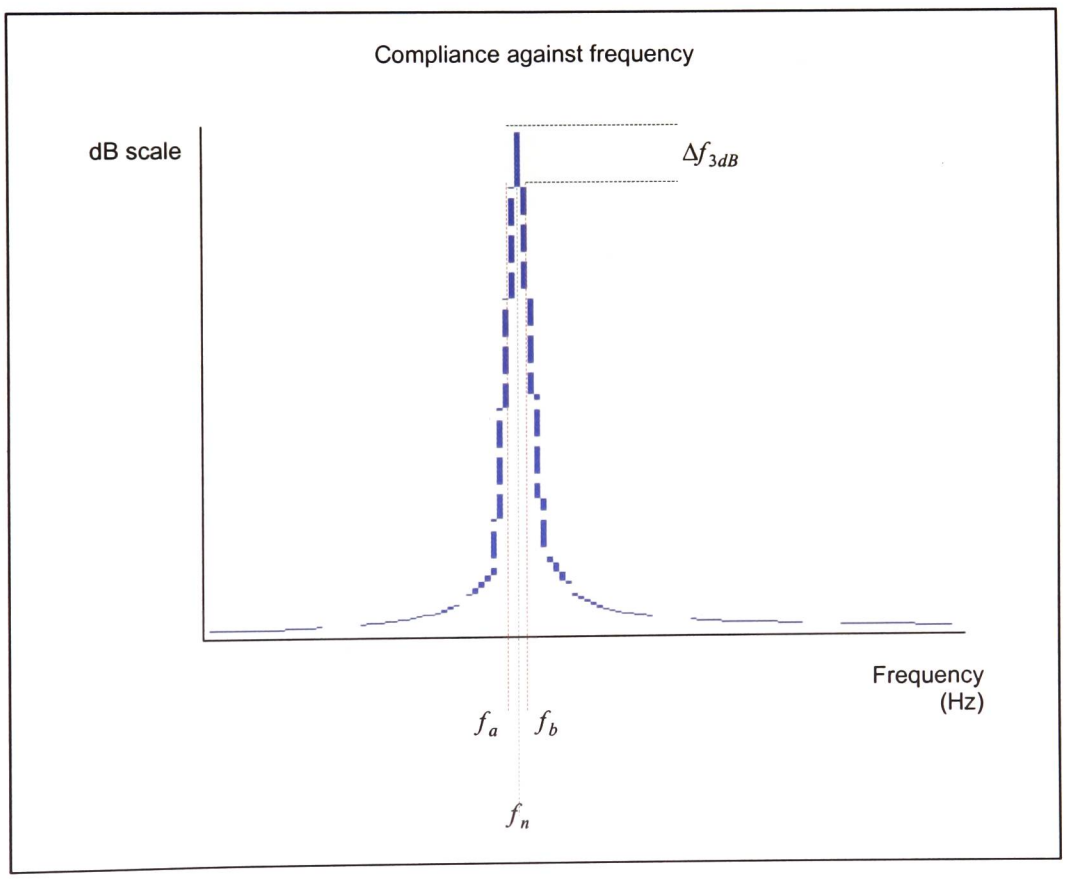

Figure C-1: Quantifying damping from frequency response measurements

From the frequency response curve (on a decibel scale), the resonant frequency can be determined by identifying the frequency (f_n) of maximum response. The damping factor can be found by locating the frequency (f_a and f_b) of the response 3dB down from the maximum value (see figure C–1):

i.e., $$\zeta = \frac{(f_b - f_a)}{2f_n} = \frac{\Delta f_{3dB}}{2f_n}. \qquad [C\text{-}2]$$

Sampling frequency has to be satisfactorily high enough to provide the required resolution to be able to identify f_a and f_b.

The relationship between the different damping descriptors is summarised by Gade and Herlufsen [1994] – see table C–1.

	$\Delta w =$	$\Delta f_{3dB} =$	$\zeta =$	$\sigma =$	$\tau =$
3dB Bandwidth, Δw (rad/s)	Δw	$\frac{\Delta w}{2\pi}$	$\frac{\Delta w}{2w_o}$	$\frac{\Delta w}{2\pi}$	$\frac{2}{\Delta w}$
3dB Bandwidth, Δf_{3dB} (rad/s)	$2\pi\Delta f_{3dB}$	Δf_{3dB}	$\frac{\Delta f_{3dB}}{2f_o}$	$\pi\Delta f_{3dB}$	$\frac{1}{\pi\Delta f_{3dB}}$
Fraction of critical damping, ζ	$2\zeta w_o$	$2\zeta f_o$	ζ	$2\pi\zeta f_o$	$\frac{1}{2\pi f_o}$
Decay constant, σ (s^{-1})	2σ	$\frac{\sigma}{\pi}$	$\frac{\sigma}{w_o}$	σ	$\frac{1}{\sigma}$
Time constant, τ (s)	$\frac{2}{\tau}$	$\frac{1}{\pi\tau}$	$\frac{1}{2\pi f_o\tau}$	$\frac{1}{\tau}$	τ
Natural frequency $w_o = 2\pi f_o$ ($\approx w_d$ for lightly damped resonances)					

table C-1: Interrelationship between different damping descriptors
(produced with reference to Gade and Herlufsen [1994])

An alternative method for carrying out impulse analysis would be to use an impact hammer to excite the fore-body of the ski, cantilever supported at the MRS. Again, an accelerometer is attached to the fore-body to measure the output, with the input being measured by the dynamic load cell on the impact hammer.